Scale-up of gas-liquid stirred tanks using coupled computational fluid dynamics and population balance modelling

SCALE-UP OF GAS-LIQUID STIRRED TANKS USING COUPLED COMPUTATIONAL FLUID DYNAMICS AND POPULATION BALANCE MODELLING

By

Jolius Gimbun

Department of Chemical Engineering
Loughborough University

A Doctoral Thesis submitted in partial fulfilment of the requirements of the award of the degree of Doctor of Philosophy of Loughborough University

Dedication

To my wife Fiona for her love and understanding
&
To my mum & dad for their never ending love and sacrifices

Abstract

The main aim of the work was to produce scale-up methods for the design of aerated stirred tanks using a combined computational fluid dynamics (CFD) and population balance approach. First a modeling study of single phase stirred tanks was performed to evaluate the best model features (turbulence model, impeller's model, discretisation, grid etc). Good agreement was obtained between the CFD simulation and the LDA measurement on the time-averaged mean velocities and turbulence quantities. The angle-resolved mean velocities and turbulence quantities were also predicted very well as were the power number and the positions of the vortex cores.

The next stage involved the development of a population balance model (PBM) which was carried out first using a well-mixed single compartment implemented in MATLAB to reduce the modeling complexity. The algorithm was validated for various mechanisms, namely breakage, aggregation, nucleation and growth which have an analytical solution available from literature. Tests using realistic models for bubble coalescence and breakage were also carried out with the results showing a reasonable agreement with the Sauter mean bubble sizes obtained from empirical correlations. The algorithm also responded well to changes in the turbulence dissipation rate, the initial bubble size distribution and the local gas hold-up, which suggest that the final bubble size is not affected by the initial bubble size.

A fully predictive model must combine both the fluid mechanics and bubble dynamics models which can be performed either by a four-way or three-way coupling simulation. The disadvantage of the latter is that is does not consider the effect of the bubble dynamics in- the two-phase modelling. A four-way coupling (CFD-PBM) method was carried out by implementing the PBM within the CFD code. Various drag models which take into account the effect of distorted bubbles and dense gas dispersion are also considered. Mass transfer models are also implemented using the bubble sizes obtained from the PBM. The CFD-PBM model showed a reasonable prediction of the power number, local bubble sizes, gas hold-up, dissolved oxygen concentration and the mean velocities of the two-phase flow in comparison to experimental data taken from the literature.

Finally, the CFD-PBM model was employed to evaluate the consequences of scale-up on the mass transfer rate in aerated stirred tanks agitated either by Rushton turbine or CD-6 impeller with operating volume ranged from 14L to 1500L. Three scale-up rules, namely a constant P_g/V combined with either constant Fl_g, v_g and VVM were studied. The simulation results suggest, that a successful scale-up may be achieved by keeping the P_g/V and VVM constant, which led to a slightly higher $\langle k_L a \rangle$ representing a more conservative approach. In contrast, constant P_g/V and v_g led to a slight reduction in the rate of mass transfer at larger scale which is in agreement with experimental measurement from the literature. Results from the CFD-PBM simulation also suggest a similar scale-up rule may be applicable for an advanced gas dispersion impeller such as the CD-6 which yielded a similar scale-up trend to that of a Rushton turbine.

Acknowledgement

I would like to thanks the following people and organisations;

- My supervisors Prof. C. D. Rielly and Dr. Z. K. Nagy for their guidance through an effective well arranged weekly meeting. They gave me a lot of freedom in my work, while they were always present to help me seeing things in perspective. I appreciate Prof. Rielly expertise and enthusiasm in CFD, especially on mixing and gas-liquid flows, his critical view on the technical and scientific aspect of this work, as well as his expertise in programming especially on Visual Basic; and Dr. Nagy large experience on programming especially in MATLAB where he has actually initiated the population balance algorithm development by himself from standard method of moment, quadrature method of moment, product difference and the differential algebraic equation. Prof. Rielly's extensive contact to other experts within academia (i.e. Prof. Derksen, Dr. Marchisio) and industry (FLUENT UK) also has helped a lot towards completion of this study. This study will never be possible without the endless enthusiasm, support and guidance from both of them.
- Dr. D. L. Marchisio for providing the single phase QMOM UDF for particle aggregation which has been a basis of the multiphase QMOM UDF in this work.
- Dr. Ed Wynn of Fluent UK for a fruitful discussion regarding my research work, especially on the UDF.
- Prof. Jos Derksen for the high quality LDA data for the single phase stirred tank. I would also like to thanks him for a fruitful discussion about my CFD-PBM modelling at ISMIP VI 2008.
- The two examiners, Prof.dr.ir. H.E.A. van den Akker from Department of Multi-Scale Physics at Delft University of Technology and Dr. Henk Versteeg from Wolfson School of Mechanical and Manufacturing Engineering at Loughborough University for devoting their time and effort reading and giving a valuable feedback to the final thesis.
- Prof. Alain Line for a fruitful discussion regarding the impeller vortex core.

- Dr. D. Kubicki and Fluent University Support Forum for a fruitful discussion about multiphase UDF development.
- Assoc. Prof. Dr. Ville Alopaeus and Dr. Charles D. Immanuel for a fruitful discussion about population balance modeling.
- Dr. Malalasekera for the Fluent 6.3 license.
- Public Service Department of Malaysia (later transferred to Ministry of Higher Education) and Universiti Malaysia Pahang (formerly known as KUKTEM) for the scholarship.
- My wife, Fiona for her love and courage.
- Rashmi from Universiti Putra Malaysia for a fruitful discussion about the implementation of drag coefficient model via UDF in eulerian-eulerian framework.
- Staff of Department Chemical Engineering at Loughborough University especially Mr Paul Izzard who always been there to help when needed; the main office staff Ann, Anne & Yasmin; staff at research student office, professional development, medical centre and at student accommodation services which always been helpful throughout my study.
- Uncle Joe, Nazrul, Angie, Hness, Sabrina, Chuah, Thomas, Reynold, Adeline, for encouragement.
- My best friend in Loughborough, especially those at room S169 (Anand, Elina, Mu, Ibiba, Rushdi, Erum, Boom, Pawel, Kevin), Dr. Liansong, Siti, Salemi, Heema, Savita, Ihab, Abhijeet, Godaarz and many others.
- Shawn for his friendship and encouragement.

Table of contents

List of Figures

List of Tables

Nomenclature

A_0	constant of eq.(3.6)
A_s	constant of eq.(3.6)
a	interfacial area per unit volume
$a(L_i)$	breakage kernel
$b(k, L_i)$	daughter bubble distribution function
B	nucleation kernel
C	impeller off-bottom clearance
C_o^*	oxygen solubility in water
C_D	drag coefficient
$C_o(t)$	oxygen concentration in water
C_μ	turbulent viscosity
C_{b1}	constant of eq.(3.23)
C_{b2}	constant of eq.(3.21)
C_{ij}	convection term
C_{w1}	constant of eq.(3.24)
C_{w2}	constant of eq.(3.24)
C_{w3}	constant of eq.(3.24)
C_{des}	constant of eq.(3.25)
$C_{\varepsilon 1}$	constant of eq.(3.5)
$C_{\varepsilon 2}$	constant of eq.(3.5)
C_1	constant of eq.(3.7)
C_2	constant of eq.(3.7)
$C_{1,RNG}$	constant of eq.(3.8)
$C_{2,RNG}$	constant of eq.(3.8)
D	impeller diameter
$D_{T\,ij}$	turbulent diffusion term
$D_{L\,ij}$	molecular diffusion term
d_{32}	Sauter mean diameter
$\overline{d}_{32}$	volume averaged d_{32}
$\overline{d}$	characteristic length scale for DES model
D_l	diffusion coefficient
Eo	Eotvos number
Fl_g	aeration number
$\vec{F}_{lg}$	interaction force mainly due to drag
$\vec{F}_{lift}$	lift force
Fr	Froude number
$\vec{F}_{vm}$	virtual mass force
F_{ij}	production by rotation term
g	gravity acceleration
$g(L)$	general breakage kernel
$G(L)$	growth kernel
G_v	turbulent production term for Spalart-Allmaras model
h_f	final film thickness

h_o	initial film thickness
H	liquid height
K	model constant for Danckwerts' model
k	turbulent kinetic energy
k_{tot}	total turbulent kinetic energy
k_{coh}	coherent turbulent kinetic energy
k_{ran}	random turbulent kinetic energy
K_{gl}	interphase momentum exchange coefficient
k_L	liquid side mass transfer coefficient
k_La	local mass transfer coefficient
$\langle k_La \rangle$	global mass transfer coefficient
L	abscissa for QMOM
L_D	impeller blade length
L_s	subgrid scale mixing length
N	rotation speed
N_{CD}	complete dispersion impeller speed
n_e	number of eddies per unit volume
n_i	number of bubbles per unit volume
$n(L)$	number density of particle of size L
N_{p0}	single phase power number
P	pressure
P_0	single phase power input
P_g	gas-liquid power input
P_k	turbulent production term
P_{ij}	stress production term
Q_g	gas flow rate
r_o	specific oxygen consumption rate
R	aspect ratio of major and minor elipsoids bubble radius
Re_b	Bubble Reynolds number
Re	Impeller Reynolds number
s	fractional rate of surface-element replacement in Danckwerts model
S_{ie}	collision cross-sectional area
S	vorticity magnitude
$\widetilde{S}^3$	characteristic vorticity magnitude
S_ε	turbulent dissipation source and sink term
T	tank diameter
t	time
u, v	velocity components
U^*	characteristic velocity
u_{slip}	slip velocity
$u_\infty(L_i)$	bubble rise velocity
$u_t(L_i)$	turbulent velocity
$u_t(L_e)$	eddy velocity
v_g	superficial gas velocity
VVM	volume per unit volume
w	weight for QMOM
W	impeller blade width
Y_v	turbulent destruction term for Spalart-Almaras model

Greek

ν_l	kinematic viscosity
θ_{ie}	collision rate of bubbles with turbulent eddies
κ_i	break-up efficiency
$\Lambda(L_i, L_j)$	bubble collision eficiency
$\omega(L_i, L_j)$	bubble collision frequency
μ_k	moments of the bubble size distribution
$\beta(L_i, L_j)$	coalescence kernel
ε	turbulent dissipation rate
ε_{ij}	turbulent dissipation term
Γ	torque
Δt	impeller thickness
η	mean strain
$\tilde{\Omega}_{ij}$	mean rotation rate
Ω_k	angular velocity
ϕ	scalar
ϕ_{ij}	pressure strain term
$\dot{\gamma}$	strain rate
Λ	integral length scale
μ	fluid viscosity
ρ	fluid density
σ	surface tension
σ_k	dimensionless constant in eq.(3.1)
σ_ε	dimensionless constant in eq.(3.2)
τ_{ij}	stress tensor
σ_{ij}	subgrid scale molecular viscosity stress tensor
Δ	maximum grid spacing

Subscripts

b	bubble
$dense$	dense bubble
g	gas
l	liquid
eff	effective

List of Abbreviations

CARPT	Computer-automated radioactive particle tracking
CFD	Computational fluid dynamics
CSP	Capillary suction probe
CT	Computer tomography
DAE	Differential algebraic equation
DES	Detached eddy simulation
DI	Digital imaging
EIT	Electric impedance tomography
ERT	Electric resistance tomography
FFT	Fast Fourier transform
GRT	Gamma ray tomography
IZ	Ishii-Zuber drag model
LDA	Laser doppler anemometry
LES	Large eddy simulation
LIF	Laser image fluorescence
PBE	Population balance equation
PBM	Population balance modelling
PDA	Phase doppler anemometer
PIV	Particle image velocimetry
PLIF	Planar laser induced fluorescence
MOC	Method of classes
MOCh	Method of characteristic
MOM	Method of moment
MRF	Multiple reference frame
PD	Product difference
QMOM	Quadrature method of moment
RDT	Rushron turbine
RANS	Reynolds averaged Navier-Stokes
RNG	Renormalised k-ε
RSM	Reynolds stress model
SA	Spalart-Allmaras model
SGS	sub-grid scale
SMM	Sliding mesh method
SN	Schiller-Naumann drag model
SST	Shear stress transport model

1 INTRODUCTION

1.1 Motivation

Mixing tanks are widely used in the chemical, pharmaceutical, and biochemical process industries. It is estimated that about 50% of all chemical productions, by value, takes place in stirred vessels, representing an annual turnover value of around €1370 billion worldwide, indicating the importance of stirred tank reactors (Butcher and Eagles, 2002). Despite being a basic unit operation in most of the chemical process industries, the design of stirred tanks is still primarily based on global correlations using for example the power number, aeration number, Froude number or other semi empirical scale-up correlations derived from laboratory scale experiments. Such methods cannot provide detailed insight into the local flow phenomena involved in achieving desired process results.

Experimental measurements in stirred tanks are often only available for a limited range of vessel geometries and for small scale vessels; often these measurements comprise global values obtained. It is hard to find single measurement techniques that could provide all information on the gas-liquid stirred tanks. For instance, gamma ray or x-ray tomography is an excellent method for measuring the gas hold-up distribution, but it does not give information regarding the two-phase flow field and the bubble size. Similarly, the computer-automated radioactive particle tracking (CARPT) method is capable of measuring the two-phase flow field at high gas loading, but it cannot be applied to measure the bubble size distributions and gas hold-up. Some of the newest techniques like planar laser induced fluorescence (PLIF) could give more comprehensive measurement, but it has yet to be applied for aerated stirred tanks. A combined approach consisting of gamma ray tomography (GRT)-CARPT-capillary suction probe (CSP) is needed for a comprehensive experimental study on gas-liquid stirred tanks. Investment and operating costs to acquire and to run those entire instruments are expensive. Alternatively, a computational method such as a combined computational fluid dynamics and population balance model (CFD-PBM) also would be capable of providing a detailed description of the two-phase flow in aerated stirred tanks, at far lower

investment and running costs. Therefore, this study is devoted into development of a computational approach with improved capabilities which may be used in designing, troubleshooting and scaling up of aerated stirred tank.

Modelling of aerated stirred tanks is still highly complicated, despite the many years of studies which have been undertaken to elucidate numerically these flow phenomena. Many attempts to model a gas-liquid stirred tank have been performed in the past (see further reviews in sections 5.2 and 6.2). However, most of these studies are oversimplified and thus cannot be regarded as a priori design methods. The following are the most common simplifications employed by previous works:

1) Treating a gas-liquid flow as a one-way coupled simulation

2) Employing a uniform bubble size throughout the tanks which may not be valid, since the bubbles near the impeller should be a lot smaller than the those in the bulk region due to intense turbulence

3) Using an inappropriate drag model for bubble i.e. drag model for spherical particle e.g. Schiller and Naumann (1935) model or using a constant correction for turbulence induced drag throughout the tank e.g. Brucato *et al.* (1998) model

4) Using an inappropriate model for bubble size modelling such as the bubble density method which does not consider the bubble-bubble and eddy-bubble collisions in a proper way, or even worse using a volume averaged correlation such as that from Calderbank (1958)

5) "Correcting" the constants in the bubble breakage and coalescence kernels in order to obtain a good prediction of the local bubble sizes rather than using appropriate kernels combined with the fluid mechanics properties obtained from a proper CFD simulation

6) Lack of grid analysis study which will affect the accuracy of turbulence dissipation rate prediction and hence the bubble size since the breakage and coalescence kernels depend on the turbulent dissipation rate

This work attempts to address the above-mentioned simplifications with the intention of producing a model which combines both CFD and PBM with improved capabilities for predicting the dynamics and mass transfer characteristics of gas-liquid flows in stirred tanks.

1.2 Objective and Scope

The aim of this study is to develop a modelling method for hydrodynamics and gas dispersion in single phase and aerated stirred tanks, with the intention of elucidating design and scale-up methods for gas-liquid stirred tanks via CFD. The first part of this work deals with the modelling of a single phase stirred tank and was carried out to evaluate the most appropriate turbulence model and modelling strategy (impeller modelling, discretisation, grid) for prediction of mean and turbulence flow in stirred tanks. The study considers a wide range of variables in stirred tanks such as the mean velocities, turbulence kinetic energy, turbulent dissipation rate, power number and vortex core position, in comparison to experimental results. A critical assessment of the angle-resolved turbulence quantities was also carried out, besides evaluating the angle-averaged flows.

The second stage of this work involves algorithm development and testing: the PBM implementation is validated for breakage, aggregation, nucleation and growth problems. Once the implementation and validation had been completed, the real bubble coalescence and breakage kernels were implemented for a single compartment PBM. Testing and sensitivity analyses were also performed to ensure the model responds correctly to changes in the fluid hydrodynamics (predominantly through the turbulence dissipation rate and gas hold-up) and the initial bubble size conditions. The single compartment PBM was then extended into a multi-compartment PBM for an aerated stirred tank. Initially all the algorithms were developed and tested in MATLAB, due to the availability of the required mathematical / numerical solvers. Furthermore, the MATLAB programming language allowed easy access to debugging and visualisation techniques. Once the calculation methods had been established, the programming language was changed from MATLAB to C, to make the codes suitable for inclusion as User Defined Functions (UDF) in the Fluent CFD package. Apart from the PBM, a UDF to account for the interfacial force i.e. using

a drag law suitable for bubbly flow, and the mass transfer model were also implemented. Once completed, the UDF was employed to predict the hydrodynamics, aerated power number, gas hold-up, local bubble sizes and mass transfer coefficient of stirred tanks of various volumes for which experimental data are available from literature for necessary validation.

Finally, the developed UDF is then employed to evaluate numerically the effect of scale-up on gas-liquid stirred tanks of volumes ranged from 14 L to 1500 L agitated either by a Rushton turbine or a CD-6 impeller. Various scale-up strategies such as constant aeration rate (VVM), aeration number (F_{lg}) and superficial gas velocity (v_g) combined with a constant power input per unit volume (P_g/V) were evaluated for gas-liquid stirred tanks. The effect of scale-up was evaluated by comparing the volumetric mass transfer coefficient, local mass transfer coefficient and oxygen concentration profile in the tanks.

1.3 Main Contributions of This Work

The Detached Eddy Simulation (DES) employed to solve a turbulence flow in a single phase stirred tank in this work is relatively new and has not been previously applied to solve for a stirred tank flow. In this work an extensive validation of the DES model for predicting the turbulence quantities in stirred tanks is presented. This study covers both angle-averaged and angle-resolved predictions of mean velocities and turbulent quantities in stirred tanks. Some issues like the influence of the vortex core on the tangential velocity prediction and CFD prediction of the vertical position of the vortex core in the wake of the impeller is believed to be the first of its kind. A PIV-like data extraction from a transient DES simulation using a macro instruction was employed in this work. This marks a significant improvement in stirred tank modelling, which enable a direct comparison with PIV experimental data.

Many solution techniques have been introduced for quadrature method of moments (QMOM) in the past, however, no one has actually tried to solve the QMOM via the differential algebraic equation (DAE) solution method. This work explores the possibility of solving QMOM via DAE method. Numerical stability and accuracy of the DAE method are compared to the well established QMOM

solution via the product difference (PD) algorithm. The DAE method is proven to be a more robust and accurate solution in most of the cases tested in this study. The DAE method also offers a significantly faster solution than the PD based method. The DAE method could be a better approach for solving QMOM in the foreseeable future. However, the DAE-QMOM cannot be implemented within a commercial CFD software, e.g. FLUENT at present due to unavailability of the DAE solvers.

The three-way coupling simulations of an aerated stirred tank which combined both CFD and PBM via multi-compartment model have been performed in the past by Laakkonen *et al.* (2006a; 2006b; 2007). Details about the phase coupling in gas-liquid stirred tanks is given in section 5.2. However, solution of the population balance equation is provided by the method of classes instead of QMOM in their work. Thus, the multi-compartment modelling via QMOM method in this work is a significant contribution.

The QMOM has not been employed to solve the bubble dynamics in gas-liquid stirred tanks, apart from the work by Petitti *et al.* (2007) which has used a simple break-up kernel instead of one based on realistic physics. They also did not include a coalescence kernel in their work. Apart from Petitti *et al.*'s (2007) study there has been no other attempt to implement the QMOM method to model the bubble size distribution in gas-liquid stirred tanks. Therefore, the solution of bubble dynamics in gas-liquid stirred tanks via QMOM through UDF (CFD-PBM) is a significant contribution.

A numerical assessment of the effect of scale-up on the mass transfer in gas-liquid stirred tanks agitated by a conventional and advanced gas dispersion impeller has not been attempted in the past. The scale-up methods assessed the most technically sound parameters i.e. a combination of a constant power input per unit volume with either constant aeration rate, aeration number or gas superficial velocity. The CFD-PBM models developed in this work are also able to reproduce correctly the findings obtained experimentally for scale-up of gas-liquid stirred tanks by Figueiredo and Calderbank (1979) which further confirm the prediction ability of the model.

1.4 Structure of the Thesis

The structure of the reminder of the thesis is outlined as follow:

Chapter 2 provides a description of the applications and general design features of aerated stirred tanks. A general description on the flow characteristics of the system, as well as the dimensionless groups and correlations to account for the flow phenomena are presented. This chapter also provides a brief discussion of the advanced experimental techniques available for aerated stirred tanks, mentioning their applications and limitations for bubbly flow analysis. A summary of the previous experimental work on gas-liquid stirred tanks is also presented. A brief discussion on the scale-up methods for aerated stirred tanks is also provided.

Chapter 3 gives a review of the CFD approach applied for stirred tanks modelling of single and multi-phase flows including the turbulence modelling, discretisation schemes, impeller modelling and solution procedures. The performances of three different RANS models, DES and LES models were compared with angle-averaged and angle-resolved experimental data. The results for mean velocities, turbulent kinetic energy, turbulence dissipation rate, position of the vortex core, and power number for stirred tanks agitated by Rushton turbine and pitched blade impeller are presented and compared with experiments.

Chapter 4 is devoted to a population balance model development where the implementation is validated using various simplified functions and the prediction is compared against analytical solutions. A brief review of the common method for solving the population balance equation is also presented. A detailed description of the algorithm used to solve the population balance equation is also outlined. The new solution technique for solving QMOM via a differential algebraic equation solver is also presented.

Chapter 5 discusses the modelling method for gas-liquid stirred tanks including the two-phase CFD model and the bubble coalescence and breakage kernels. A test result for PD-QMOM using a realistic model for bubble coalescence and breakage in a single compartment assuming a homogeneous and well mixed flow is also presented. The effect of the turbulence dissipation rate and the initial

bubble size distribution on the final bubble size is also outlined. Implementation and prediction of local bubble size in aerated stirred tanks using a multi-compartment model combining both the two-way CFD simulation and PBM is also presented.

Chapter 6 is dedicated to a coupled CFD-PBM study in which simulations of aerated stirred tanks were performed. A review of the previous work on CFD and population balance models related to the gas-liquid system is also presented in this chapter. The mathematical model used to account for the two-phase turbulence flow is also described. A brief review of the bubble breakage and coalescence kernels is outlined. Implementation of the population balance model via CFD-PBM is also discussed. Detailed assessments of the model predictions for the two-phase hydrodynamics, power number, local bubble sizes, gas hold-up and mass transfer rate are also presented. After the validation, a scale-up study of aerated stirred tanks with operating volumes ranging from 14L to 1500L is presented. Two different impellers namely the Rushton turbine and the CD-6 are considered for three different scale-up cases. The implications for scale-up of the oxygen transfer rate and mass transfer coefficient for tank sizes from 14 L to 1500 L are discussed.

Chapter 7 draws together a summary of the thesis and outlines the future work which might be derived from the model developed in this work.

2 HYDRODYNAMICS AND DESIGN OF GAS-LIQUID STIRRED TANK

2.1 Overview

This chapter gives a brief description of the applications of aerated stirred tanks in industry. The typical design of an aerated stirred tank is described and a wide range of impeller designs and applications are also discussed. In addition, the experimental techniques used to characterise the gas-liquid flows in stirred tanks are also described. A brief summary about the experimental data available from literature and adopted for comparison with the CFD simulation is also presented. This chapter also provides a summary of the previous experimental work on gas-liquid stirred tanks; the often-used empirical correlations for stirred tanks are also listed and the scale-up issues are outlined. These correlations present numerous limitations in the case of complex flow phenomena in stirred tanks, indicating the need for development of CFD approaches for the design and scale-up of aerated stirred tanks.

2.2 Application of Aerated Stirred Tanks

According to Butcher and Eagles (2002), about 50% of all chemical productions, by value, takes place in stirred vessels representing an annual turnover value of €1370 billion worldwide and indicating the importance of stirred tank reactors. Gas-liquid stirred tanks are used for a variety of processes which may involve reactions such as bioleaching, neutralisation, oxidation, chlorination and hydrogenation or pH control and oxygen supply in fermentation systems. Some examples of such industrial processes are described below.

2.2.1 Bioleaching

Specific metals can be extracted from their ores via a process called bioleaching through the use of bacteria. It is a technique used by the mining industry to extract minerals such as gold and copper from their ores. A key success factor is the ability to control the rate of microbial growth in a stirred tank reactor. This is influenced by metal concentrations, nutrient addition, CO_2 levels and oxygen supply, pH and temperature. Therefore, air and CO_2 are sparged into the tank to meet the microorganisms requirements.

2.2.2 pH control

CO_2 and NH_3 are often sparged into a stirred tank (e.g. a fermenter) to adjust the pH to the optimum condition of the fermentation organism. Gas sparging offers much better dispersion and faster mixing with the growth media, besides providing a very low change in pH which might be difficult to achieve via a liquid (acid or base) addition.

2.2.3 Aerobic fermentation

Stirred tank fermenters are widely used in the food and pharmaceutical industries to produce a variety of products such as antibiotics, yeasts, enzymes, amino acids, vitamins, flavour enhancers and thickening agents with the assistance of microorganisms (Benz, 2003). In this process air is sparged to provide oxygen, enhancing the cell growth or desired product formation in fermentation reactions.

2.2.4 Hydrogenation

Hydrogenations involve the direct addition of diatomic hydrogen under pressurised condition in the presence of a catalyst. One example is the production of margarine from vegetable oil. In many hydrogenation processes, mechanical agitation is required to suspend catalyst particles (e.g. nickel-based for margarine production) and disperse the hydrogen which is sparged into the bottom of the tank.

2.2.5 Biodegradation/Bioremediation

Biodegradation or bioremediation can be any process that uses microorganisms, fungi, green plants or their enzymes to return the environment altered by contaminants to its original condition. Some examples of such process carried out in aerated stirred tanks have been reported by Mohorcic *et al.* (2004) and Bustard *et al.* (2002). The main purpose of air sparging in bioremediation is to stimulate growth of bacteria (oxygen is required for respiration) for hazardous waste treatment.

It is clear from the examples explained above that aerated stirred tanks are widely used in the process industries. It should be also noted that many of the relevant industrial processes are actually three-phase, since they involve gas, liquid and solid phase. In general gas dispersion seems to have more effect on the overall tank performance, rather than the solid mixing, as the sparged gas is

typically involved in the reaction (pH control, hydrogenation) or consumed by the microorganism (bioreactor, bioremediation, bioleaching). It is possible to increase the mass transfer rate from or to solid particles by making the particles size smaller (increasing the interfacial area) but the same method cannot be applied to the gas-liquid systems because a balance between coalescence and breakage determines the bubble size distribution. Therefore, the mass transfer to and from bubbles may become a limiting rate of the overall process i.e. mass transfer limited reactions in bioreactor. Such a problem might be addressed using a combination of a better gas dispersion impeller (e.g. CD-6, BT-6, A315 summarised in Table 2-1 and 2-2) and well designed stirred tanks in which the baffles, the shape of tank bottom, sparger position and the ratio of tank height over tank diameter are optimised to promote better mass transfer rates. Apart from the vessel design, the operating variables like the impeller speed and gas sparging rate also affect the tanks performance and a proper validated CFD model can assist the design and scale-up of aerated stirred tanks.

2.3 Design of Aerated Stirred Tank

A design with a good mass transfer capability is important because most of the time the sparged gas plays an important role in product formation or reaction (except in some cases like a froth flotation system). Therefore, most aerated tanks are designed to achieve a high mass transfer rate. Interfacial area is well known as a major indicator of mass transfer performance in an aerated system and thus it becomes a primary concern in aerated stirred tank design (Tatterson, 1994). According to Lane (2005), a condition of large interfacial area can be achieved through a combination of sufficiently fine bubbles and sufficiently high volumetric hold-ups. Such conditions can be achieved at economic power input, depending on the impeller choice.

The typical design of aerated stirred tanks include a centrally top or bottom mounted shaft with single or multiple impellers, baffles near the wall, and a sparger device of either an open ended pipe or a ring sparger below the impeller. Baffles are attached at the tank perimeter to prevent the liquid from performing a solid-body rotation or vortex which would provide poor mixing. A tank with a high aspect ratio is also often used, for example up to $H:T$ = 4:1 for an aerated

fermenter (Soderberg, 1997) to increase the gas residence time. A tall tank also has larger surface area for heat transfer which may be needed because most fermentations processes are exothermic. Soderberg claimed that a taller bioreactor ($H:T$ = 4:1) needs less aeration power input (from a compressor) compared with the shorter one ($H:T$ = 2:1) to get a similar level of gas dispersion. A taller bioreactor also uses a smaller impeller diameter than a shorter one, thus further reducing the power requirement. Multiple impellers are needed for a tall bioreactor in order to achieve an adequate aeration-agitation regime (Stanbury and Whitaker, 1984). In such cases multiple impellers from a combination of gas dispersion and axial flow impeller are said to be more appropriate (Arjunwadkar *et al.*, 1998).

There are many types of impeller available commercially, and they are usually selected for specific applications. Impellers with excellent gas dispersion capability like the BT-6, A315, CD-6 and Scaba impeller are often used in aerated stirred tanks. A conventional impeller design like the Rushton turbine can produce higher turbulence dissipation rates, desired for bubble break-up but experimental observation shows they tend to suffer from a higher gassed power drop than the advanced impeller (refer section 2.7). That might explain why the Rushton turbine is no longer a popular choice for industrial applications, especially when dealing with aerated tanks, although it is still widely used in research studies. Gas dispersion impellers often make use of a disc (CD-6, BT-6, Scaba) or overlapping blades (A315) to prevent short circulating of the gas along the shaft.

A standard tank configuration, widely studied experimentally and numerically, is shown in Fig. 2-1. There is no such thing as a standard geometry stirred tank, however most of the previous study deals with a geometry consisting of a flat bottomed cylindrical tank (e.g. Yianneskis and Whitelaw, 1993; Derksen *et al.*, 1999; Yeoh *et al.*, 2004; Montante *et al.*, 2007), filled to a depth, H, which is equal to the tank diameter, T, and mounted with four baffles of width $B = 0.1T$. The impeller usually is a Rushton turbine of diameter $D = T/3$ and is centrally mounted at the bottom clearance of $C = H/3$. The impeller disc diameter is $D_2 = 0.75D$, blade length $L = 0.25D$ and blade width $W = 0.2D$. A sparger is usually

placed below the impeller with clearance of $C_2 = 0.1C$ and has a diameter ranging from $0.5D$ to $0.8D$. Experimental measurements by Baker (1992) suggest that a bigger sparger diameter is less prone to flooding than a smaller one and also requires less power to reach a fully disperse regime, especially when the sparger ring has a diameter greater than the impeller.

In contrast with the standard configuration, many of the industrial designs of stirred tanks have a dished bottom. However, experimental data for advanced impellers such as the CD-6 and BT-6 are often limited, whilst such information is abundantly available for a conventional impeller like the Rushton turbine. Therefore, a tank agitated with Rushton turbine has been chosen in this study as a basis for most of the modelling development. Nonetheless, a study of a more advanced gas dispersion impeller like the CD-6 will be also carried out after a successful validation of the Rushton turbine simulation.

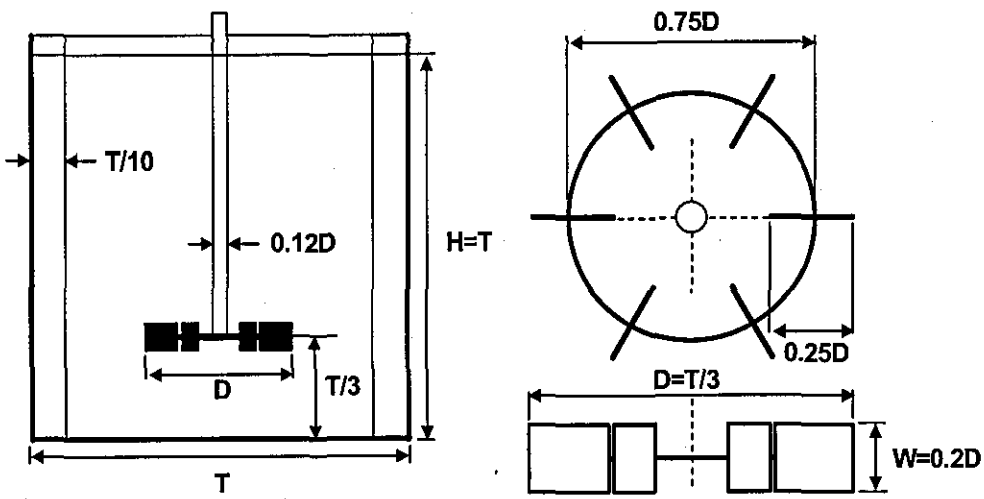

Figure 2-1: Standard tank geometry

2.4 Impeller Design

There is a wide range of impellers available commercially and designed for specific functions such as gas dispersion, solid mixing and mixing of high viscosity media. In general all impellers can be classified either as radial, axial or mixed flow depending on the discharge direction induced by the blades. General classifications and applications of various commercially available impellers are summarised in Tables 2-1 and 2-2.

Table 2-1: Summary of radial flow impeller (Lightnin, 2006; Chemineer, 2006)

Impeller	Commercial name	Technical specification	Application/Characteristic
Rushton turbine 	Chemineer D-6 Lightnin R100 Hayward Gordon RD	Rushton Turbine with 6 blades N_{p0} = 5.2, N_Q = 0.72 N_{p0} = 6.0, D/T =0.33, W/T = 1/12 N_{p0} = 6.0, D/T =0.33, W/T = 0.1 Available from 3 to 12 blade	Rushton turbine is recommended for high-shear mixing and gas-liquid applications but it should be noted that aeration number, Fl_g, is limited to 0.1. Radial design provides sufficient shear to achieve good contacting for liquid-liquid dispersions and emulsions.
Paddle impeller 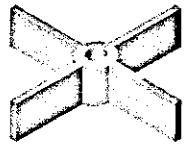	Lightnin R200 Chemineer S-4	Paddle with 4 blades No disk (disc) N_{p0} = 3.4, N_Q = 0.62 Available from 2 to 6 blade	Paddle impeller is suitable for solids suspension applications especially when the impeller operates near the floor of the tank. It also an effective impeller in laminar flow applications, especially when impeller Reynolds numbers drop below 50.
Concave impeller 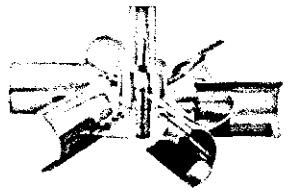	Chemineer CD-6 Lightnin R130 Smith Turbine Hayward Gordon RDC	Symmetric concave attached on a disk N_{p0} = 3.2, N_Q = 0.61	The concave impeller is a second generation gas and immiscible liquid dispersion impeller. It can handle about 2.4 times the maximum gas capacity of the Rushton turbine at the same impeller speed. This impeller has been used at aeration numbers as high as 2.1.
Asymmetric concave impeller 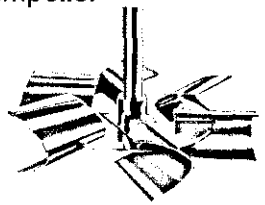	Chemineer BT-6	Asymmetric concave attached on a disk N_{p0} = 2.3, N_Q = 0.55	BT6 impeller provide the highest gas dispersing capability (Chemineer) as it can disperse nearly six times the gas handling capability of the Rushton impeller at the same impeller speed. It has 10% better mass transfer capability than the concave impeller at the same speed.

Table 2-2: Summary of axial flow impeller (Lightnin, 2006; Chemineer, 2006)

Three blade hydrofoil 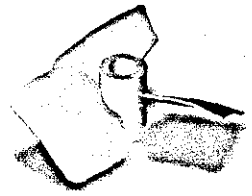	Lightnin A320	N_{p0} = 0.64, N_Q = 0.64 (A320)	A320 is recommended for higher-viscosity applications requiring high flow in the transitional flow regime. It can reduce blend time by half of Rushton turbine at same speed, besides having a modest shear rate for both high- and low-viscosity conditions. The fluid foil design delivers better axial motion and reduces power consumption.
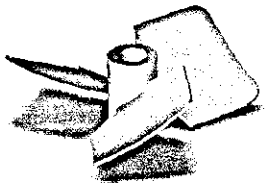	Lightnin A340	N_{p0} = 0.64, N_Q = 0.64 (A340)	The A340 impeller is recommended for up-pumping applications suitable for multi-phase flow, such as fermentation, polymerisation and hydrogenation. A340 provide a higher gas induction from surface (Lightnin).
Four blade hydrofoil 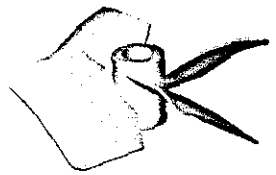	Lightnin A315 Lightnin A345	N_{p0} = 0.75, N_Q = 0.73 N_{p0} = 0.75, N_Q = 0.73	A315 is recommended for gas-liquid dispersion and mass transfer-controlled applications. It can improve mass transfer by 30% compared with Rushton turbines beside decreases shear rates up to 75% thus potentially improves yields in shear-sensitive processes. A low power number mean it can reduce energy costs up to 45% compare to Rushton turbine.
Pitched blade turbine (PBT) 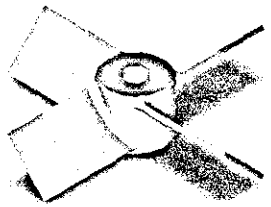	Chemineer P-4 Lightnin A200	Pitched blade turbine - Down- and Up-pumping with 4 blades N_{p0} = 1.27, N_Q = 0.79 Also available in 6 blade and various degree of pitch	PBT is suitable for applications where the viscosity changes over a wide range causing the flow regime to vary between turbulent and laminar flow. It could also be applied for solids suspension and gas dispersion (up pumping).

Radial and axial flow impellers such as the Rushton turbine, CD-6, BT-6 and A315 impeller have been recommended for gas dispersion applications (e.g. Lightnin, 2006; Chemineer, 2006). The A315, which has an axial flow characteristic, seem to be the most suitable impeller when dealing with a three-phase system. The suspension of solid particles must be accounted for in the three-phase system besides the gas dispersion, and the axial flow impeller is a good choice for particles mixing. An impeller like the BT-6 is more likely to be applied when the gas dispersion is vital to the process, as it is capable of handling about six times more gas flow rate than Rushton turbine (Myers *et al.*, 1999) before the flooding limit is reached. Meanwhile, the Rushton turbine and CD-6 can be applied when particles suspension is not an issue and moderate to lower gas dispersion is required.

2.5 Experimental Methods for Bubbly Flow

The focus of this thesis is on the development of computational tools to design gas-liquid stirred tanks. Nevertheless, it is important to have an appreciation of the experimental techniques that are available and which provide validation data for two-phase CFD predictions. There are several advanced techniques of elucidating the flow phenomena in aerated stirred tanks. Among them are digital imaging (DI), particle image velocimetry (PIV), laser doppler anemometry (LDA), computer automated radioactive particle tracking (CARPT), phase doppler anemometry (PDA) and particle image velocimetry laser-induced fluorescence (PIV-LIF). There are several options available for bubble size measurement like capillary suction probe (CSP), PDA, PIV, LDA, and PIV-LIF. An overview of each measurement technique including a brief description of its underlying principle and limitations is outlined in the following section.

2.5.1 Phase/Laser doppler anemometry (PDA/LDA)

PDA/LDA is a non-intrusive single point optical technique applicable for the simultaneous measurement of bubble size distributions and liquid velocities. Both LDA and PDA have a similar working principle except for a simultaneous measurement of bubble or particle velocity and size distribution capability in PDA. PDA was said to be an extension of the LDA principle (Dantec dynamics, 2006). In LDA/PDA technique two laser beams are focused into a small measurement volume where they produce interference fringes. The laser light is

scattered when a particle or bubble passes through the measurement volume. The seed particles or bubbles act as moving light sources causing Doppler shifts of the scattered light. The Doppler shift of the light is proportional to the bubble velocity while the phase differences between the lights scattered in different directions are linearly related to the bubble size. However, it must be noted that the measurement of the real bubbles size is not simple as it is subject to a calibration procedure. Bubbles with diameters larger than 3 mm are known to form either ellipse or cap shapes, and it may cause a problem in calibration as PDA/LDA is only known to determine correctly a spherical particle size. PDA/LDA requires disturbance-free optical access to the measurement plane and high void fraction (> 5%) could hamper the visibility of the measurement volume and thus attenuate the intensity of light. Therefore, PDA/LDA applications are strictly limited to a low gas void fraction (< 5% according to Miettinen *et al.*, 2002) and to transparent dispersions.

2.5.2 Particle image velocimetry (PIV)

PIV is a whole-field optic technique with ability to measure simultaneously the flow fields, local bubble size distributions and relative velocities (slip) between the dispersed and continuous phase in transparent dispersions. PIV has been applied to measure the flow-field in an aerated stirred tank by many researchers (Deen, 2001; Laakonen *et al.*, 2005a; Aubin *et al.*, 2004b; Montante *et al.*, 2007). In the PIV technique, a transparent dispersion, which is seeded with light scattering particles of equivalent density, is illuminated with a laser sheet. The light scattered by the particles and bubbles is recorded on a sequence of frames by a CCD camera placed perpendicular to the laser sheet. The local displacement vector for the images of the tracer particles and bubbles between the first and second illumination of the laser pulse is determined, and hence the local gas and liquid velocities in the plane of light sheet are calculated. A large amount of bubbles have to be recorded to get statistically significant results. As mentioned by Miettinen *et al.* (2002) sophisticated post-processing software is needed in order to be able to handle the large amount of data that can be collected by the PIV technique and to separate the information from the gas and liquid phases. The PIV technique has the same restrictions as the PDA method concerning the disturbance-free optical access to the measurement plane.

2.5.3 Capillary suction probe (CSP)

A capillary suction probe is a single point intrusive technique, which has been used for determination of local bubble size distributions and gas volume fractions in stirred tanks by many researchers (e.g. Barigou and Greaves (1991); Alves *et al.* (2002); Laakkonen *et al.* (2005b). The basic idea of this technique is to withdraw a representative sample stream from the investigated gas-liquid dispersion through a transparent capillary by a pump or a vacuum. The bubbles are then transformed into cylindrical slugs of gas in the capillary; their velocities and lengths are measured by an enclosed optical probe based on the difference of light refraction between the two phases. This method is useful for opaque media and dispersions with high gas volume fraction, which are beyond the application range of most optical techniques. In a small vessel, a continuous sample stream steadily reduces the volume of the dispersion and disturbs the flow pattern, although this problem can be minimised by returning the sample back to the vessel (Miettinen *et al.*, 2002). There is also a problem to measure wide bubble size distributions by CSP as the small bubbles (< 0.4 mm in Laakkonen *et al.* (2005b), depending on capillary diameter) do not form a slug in the capillary and big bubbles break easily in a narrow capillary. Other problems which may arise in suction probes are the velocity fluctuations in the capillary and expansion of bubbles in the probe as a consequence of pressure drop. Another issue in CSP technique is that it is difficult to determine a representative and isokinetic sampling of both gas and liquid especially in turbulence flow. According to Greaves and Kobbacy (1984), isokinetic sampling can be obtained when the sampling rate of bubbles is equal to the arriving rate of the bubbles at the tip zone of capillary. However, it is not always easy to obtain an isokinetic sampling in practice as it shown by Miettinen *et al.* (2002) which observed up to more than three times higher local hold-up from CSP compared to PIV measurement.

2.5.4 Tomography

Tomography techniques have been applied to measure the gas hold-up in aerated stirred tanks in recent years by Wang *et al.* (2000), Holden *et al.* (1999), Patwardhan *et al.* (2005), Khopkar *et al.* (2005b), Hampel *et al.* (2007) and Ford *et al.* (2008). There are several techniques related to tomography like electrical

impedance tomography (EIT), electrical resistance tomography (ERT), electrical capacitance tomography (ECT), x-ray tomography (CT), gamma ray tomography (GRT), etc. With the exception of GRT and CT, all other tomography methods suffer a similar drawback i.e. low spatial resolution and difficulty in the data field reconstruction. For that reason, only GRT and EIT will be discussed here.

EIT involves injecting currents into the dispersion being imaged, so the bulk phase must be electrically conducting and make contact with the electrodes. Electrode arrays composed of electric dipoles are arranged around the region of interest to measure the resistive distribution in the dispersion between the electrode arrays. The conduction distribution of the region from multiple measurements of electrical signals taken from electrode dipoles is reconstructed using EIT. In EIT, every electrode dipole can act both as a current-source electric dipole and a potential measuring dipole. Current is conducted through one electrode dipole at a time and the potential difference between it and the other electrode dipoles is measured. The procedure is repeated in fast succession for many vertical and horizontal positional combinations of source and receiver electrode dipoles to obtain the data for 3D images. According to Miettinen *et al.* (2002) reconstruction of the unknown resistivity field distribution in the system based on the voltage data measured at the system boundaries is the main problem for tomography techniques. Measurement of individual bubbles via tomography is impossible because the spatial resolution of electrical tomography techniques is quite low between 5 to 10% of the vessel diameter depending on the number of electrodes. Tomography techniques also cannot be applied to a non-conductive medium, for example containing an organic liquid. Calibration of tomography techniques is needed, as the resistivity field is sensitive to bubble size and shape, as well as the process conditions leading to a non-linear dependence on gas volume fraction (Chaouki *et al.*, 1997).

Unlike the other tomography techniques, CT and GRT are capable of producing a higher spatial resolution up to a sub-milimetre (Kalender, 2006) for newer designs. This is because the GRT and CT measurement is carried out using a high intensity light beam in comparison to the lower intensity electric resistance field in EIT. The GRT and CT share the similar operating principles. CT was first

designed for clinical application by Hounsfield (1973) to allow imaging of human organs. However, its application has diversified since it first introduction and has been applied for the evaluation of gas-liquid flows by many researchers (e.g. Bukur *et al.*, 1996; Boden *et al.*, 2008; Hampel *et al.*, 2007; Ford *et al.*, 2008; Veera, 2001; Heindel *et al.*, 2008). Both GRT and CT consist of many pairs of x-ray/gamma ray sources and detectors. The data obtained from both GRT and CT can be reconstructed to obtain a 3D image of the specimen. The main advantage of these techniques that they are not restricted to transparent liquid, or transparent vessels.

2.5.5 Digital imaging (DI)

A high speed imaging system has been employed recently by Laakkonen *et al.* (2005b), Laakkonen *et al.* (2006a), Bouaifi *et al.* (2001), Hebrard *et al.* (2000) and Machon *et al.* (1997) to visualise and record bubbly flow phenomena that are too fast for human eyes. For example it is possible to visualise the event of bubble breakage and coalescence using a high speed camera (Miettinen *et al.*, 2002). There is also a possibility to measure local bubble size distribution and population densities from the depth of focused area (Miettinen *et al.*, 2002). Application of high speed imaging is however limited to a small vessel and low void fraction as it requires a lot of well-directed light to freeze the motion and eliminate blur. Bubble images can overlap with each other at high void fraction and this make the identification of bubble size impossible. It might be also impossible to get a good image quality for a bigger tank due to limited direct light penetration. The main concern in the digital imaging technique is the method for bubble identification which determines the bubble size distributions. Such a task is difficult since the images quality varies with lighting conditions and other factors like overlapping bubbles, blurriness of bubbles and the varying shapes of the bubbles (Laakkonen *et al.*, 2005b) are a problem.

2.5.6 CARPT

CARPT has been applied to measure the flow field, instantaneous and time-averaged velocities, and turbulent parameters of high void fraction aerated stirred tanks by Khopkar *et al.* (2005b). It is based on the principle of tracking the motion of a single radioactive particle as a marker of a typical element of the fluid phase (usually the liquid phase) whose velocity field is to be mapped

(Devanathan, 1991). The tracer particle representing a typical liquid element is tracked by an array of NaI(Tl) scintillation detectors, placed at strategic positions around the stirred tank. If the liquid phase is to be tracked, the tracer particle must have a density which matches that of the liquid phase. Calibration for each detector in CARPT is necessary in order to determine the exact position of the tracer particle at each instant in time. Application of CARPT is not affected by opacity and void fraction, but it cannot be applied to measure the bubble size distributions and gas hold-up.

2.5.7 Fibre Optic Probe

A fibre optic probe has been employed to evaluate the gas hold-up in aerated stirred tanks by Bakker (1992) and Wang *et al.* (2006). The gas phase characterization by optic probes exploits the difference between the refractive index of gas and liquid. Light produced by an opto-electronic apparatus is injected into a glass fibre and sweeps along the fibre to the tip. The probe tip is immersed inside the gas-liquid dispersion at the measurement point. Some portion of the light flux is refracted into the fluid around the fibre tip while the rest is reflected back to the opto-electronic apparatus. The refractive index of fluid around the fibre tip influences the amount of light that is reflected back to the apparatus. If the tip lies in the gas phase, a large fraction of the light intensity will be returned to the apparatus. When a rising bubbles strikes the probe, it delivers a square-pulsed signal. The peak of the signal corresponds to the gas phase and the lower parts correspond to the liquid phase (Chaumat *et al.*, 2005). The gas hold-up can be obtained from the cumulative gas part of the signal, referred to total signal length (Chaumat *et al.*, 2005). It is also possible to measure the bubble velocity and diameter using the fibre optic technique by locating a two point probe aligned with the direction of bubbles movement. This method has been employed to measure a bubble axial velocity and chord length distribution by Chaumat *et al.* (2005) for a gas-liquid flow in bubble column. However, this method might not work for stirred tanks where the bubble movement direction is not easily predictable. In a bubble column, it is safe to assume that bubbles move upwards in an axial direction, but the same is not true for stirred tanks because bubbles can move radially and also possibly following the liquid circulation, especially for the smaller bubbles.

2.5.8 PIV-LIF

PIV-LIF method is a relatively new development in multiphase flow experimentation. This technique can provide whole-field velocity data in two-phase water-bubble flows, with simultaneous separation and measurement of the different phases. In the LIF technique orange-coloured light is scattered from fluorescent particles which are illuminated by green laser light. In combined PIV-LIF studies, the water phase of the flow field is seeded with tiny fluorescent particles. PIV-LIF recording system simultaneously separates and samples the two phases: the first camera with an orange filter detects the fluorescent water seeding and a second camera, with a filter corresponding to the laser wavelength, detects only the bubble phase (Dantec dynamics, 2006) i.e. it collects the scattered light from the dispersed phase. The PIV-LIF technique has not yet been used to evaluate the gas-liquid flow in stirred tanks but it has been tested by Lindken and Merzkirch (2002) to measure the bubble rise velocities, mean liquid velocities and the velocities fluctuations in a bubble column.

2.5.9 Conclusion

There are many measurement techniques available for a bubbly flow with a low void fraction but none is suitable for a dense bubbly flow, except CARPT, gamma ray tomography and the fibre optic probe. Although CARPT is applicable for a dense bubbly flow, it has a troublesome calibration procedure and does not give information about the bubble size distribution. A fibre optic probe may be used in a dense dispersion, but it is not capable of measuring the gas-liquid velocities for the complex flow in stirred tank. Some newly introduced method like PIV-LIF might offer a better insight on bubbly flow (as it could measure the bubble distribution and velocity as well as the primary phase velocity), but as it involves an optical technique, it is also be limited to applications with a low void fraction. However, up to now there is no published work on bubbly flows related to the PIV-LIF method.

The accuracy of bubble distribution measurement is another important issue underlying the current measurement techniques. Laakkonen *et al.* (2005b) proved that the bubble size distribution taken from three different methods namely the CSP, DI and PDA may not give similar results especially for the arithmetic mean bubble size (d_{10}) which is sensitive to the number of small

bubble. The difference in the measured d_{10} is understandable given the limitation of CSP to measure a smaller bubble than the diameter of its capillary. Despite a small difference in the detection range especially for the smaller bubble (d_b = 0.4 mm for CSP, d_b = 0.005 mm for PDA, d_b = 0.1 mm for DI), Laakkonen *et al.* (2005b) shows that all three measurement techniques give almost a similar value for the bubble Sauter mean diameter (d_{32}). Laakkonen *et al.* (2005b) reported up to 0.6 mm difference in the measured d_{32} (DI and CSP) near the tank baffle just above the impeller discharge stream at higher impeller speed (490 rpm) probably due to generation of many small bubble by the breakage mechanism. Their result showed the difference in the measured d_{32} is not significant (0.1 mm) at lower impeller speed (340 rpm). Therefore, selection of the measurement technique for bubble size distribution is not critical and is very much affected by the nature of the system i.e. DI and PDA may not be applicable for opaque liquids, but the CSP may work.

2.6 Experimental Studies on Aerated Stirred Tank

Many experimental and numerical studies have been performed for aerated stirred tanks. Some of the most significant work is summarised in Table 2-3. Earlier work is limited to a simple study like the evaluation of power number and the flooding limit (e.g. Bruijn *et al.*, 1974; Warmoeskerken and Smith, 1985; 1989; Lu and Chen, 1986). Some researchers (e.g. Greaves and Kobbacy, 1984; *Lu et al.*, 1993; Alves *et al.*, 2002; Laakkonen *et al.*, 2005a; 2005b; Miettinen *et al.*, 2002) measured local bubble sizes and hold-up using various techniques discussed previously in section 2.5. Many studies of the gas-liquid hydrodynamics have been performed as the more advanced techniques such as LDA, PDA and PIV become available (e.g. Morud and Hjertager, 1996; Deen, 2001; Laakkonen *et al.*, 2005a; 2005b; Montante *et al.*, 2007). As discussed in the section 2.5 application of these optical based measurement (LDA, PDA and PIV) is limited to a tank operating at lower gas loading. Measurement of the gas-liquid stirred tank operating at high gas loading has been performed recently by Hampel *et al.* (2007) and Ford *et al.* (2008) via GRT method. Ford *et al.* (2008) measured the gas hold-up of gas-liquid stirred tank operating from loaded to flooding regime. Detailed explanation about the flow regime transition in gas-liquid stirred tanks is explained in the following section 2.7. The main issue is that

no single method can measure all the main variables in gas-liquid flows. For instance, gamma ray tomography is an excellent method for measuring the gas hold-up, but it does not give information regarding the two-phase flow velocity field and the bubble size. Similarly, the CARPT method (Khopkar *et al.*, 2005b) is capable of measuring the two-phase flow velocity field at high gas loading, but it cannot be applied to measure the bubble size distributions and gas hold-up.

As discussed in the previous section (2.5), selection of the measurement technique is not critical as far as the measurement of d_{32} is concerned. Although a careful selection of the measurement technique must be taken when measuring d_{10}. A combined approach consisting of GRT-CARPT-CSP might be needed for a comprehensive experimental study on gas-liquid stirred tanks. Investment and operating costs to acquire and to run all those experimental instrument are expensive. Alternatively, a computational method like a combined computational fluid dynamics and population balance model (CFD-PBM) may also be capable of providing a detail description of two-phase flow in aerated stirred tanks at far lower investment and running cost. Therefore, this study is devoted to the development of a computational approach suitable for predicting the two-phase flow in aerated stirred tanks. Details of the CFD-PBM approach are discussed in detail in chapter 5. Literature data using the measurement techniques described in this section will be used to validate the CFD predictions.

2.7 Correlations and Dimensionless Number Used in the Design of Gas-Liquid Stirred Tanks

There are a number of dimensionless groups which have been found useful in characterising the performance of stirred tanks. These dimensionless groups are known to vary with geometric configuration and operating conditions and have been widely studied by many researchers (e.g. Patwardhan and Joshi, 1999; Kumaresan and Joshi, 2006) in the past. The power number is one of the important parameters as it characterises the power consumption of the stirred tank. The power number is given by:

$$N_p = \frac{P}{\rho_l N^3 D^5} \tag{2.1}$$

where N is the impeller speed, P is power consumption, D is impeller diameter and ρ_l is the liquid density.

Table 2-3: Experimental study on gas-liquid stirred tank

Authors	Experiments					Remarks
	Bubble size	Power Number	Two-phase flow	Hold-up	k_La	
Bakker (1992)	No	Yes	No	Yes	Yes	P_g/P_o profile and gas hold-up for gas-liquid stirred tank agitated 3 different axial impeller i.e. PBT, Leeuwrik and A315 A315 yield a higher k_La than PBT
Bakker and van den Akker (1994a)	Yes (4 points fibre optic)	Yes	Yes	Yes (single point fibre optic)	Yes	The four points fibre optic is not capable to measure the smaller bubble (≤ 1.4 mm) Lack of local hold-up measurement & numerical result at impeller discharge One way coupling BDM solved on a result of single phase CFD simulation.
Bakker *et al.* (1994a)	Yes (fibre optic probe)	Yes	No	Yes (fibre optic probe)	Yes	Measurement of local gas hold-up and bubble size via fibre optic probe One-way coupling BDM modelling on aerated stirred tank; a satisfactory prediction is obtained for local bubble size and gas hold-up but no comparison was presented at impeller discharge An encouraging agreement of the k_La prediction
Barigou and Greaves (1992)	Yes (CSP)	No	No	No	No	Local bubble size measurement via CSP
Barigou and Greaves (1994)	No	No	No	Yes (conductivity probe)	No	Measurement of interfacial area and gas hold-up via conductivity probe

Table 2.3: Experimental study on gas-liquid stirred tank (continued)

Authors	Experiments					Remarks
	Bubble size	Power Number	Two-phase flow	Hold-up	k_La	
Birch and Ahmed (1996)	No	Yes	No	Yes	No	PBT with Upward and Down pumping configuration, they found the PBTU is a better configuration for gas dispersion (higher void fraction, flooding limit)
Boden *et al.* (2008)	No	No	No	Yes (GRT)	No	Local gas hold-up measurement of gas-inducing impeller via high resolution GRT.
Bombac *et al.* (1997)	No	No	No	Yes	No	Measurement of a local void fraction via micro resistivity probe. A 2D map of void fraction at three different flow regime namely vortex clinging, small 3-3 cavities and large 3-3 cavities is presented.
Bruijn *et al.* (1974)	No	Yes	No	No	No	P_g/P_o for Rushton turbine (RDT) of blades number from 6 to 18. The drop on P_g/P_o at higher number blades (e.g 18) is much smaller compared to those with lesser number of blades (6).
Cooke and Heggs (2005)	No	Yes	No	No	No	Comparison of performance of RDT and Hyperbolic Blade (HBT) (scaba, CD6, BT6, parabolic disc & parabolic arm) HBT is more effective dispersing gas than RT because lower gassed power drop. At lower speed HBT is more energetically efficient to dispersed gas because it achieved a minimum Fr to dispersed gas at lower power.

Table 2.3: Experimental study on gas-liquid stirred tank (continued)

Authors	Experiments					Remarks
	Bubble size	Power Number	Two-phase flow	Hold-up	k_La	
Cui *et al.* (1996)	No	Yes	No	No	No	Correlation for P_g/P_o and Flooding for single and multiple impeller.
Deen (2001)	No	Yes	Yes (PIV)	No	No	PIV measurement on gas-liquid flow CFD simulation is performed using a monodispersed bubble size resulting in a poor prediction on two-phase flow
Figueiredo and Calderbank (1979)	Yes	Yes	No	No	Yes	Scale-up study of gas liquid stirred tank operating either at constant P_g/V and VVM or P_g/V and v_g. Their finding suggest a higher k_La can be achieved by keeping constant P_g/V and VVM whilst a smaller k_La value obtained at fixed P_g/V and v_g.
Ford *et al.* (2008)	No	Yes	No	Yes (Local via x-ray tomography)	No	RDT, gas sparged from a sparger ring Assessment on the gas hold-up in an aerated stirred tank using a x-ray tomography under flooding, loaded and fully dispersed condition
Gezork *et al.* (2000)	Yes (video)	Yes	No	Yes (visual)		Correlation for flooding/loading and fully dispersed transition for gas-liquid stirred tank agitated with RT and Scaba.
Greaves and Kobbacy (1984)	Yes (CSP)	No	No	Yes (CSP)	No	Local measurement of bubble size and gas hold-up via CSP.

Table 2.3: Experimental study on gas-liquid stirred tank (continued)

Authors	Experiments					Remarks
	Bubble size	Power Number	Two-phase flow	Hold-up	k_La	
Kapic and Heindel (2006)	No	Yes	No	No	Yes	k_La measured via dissolved oxygen probe but such measurement is a local value at the probe location only Correlation for k_La at various impeller speed and gas loading
Kawase & Moo-Young (1988)	No	No	No	No	Yes	k_La assessment on gas-liquid stirred tank with Newtonian and non-Newtonian fluid Correlation for volumetric k_La based on assumption of a perfect mixing
Khopkar *et al.* (2005a)	No	Yes	No	No	No	Characterisation of gas-liquid flow via torque and pressure fluctuation. The spectrum plot of pressure fluctuations can be employed to distinguish a different flow regime in aerated stirred tank i.e. fully dispersed, cavity and flooding regime.
Khopkar *et al.* (2005b)	No	No	Yes (CARPT)	Yes (ET)	No	Combined CARPT & CT measurement on aerated stirred tank hold-up and mean velocity CFD simulation using a monodispersed bubble size and consequently the mean velocity at impeller discharge is not predicted correctly The gas hold-up is not predicted correctly.
Laakkonen *et al.* (2005a)	Yes (PIV)	No	No	Yes (PIV)	No	Measurement of local bubble size distribution and gas hold-up via PIV.

Table 2.3: Experimental study on gas-liquid stirred tank *(continued)*

Authors	Experiments					Remarks
	Bubble size	Power Number	Two-phase flow	Hold-up	k_La	
Laakkonen *et al.* (2005b)	Yes (CSP, PDA, DI)	No	No	No	No	Comparison of the local bubble size measured by different techniques namely DI, PDA and CSP. Measurement of DI and CSP show a good agreement but not the PDA due to the different detection range between the PDA to the CSP and DI method.
Laakkonen *et al.* (2005c)	Yes (CSP)	No	No	No	No	Local bubble size measurement of aerated stirred tank consisting a different fluid type i.e. water, water-NaCl, water-starch & water-butanol.
Linek *et al.* (1982)	No	Yes	No	No	Yes	Experimental measurement for k_La in stirred tank (employing a well mixed assumption) Empirical correlation for k_La has been suggested.
Lu and Chen (1986)	No	Yes	No	No	No	Flooding and critical impeller speed of aerated stirred tank agitated by RDT P_g/P_o and correlation for flooding
Lu and Ju (1987)	No	No	Yes (HWA)	Yes (local, HWA)	No	Local measurement on gas hold-up, mean and turbulence flow in gas-liquid stirred tank via hot wire anemometry (HWA) method
Lu and Ju (1989)	No	Yes	No	No	No	Experimental quantification on cavity and flooding regime Correlation for flooding transition

Table 2.3: Experimental study on gas-liquid stirred tank (continued)

Authors	Experiments					Remarks
	Bubble size	Power Number	Two-phase flow	Hold-up	k_La	
Lu *et al.* (1993)	Yes (CSP)	Yes	No	Yes (Local, CSP)	No	P_g/P_o and local bubble size measurement on gas-liquid flow agitated by RDT of a different number of blades (4-8) operating at various gas loading Number of blades did not significantly affect the bubble size
Lu and Wu (2001)	Yes (CSP)	No	No	Yes (Local, CSP)	No	Local measurement on bubble size and gas hold-up around the trailing vortex under vortex cavity, clinging cavity and large cavity flow regime
Lu *et al.* (2000)	Yes (CSP)	Yes	No	Yes (Local, CSP)	No	Local bubble size measurement on gas-liquid flow agitated by RDT of a different blade width operating at various gas loading The smaller blade produces a strongest shear rate and turbulent kinetic energy when operating at constant P_g/V The bigger blades dispersed gas more effectively at constant impeller speed although this would mean a higher P_g/V
Miettinen *et al.* (2002)	Yes (CSP, PIV, PDA)	No	Yes (PIV, limited)	Yes (EIT)	No	Local bubble size measurement using different techniques namely PIV, PDA and CSP. There is no direct comparison made on the bubble size distribution obtained from various technique but the authors acknowledge the difference in the measured bubble size due to the limitation of each method.

Table 2.3: Experimental study on gas-liquid stirred tank (continued)

Authors	Experiments					Remarks
	Bubble size	Power Number	Two-phase flow	Hold-up	k_La	
Montante *et al.* (2007)	No	Yes	Yes (PIV)	No	No	Measurement of two-phase mean velocities via PIV
Montante *et al.* (2008)	Yes (DI)	Yes	Yes (PIV)	No	No	Measurement of local bubble size using a digital imaging method. A good prediction of the mean flow and local bubble size via CFD-PBM (musig)
Morud and Hjertager (1996)	No	No	Yes (LDA)	Yes (overall)	No	LDA measurement on two-phase flow in gas-liquid stirred tank agitated with RDT at various aeration rate and impeller speed Monodispersed bubble size for CFD simulation and consequently the mean velocity is not predicted correctly especially at impeller discharge.
Myers *et al.* (1999)	No	Yes	No	Yes (overall)	Yes	RDT, CD6, PD6 (deep elliptical), BT6 P_g drop for CD6, PD6 and BT6 is much lower than the RDT Retrofit gas dispersion for BT6 is the best among the tested impeller (5.4 times better than the RDT). The relative gas dispersion capability for CD6 and PD6 has 2.4 and 3.2, respectively.
Nienow (1996)	No	Yes	No	No	Yes	Comparison of RDT against modern impeller Scaba, A315, Maxflo T Modern impeller has a lower gassed power drop and but there is no significant improvement in k_La

Table 2.3: Experimental study on gas-liquid stirred tank (continued)

Authors	Experiments					Remarks
	Bubble size	Power Number	Two-phase flow	Hold-up	k_La	
Nocentini *et al.* (1988)	No	Yes	No	No	No	Evaluation on the flooding regime transition via P_g/P_o
Otomo *et al.* (2003)	No	Yes	No	Yes (global)	Yes	RDT, Scaba, Shallow concave, A315 P_g/P_o drop for scaba, shallow concave and A315 is lower than the RDT with A315 being the lowest at lower impeller speed (175 rpm) but it reduces up to 50% at higher impeller speed (350 rpm). Gas hold-up is broadly similar for all impeller tested.
Paglianti *et al.* (2000)	No	Yes	No	No	No	Proposed a conductance fluctuation method to determine the flooding transition.
Parthasarathy *et al.* (1992)	Yes (DI)	Yes	No	Yes (Global)	No	RDT, PBTU, PBTD PBTU provide a higher gas hold-up at similar v_g and specific dissipation rate but also produces a larger bubbles (2-4 times larger)
Sardieng *et al.* (2004)	No	Yes	No	Yes (Global)	Yes	In terms of gas handling capacity (from gassed power consumption), A315U and Scaba 6SRGT > A315D and PBTU, Rushton turbine > PBTD. In terms of gas hold-up capacity, A315U and Rushton turbine > PBTU > A315D and PBTD > Scaba 6SRGT. In terms of k_La, Rushton turbine > A315U and PBTU > Scaba 6SRGT, A315D and PBTD. Comparison for gas hold-up were made at 300 rpm instead of constant P_g/V

Table 2.3: Experimental study on gas-liquid stirred tank (continued)

Authors	Experiments					Remarks
	Bubble size	Power Number	Two-phase flow	Hold-up	k_La	
Smith and Gao (2001)	No	Yes	No	No	No	Higher P_g/P_o for heated gas-liquid stirred tank thus affecting its flooding-loading transition
Sudiyo and Andersson (2007)	Yes (DI)	No	Yes	No	No	More coalescence at the leeward side of the tank baffles due to increases in hold-up and the additional forces resulted from the localise stationary rotational vortex.
Torre *et al.* (2007)	No	No	Yes (PIV)	No	No	Measurement of two-phase flow in gas-liquid tanks agitated by retreat curve impeller via PIV
Wang *et al.* (2006)	No	No	No	Yes (Fibre optic probe)	No	Study of gas hold-up in aerated stirred tank operating under flooding to fully dispersed regime using fibre optic probe CFD simulation is performed using a monodispersed bubble size and consequently the local gas hold-up is not predicted correctly
Warmoeskerken and Smith (1989)	No	Yes	No	Yes (Global)	Yes	Comparison of performance by concave CD6, convex CD6 and RDT Concave CD6 handle higher Fl_g before floding occur compare to RDT When operating at loaded and fully dispersed regime the concave CD6 drop less P_g than RDT and also has a slightly higher k_La at similar Fl_g Suggested a correlation for k_La for CD6 and RDT Flow regime map for RDT and CD-6

Table 2.3: Experimental study on gas-liquid stirred tank (continued)

Authors	Experiments					Remarks
	Bubble size	Power Number	Two-phase flow	Hold-up	k_La	
Warmoeskerken and Smith (1985)	No	Yes	No	No	No	Suggested a correlation for flooding regime Flooding transition observation from P_g/P_o against Q_g profile
Zhu *et al.* (2001)	No	No	No	No	Yes	Comparison of k_La in aerated stirred tank agitated either by A315, A310, PBT, RDT, RDT (with hole) or CD6 k_La for radial flow impeller is slightly higher than the axial impeller at similar P_g/V and v_g

For fully baffled vessels, N_p is a function of the impeller Reynolds number (Re) in single phase flow which is given by:

$$\mathrm{Re} = \frac{\rho_l N D^2}{\mu_l} \tag{2.2}$$

where μ_l is the liquid viscosity. In the fully turbulent region (Re > 10^4), the power number is normally constant; for Re < 10^4, in the laminar and transitional regimes, N_p decrease with increasing Reynolds number. In a lab scale stirred tank, the impeller blade thickness to diameter ratio is larger than in an industrial scale tank. The turbulent power number was found to be dependent on impeller blade thickness by Bujalski *et al.* (1987) and Rutherford *et al.* (1996). For a Rushton turbine operating in a single phase system Bujalski *et al.* (1987) suggested the following correlation for estimation of N_{p0}:

$$N_{p0} = \frac{P_0}{\rho_l N^3 D^5} = 2.512\left(\frac{t}{D}\right)^{-0.195} T^{0.063} \tag{2.3}$$

where t is the impeller blade thickness, P_0 is the single phase power consumption and T is the tank diameter (m). The subscript 0 represents the conditions in a liquid only system. Rutherford *et al.* (1996) also suggested a correlation for N_{p0} as a function of impeller thickness for a Rushton turbine:

$$N_{p0} = 6.405 - 55.673\left(\frac{t}{D}\right) \tag{2.4}$$

According to Rutherford *et al.* (1996), the difference between the N_{p0} values from equations (2.3 and 2.4) is within 5%. It should be noted however that Rutherford *et al.*'s correlation is obtained for specific tank size (T = 294 mm), thus neglecting the effect of T on N_{p0}. Therefore, the correlation proposed by Bujalski *et al.* (1987) may have much wider application than the one proposed by Rutherford *et al.* (1996).

In aerated stirred tanks, a reduction in the power number is often observed at a constant impeller speed, compared to the single phase operation. As much as 60% of power loss might be observed before the flooding point (discussed later in this section) is reached for a Rushton turbine and a pitched blade impeller (Middleton and Smith, 2004). Meanwhile the power numbers for advanced gas dispersion impellers like the Scaba SRGT or Chemineer BT-6 only fall 10% compared to the single phase power numbers (Middleton and Smith, 2004).

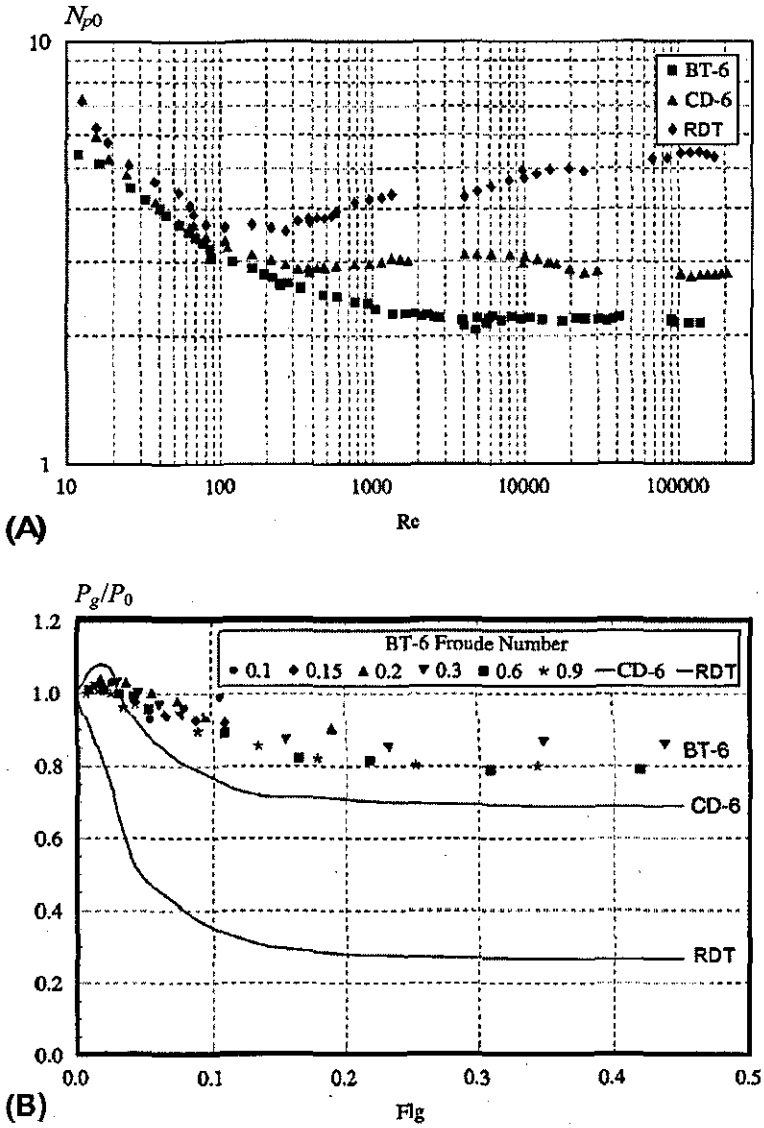

Figure 2-2: Power number of gas dispersion impeller at various aeration rate from Myers *et al.* (1999), A) single phase, B) gassed

Experimental measurement by Myers *et al.* (1999) in Fig. 2-2 shows clearly the large power drop by a Rushton turbine, whereas only a small power drop observed from the CD-6 and BT-6 impeller. For a conventional impeller, there is a pair of trailing vortex formed behind the impeller blades in a single phase flow (see Fig. 2-3). This vortex is replaced by the clinging gas cavities (see Fig. 2-4) under aerated condition (Deen, 2001) thus contributing to a huge power loss. The gas cavities are formed due to the increasing tendency of gas to accumulate in the lower-pressure regions behind the blades, as the gas flowrate increases or the impeller speed diminished. At higher aeration rates these vortex cavities turn into large cavities (see Fig. 2-4B) before the flooding point is eventually reached.

Transition of the flow regimes in stirred tanks may be better appreciated by referring to Figs. 2-5 and 2-6 in the discussion that follows. The advanced gas dispersion impellers like CD-6 and BT-6 are designed to minimise the vortex formation, therefore their aerated and non-aerated power numbers are almost the same. The vortex formation of advanced gas dispersion impeller was reduced significantly by the lower pressure difference in front and behind the impeller blades compared to the Rushton turbine. The pressure difference at the impeller blades is also reflected by the impeller power number, where the Rushton turbine has a turbulent power number around 5 and most of the advanced impeller have a power number around 3 or less (3 for CD-6 and 2.1 for BT-6 see Fig. 2-2).

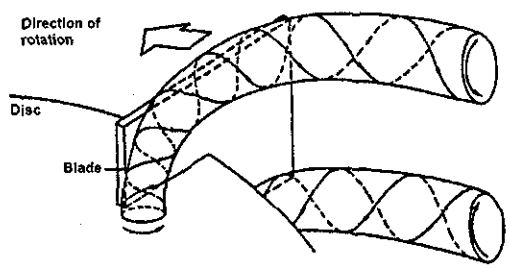

Figure 2-3: Illustration of the trailing vortex behind the impeller blade by Van't Riet and Smith (1975)

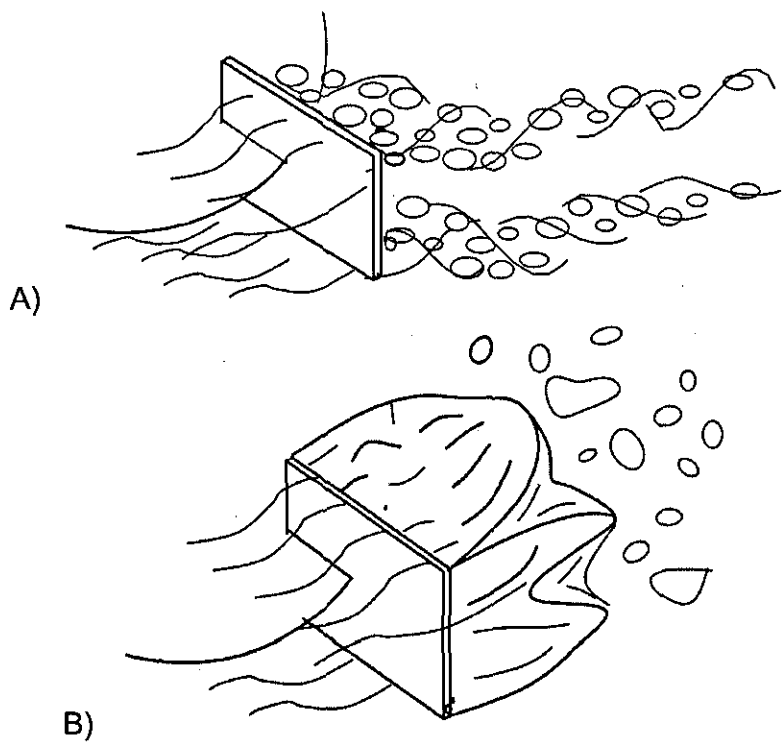

Figure 2-4: Illustration of the vortex cavities (A) and large cavities (B) by Middleton and Smith (2004)

Smith (2006) proposed the following correlation for the relative power draw, P_g/P_0, for stirred tanks agitated by a Rushton turbine, based on the measurements of Warmoeskerken and Smith (1982) and Gezork *et al.* (2000):

$$P_g/P_0 = 0.18Fr^{-0.2}Fl_g^{-0.25} \tag{2.5}$$

where Fr and Fl_g are the Froude number and the aeration number, respectively. Correlations for P_g/P_0 are not well established for the advanced gas dispersion impeller despite many published experimental measurements (e.g Myers *et al.*, 1999; Smith and Gao, 2001; Pinelli *et al.*, 2001; Paglianti *et al.* 2008).

The discharge flow rate of liquid produced by an impeller at given speed is another useful characteristic in stirred tanks. This is expressed in terms of a dimensionless impeller pumping number:

$$N_Q = \frac{Q_l}{ND^3} \tag{2.6}$$

where Q_l is the liquid flow rate through the discharge area swept by the impeller.

Gas-liquid dispersion in aerated stirred tanks is often characterised by gas flow number (Fl_g) and the Froude number (Fr). The gas flow number is also called aeration number is given by:

$$Fl_g = \frac{Q_g}{ND^3} \tag{2.7}$$

where Q_g is the volumetric gas flow rate to the vessel. The Froude number is given by:

$$Fr = \frac{N^2D}{g} \tag{2.8}$$

where g is the gravitational acceleration. Some researchers (e.g. Bakker *et al.*, 1994b; Cooke and Heggs, 2005; Poncin *et al.*, 2002) have employed these dimensionless groups to correlate the gassed power draw of various impellers. The aeration and Froude numbers have also been used to develop maps of the flow regimes of radial and axial pumping impellers which indicate the formation of various types of cavity, or where the flooding point is reached (Warmoeskerken and Smith, 1982; Middleton and Smith, 2004). Bruijn *et al.* (1974) for example use the aeration number to classify different categories of gas cavities such as

the vortex cavity, clinging cavity and the large cavity, before the flooding condition is eventually reached at Fl_g ~ 0.043. Meanwhile, Nocentini *et al.* (1988) use the Froude number to determine the loading to flooding transition which occurred at Fr < 0.2 in their study. The loaded regime is a condition which the impeller disperses the gas through the upper part of the vessel as illustrated in Fig.2-5B. The flooding limit (see Fig. 2-5A) of stirred tanks is not always similar as it is influenced by the sparger type, tank geometry, impeller type and operating conditions, such as the impeller speed and the gas flow rate.

Flooding is an undesirable situation where the impeller is unable to disperse the aerated gas effectively to the whole tank and as a result the gas rises in a limited region around the impeller shaft (Fig. 2-5A). Flooding can be eliminated by either reducing the gas volumetric flow rate or increasing the impeller speed. At constant gas volume flow rate, a complete dispersion of the gas (Fig. 2-5C) can be achieved by increasing the impeller speed.

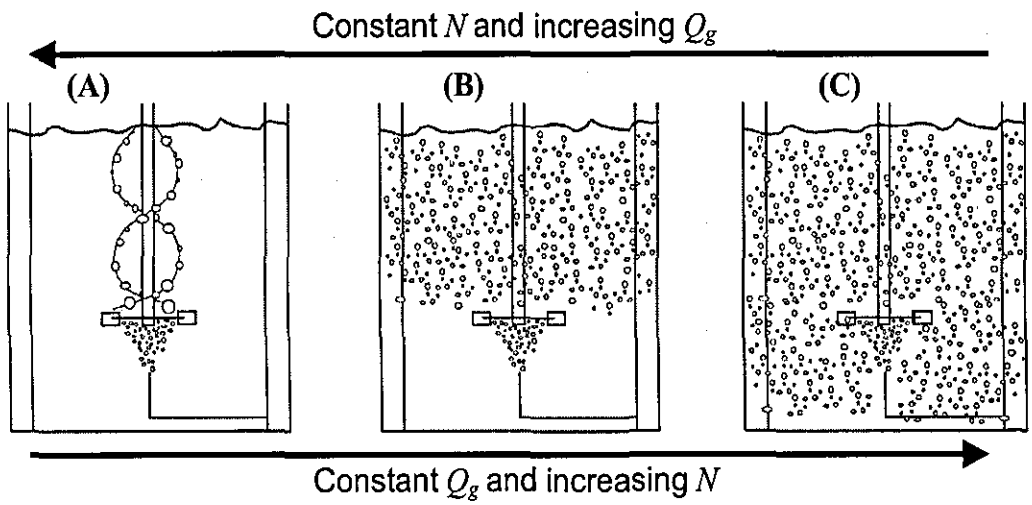

Figure 2-5: Illustration of the gas-liquid flow pattern by Paglianti *et al.* (2000), A) Flooded, B) Loaded regime, C) Complete dispersed

Transition between the various flow regime is much better illustrated by the impeller flow regime maps. The flow map for a six-blade disk turbine has been presented earlier by Warmoeskerken and Smith (1986). According to Smith *et al.* (1987), the transitions between the various flow regimes generated by a gassed Rushton turbine can be characterized with the dimensionless numbers, the Froude number, the aeration number and the ratio of impeller diameter over the

tank diameter. Bakker *et al.* (1994b) also has formulated the flow regimes map for Rushton turbine and CD-6 impeller using a similar set of equations.

Below a certain impeller speed, the impeller motion has no discernible action. This point is approximately when (Warmoeskerken and Smith, 1989)

$$Fr < 0.045 \tag{2.9}$$

Flooding occurs if

$$F_{lg} > C_F Fr\left(\frac{D}{T}\right)^{3.5} \tag{2.10}$$

For a Rushton turbine, C_F = 30 and for CD-6 impeller C_F = 70 (Warmoeskerken and Smith, 1989). Large cavities are developed when

$$F_{lg} >\sim C_{LC}\left(\frac{D}{T}\right)^{-0.5} \tag{2.11}$$

Warmoeskerken and Smith (1989) suggested a C_{LC} = 0.025 for Rushton turbine and C_{LC} = 0.058 for CD-6 impeller.

According to Nienow *et al.* (1977), for a Rushton turbine at a given aeration rate, bubble recirculation occurs when

$$F_{lg} < 13Fr^2\left(\frac{D}{T}\right)^5 \tag{2.12}$$

According to Bakker *et al.* (1994b), the bubble recirculation for CD-6 impeller occurs when

$$F_{lg} = 0.4Fr^{0.5}\left(\frac{D}{T}\right)^{0.5} \tag{2.13}$$

The flow regimes map for Rushton turbine and CD-6 impeller can be constructed using the eq.(2.9) to eq.(2.13). At least five flow regimes can be identified from the Rushton turbine flow regimes map shown in Fig 2-6 namely the flooding, vortex cavities without recirculation, vortex cavities with recirculation, large cavities without recirculation, and large cavities with recirculation. The flow regimes with recirculation are also referred to as a fully dispersed regime, whereas the flow regimes without recirculation also known as the loaded regime. The flow regimes map for CD-6 impeller in Fig. 2-6 shows clearly that the CD-6 impeller can handle a higher gas flowrate (characterised by Fl_g) before experiencing flooding. The flow regime map also suggests that it is easier to achieve a full dispersion with a CD-6 than a RDT. In this work, all cases

considered for the CFD scale-up study were outside the flooding regime, under conditions where the impeller would be loaded or the gas completely dispersed.

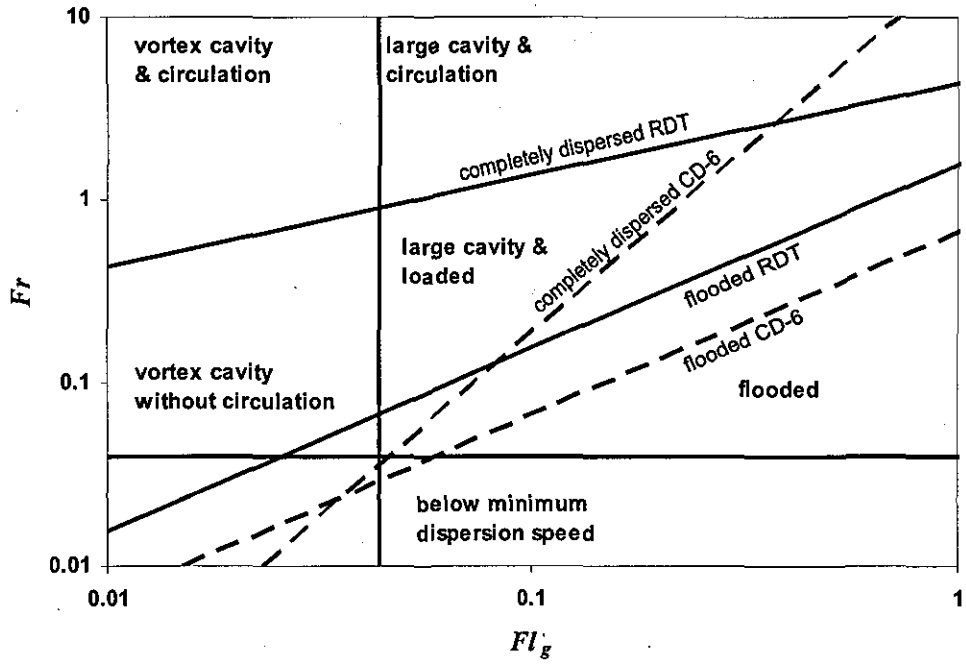

Figure 2-6: Rushton turbine flow regimes map for a D/T = 1/3. The complete dispersion and flooding line for CD-6 is also added for comparison.

The most important variables for aerated stirred tanks are the interfacial area and the gas liquid mass transfer coefficient. Various correlations have been proposed for gas hold-up and bubble size which together account for the interfacial area (Tatterson, 1994). Such correlations are derived from lab scale experiments for a limited number of impellers and tank configurations, often with a Rushton turbine in a standard tank design.

Most published correlations for gas hold-up (α_g) have the form:

$$\alpha_g = C_h \left(\frac{P_g}{V_l} \right)^A v_{sg}^B \tag{2.14}$$

where P_g is the gassed power, V_l is the tank liquid volume, and v_{sg} is the superficial gas velocity. Bakker *et al.* (1994b) recommend an equation of this form with values for air-water system of C_h = 0.16 ± 0.04, A = 0.33 and B = 0.67. It is important to keep the parameter P_g, V_l and v_{sg} in SI unit since the constant C_h ($kg^{0.33}m^{0.33}s^{-1.67}$) is not dimensionless.

The Sauter mean diameter (d_{32}) is the bubble size which has the same ratio of volume to surface area as the complete distribution. It is especially important in calculations where the active surface area is important. Previously proposed correlations for the "average" bubble size in stirred tanks (Bouaifi *et al.*, 2001) are usually presented in terms of d_{32}, defined by

$$d_{32} = \frac{\sum_i n_i d_i^3}{\sum_i n_i d_i^2} \tag{2.15}$$

where n_i is the number of particles with the diameter, d_i. The Sauter mean diameter is related directly with interfacial area (a) and for spherical bubbles it can be estimated by:

$$a = \frac{6\alpha_g}{d_{32}} \tag{2.16}$$

Calderbank (1958) proposed a correlation for d_{32} (m) for coalescing system which includes the effect of gas hold-up:

$$d_{32} = 4.15\left(\frac{\sigma^{0.6}}{\varepsilon^{0.4}\rho_l^{0.2}}\right)\alpha_g^{0.5} + 0.0009 \tag{2.17}$$

where σ is the surface tension. Calderbank's equation does not refer to a local bubble size instead it is a global value assuming that d_{32} is uniform throughout the tank. Such an assumption might be correct for a small tank where complete dispersion (see Fig. 2-5C) is achievable but is less likely to be true for a bigger tank.

Calderbank (1958) proposed a correlation for overall interfacial area as a function of power per unit volume and superficial gas velocity as follow

$$a = 1.44\left(\frac{\varepsilon^{0.4}\rho^{0.2}}{\sigma^{0.6}}\right)\left(\frac{v_g}{u_\infty}\right)^{0.5} \tag{2.18}$$

This correlation may be applied easily but its has limited use in practice because the interfacial area is not uniform throughout the tank. A correlation for the overall interfacial area as a function of hold-up and bubble size distribution has been proposed by Hughmark (1980) for a disc turbine:

$$a = 1.38\left(\frac{g\rho_l}{\sigma}\right)^{0.5}\left(\frac{Q_g}{NV_l}\right)^{0.33}\left(\frac{N^2D^4}{gWV_l^{2/3}}\right)^{0.592}\left(\frac{dN^2D^4}{\sigma V_l^{2/3}}\right)^{0.187} \tag{2.19}$$

where W is the impeller blade width and d is bubble size. The constant, 1.38, has a dimension kg $m^{0.439}$. Application of this equation is also limited because d is a dependent variable and is often unknown.

A correlation to estimate the volumetric mass transfer coefficient, $\langle k_L a \rangle$, is also proposed as a function of tank operating conditions by Bakker *et al.* (1994b):

$$\langle k_L a \rangle = C_{k_L a} \left(\frac{P_g}{V_l} \right)^a v_{sg}^b \tag{2.20}$$

For the air-water system the constants are given as $C_{k_L a}$ = 0.015 ± 0.005 and a = b = 0.6 obtained from fitting of experimental measurements. These constants have been the subject of many studies and their values vary from author to author depending on the tank size and gas loading. The correlation in eq.(2.20) is reported to predict satisfactorily the $\langle k_L a \rangle$ of similar size vessels, but they do not necessarily apply for scale-up to an industrially sized tank (Lines, 2000; Stenberg and Andersson, 1988). Earlier, Van't Riet (1979) proposed the value of $C_{k_L a}$ = 0.026, a = 0.4 and b = 0.5 for a T = 0.19 m stirred tank agitated by Rushton turbine. Sardieng *et al.* (2004) found favourable agreement between Van't Riet's correlation and their experimental measurements. There are many reasons for the variation of this constant including the operating flow regime (e.g. Warmoeskerken and Smith, 1989), impeller type and position (e.g. Bakker *et al.*, 1994b; Sardieng *et al.*, 2004), type and position of sparger (e.g. Bakker *et al.*, 1994b) and addition of chemical such as surfactants and antifoams (e.g. Alves *et al.*, 2004). Alves *et al.* (2004) showed the liquid film mass transfer coefficient reduces significantly when sodium sulphate or sodium chloride is added into the tap water. This is due to the contamination of the water by sodium chloride and thus reduces the liquid side mass transfer coefficient by up to one order of magnitude (Alves *et al.*, 2004).

The correlation in eq.(2.20) represents a volume-averaged value and no correlations are available to calculate the local $k_L a$. Information about the local $k_L a$ is important in the study of gas-liquid stirred tanks to spot the occurrence of very low $k_L a$ values, often referred to as 'dead zones'. Ideally, a uniform $k_L a$ is desired for the scale-up of aerated stirred tanks. The local $k_L a$ is not uniformly distributed inside the tank depending on the local gas hold-up and the local

bubble sizes. Hence it is important to calculate the local k_La for assessing the local oxygen transfer rate. Calculation of local k_La requires information such as the local bubble size distribution and the two-phase flow field i.e. the slip velocity and the turbulence dissipation rate. Those parameters may be acquired using the experimental methods described earlier in section 2.5, but such measurements require extensive experimental work and expensive investment cost for the instrumentation. Alternatively, CFD can provide similar information when coupled with PBM and this work focuses on the development of such a code. A more comprehensive method of calculating the local k_La is presented in chapter 5 (see subsection 5.3.4).

Most of the correlations described in this section have been formulated for the air-water system in a standard stirred tank, often fitted with a Rushton turbine. However, many newer impeller designs with much better performance such as CD-6, BT-6 and Scaba have since become available. Therefore, it is hard to generalise the correlations for assessment of the performance by these advanced impellers. Furthermore, most new stirred tanks will not use a Rushton turbine anymore and thus advanced design exploratory tools (i.e. CFD-PBM) are needed to provide a good prediction for single and multi-phase stirred tanks. With the addition of bubble break-up and coalescence models, CFD-PBM could provide a better prediction of design and scale-up variables than the ones provided by the present correlations.

2.8 Scale-up of Aerated Stirred Tank

Scale-up is a part of the commercialisation process which involves a change in production capacity often from a laboratory scale study into a pilot or production scale. Aerated bioreactors are some of the most important industrial applications of gas-liquid stirred tanks. The main aim for bioreactor scale-up is to achieve a similar performance such as the growth rate and product yield, for both the production and laboratory scales. Theoretically, performance of the bigger tank should match the smaller one (lab scale vessel) if the production rate can be maintained at the bigger scale. However, in most cases the production rate in aerated bioreactors is hampered by poor mass transfer, mainly due to the oxygen transfer from gas to the liquid phase. As mentioned earlier in section 2.2, the mass transfer from or to the solid particles can be easily manipulated by

increasing or decreasing the particle interfacial area but the same cannot be applied to bubbles because they can coalesce, resulting in a lower interfacial area and poor mass transfer. Another issue related to the mixing of liquid substrate also can be addressed by manipulating the fed pipe location i.e. locating them near the impeller discharge. There are many empirical correlations available (see section 2.7) to estimate the mass transfer coefficient of aerated stirred tanks, however these correlations represent a global value rather than local ones. Most of the empirical correlations are also only valid for a homogeneous system, (e.g. uniform driving force) which is not always the case for a bigger tank. It might be safe to assume a homogenous dispersion for a lab scale vessel, where the mixing time is fairly short but the same assumption cannot be applied for a bigger vessel. The dissolved oxygen concentration for a bigger vessel can be a lot more inhomogeneous compared to a smaller one (Schutze and Hengstler, 2006) and the bubble size also might be much bigger hence resulting in a smaller interfacial area and poor mass transfer.

Currently the methodology for bioreactor scale-up is very much dependent on the organism type and their behaviour. According to Wong *et al.* (2002) and (2003), it is sufficient to perform a bioreactor scale-up by just keeping the k_La constant for a non-shear sensitive organism like the *Escherichia coli*. Prior to that, Hewitt *et al.* (1998) have proven that *Escherichia coli* fermentation is not a shear stress affected process. However, k_La is not the most important thing because it just represents the mass transfer coefficient in the system. The most important thing is the local oxygen transfer rate and thus the ability to predict these quantities serve a more meaningful purpose.

The scale-up of gas-liquid stirred tanks bioreactors has often been performed through experimentation in the past. All these experiments are time consuming and expensive to run. Although correlations have been developed to estimate the scale-up rules in a stirred tank bioreactor, they are only valid for conventional impellers, like the Rushton turbine, and they often represent a global value. Therefore, it is necessary to develop more advanced numerical models (CFD) to serve as a tool to perform the bioreactor scale-up. CFD presents an economic route to study the effect of various operating setups and impeller types in a bioreactor. However, commercially available CFD codes are insufficient to

perform such work, and they need to be extended by taking into account the bubble size distribution model to enable a correct estimation of the oxygen transfer rate.

2.9 Summary

The design and applications of aerated stirred tanks have been outlined in this chapter. Correlations related to aerated stirred tanks design and scale-up were also discussed. Most of those correlations are developed from data, which are taken from lab scale tanks and thus might not be applicable for an industrial scale aerated tank. Even though some of the correlations derived from pilot or large scale experiment (e.g. 1 m tank in Barigou and Greaves, 1996), they are only suitable for a conventional impeller like a Rushton turbine. For that reason, a more advanced model using CFD and a population balance should be developed for a improved scale-up of gas-liquid stirred tanks.

Meanwhile there is still a lot of discussion about currently available measurement techniques for bubbly flow. Of the non-intrusive techniques, none except CARPT and GRT or CT is applicable to a dense bubbly flow. However, CARPT can only measure the fluid velocity and not the bubble size distribution, whilst GRT and CT only can measure the gas hold-up. There is a cheaper method to measure the gas hold-up distribution using an electric resistance tomography technique, but it can only provide low spatial resolution and suffers from troublesome reconstruction of the unknown resistivity field. Issues also arise from the inherent limitation of each measurement technique which results in inconsistent measurement of bubble size distributions when compared to other techniques. Most importantly, none of the methods is capable of measuring both the bubble volume and number distribution at the same time. Thus it is important to use a combined approach such as CSP-PIV in order to get a more comprehensive bubble size measurement. In addition, some newly invented techniques like PIV-LIF have never been rigorously compared with currently available technique; thus their actual capabilities still remain unclear. Issues related to measurement techniques in bubbly flow are likely to remain a subject of further research and improvements of the measurement techniques are still greatly needed.

Many studies have been undertaken in the past to compare the CFD result and the experimental measurement for the single phase (see section 3.1) and gas-liquid (see section 5.1) stirred tanks. In most cases, only the time-averaged mean velocities and turbulence flow have been compared (e.g. Ranade and Joshi, 1990; Brucato *et al.*, 1998a; Aubin *et al.*, 2004a; Delafosse *et al.*, 2008). A further review of the application of CFD in a single phase stirred tank is given in section 3.2. For a comprehensive assessment of the CFD predictions high quality angle-resolved data are required. Some examples of the angle-resolved measurement available in the literature are those from Li *et al.* (2005), Yeoh *et al.* (2004) and Derksen *et al.* (1999). Of course there are many other authors who performed angle-resolved measurement (Deen *et al.*, 2002; Khan *et al.*, 2004) but their experimental data is not readily available from their original paper. In this work, the CFD simulation for a single phase flow is compared to the experimental measurement from Derksen *et al.* (1999) who agreed to share his LDA data.

Two phase measurement of the gas-liquid hydrodynamics in an aerated stirred tank have been performed by Lu *et al.* (1987), Morud and Hjertager (1996), Deen (2001), Khopkar *et al.* (2003) and Montante *et al.* (2007). Some of these workers e.g. Khopkar *et al.* (2003) and Montante *et al.* (2007) only presented the result for mean velocities, although they may have performed detailed measurements of the turbulence flow. Morud and Hjertager (1996), Lu *et al.* (1987) and Deen (2001) presented the result for the mean velocities and turbulence flow. Therefore, Deen (2001) data was selected for comparison with the prediction from CFD simulation in this work.

Detailed measurements of the local gas hold-up distribution in aerated stirred tank have been performed by many authors, mostly using the fibre optic probe e.g. Sun *et al.* (2006), Wang *et al.* (2006), Bombac *et al.* (1997), Lu *et al.* (1987) and Barigou and Greaves (1996). Sun *et al.* (2006) and Wang *et al.* (2006) deals with the surface aeration system while Bombac *et al.* (1997), Lu *et al.* (1987) and Barigou and Greaves (1996) deals with a common gas-liquid stirred tank (described in section 2.3). In this work, the CFD predictions of the local gas hold-up are compared to the experimental measurement by Bombac *et al.* (1997).

Measurements of the local bubble size distribution in a gas-liquid stirred tank have been performed by many authors in the past (e.g. Laakkonen *et al.*, 2005a; Laakkonen, 2005b; Laakkonen *et al.*, 2007a; Barigou *et al.*, 1992; Lu *et al.*, 1993, Alves *et al.*, 2002 and Miettinen *et al.*, 2002). However, in most cases only the bubble size is measured and not the mass transfer rate, except in the work by Laakkonen *et al.* (2007b) and Alves *et al.* (2002; 2004). Therefore, the experimental measurements from Laakkonen *et al.* (2007b) were chosen for initial validation of the CFD result due to availability of the mass transfer data which can be used to further validate the prediction of the developed model. Moreover, the main aim of this study is to evaluate the effect of scale-up to the mass transfer in aerated stirred tank.

3 MODELLING OF A SINGLE PHASE STIRRED TANK

3.1 Overview

This chapter mainly presents the detached eddy simulation (DES) and Reynolds averaged Navier-Stokes (RANS) calculations on the single phase turbulent flow in a fully baffled stirred tank, agitated by a Rushton turbine. The DES employed in this work is based on the Spalart-Allmaras turbulence model and it was solved on a grid containing about a million control volumes. For comparison, four RANS models, namely k-ε, realizable (Rk-ε), renormalized k-ε (RNG) and Reynolds stress model (RSM) were evaluated in this study, using a simplified, half-tank modelling domain containing about half a million control volumes. A large eddy simulation (LES) was also performed to verify that the prepared grid was not fine enough to resolve the large eddies around the boundary layer and for comparison with the DES simulation.

Predictions of the angle-resolved and time-averaged turbulent flow have been evaluated and compared with LDA measurements. A detailed study in the highly anisotropic region in the trailing vortex has uncovered the effects of the turbulence model on the unsteady predictions of the turbulent kinetic energy and mean velocity components. This study also reveals the great potential of the DES to predict accurately the time averaged and angle-resolved turbulent flow in a stirred tank. Both the radial and the axial positions of the trailing vortex pair behind the impeller blade have also been successfully reproduced computationally. The findings suggest that DES provides a more accurate and detailed prediction of the features of the turbulent flows in a stirred tank than the RANS models.

3.2 Introduction

Stirred tanks are widely used in the chemical and biochemical process industries. Mixing, fermentation, polymerisation, crystallisation and liquid-liquid extractions are significant examples of industrial operations usually carried out in tanks agitated by one or more rotating impellers. The flow phenomena inside the tank are of great importance in the design, scale-up and optimisation of stirred tanks.

Although several advanced methods such as LDA and PIV are capable of evaluating the flow phenomena in stirred tanks, these methods still have their own limitations. PIV and LDA techniques cannot be applied to opaque fluids, hazardous conditions, non-transparent vessels or when the system is sensitive to the laser radiation. Furthermore most pilot and industrial scale stirred tanks are made of a non-transparent material like steel, thus further limiting the application of LDA and PIV to evaluate such processes. In the cases where PIV and LDA cannot be applied, CFD presents an alternative quantitative route of describing a stirred tank flow, so long as suitable validation can be established. CFD provides a powerful tool for investigating flows at lower expense than would be required by a high quality experimental facility. However, attention should be paid to evaluate the level of accuracy offered by CFD on the prediction of turbulent flows in stirred tanks.

Simulation of the single phase stirred tanks is necessary because there are still a lot of discussions and arguments related to the prediction of turbulent flows in stirred tanks. A good prediction of the turbulent kinetic energy and turbulent dissipation rate is important because the latter affects the bubble coalescence and break-up in an aerated stirred tank.

Modelling of turbulence in stirred tanks is challenging because the flow structures are highly three-dimensional and cover a wide range of spatial and temporal scales. The impeller rotation circulates the fluid through the tank and there are three-dimensional vortices formed in the wakes behind the impeller blade (Yianneskis *et al.*, 1987). Baffles at the tank wall prevent the liquid from performing a solid-body rotation, thus enhancing the mixing, as well as generating strong axial and radial velocity components.

Many researchers (Ranade and Joshi, 1990; Harris *et al.*, 1996; Brucato *et al.*, 1998; Patwardhan 2001; Jones *et al.*, 2001; Jaworski and Zakrzewska, 2002; Aubin *et al.*, 2004a; Li *et al.*, 2004; Ochieng *et al.*, 2008) have studied Reynolds averaged Navier-Stokes (RANS) based turbulence models (mainly k-ε models) applied to a stirred tank. As a general conclusion, the authors claim that CFD predicts satisfactorily the axial and radial mean flow patterns, but either under- or over-predicts the tangential velocity component and turbulence quantities, such

as the turbulent kinetic energy (k) and the turbulent energy dissipation rate (ε). Some researchers (Harris *et al.*, 1996; Jaworski and Zakrzewska, 2002) have studied more elaborate RANS models such as the Reynolds stress model (RSM), but these also suffer from similar drawbacks. Armenante *et al.* (1997) reported a good prediction of the mean flow and turbulence quantities using the algebraic stress model (ASM) but it should be noted that their studies were performed using a black box approach (whereby experimental data near the impeller is prescribed as a set of boundary conditions). It also has to be noted that Armenante's *et al.* (1997) work deals with unbaffled stirred tanks where the swirling flow is predominant hence, making the case more favourable to ASM model. Apart from Armenante's *et al.* (1997) study, ASM models have never been proven to provide good predictions for turbulent flows in stirred tanks. Furthermore, ASM which is a simplified version of the Reynolds stress model is difficult to implement in a re-circulating flow. With regard to that issue, ASM has been eliminated in newer versions of many commercial CFD codes (e.g. FLUENT), and instead the full RSM is now implemented.

It is possible to solve for the turbulent flow in a stirred tank directly using the exact Navier-Stokes equations, without any modelling. Such a method is known as a Direct Numerical Simulation (DNS). Recently, DNS has been applied to predict the turbulent flows in a stirred tank by Verzicco *et al.* (2004) and Sbrizzai *et al.* (2006). These authors concluded that DNS predicts the turbulence related quantities such as turbulent kinetic energy and turbulent energy dissipation rate much better than the RANS models. However, both works only involved a low Reynolds Re = 1636 (a transitional flow) in an unbaffled tank, suggesting that DNS for a baffled stirred tank at high Reynolds number is still far beyond the reach of current computer resources.

The main issue about RANS modelling of stirred tanks agitated by Rushton turbines is poor prediction of the turbulence related quantities i.e. k, ε and the tangential mean velocity. It is well known from the literature that large eddy simulation (LES) can predict excellently the time-averaged mean and turbulent flows (Derksen, 2001; Derksen and Van den Akker, 1999; Revstedt *et al.* 1998, Yeoh *et al.*, 2004; Hartmann *et al.*, 2004; Li *et al.*, 2007; Jahoda *et al.*, 2007; Tyagi *et al.*, 2007; Yapici *et al.*, 2008, Delafosse *et al.*, 2008). The LES method is

a three-dimensional numerical simulation of turbulent flow, in which the large eddies are resolved and the effects of sub-grid-scale eddies, which are more universal and isotropic in nature, are modelled. LES to some extent tends to over-predict the turbulent kinetic energy (Hartmann *et al.*, 2004) but generally it predicts turbulent flows much better than the RANS models. However, full LES simulations are still very expensive to solve on a personal computer at present. For example Alcamo *et al.* (2005) need 33 days to solve an LES of an unbaffled tank on a Pentium IV 3 GHz computer. Earlier Derksen (2001) also spent a month (up to 44 hours per impeller revolution) to solve the LES of a baffled stirred tank in four clusters of parallel computers. Such problems led to the idea of formulating a turbulence model that is cheaper to run and has a better prediction of turbulent flows, called DES or hybrid (RANS-LES) turbulence model. The main idea of this approach is to combine RANS modelling with LES for applications in part of the domain which classical LES is not affordable i.e. in a thin boundary layer. For a boundary layer at high Reynolds number, LES may not yield sufficient resolution of the near wall flow structure, because large eddies close to the wall are physically small in scale (Squires *et al.*, 2005) and also non-isotropic. Thus an LES model needs a very fine grid within the boundary layer, which means the computational cost of the whole domain does not differ appreciably from that of DNS (Spalart *et al.*, 1997). Inadequate grid resolution of boundary layers can severely degrade the large eddy approximation and thus separated flows are not accurately predicted. Therefore, DES was invented by Spalart *et al.* (1997) in an attempt to reduce the computational cost, as well as to provide a good prediction of turbulent flows near the boundary layer. DES reduces to a RANS model in the boundary layer, thus permitting a coarser grid than a conventional LES grid, resulting in fewer grid cells overall and faster computation. However, the modelling grid for DES must be different from a conventional RANS grid and for that purpose Spalart (2001) has prepared a detailed guide to mesh preparation. To the authors knowledge, DES has never been used previously for prediction of stirred tank flows.

Only a few studies of angle-resolved modelling comparison are available in the literature. Li *et al.* (2004) have presented an angle-resolved CFD and LDA comparison on turbulent flows produced by a retreat curve impeller in a tank

fitted with a single cylindrical baffle. These authors employed a shear-stress-transport (SST) model in their work, which is a combination of the k-ω model near the wall and the k-ε model away from the wall. In this way, both models are used in areas where they perform best. Tangential velocities and the turbulent kinetic energy were largely under-predicted in their study. Yeoh *et al.* (2004) also have presented an angle-resolved comparison of turbulent flows in a stirred tank. They employed a deforming mesh method with LES and reported a good prediction of total kinetic energy. However there was no comparison made on the angle-resolved random kinetic energy. Hartmann *et al.* (2004) have presented an angle-resolved comparison of turbulent flows generated by a Rushton turbine at a Reynolds number of 7300. The authors compared LES and SST models in their work and concluded that LES predicts both angle-resolved and time-averaged turbulent flow very well. The previous work of Yeoh *et al.* (2004) and Hartmann *et al.* (2004) only presented a limited number of angle-resolved comparisons of turbulent kinetic energy i.e. for three different angles at a single radial position. Therefore, such a comparison may not take into account the effect of the vortex core on the CFD prediction.

Up to recently, no detailed study has been reported on CFD prediction of angle-resolved mean and turbulent flows in a stirred tank, especially in the vortex core region. An accurate prediction of both mean velocities and turbulent quantities in the trailing vortex core is important, as this region plays an important role in mixing and phase dispersion. It is therefore interesting to elucidate the capability of CFD to predict the mean velocities and turbulence related quantities in the trailing vortex core. Therefore, this study is carried out in an attempt to elucidate numerically the angle-resolved mean and turbulent flows especially in a high anisotropic region i.e. the impeller discharge region and trailing vortex core.

Various aspects of stirred tanks modelling are discussed in this chapter, including the ability of CFD to predict the angle-averaged and angle-resolved turbulence and mean flows, trailing vortices and the power number. The limitations of the various turbulence models in predicting the turbulent flows in a single phase stirred tank are identified, as this issue is likely to follow-on in two-phase modelling.

3.3 Tank Configuration

The modelling result presented in this chapter is mainly taken from a standard configuration of a stirred tank, with the tank dimensions illustrated in Fig. 2-1. The system is a flat bottomed cylindrical tank, $T = H = 0.288$ m, with four equally spaced baffles and it has exactly the same dimensions as the one studied experimentally by Derksen *et al.* (1999). A Rushton turbine with diameter, $D = T/3$, without a hub, was positioned at a clearance of $C = T/3$. The impeller blade and disc thickness was $t = 2$ mm. The impeller was modelled with a rotational speed (N) of 3.14 rps corresponding to a Reynolds number of 29000. In this study, the level of $z = 0$ was set to correspond to the impeller disk plane.

3.4 CFD Approach

3.4.1 Modelling grid

Gambit 2.2 was employed to create an structured, non-uniform multi-block grid with the impeller (rotating) and static zones being separated by an interface to enable the use of the Multiple Reference Frame (MRF) or Sliding Grid (SG) techniques. The computational grid for the RANS modelling was defined by 516k of structured, non-uniformly distributed hexahedral cells representing only a half-tank domain (Fig. 3-1A). A local grid refinement containing 212k cells was applied in the rotating zones to better resolve this highly turbulent region.

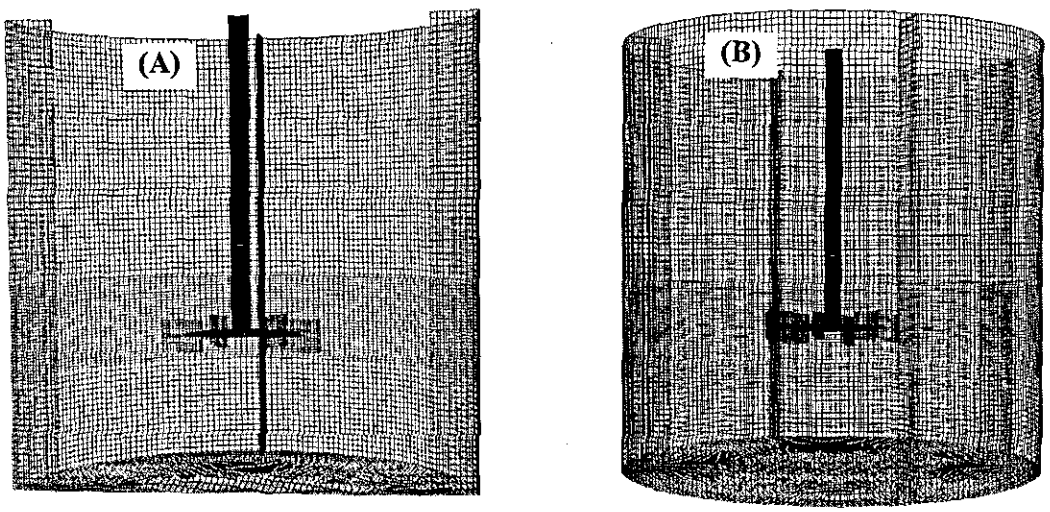

Figure 3-1: Surface mesh of stirred tank, A) half-tank of Derksen *et al.* (1999) configurations, B) full tank of Derksen *et al.* (1999) configurations

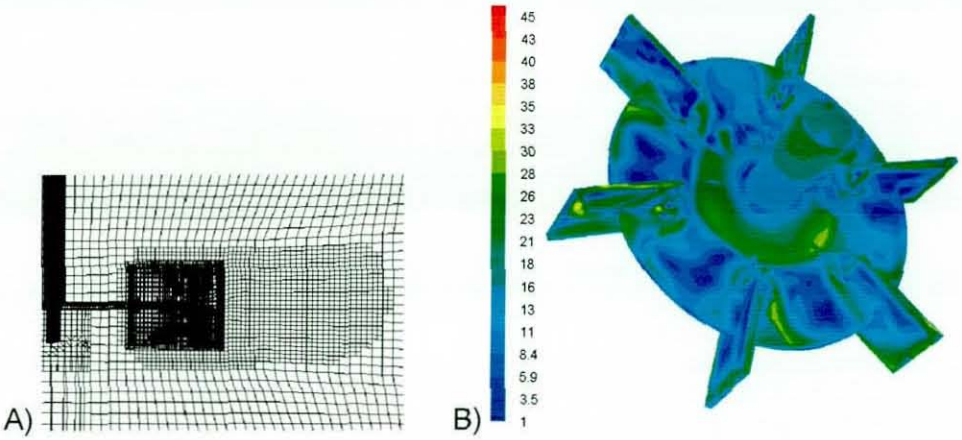

Figure 3-2: Detailed mesh around the impeller for the DES and LES simulations, A) Grid at impeller height, B) Instantaneous y^+ at impeller wall

The grid for a DES cannot make use of the half-tank and periodic boundary conditions, because here the simulation is fully unsteady and therefore not symmetric. Thus the existing grid was extended to a full tank grid for the DES. As a result the extended grid of the whole tank domain contained about a million control volumes (1.01 million) (refer to Fig. 3.1B). The DES grid was prepared according to Spalart (2001) with $y^+ \sim 20$ around the impeller wall (see Fig. 3-2). A grid adaptation is applied very closed to the impeller at $0 < 2r/D < 1.7$ to control the mesh size in this highly turbulent region at $d_{max} < 0.7$ mm.

The reason for using the following grid would not be clear without a review of some recent applications of LES to stirred tank equipped with a Rushton turbine. Earlier, Revstedt *et al.* (1998) presented computational results for the turbulent flow in a stirred tank of $H = T = 0.44$ m. About 250k cells on a hexahedral mesh were used in the whole tank with a local refinement applied in the impeller region (see Fig. 3-2). They reported an excellent prediction of turbulent kinetic energy and mean velocities. Derksen and Van den Akker (1999) employed the lattice-Boltzmann method and LES with a Smagorinsky sub-grid model to simulate the turbulent flow in baffled stirred tank agitated by a Rushton turbine. The lattice-Boltzmann method solves a simplified kinetic model which is an approximation of the complete Navier-Stokes equations, thus allowing them to use a very fine computational grid (up to 5.8 million cells for the whole tank). Bakker and Oshinowo (2004) employed 763k cells for the full tank domain for their study of a baffled stirred tank of $H = T = 0.2$. Recently, Alcamo *et al.* (2005) employed 762k

cells for a full tank domain in their study on an unbaffled stirred tank of $H = T =$ 0.19 m. Yeoh *et al.* (2004) in their study of mixing in stirred tank of $H = T = 0.1$ m employed 490k cells. All of the above mentioned work reported an excellent prediction of turbulence quantities, which is why around a million grid cells grid have been employed in the current study. The grid size in impeller region in the current work is smaller than $0.015D$, which is finer than the locally refined grid ($0.023D$) used by Revstedt *et al.* (1998). The number of grid cells does not indicate whether the grid is fine or coarse, as it very much depends on the tank size. In a small tank (T = 0.1 m, Yeoh *et al.*, 2004), a grid with 500k cells is considered fine and is sufficiently resolved for LES. According to Derksen *et al.* (1999) a proper grid for stirred tanks modelling should be able to resolve the trailing vortex behind the impeller blade. They recommended using at least 8 nodes along the impeller height to resolve the trailing vortex for RANS modelling. The trailing vortex is an important flow feature in stirred tanks which significantly affects prediction of the turbulence and mean flow. In this work, 12 nodes along the impeller blade height were assigned for the RANS modelling and 23 nodes were used for the LES and DES modelling (see Fig. 3-2A). The grid prepared in this work is capable of resolving accurately the radial and axial trailing vortex, as shown in section 3.5.2, thus further confirming its suitability.

3.4.2 Turbulence modelling and discretisation

The selection of a turbulence model for stirred tank simulation is very important, especially when dealing with higher Reynolds numbers and baffled tanks. LES is of course an excellent model, but it is still too computationally expensive to run on a personal computer; see section 3.2. Comparatively new turbulence models such as DES need to be validated further before they can be applied routinely to stirred tank modelling. It is also interesting to explore in detail the strength and weakness of the currently available RANS models, when dealing with angle-resolved turbulent flows in stirred tank. Therefore the predictive capabilities of four RANS models, namely k-ε, Rk-ε, RNG and RSM as well as DES and LES, on turbulent flows in a single-phase stirred tank have been extensively compared in this study. These models are described in more detail below.

The standard k-ε model is based on transport equations for the turbulent kinetic energy and its dissipation rate. Transport equations for k and ε for all k-ε variant models can be generalised as follow:

$$\underbrace{\frac{\partial(\rho k)}{\partial t}}_{\text{time derivative}} + \underbrace{\frac{\partial}{\partial x_i}(\rho u_i k)}_{\text{convection}} = \underbrace{\frac{\partial}{\partial x_i}\left(\left(\mu + \frac{\mu_t}{\sigma_k}\right)\frac{\partial k}{\partial x_i}\right)}_{\text{diffusion}} + \underbrace{\rho P_k}_{\text{production}} - \underbrace{\rho\varepsilon}_{\text{destruction}} \tag{3.1}$$

and

$$\underbrace{\frac{\partial(\rho\varepsilon)}{\partial t}}_{\text{time derivative}} + \underbrace{\frac{\partial}{\partial x_i}(\rho u_i \varepsilon)}_{\text{convection}} = \underbrace{\frac{\partial}{\partial x_i}\left(\left(\mu + \frac{\mu_t}{\sigma_\varepsilon}\right)\frac{\partial \varepsilon}{\partial x_i}\right)}_{\text{diffusion}} + \underbrace{S_\varepsilon}_{\text{source term}} \tag{3.2}$$

The turbulent (eddy) viscosity, μ_t, is obtained from:

$$\mu_t = \rho C_\mu \frac{k^2}{\varepsilon} \tag{3.3}$$

The relation for the production term, P_k, for the k-ε variant models (i.e. k-ε, Rk-ε and RNG) is given as:

$$P_k = \mu_t\left(\frac{\partial u_j}{\partial x_i} + \frac{\partial u_i}{\partial x_j}\right)\frac{\partial u_j}{\partial x_i} \tag{3.4}$$

For the standard k-ε model the source term, S_ε, is given by:

$$S_\varepsilon = \rho\left(C_{1\varepsilon}\frac{\varepsilon}{k}P_k - C_{2\varepsilon}\frac{\varepsilon^2}{k}\right) \tag{3.5}$$

The model constants are (Launder and Spalding, 1974): $C_{\varepsilon 1} = 1.44$ $C_{\varepsilon 2} = 1.92$ $C_\mu = 0.09$ $\sigma_k = 1$ $\sigma_\varepsilon = 1.3$ derived from correlations of experimental data.

As the strengths and weaknesses of the standard k-ε model have become known, improvements have been made to the model to improve its predictive capability, leading to an introduction of variants such as the Rk-ε model, which was first introduced by Shih *et al.* (1995). The Rk-ε model is said to be a substantial improvement over the standard k-ε model, as it consider flow features such as strong streamline curvature, vortices and rotation. Rk-ε differs from the standard k-ε model in two important ways: first it has a new formulation of the turbulent viscosity and second it employs a new transport equation for the dissipation rate. Rk-ε still has a similar equation for μ_t as k-ε, but C_μ is no longer a constant and instead is a function of velocity gradients given as:

$$C_\mu = \frac{1}{A_o + A_s \frac{U^* k}{\varepsilon}} \tag{3.6}$$

with A_o = 4.04, $A_s = \sqrt{6}\cos\phi ; \phi = \frac{\cos^{-1}\left(\sqrt{6}w\right)}{3}, w = \frac{S_{ij}S_{jk}S_{ki}}{\tilde{S}^3}$, $U^* = \sqrt{S_{ij}S_{ij} + \tilde{\Omega}_{ij}\tilde{\Omega}_{ij}}$ and $\tilde{S} = \sqrt{S_{ij}S_{ij}}$ to ensure positivity of normal stresses ($\overline{u_i^2} \geq 0$) and Schwarz's inequality for shear stress ($(\overline{u_i u_j})^2 \leq \overline{u_i^2}\,\overline{u_j^2}$). The Schwarz inequality for shear stresses in the k-ε model can be violated when the mean strain rate is large, but it can be eliminated by having a variable C_μ (Fluent, 2005).

The source term, S_ε for Rk–ε is now given as:

$$S_\varepsilon = \rho\left(C_1 S\varepsilon - C_2 \frac{\varepsilon^2}{k + \sqrt{\upsilon\varepsilon}}\right) \tag{3.7}$$

The model constants are (Shih *et al.*, 1995): $C_1 = \max\left[0.43; \frac{\eta}{\eta + 5}\right]$, $C_2 = 1.9$, $\sigma_k = 1$ and $\sigma_\varepsilon = 1.2$ with $\eta = Sk/\varepsilon$, and $S = \sqrt{2S_{ij}S_{ij}}$ is a modulus of mean rate of strain tensor.

The RNG model was obtained from renormalization group theory by Yakhot and Orzag (1986). RNG differs from standard k-ε because it has an additional term, σ^{-1}, in the ε transport equation, besides providing an analytical formula for the turbulent Prandtl numbers derived using RNG theory. Thus the source term S_ε for RNG is given by:

$$S_\varepsilon = \rho\left(C_{1,RNG}\frac{\varepsilon}{k}P_k - \sigma^{-1}\frac{\varepsilon^2}{k} - C_{2,RNG}\frac{\varepsilon^2}{k}\right) \tag{3.8}$$

where σ^{-1} is the inverse effective Prandtl number given by

$$\sigma^{-1} = \frac{C_\mu \eta^3 (1 - \eta/\eta_0)}{1 + \beta\eta^3} \tag{3.9}$$

Instead of a constant value for the turbulent Prandtl number in k-ε, it is provided analytically in RNG by the following equation:

$$\left|\frac{\sigma^{-1} - 1.3929}{\sigma_0^{-1} - 1.3929}\right|^{0.6321}\left|\frac{\sigma^{-1} - 2.3929}{\sigma_0^{-1} - 2.3929}\right|^{0.3679} = \frac{\mu_{mol}}{\mu_{eff}} \tag{3.10}$$

where σ_0^{-1} = 1.0. In the high Reynolds number limit ($\mu_{mol}/\mu_{eff} << 1$), the inverse turbulent Prandtl number is $\sigma_k^{-1} = \sigma_\varepsilon^{-1} \approx 1.393$.

The RNG model uses a term called the effective viscosity for a flow at low Reynolds numbers, but it is not relevant in the current work, which is in the fully turbulent region (Re > 20000). The effective viscosity is modelled as eq. (3.3) for the RNG model at high Reynolds number (Fluent, 2005). Similar to the Rk-ε model, $\eta = Sk/\varepsilon$, and $S = \sqrt{2S_{ij}S_{ij}}$ is a modulus of mean rate of strain tensor, $\eta_0 = 4.38$, $\beta = 0.012$. The model constants are $C_{\varepsilon 1} = 1.42$, $C_{\varepsilon 2} = 1.68$, $\sigma_k = 1.393$, $\sigma_\varepsilon = 1.393$ derived from RNG theory by Yakhot and Orzag (1986).

RSM abandons the assumption of the isotropic eddy-viscosity hypothesis, to close the Reynolds-averaged Navier-Stokes equations, by solving transport equations for the individual Reynolds stresses, together with a transport equation for the dissipation rate. RSM has a greater potential to give accurate predictions for complex flows, as it takes into accounts the effects of streamline curvature, swirl, rotation, and rapid changes in strain rate in a more rigorous manner than two-equation models such as k-ε. The foundation of RSM is the exact set of transport equations:

$$\underbrace{\frac{\partial}{\partial t}\left(\rho\overline{u_i'u_j'}\right)}_{\text{Time derivative}} + \underbrace{\frac{\partial}{\partial x_k}\left(\rho u_k\overline{u_i'u_j'}\right)}_{C_{ij}=\text{Convection}} = \underbrace{-\frac{\partial}{\partial x_k}\left[\rho\overline{u_i'u_j'u_k'} + \overline{p\left(\delta_{kj}u_i' + \delta_{ik}u_j'\right)}\right]}_{D_{T,ij}=\text{Turblent diffusion}} + \underbrace{\frac{\partial}{\partial x_k}\left[\mu\frac{\partial}{\partial x_k}\left(\overline{u_i'u_j'}\right)\right]}_{D_{L,ij}=\text{Molecular diffusion}}$$

$$\underbrace{-\rho\left(\overline{u_i'u_k'}\frac{\partial u_j}{\partial x_k} + \overline{u_j'u_k'}\frac{\partial u_i}{\partial x_k}\right)}_{P_{ij}=\text{Stress production}} + \underbrace{\overline{\frac{p}{\rho}\left(\frac{\partial u_i'}{\partial x_j} + \frac{\partial u_j'}{\partial x_i}\right)}}_{\phi_{ij}=\text{Pressure strain}} \underbrace{-2\mu\overline{\frac{\partial u_i'}{\partial x_k}\frac{\partial u_i'}{\partial x_k}}}_{\varepsilon_{ij}=\text{Dissipation}}$$

$$\underbrace{-2\rho\Omega_k\left(\overline{u_j'u_m'}\,\varepsilon_{ikm} + \overline{u_i'u_m'}\,\varepsilon_{jkm}\right)}_{F_{ij}=\text{Production by system rotation}} \qquad (3.11)$$

The Ω_k is an angular velocity and both ε_{ikm} and ε_{jkm} are permutation tensors. Of the various terms in these exact equations, C_{ij}, $D_{L,ij}$, P_{ij}, and F_{ij} do not require any modelling. However, $D_{T,ij}$, ϕ_{ij}, and ε_{ij} need to be modelled to close the equations. The reason is simply because the averaging procedure of $\overline{u_i'u_j'u_k'}$ will

generate a lot of unknown variables and it becomes impossible to solve them directly.

The turbulent diffusivity transport term is modelled using a simplified form of the generalised gradient diffusion hypothesis as:

$$D_{T,ij} = \frac{\partial}{\partial x_k}\left[\frac{\mu_t}{\sigma_k}\frac{\partial\left(\overline{u_i'u_j'}\right)}{\partial x_k}\right] \tag{3.12}$$

The pressure strain term is modelled as:

$$\phi_{ij} = \overline{\frac{p}{\rho}\left(\frac{\partial u_i'}{\partial x_j}+\frac{\partial u_j'}{\partial x_i}\right)} = -C_1\frac{\varepsilon}{k}\left[\overline{u_i'u_j'}-\frac{2}{3}\delta_{ij}k\right]-C_2\left[P_{ij}-\frac{2}{3}\delta_{ij}P\right] \tag{3.13}$$

where $P = 0.5P_{ij}$ is the turbulence production due to shear, and the constants are $C_1 = 1.8$ and $C_2 = 0.6$.

The dissipation term is assumed to be isotropic and is approximated by:

$$\varepsilon_{ij} = 2\mu\overline{\frac{\partial u_i'}{\partial x_k}\frac{\partial u_i'}{\partial x_k}} = \frac{2}{3}\delta_{ij}\varepsilon \tag{3.14}$$

The scalar dissipation rate is computed with a model transport equation similar to the one in the standard k-ε model.

The LES model assumes that the large eddies of the flow are dependent on the flow geometry and boundary conditions, while the smaller eddies are self-similar and have a universal character. Thus, in LES the large unsteady vortices are solved directly by the filtered Navier-Stokes equations, while the effect of the smaller universal scales (sub-grid scales) are modelled using a sub-grid scale (SGS) model. A filtered Navier-Stokes equation is given by:

$$\frac{\partial}{\partial t}\left(\rho\overline{u}_i\right)+\frac{\partial}{\partial x_j}\left(\rho\overline{u}_i\overline{u}_j\right)=\frac{\partial}{\partial x_j}\left(\mu\frac{\partial\sigma_{ij}}{\partial x_j}\right)-\frac{\partial\tau_{ij}}{\partial x_j}-\frac{\partial\overline{p}}{\partial x_i} \tag{3.15}$$

where σ_{ij} is the stress tensor due to molecular viscosity given by:

$$\sigma_{ij} = \left[\nu\left(\frac{\partial\overline{u}_i}{\partial x_j}+\frac{\partial\overline{u}_j}{\partial x_i}\right)\right]-\frac{2}{3}\mu\frac{\partial\overline{u}_l}{\partial\overline{x}_l}\delta_{ij} \tag{3.16}$$

and τ_{ij} is the SGS stress given by:

$$\tau_{ij}-\frac{1}{3}\tau_{kk}\delta_{ij} = -2\mu_t\overline{S}_{ij} \tag{3.17}$$

The μ_t is the SGS turbulent viscosity, and $\overline{S}_{ij}$, is rate-of-strain tensor for the resolved scale defined by:

$$\overline{S}_{ij} = \frac{1}{2}\left(\frac{\partial \overline{u}_i}{\partial x_j} + \frac{\partial \overline{u}_j}{\partial x_i}\right) \tag{3.18}$$

The overbar from eq.(3.15) to eq.(3.19) denotes a resolved scale quantity rather than a time-averaged. The most commonly used SGS model is the Smagorinsky (1963) model, which has been further developed by Lilly (1966). They compensate for the unresolved turbulent scales through the addition of an isotropic turbulent viscosity into the governing equations. In the Smagorinsky-Lilly model the turbulent viscosity is modelled by:

$$\mu_t = \rho L_s^2 \left|\overline{S}\right| \tag{3.19}$$

where L_s is the mixing length for sub-grid scales and $\left|\overline{S}\right| = \sqrt{2\overline{S}_{ij}\overline{S}_{ij}}$. L_s can be calculated from:

$$L_s = \min\left(\kappa d, C_s V^{1/3}\right) \tag{3.20}$$

where κ = 0.42, d is the distance to the closest wall, C_s = 0.1 is the Smagorinsky constant, and V is the volume of the computational cell. A LES was performed in this work to evaluate the effect of unresolved eddies near the impeller wall and hence on the turbulence and mean velocities predictions. It has to be noted that the y^+ around the impeller wall in this work ranging from 5 to 40 which is not optimal for LES (see Fig. 3-2B). To our best of knowledge, the effect of the unresolved eddies near the impeller wall on the LES prediction has not been evaluated comprehensively for a stirred tank flow, especially when dealing with angle-resolved flow quantities.

DES as mentioned earlier belongs to a class of a hybrid turbulence models which blend LES away from boundary layer and RANS near the wall. This model was introduced by Spalart *et al.* (1997) in an effort to reduce the overall computational effort of LES modelling by allowing a coarser grid within the boundary layers. The DES employed for the turbulence modelling in this work is based on the Spalart-Allmaras (SA) model (Fluent, 2005).

The SA one-equation model solves a single partial differential equation for a variable $\tilde{\nu}$ which is related to the turbulent viscosity. The variable $\tilde{\nu}$ is identical to

the turbulent kinematic viscosity except in the near-wall (viscous-affected) region. The model includes a wall destruction term that reduces the turbulent viscosity in the log layer and laminar sub-layer. The transport equation for DES is:

$$\frac{\partial}{\partial t}(\rho\tilde{\nu})+\frac{\partial}{\partial x_i}(\rho\tilde{\nu}u_i)=G_\nu+\frac{1}{\sigma_{\tilde{\nu}}}\left[\frac{\partial}{\partial x_j}\left\{(\mu+\rho\tilde{\nu})\frac{\partial\tilde{\nu}}{\partial x_j}\right\}+C_{b2}\rho\left(\frac{\partial\tilde{\nu}}{\partial x_j}\right)^2\right]-Y_\nu \tag{3.21}$$

The turbulent viscosity is determined via:

$$\mu_t=\rho\tilde{\nu}f_{\nu1},\quad f_{\nu1}=\frac{\chi^3}{\chi^3+C_{\nu1}^3},\quad \chi\equiv\frac{\tilde{\nu}}{\nu} \tag{3.22}$$

where $\nu = \mu/\rho$ is the molecular kinematic viscosity. The production term, G_ν, is modelled as:

$$G_\nu=C_{b1}\rho\tilde{S}\tilde{\nu},\quad \tilde{S}\equiv S+\frac{\tilde{\nu}}{k^2d^2}f_{\nu2},\quad f_{\nu2}=1-\frac{\chi}{1+\chi f_{\nu1}} \tag{3.23}$$

S is a scalar measure of the deformation rate tensor which is based on the vorticity magnitude in the SA model. The destruction term is modelled as:

$$Y_\nu=C_{w1}\rho f_w\left(\frac{\tilde{\nu}}{d}\right)^2,\quad f_w=g\left[\frac{1+C_{w3}^6}{g^6+C_{w3}^6}\right]^{1/6},\quad g=r+C_{w2}\left(r^6-r\right),\quad r\equiv\frac{\tilde{\nu}}{\tilde{S}k^2d^2} \tag{3.24}$$

The closure coefficients for SA model (Spalart and Allmaras, 1992) are

$C_{b1}=0.1355$, $C_{b2}=0.622$, $\sigma_{\tilde{\nu}}=\frac{2}{3}$, $C_{\nu1}=7.1$, $C_{w1}=\frac{C_{b1}}{k^2}+\frac{(1+C_{b2})}{\sigma_{\tilde{\nu}}}$, $C_{w2}=0.3$,

$C_{w3}=2.0$, $k=0.4187$.

In the SA model the destruction term (eq. 3.24) is proportional to $(\tilde{\nu}/d)^2$. When this term is balanced with the production term, the eddy viscosity becomes proportional to $\tilde{S}d^2$. The Smagorinsky LES model varies its sub-grid-scale (SGS) turbulent viscosity with the local strain rate, and the grid spacing is described by $\nu_{SGS}\ \alpha\ \tilde{S}\Delta^2$ in eq.(3.19), where Δ = max(Δx, Δy, Δz). If d is replaced with Δ in the wall destruction term, the SA model will act like a LES model. To exhibit both RANS and LES behaviour, d in the SA model is replaced by:

$$\tilde{d}=\min\left(d,\ C_{des}\Delta\right) \tag{3.25}$$

where C_{des} is a constant with a value of 0.65. Then the distance to the closest wall d in the SA model is replaced with the new length scale $\tilde{d}$ to obtain the

DES. The purpose of using this new length is that in boundary layers where Δ far exceeds d, then the standard SA model applies since $\tilde{d} = d$. Away from walls where $\tilde{d} = C_{des}\Delta$, the model turns into a simple one equation SGS model, close to Smagorinsky's in the sense that both make the mixing length proportional to Δ. The Smagorinsky model is the standard eddy viscosity model for LES. On the other hand, this approach retains the full sensitivity of RANS model predictions in the boundary layer. This model has never been applied to predict the stirred tank flows in the past and so this is an objective of the current study.

3.4.3 Modelling strategy

A multiple reference frame (MRF) model was applied to represent the impeller rotation for all the RANS simulations, with a second-order discretisation scheme and standard wall functions. For the DES modelling a bounded central differencing (BCD) scheme was applied for spatial discretisation of the momentum equations, and time-advancement was achieved by a second-order accurate implicit scheme. The central differencing scheme is an ideal choice for LES due to its lower numerical diffusion, however it often leads to unphysical oscillations in the solution field (Fluent, 2005). The BCD scheme was introduced to reduce these unphysical oscillations. Basically, BCD blends together the pure central differencing scheme with first- and second-order upwind schemes. The first-order scheme is applied only when the convection boundedness criterion is violated (Fluent, 2005).

The transient impeller motion for the DES study was modelled using the sliding mesh scheme. PRESTO was applied for pressure-velocity coupling for all cases, as it is optimised for swirling and rotating flow (Fluent, 2005). The DES modelling was initialised using the data from a k-ε simulation. A text user interface command was used to generate the instantaneous velocity field out of the steady-state RANS results. This command must be executed before DES is enabled to create a more realistic initial field for the DES run. This step is necessary to reduce the time needed for the DES simulation to reach a statistically steady-state. Apart from the DES modelling, a LES study was also carried out to confirm that the prepared grid was not fine enough to resolve the large eddies near the boundary layer. The LES and DES were solved using the

same grid because the main aim of this work was to carry out the simulation using a fairly coarse grid (y^+ ~ 20), where the DES should be working well. The LES was initialised using the data from the final DES simulation.

The time step and the number of iterations are crucial in both DES and LES modelling because they involve a transient solution. The time step must be small enough to capture all flow features induced by the motion of the impeller blade. Selection of the iteration time step would not be clear without a review of some recent LES studies on stirred tanks. The time steps for LES simulations taken from the literature were normalised with the impeller speed (ΔtN) to make the value dimensionless. Bakker and Oshinowo (2004) employed a ΔtN ranging from 0.01 to 0.025, Revstedt *et al.* (1998) employ a ΔtN of 0.0027, Alcamo *et al.* (2006) use a ΔtN of 0.0083 and Yeoh *et al.* (2004) employed a ΔtN of 0.0046. Fluent (2005) recommend that in one time step the sliding interface should move by no more than one grid size in order to get a stable solution. In this study a ΔtN of 0.00278 was employed throughout the final simulation corresponding to 1° impeller movement for the DES simulation. The grid size at the impeller interface was set at 0.002 m and the circumference of the impeller interface was 0.69 m. Thus one grid cell movement per time step would require a ΔtN of 0.00289 which is larger than the one employed in this work. About 7 s of actual time was simulated corresponding to about 22 impeller revolutions. Prior to that, about 145 impeller revolutions had been simulated using a ΔtN of 0.00833 corresponding to 3° of impeller movement. About 10 s of actual time has been simulated for a time step corresponding to 1° impeller movement for the LES modelling starting from the final DES simulation. The three component instantaneous velocities were recorded at every time step at various monitoring points (analogous to LDA measurements) and data monitoring on a plane (analogous to 2D PIV).

3.5 Prediction of Turbulent Flows Induced by a Rushton Turbine

The CFD simulations of a Rushton turbine described in this paper were compared with the experimental LDA results reported by Derksen *et al.* (1999). The three component LDA data used for these validation purposes were of high quality angle-resolved mean and fluctuating velocities taken at 3° intervals of

blade rotation, starting from 1° behind the blade (see Derksen *et al.* (1999) for details). All comparisons of the mean, k or ε were made dimensionless by dividing them by either V_{tip}, V_{tip}^2 or N^3D^2, respectively. The experimental LDA data were processed as time-averaged, or angle-resolved mean and turbulence quantities.

The grid analysis was not performed in this chapter but the prepared grid was assumed to be fine enough to yield a grid independent solution. According to Derksen and Van den Akker (1999), about 80% of the turbulence generated by a rotating impeller is dissipated within the impeller swept volume and the impeller discharge region. Derksen *et al.* (1999) also stated that the trailing vortex behind the impeller blade must be well resolved in order to obtain a reasonable prediction of the turbulence and mean velocities. They suggested at least 8 nodes should be placed along the impeller blade height to resolve the trailing vortex, and the grid employed in this chapter was prepared sufficiently fine with 12 nodes for the RANS simulation and 23 nodes for the DES and LES simulation (see earlier discussion in section 3.4.1). A grid analysis performed in chapter 5 based on the grid refinement around the impeller and its discharge region also confirmed the suitability of the prepared grid to produce a grid independent solution.

CFD results for the time averaged and angle-resolved single phase turbulent flows in a stirred tank agitated by a Rushton turbine are discussed thoroughly in this section. All results presented here are taken from a well converged simulation, where the residuals have fallen below three orders of magnitude ($< 1 \times 10^{-3}$) for all RANS model simulations. Of course there is no such convergence term for the transient simulations using DES and LES. However a sufficient number of iterations per time step (up to 35 iterations per time step) have been applied to make sure the residuals fell below 1×10^{-3} at each time step. The results for the DES and LES presented here were averaged over the 4 final impeller revolutions.

Angle-resolved result from $2r/D$ = 1.1 to 1.52 for mean velocities and turbulent kinetic energy are compared with angle-resolved LDA experiments from Derksen *et al.* (1999). A broad range of angle-resolved comparisons are necessary to

capture the effect of the trailing vortex core on the prediction of mean and turbulent flow quantities. Furthermore, the accuracy of CFD prediction in multi-phase flows might be critically dependent on proper simulation of the trailing vortex core. Thus it is interesting to elucidate further the weakness or strength of DES and RANS based turbulence models in predicting the turbulent flows in the trailing vortex core. A detailed comparison between the CFD predictions and the published measurements, very close to the impeller tip is presented in this section. The effects of the vortex core on the prediction of mean and turbulent flows are accounted by comparing the angle-resolved data and the CFD predictions at different radial positions. Besides the mean and turbulent flow, the axial and radial position of the vortex core were also deduced from the CFD results and compared with Derksen *et al.*'s (1999) data.

3.5.1 Time-averaged study

Generally, predictions of the LES, DES and all the RANS models employed in this study (k-ε, Rk-ε, RNG, and RSM) for time averaged axial, radial and tangential velocities were in good agreement with Derksen *et al.*'s (1999) LDA measurements, as shown in Figs. 3-3 to 3-8. All the turbulence models were capable of predicting the angle averaged radial and tangential velocity very well however the LES and RSM models had the upper hand in predicting the axial velocity as shown in Fig. 3-3. The DES prediction of the time-averaged axial velocity is not very good, although the overall trend is still predicted well. Predictions by the k-ε and Rk-ε are quite good away from the impeller at $2r/D$ = 1.3 and 1.52, but near the impeller ($2r/D$ = 1.1) both model fails to predict accurately the axial velocity at impeller level (z = 0). Amongst the turbulence model studied, the DES was found to have the best prediction of the time-averaged radial and tangential velocity (see Figs. 3-4 and 3-5), although predictions of other models are not much different. In the impeller discharge stream ($z \leq W/2$), the mean velocities predicted by the RNG and RSM methods were slightly higher than Derksen's measurements, but they are still acceptable considering the predictions at the points where the experimental data were available. It is hard to comment on the predictions for $z \geq W/2$ (above the centreline) as no measurements from Derksen were available for comparison. However, there is evidence (Wu and Patterson, 1989; Escudie and Line, 2003)

that the tangential and radial velocity peaks are located above the impeller centreline ($z > 0$). Consistent with these previous experimental findings, the predicted velocity peak is located slightly above the impeller disc in the LES and DES simulations, as shown by the mean velocity profiles of Figs. 3-3 and 3-4. There are two reasons why the tangential and radial velocity peaks are located above the impeller disc, first the bottom impeller clearance, and second the different boundary conditions applied to liquid surface and tank bottom. The impeller clearance of $C = T/3$, is favourable for an upward flow direction at impeller discharge stream due to uneven size of the upper and lower flow circulation loops inside the tank. As the top liquid boundary is a free surface while the tank bottom is a no-slip wall, the flow in the lower circulation loop becomes confined, thus forcing the velocity direction slightly upward at impeller discharge. The upward flow pattern at the impeller discharges stream can be appreciated much better from the vector map of the velocity magnitude in Fig. 3-9.

The velocity fluctuations in a stirred tank may be categorised as periodic (related to the blade passage) and random (turbulence). As a result, the kinetic energy can be divided into a coherent (k_{coh}) and random (k_{ran}) part. The total kinetic energy (k_{tot}) in the velocity fluctuations is therefore:

$$k_{tot} = k_{coh} + k_{ran} = \frac{1}{2}\left(\overline{u_i^2 - \overline{u}_i^2}\right) \tag{3.26}$$

where u_i is the instantaneous velocity in direction i and $\overline{u_i}$ is the time-averaged velocity. The averages are over all velocity samples irrespective of the angular position of the impeller and the summation convention is applied over the repeated suffix i. The random part of the kinetic energy can be determined if angle-resolved data are available:

$$\overline{k_{ran}} = \frac{1}{2}\left(\overline{\left\langle u_i^2 \right\rangle_\theta - \left\langle u_i \right\rangle_\theta^2}\right) \tag{3.27}$$

with $\langle\ \rangle_\theta$ denotes the average value at angular position θ. The overbar in equation (3.27) denotes averaging over all angular positions (equivalent to time averaging).

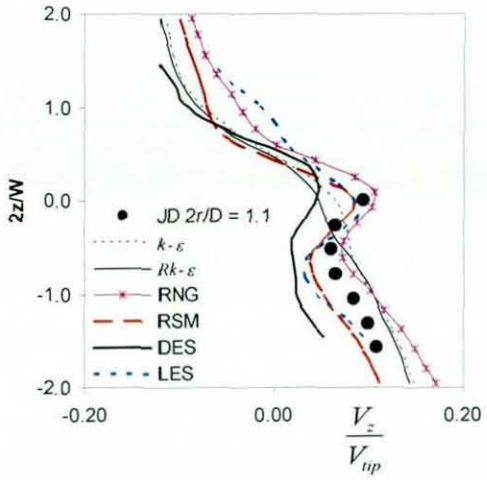

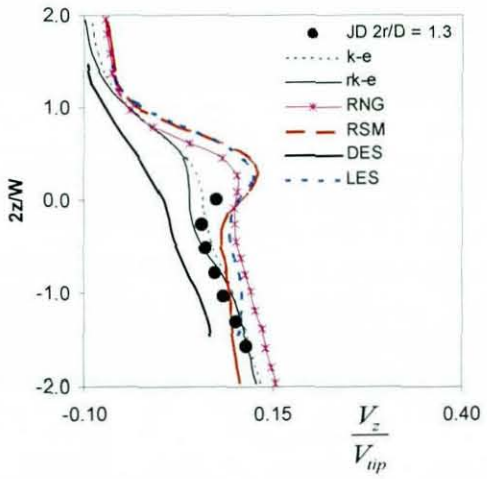

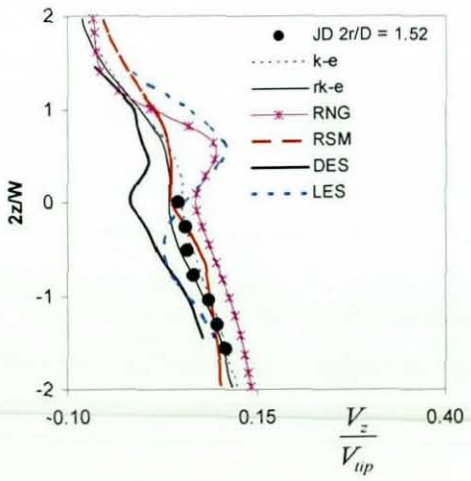

Figure 3-3: Prediction of time-averaged axial velocity at three different radial positions, the data points is the LDA data from Derksen *et al.* (1999)

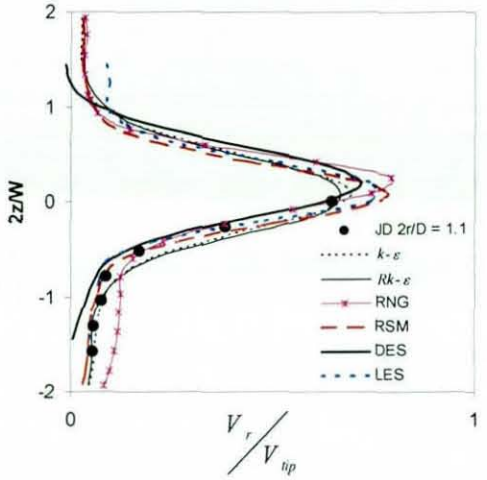

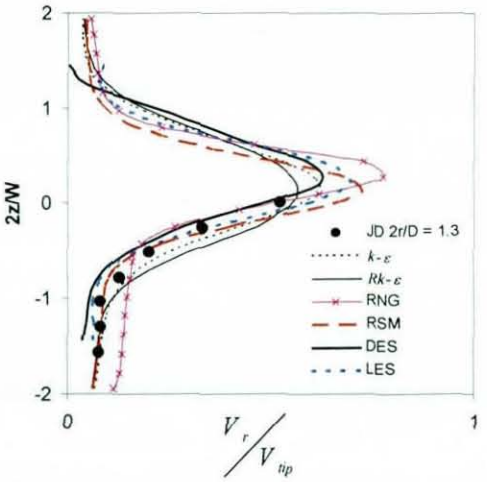

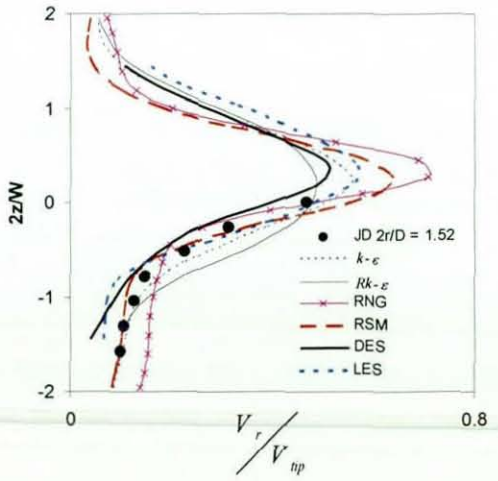

Figure 3-4: Prediction of time-averaged radial velocity at three different radial positions, JD corresponds to LDA data from Derksen *et al.* (1999)

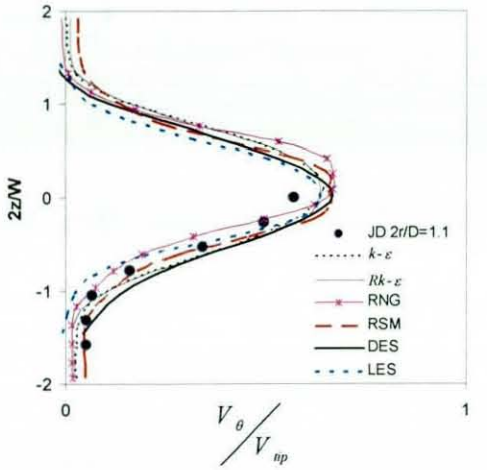

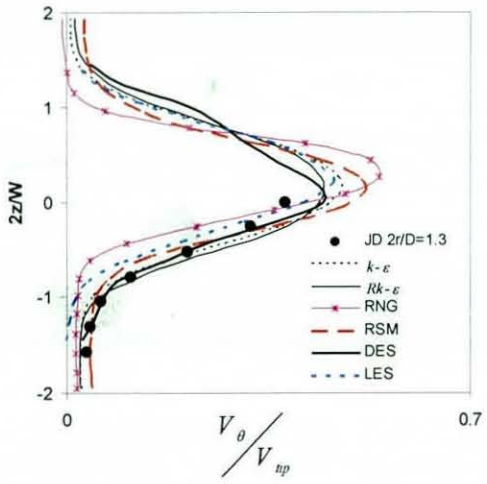

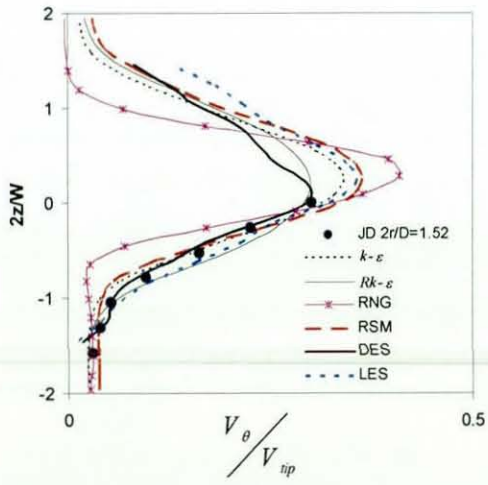

Figure 3-5: Prediction of time-averaged tangential velocity at three different radial positions, JD corresponds to LDA data from Derksen *et al.* (1999)

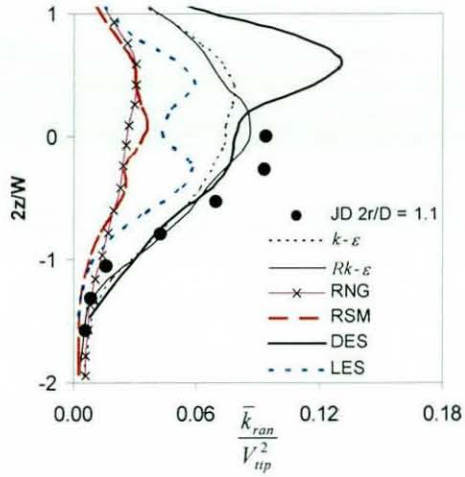

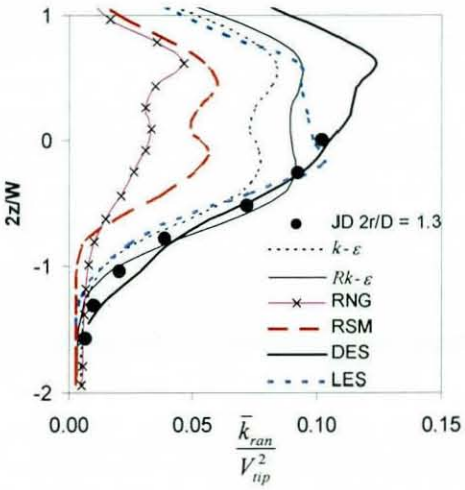

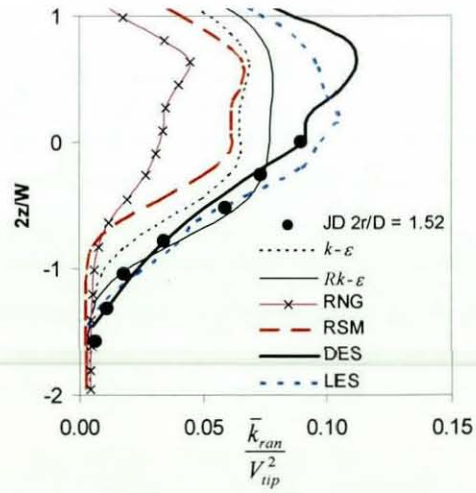

Figure 3-6: Prediction of $\overline{k_{ran}}$ at three different radial positions, JD corresponds to LDA data from Derksen *et al.* (1999)

It has been known for some time that the turbulent kinetic energy is under-predicted by RANS based turbulence models, no matter how complicated the models are *e.g.* RSM (Jaworski and Zakrzewska, 2002). The predictions from all RANS models tested in this work on turbulent kinetic energy only represent the random and angle-resolved values since the modelling was carried out using a steady-solver and MRF applied to a half-tank domain. Derksen *et al.* (1999) have measured the angle-resolved fluctuating velocities (axial, radial and tangential rms) very close to the impeller, thus enabling direct comparisons to be made for both angle-resolved and time-averaged turbulent flows.

Predictions of the angle-averaged $\overline{k_{ran}}$ by the k-ε and Rk-ε model shown in Fig. 3-6 are only about 20% and 10% lower than Derksen et al.'s data. The k-ε model also yielded a closer agreement to Derksen's measurement although its prediction is not as good as the Rk-ε model. This is notable since from our best of knowledge k-ε model generally under predicts $\overline{k_{ran}}$ by more than 30%. The exception is by Nere *et al.* (2001), who empirically adjusted the values of the standard constants in the k-ε model in their study. This is not thought to be a good practice, since these constants have already been tuned using experimental data and should be retained. Good predictions of $\overline{k_{ran}}$ by the RANS model in this study is believed to be attributable to the application of very fine grid around the impeller. A local refinement in the impeller region was also employed here, but with much finer grid size (<0.015D) compared to 0.023D in the same region of Revstedt *et al.*'s LES study. Among the RANS models studied (see Fig. 3-6), it can be observed that Rk-ε and k-ε give much better predictions of the $\overline{k_{ran}}$, while RNG has the poorest prediction. RSM predictions of $\overline{k_{ran}}$ at radial positions nearer to impeller ($2r/D$ = 1.1) are as poor as RNG, with more than 60% under prediction, but are improved up to only 30% under prediction at $2r/D$ = 1.52. In contrast with RSM, RNG prediction of $\overline{k_{ran}}$ does not improve even at positions far from impeller tip.

No comparisons can be made for the k_{tot} prediction by the RANS model, because the impeller is actually 'frozen' at a single position in the MRF model. The DES yielded the best prediction of the $\overline{k_{ran}}$ (see Fig. 3-6) and k_{tot} (see Fig. 3-7)

although prediction by LES away from the impeller ($2r/D$ = 1.3 and 1.52) were as good as those obtained from DES. The LES predictions were not very good close to the blade tip ($2r/D$ = 1.1). This is due to unresolved eddies near the impeller wall because the grid was prepared for DES (y^+ ~ 20). As mentioned earlier, the LES modelling in this work is carried out to prove that the grid prepared in this study is far from capable of resolving the LES around the boundary layer. At positions closer to the impeller ($2r/D$ = 1.1) the DES is capable of producing the double peak in k_{tot} often observed experimentally whilst the LES fails (although the LES predictions of k_{tot} are still close to the experimental measurements). Similar trends were also observed for the $\overline{k_{ran}}$ predictions where the LES fails to predict correctly the $\overline{k_{ran}}$ at $2r/D$ = 1.1). The k_{tot} is predicted reasonably well by the unresolved LES because the k_{tot} is calculated mainly from periodic velocity fluctuation due to the impeller passage, whilst $\overline{k_{ran}}$ depends only on the velocity fluctuations due to the turbulent flow, which explains the poor prediction at $2r/D$ = 1.1. The result for $\overline{k_{ran}}$ demonstrates that the grid prepared in this work is not suitable for LES, but it is good enough for DES. The DES does not need to resolve the small eddies in the boundary layer, since the DES turns into a RANS model in this region and hence works well even for a coarser grid. There are some other studies on LES prediction of turbulent flow in stirred tanks using a relatively coarse grid (e.g. Yeoh *et al.*, 2004) and they reported a good prediction of the turbulent kinetic energy. However, they only presented the k_{tot} which includes the periodic turbulent fluctuation due to the blade passage and they have not presented any comparison for the $\overline{k_{ran}}$ prediction alone. Such an LES study with a coarser grid may not resolve the flow near the boundary layer well enough and it may not able to resolve the $\overline{k_{ran}}$ around the impeller discharge.

Dissipation rates were not measured by Derksen *et al.* (1999), thus the ε values presented in this chapter were estimated using the following equation from Wu and Patterson (1989):

$$\varepsilon = \frac{0.85\overline{k_{ran}}^{3/2}}{\sqrt{3\Lambda^2}} \qquad (3.28)$$

where k and Λ are the turbulent kinetic energy and the integral length scale, respectively. A constant length scale value of $\Lambda = W/2$ was chosen (Kresta and Wood, 1993), considering the LDA measurements by Derksen *et al.* (1999) were located close to the impeller. Such an assumption of course may lead to a serious error in the bulk region, for example, near the liquid surface where $\Lambda = W$ (Khan *et al.*, 2004); however it was considered valid near the impeller. The dissipation rate from DES modelling was also computed using eq.(3.28). The ε values for the RANS model (k-ε, Rk-ε, RNG and RSM) were taken directly from the CFD simulation. Results from the RANS model especially the k-ε and Rk-ε model for the ε in Fig. 3-8 are surprisingly much better than the DES and LES predictions estimated using eq.(3.28). The RSM model was found to under-predict ε close to the impeller ($2r/D$ = 1.1) but was better away from the impeller ($2r/D \geq 1.3$). Meanwhile, the RNG prediction of ε was rather poor even at points away from impeller. However, it is not clear whether the ε is predicted correctly in this work, because of the use of eq.(3.28), which assumes isotropic turbulence and a constant length scale. The length scale is known to vary from around $\Lambda = 0.3W$ at the immediate vicinity of the impeller to $\Lambda = W$ in the bulk region near the liquid top surface (Khan *et al.*, 2004). Nevertheless, the results show that the RANS models, especially the k-ε and Rk-ε models may be able to predict ε reasonably well, at least for the time-averaged flow, using a well-resolved grid around the impeller.

The dissipation rates may also be estimated using the following relations for LES and DES:

$$\varepsilon_{SGS} = \tau_{ij}\bar{S}_{ij} \tag{3.29}$$

The sub-grid scale tensor, τ_{ij}, was introduced earlier in eq.(3.17). As shown in Fig. 3-8, prediction of ε using eq.(3.29) gives a severe under-prediction. Similar findings were reported recently by Delaffose *et al.* (2008) who found up to 75% under-prediction of ε using the common LES model. According to Delafosse *et al.* (2008) a better prediction of ε from LES can be obtained by adjusting the constant C_s in the Smagorinsky model (equation 3.20) from 0.1 to 0.2. As mentioned earlier, adjusting the model constant is not thought to be a good practice because it has already been tuned to match experimental data. However,

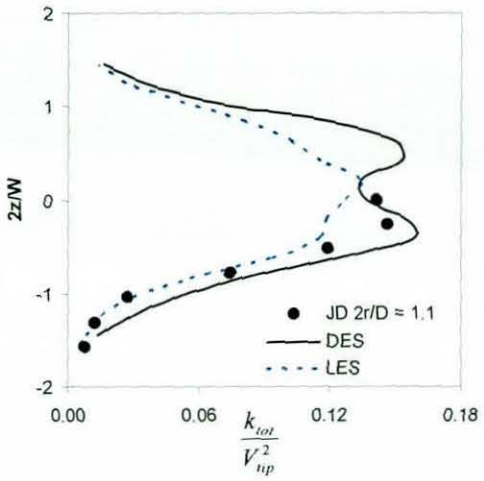

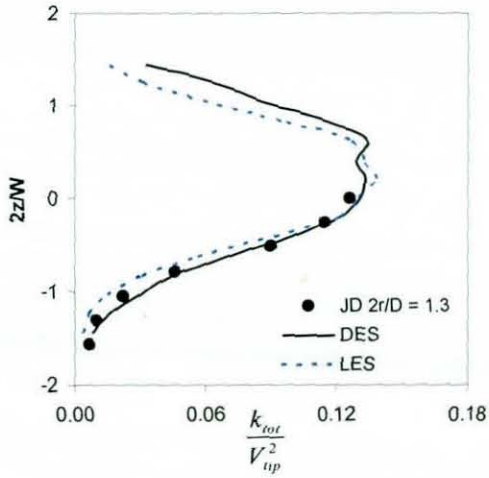

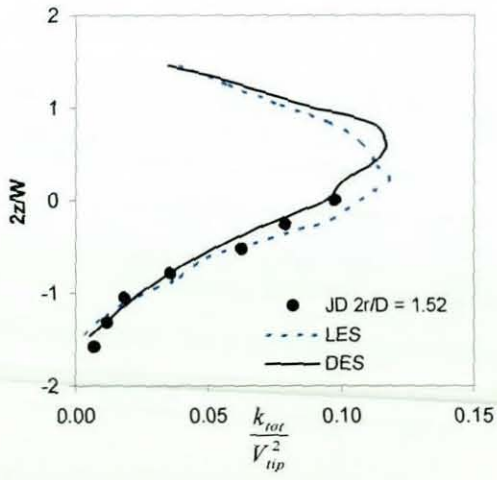

Figure 3-7: DES and LES prediction of angle-averaged total kinetic energy at three different radial positions. Data points are taken from Derksen *et al.* (1999) experimental data

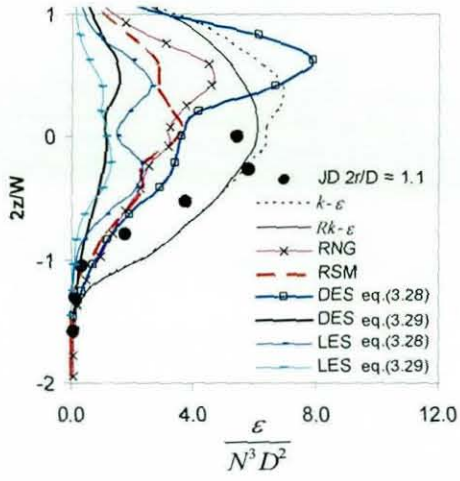

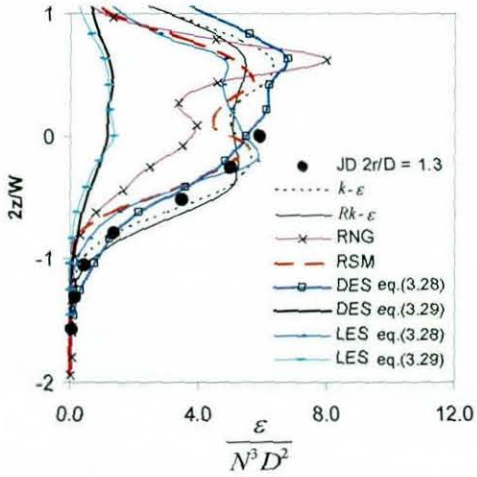

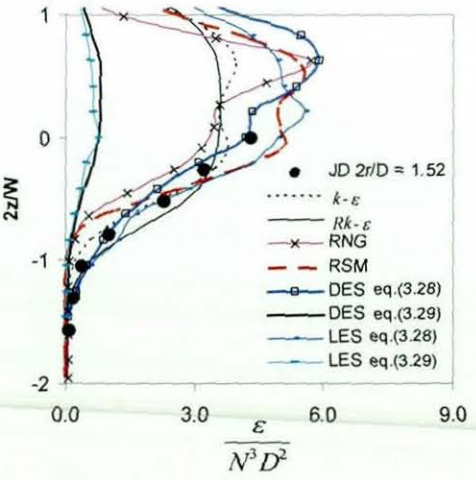

Figure 3-8: Prediction of time-averaged ε at three different radial positions, JD corresponds to LDA data from Derksen *et al.* (1999)

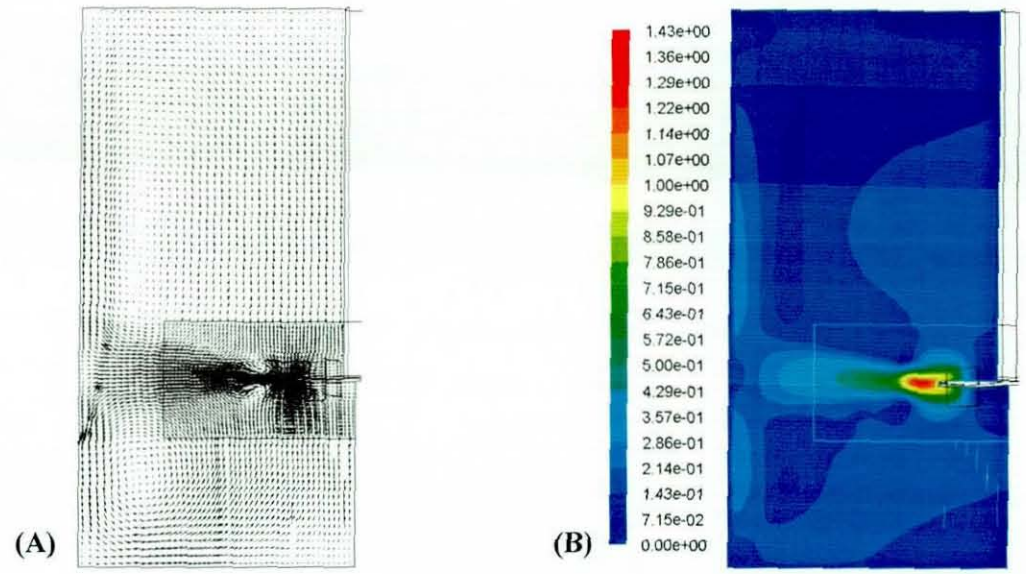

Figure 3-9: Results from a steady-state Rk-ε simulation, A) Vector of the velocity magnitude, B) Velocity magnitude (m/s)

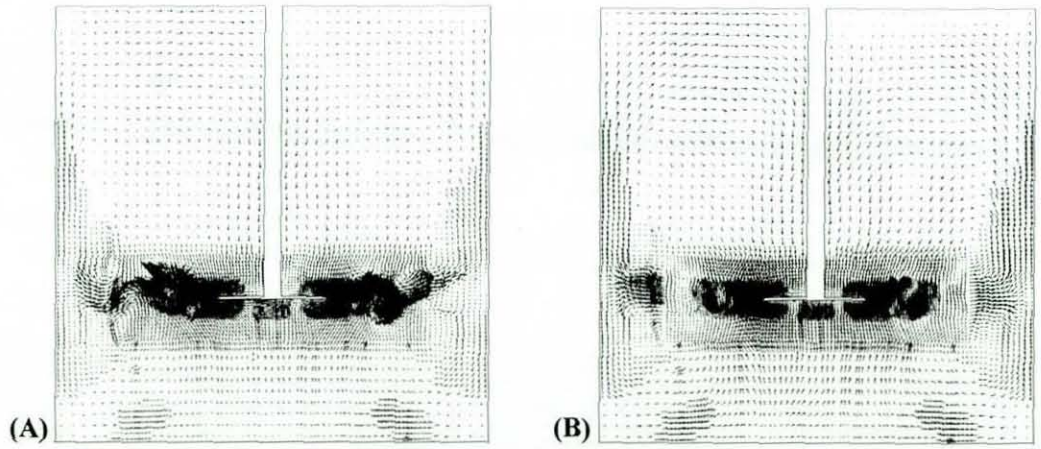

Figure 3-10: Result from DES simulation, A) Instantaneous vector of velocity magnitude, B) Time-average vector of velocity magnitude

dynamic changes in the Smagorinsky's constant may be accommodated using the model by Lilly (1992), who suggested a dynamic computation using the information provided by the resolved velocity field. Such models are now available in current version of commercial CFD code such as FLUENT 6.3 but have not yet been tested for stirred tank simulations.

Fig. 3-9 shows the velocity vectors and the contours of velocity magnitude in between two baffles obtained from a steady-state Rk-ε simulation. The common features of stirred tank flows i.e. the double loop around the lower and upper

region of the tank are clearly depicted (see Fig. 3-9A). The trend of a slightly upward velocity direction in the impeller discharge stream similar to those observed experimentally by e.g. Wu and Patterson (1989) and Escudie and Line (2003) is also reproduced correctly (see Fig. 3-9B).

The instantaneous velocity field obtained from the DES simulation in Fig. 3-10A shows the unsteadiness in the flow field especially around the impeller. The flow field is also shown to be highly anisotropic and asymmetry in nature with both side of the tank showing a different velocity field. The vortex structures can be observed in many parts of the tank, especially around the impeller region. The flows are also much more complicated than those obtained from the steady-state simulation in Fig. 3-9. However, the time-averaged velocity vector from instantaneous velocity of DES in Fig. 3-10B shows similarity to the steady-state velocity vector in Fig. 3-9 with a clear double circulation loop above and below the impeller level.

3.5.2 Identification of the vortex core

The vortex core is an important flow feature which needs to be well represented as it potentially has a great influence on the bubble behaviour and the overall turbulent flows in a stirred tank. According to Ranade *et al.* (2001) the trailing vortices play a crucial role in determining the gas accumulation behind the impeller. In turn this affects the pumping and power dissipation capacity of the impeller and thus significantly affects the performance of a gas-liquid stirred reactor. The evidence of gas accumulation in trailing vortices was further confirmed by Deen *et al.* (2002) in their PIV experiments on a gas-liquid agitated system. The trailing vortices in a gas-liquid system were replaced by gas cavities clinging to the back of the impeller blade (e.g. Brujin *et al.*, 1974; Deen *et al.*, 2002; Warmoeskerkern and Smith, 1982). Furthermore, the trailing vortices were associated with high levels of turbulent activity and high velocity gradients and thus play an important role in the mixing capability of a stirred tank (Lee and Yianneskis, 1998).

CFD predictions of the radial position of the trailing vortex core have been published by many researchers (for example Alcamo *et al.*, 2005; Yoon *et al.*, 2003; Derksen and van den Akker, 1999). However, most of the previous studies

only consider a single vortex core position (either the upper or lower); the exception is by Derksen and van den Akker (1999) who considered both cores. In addition, there has been no extensive CFD comparison made on the axial position of the vortex core with experimental measurements.

A detailed experimental study of the vortex core has been reported previously by Escudie *et al.* (2004) based on the axial and radial positions of the vortex core deduced using three different methods. The first method was called a "null velocity method": the vortex core was obtained simply by connecting the points at which the axial velocity was equal to zero, as proposed by Yianneskis *et al.* (1987). The second method was called the "vorticity method" in which the vortex core position was obtained by connecting the points of maximum vorticity magnitude. The third method, namely λ_2, was proposed by Jeong and Hussain (1995) and was based on the presence of a minimum local pressure in a plane perpendicular to the vortex axis. Escudie *et al.* (2004) found that all three methods gave almost an identical curve for the vortex radial position, however, the null velocity method gave a slightly different result compared to both vorticity and λ_2 method for the axial position. The vortex core in this work was determined by using the vorticity method, as it is relatively simple to perform and also has a similar accuracy to the λ_2 method.

The vector plots of velocity magnitude in the vicinity of the impeller are shown in Fig. 3-11 at various angles with respect to an impeller blade. The vector plot can be obtained directly from the steady-state CFD simulation for the RANS model (RSM), but a time-average of the instantaneous velocity field must be performed before a vector plot for the DES simulation can be obtained. Both the RSM and DES results show a good qualitative agreement with the measured velocity fields from Derksen *et al.* (1999). A much stronger vortex can be seen close to the impeller blade (at 10° and 19°) and the trailing vortex becomes almost invisible away from the blade (at 49°) because the velocity magnitudes become much smaller. The upward movement of the trailing vortex core as the impeller rotates from 10° to 49° is also visible, as well as the difference between the upper and lower cores. A similar pattern was also observed previously by Escudie *et al.* (2004) from analysis of their PIV measurements.

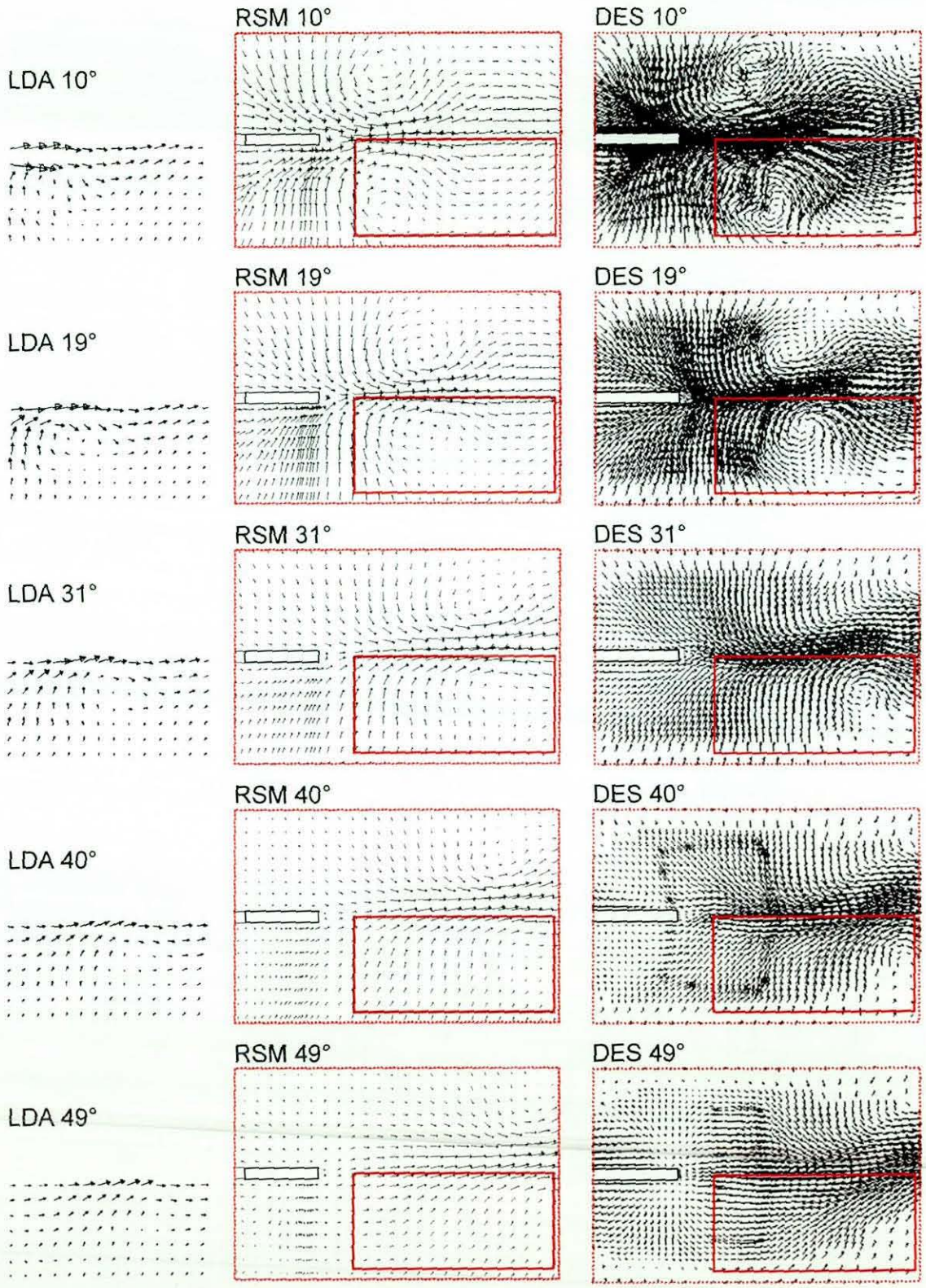

Figure 3-11: Vector plot of velocity magnitude in the vicinity of the impeller at five different angles with respect to a blade

Data on several planes behind the impeller were exported to an independent post-processing software, SURFER 8, to avoid parallax error from visual assessments of the maximum vorticity position. The vorticity surface plots on a series of *r-z* planes at different blade angles were obtained using SURFER 8 and the positions of the vortex core were determined using the build-in digitiser. A sample plot of the vorticity surface is shown in Fig. 3-12. Post-processing of the DES data was not so straightforward as for the RANS models, as the instantaneous vorticity magnitudes in the respective *r-z* planes (at blade angles 3° to 50°) have to be averaged first before further analysis can be done. A total of 540 instantaneous surface data sets at each blade angle were averaged using MS Excel, with the assistance of a simple macro to read the data (text) into an array.

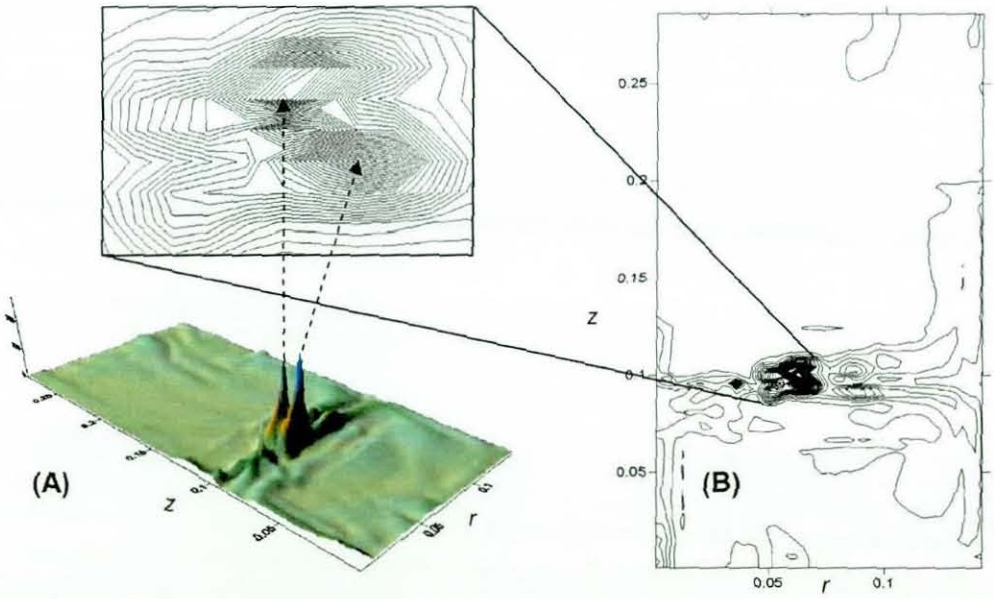

Figure 3-12: Vorticity at 40° behind the impeller blade obtained from the RSM model, A) Surface plot of vorticity, B) Contour plot of vorticity

Fig. 3-13 shows a comparison of the radial positions of the predicted and the experimental lower and upper vortex cores. The k-ε and Rk-ε models provide reasonably good agreement with the results from Derksen *et al.* (1999) for the upper vortex core, but are slightly worse for the lower vortex core. Comparisons are also made with experimental data from other authors i.e. Escudie *et al.* (2004), Yianneskis *et al.* (1987), Lee and Yianneskis (1998) and Stoots and Calabrese (1995). Escudie *et al.* (2004), Yianneskis *et al.* (1987) and Lee and

Yianneskis *et al.* (1998) worked on a geometrically similar vessel ($D = C = T/3$) to the one evaluated in this chapter but with slightly different tank diameters: T = 0.45 m for Escudie *et al.* (2004), T = 0.294 m for Yianneskis *et al.* (1987) and T = 0.1 m for Lee and Yianneskis (1998). According to Lee and Yianneskis (1998), tanks with geometrically similar dimensions may be able to produce a reasonably similar trailing vortex core, citing their results from tanks with diameter of T = 0.1 m and T = 0.294 m. Meanwhile, Stoots and Calabrese's (1995) work was based on a tank with diameter T = 0.45 m and $C = T/2$. Data from these various authors did show some differences, but they are in close agreement to those from Derksen *et al.* (1999) measurement. The RSM model gives a much better prediction of both vortex cores compared to k-ε models, although there is no significant difference in the first 20° behind the impeller. This is because the RSM model relaxes the assumption of an isotropic eddy viscosity and takes into account the effects of streamline curvature, swirl, rotation and rapid change of strain rate in a more rigorous manner than k-ε. It is well known that the trailing vortices are the most anisotropic region in a stirred tank, thus demanding the use of a more elaborate turbulence model such as RSM, DES or even LES. The DES model gives a good prediction of both the lower and upper vortex core; slightly better than both the k-ε and Rk-ε models. Predictions by RNG are not presented because it is assumed that this k-ε model variant suffers from similar drawbacks and fails to predict the difference between the upper and lower vortex core. Moreover, predictions of k-ε and Rk-ε models in Fig. 3-13 showed very little difference. Meanwhile, predictions of LES are not presented because the simulation in this work was not fully resolved. Experimentally observed differences between upper and lower vortex core were also reproduced correctly by the RSM and DES models, as shown in Fig. 3-14.

There are several arguments related to the axial position of the vortex core. For example, Yianneskis (1987) claimed that the upper vortex core moves at a constant axial position from the top of the impeller at $2z/W$ = 1, whilst Derksen *et al.* (1999) claimed that the lower vortex core moves at a constant axial position of $2z/W$ = -0.52. Escudie *et al.* (2004) found that both the lower and upper vortex core move axially upwards with the lower vortex crossing the impeller centreline ($2z/W$ = 0) and moving towards $2z/W$ = 0.3; the upper vortex appeared not to

move further than $2z/W$ = 1. Stoots and Calabrese (1995) have studied the axial position of the lower vortex core and they claim that the core was at $2z/W$ = -0.6 close to the impeller blade, while at larger blade angles, the core moves towards $2z/W$ ~ -1. It is therefore interesting to elucidate the capabilities of CFD to predict the axial position of the vortex core in stirred tanks, but bearing in mind the variability of the experimental findings.

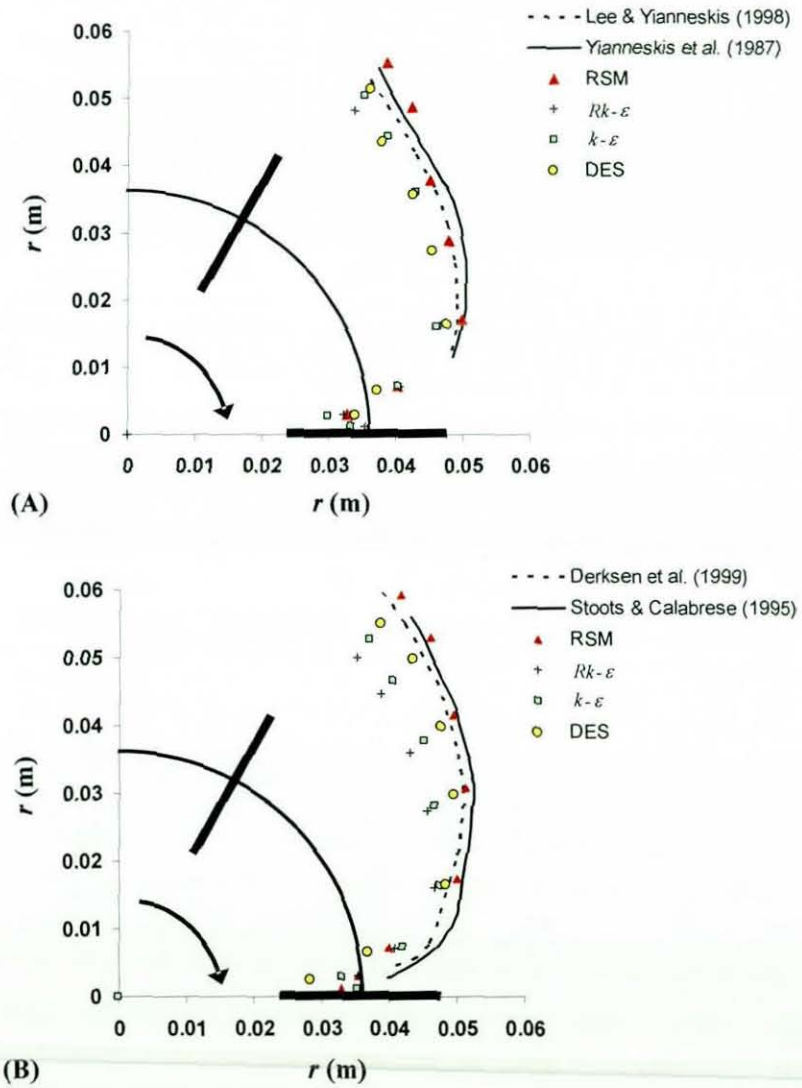

Figure 3-13: Prediction of the radial trailing vortex core, A) lower, B) upper

Fig. 3-15 shows the predicted axial positions of the vortex core behind the Rushton disk turbine blades. The RSM and DES models are in good agreement with Escudie *et al.*'s (2004) experiments which also studied a similar geometry to the present work (impeller bottom clearance and impeller size is $T/3$). The

upward movement of both trailing vortex pairs has been also successfully predicted by both the RANS and the DES model. The upward vortex movement is as expected, since it is well known that the discharge flow of the Rushton turbine is inclined slightly upward (see Fig. 3-9). It was also noted that the upward movement of the lower vortex core was greater than the upper vortex core. The k-ε model is much less successful in predicting the axial position of the vortex core correctly. This discrepancy can be explained by the isotropic assumption in the k-ε models, limiting their capability in predicting the turbulent flows in strongly anisotropic regions of the flow.

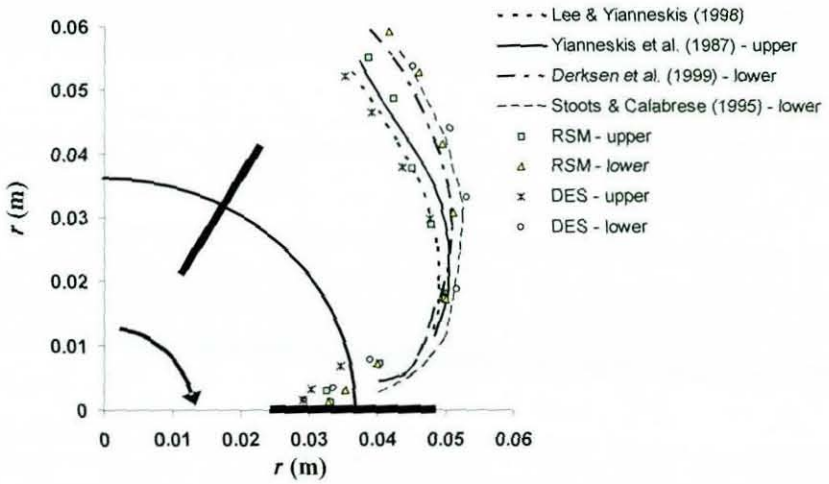

Figure 3-14: Comparison between upper and lower vortex core

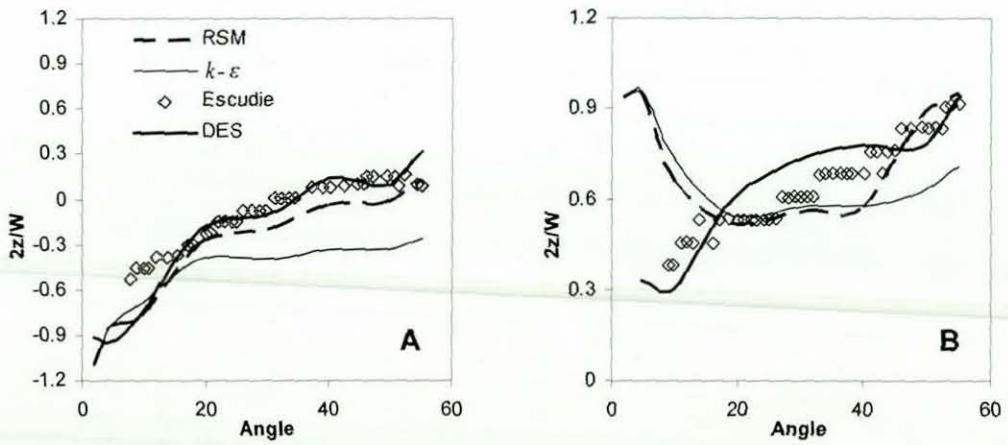

Figure 3-15: Prediction of the axial movement of the trailing vortex pairs. Data from Escudie *et al.* (2004). A) Lower vortex core, B) Upper vortex core

3.5.3 Angle resolved study

Although the angle-averaged prediction of the tangential velocities, by either RANS or DES models, looks good in Fig. 3-5, there are still some discrepancies, when comparing the angle-resolved values. Prior to discussion of the angle-resolved comparison, it is important to examine the position of the trailing vortices behind the impeller shown in Fig. 3-16. For reference, constant radial positions of $2r/D$ = 1.1, 1.3 and 1.52 are shown. At an angle of about 20° behind the blade the trailing vortices are at $2r/D$ = 1.1; around 30° to 50° they are at $2r/D$ = 1.3 and by around 60° they have reached $2r/D$ = 1.52. Predictions of the tangential velocity by the RANS models are highly affected by this trailing vortex core as observed from the angle-resolved results in Figs. 3-17 to 3-19.

Generally, the angle-resolved tangential velocities appear to be either under- or over-predicted in the trailing vortex core using the RANS models but the agreement is not bad. This might be attributed to the strongly anisotropic flows within the trailing vortices, thus demanding the application of a much more elaborate turbulence model like DES, or even LES. The DES model has great potential to predict accurately the tangential velocity just before the vortex core, as shown in Figs. 3-17 (at 10°) and 3-18 (at 19°) and 3-19 (at 40° and 49°). This is due to the fact that the large eddies are resolve directly by DES away from boundary layer. Amongst the RANS models tested, predictions of both the k-ε

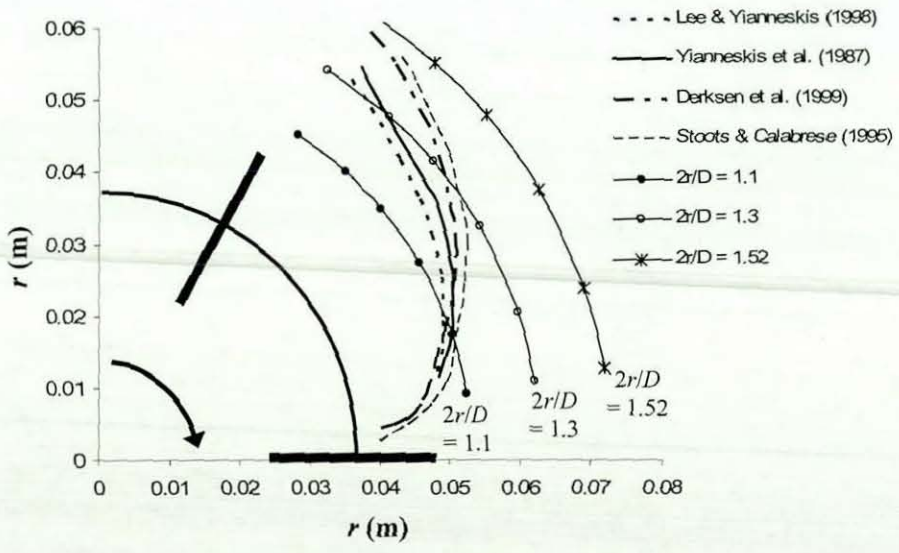

Figure 3-16: Position of the upper and lower vortex cores; symbols represent the radial positions at which data were extracted

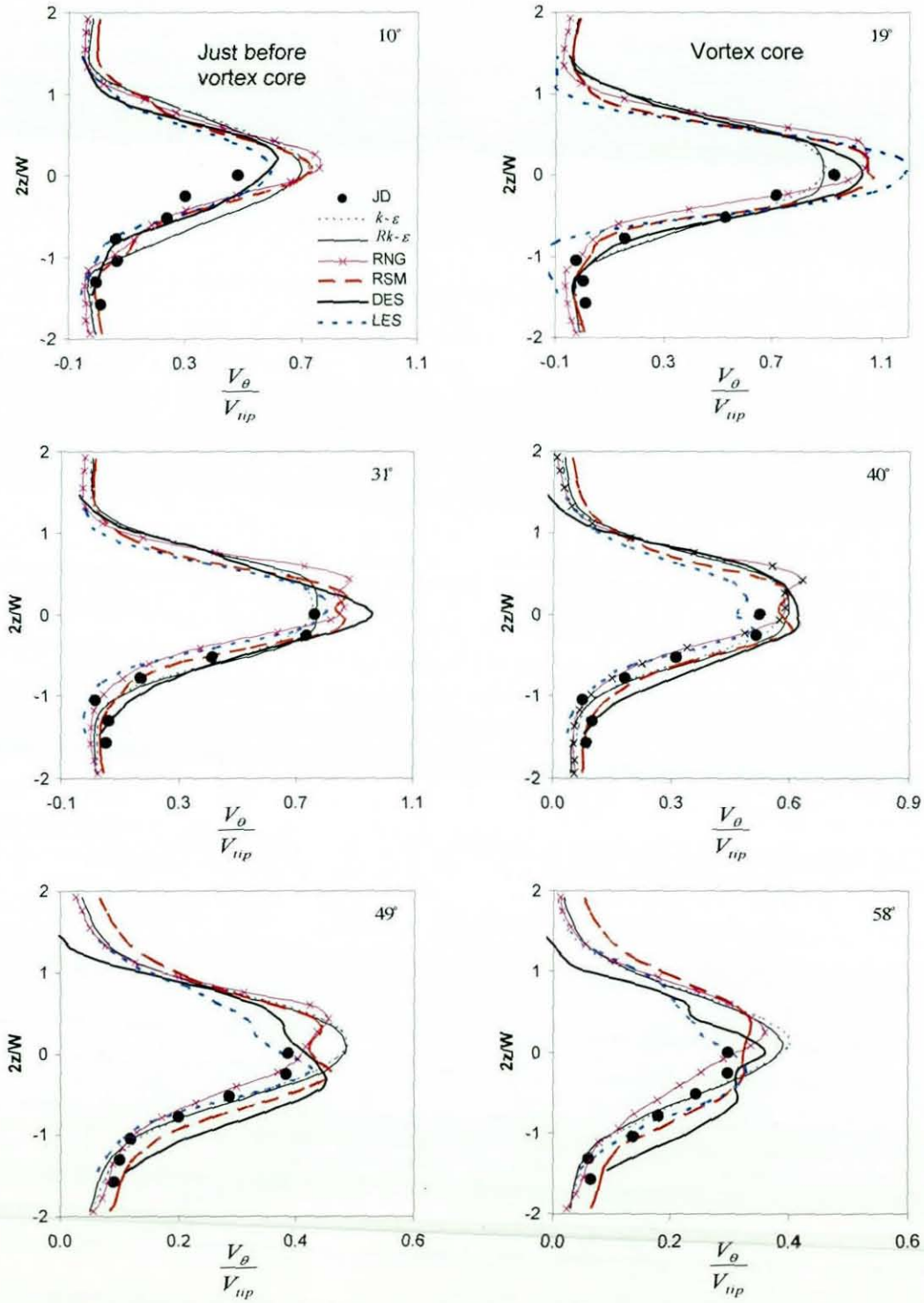

Figure 3-17: Prediction of the angle-resolved tangential velocity at radial position $2r/D$ = 1.1 for different angle positions, JD corresponds to LDA data from Derksen *et al.* (1999)

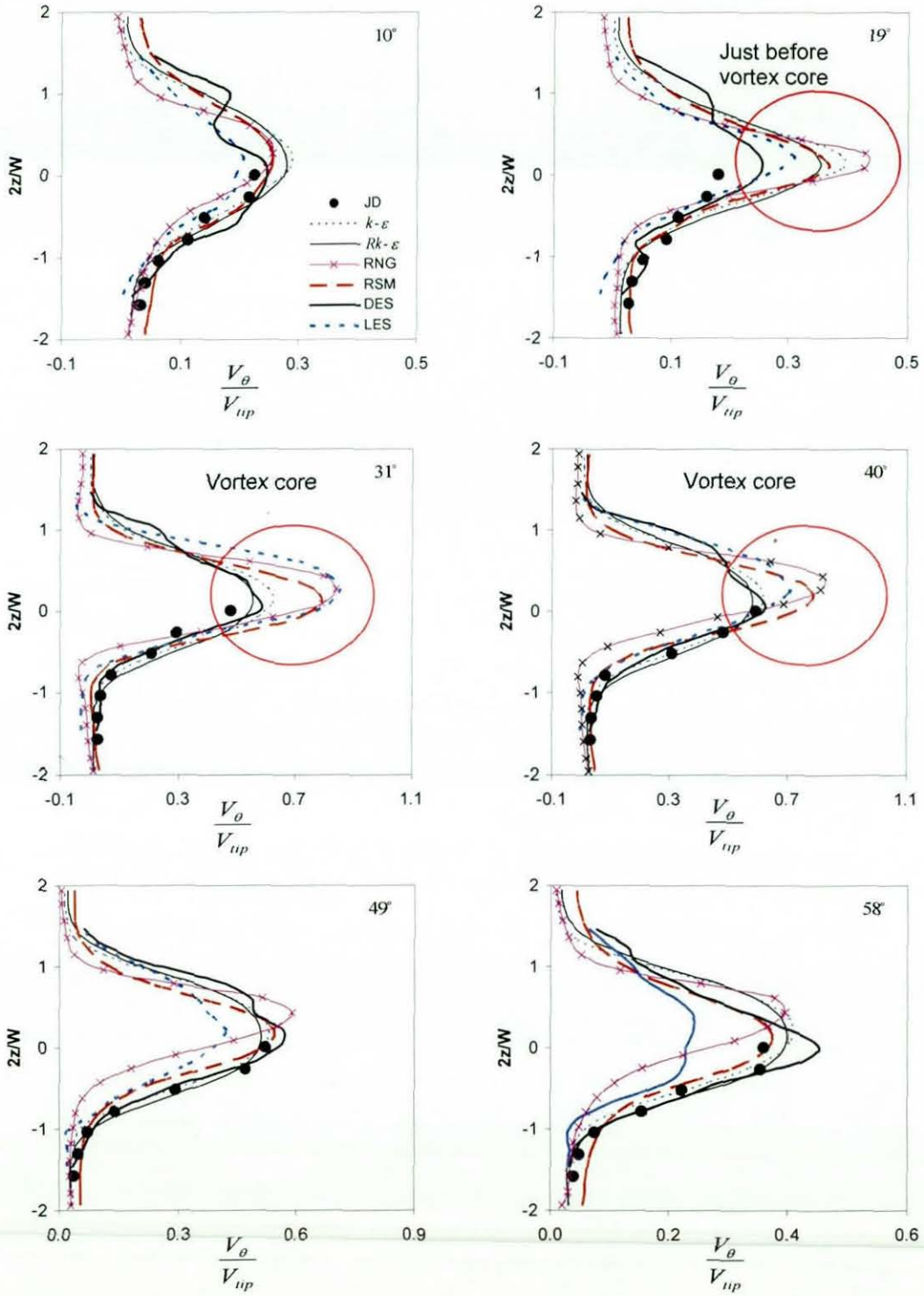

Figure 3-18: Prediction of the angle-resolved tangential velocity at radial position $2r/D$ = 1.3 for different angle positions, JD corresponds to LDA data from Derksen *et al.* (1999)

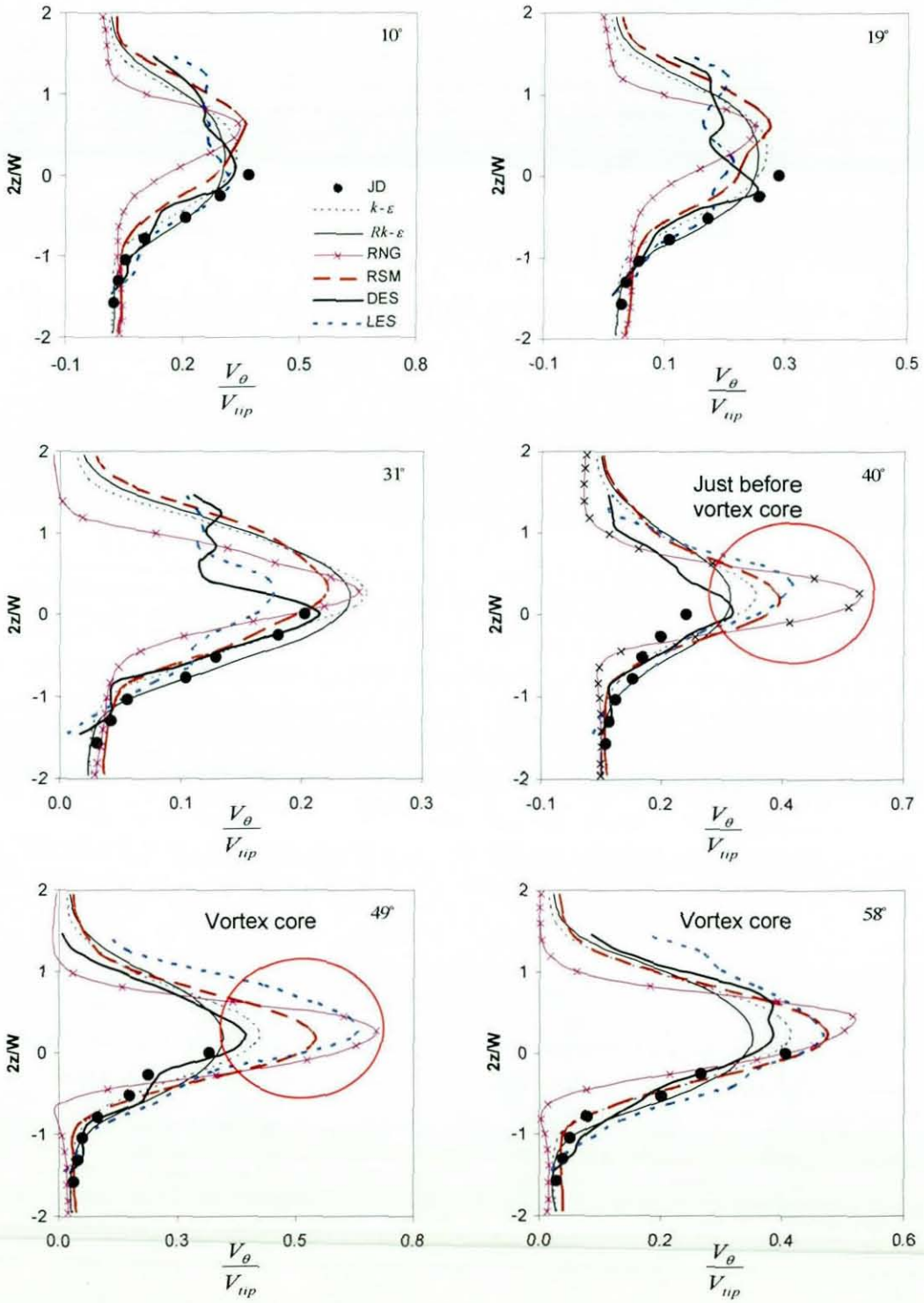

Figure 3-19: Prediction of the angle-resolved tangential velocity at radial position $2r/D$ = 1.52 for different angle positions, JD corresponds to LDA data from Derksen *et al.* (1999)

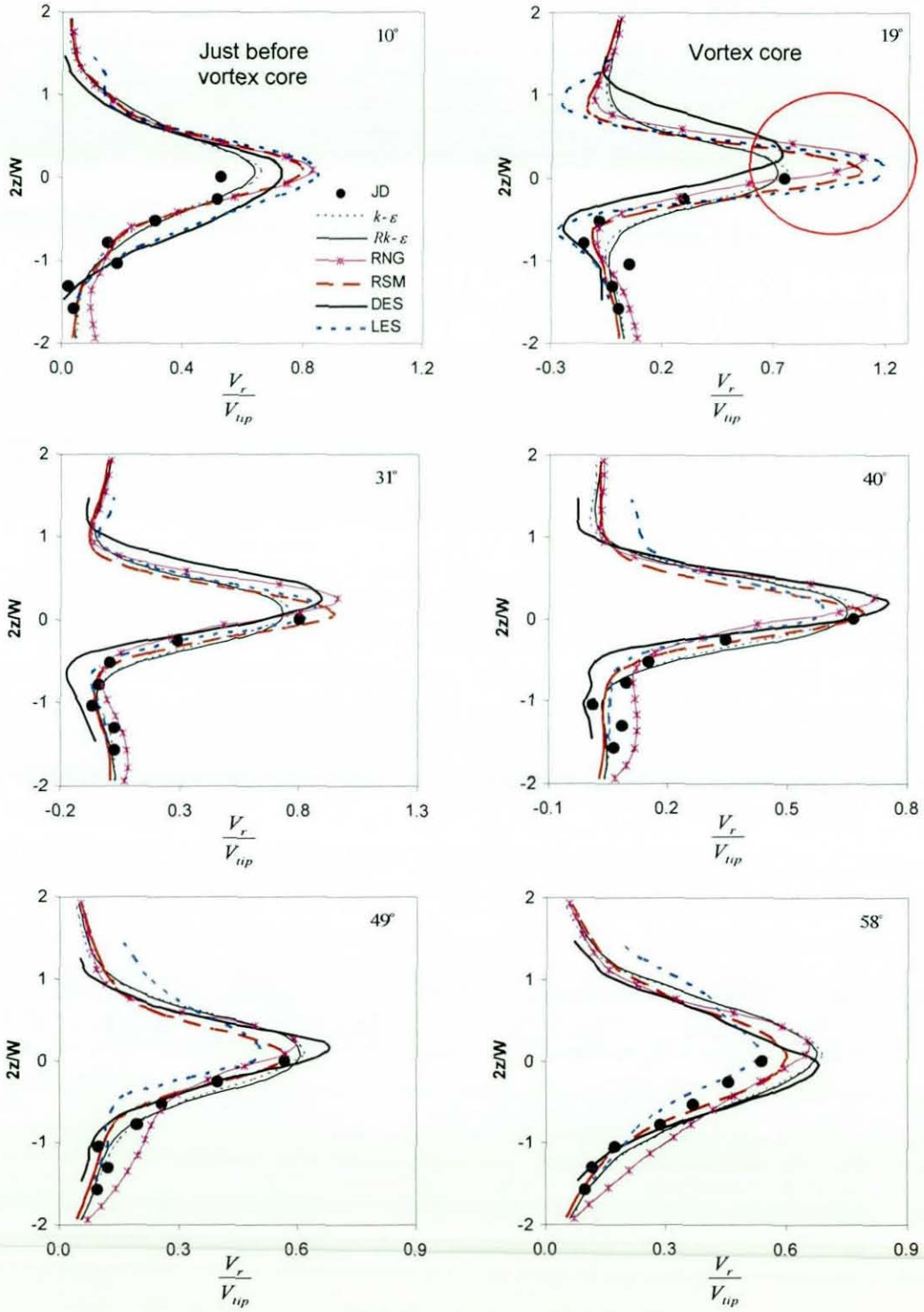

Figure 3-20: Prediction of the angle-resolved radial velocity at radial position *2r/D* = 1.1 for different angle positions, JD corresponds to LDA data from Derksen *et al.* (1999)

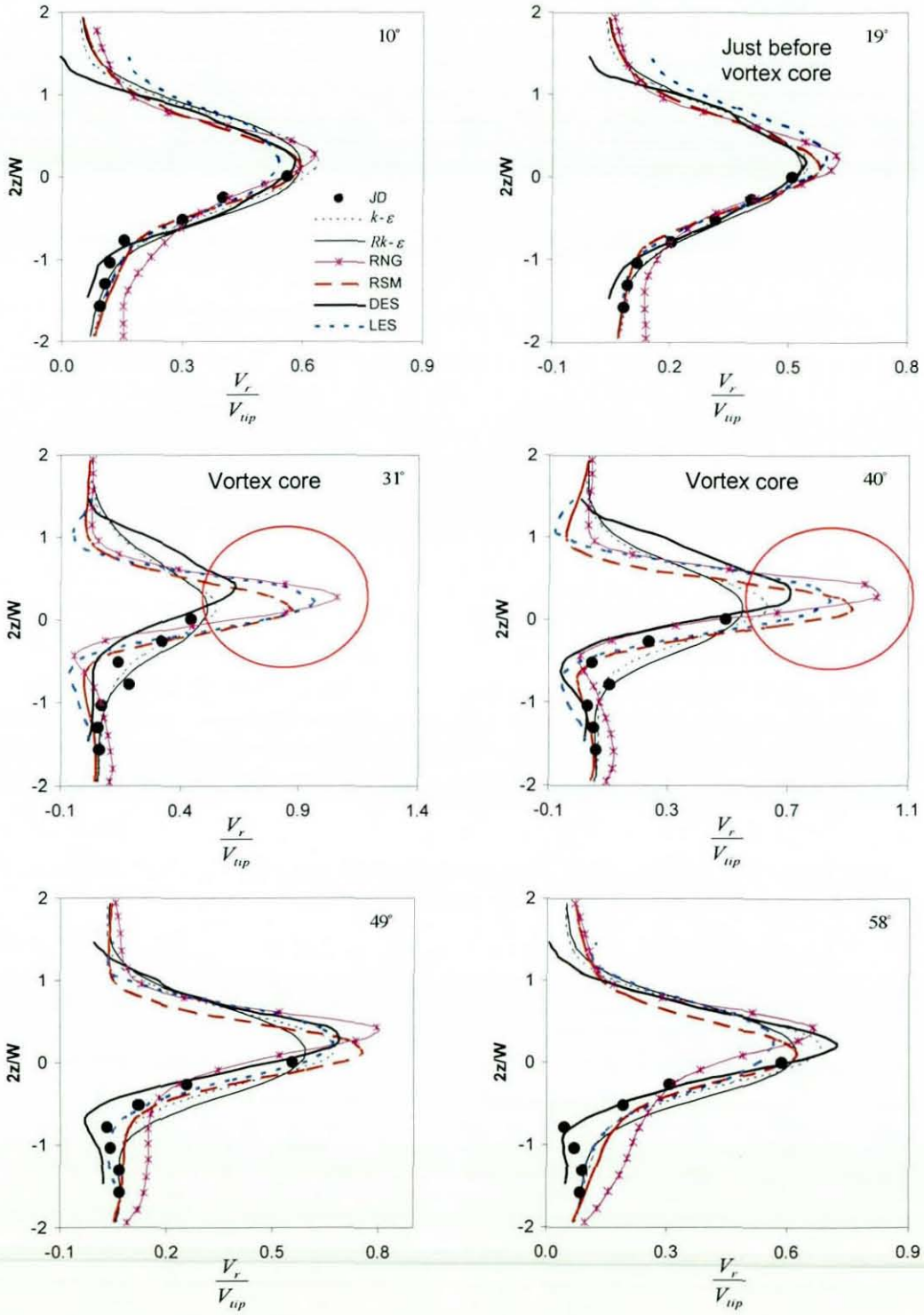

Figure 3-21: Prediction of the angle-resolved radial velocity at radial position *2r/D* = 1.3 for different angle positions, JD corresponds to LDA data from Derksen *et al.* (1999)

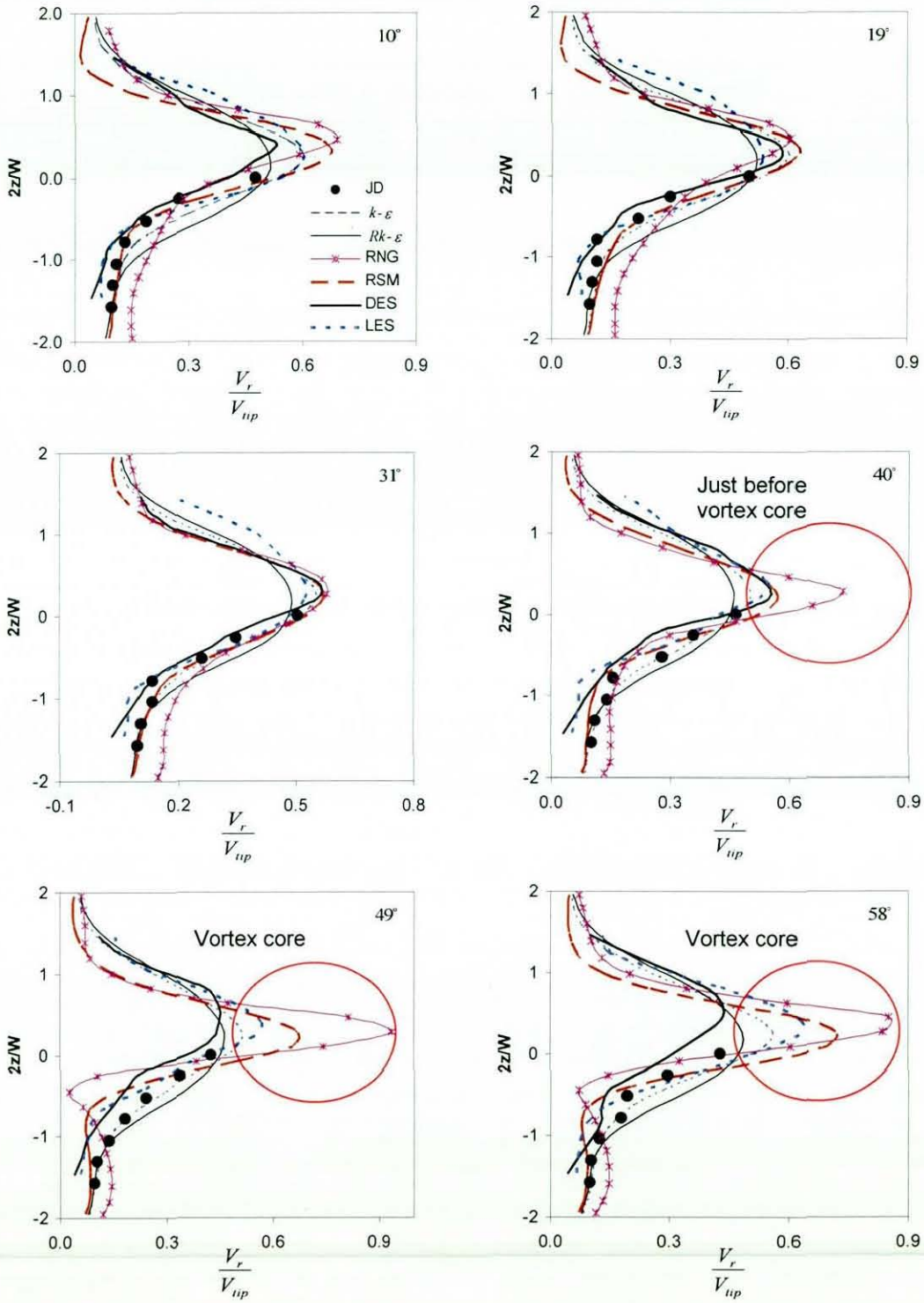

Figure 3-22: Prediction of the angle-resolved radial velocity at radial position *2r/D* = 1.52 for different angle positions, JD corresponds to LDA data from Derksen *et al.* (1999)

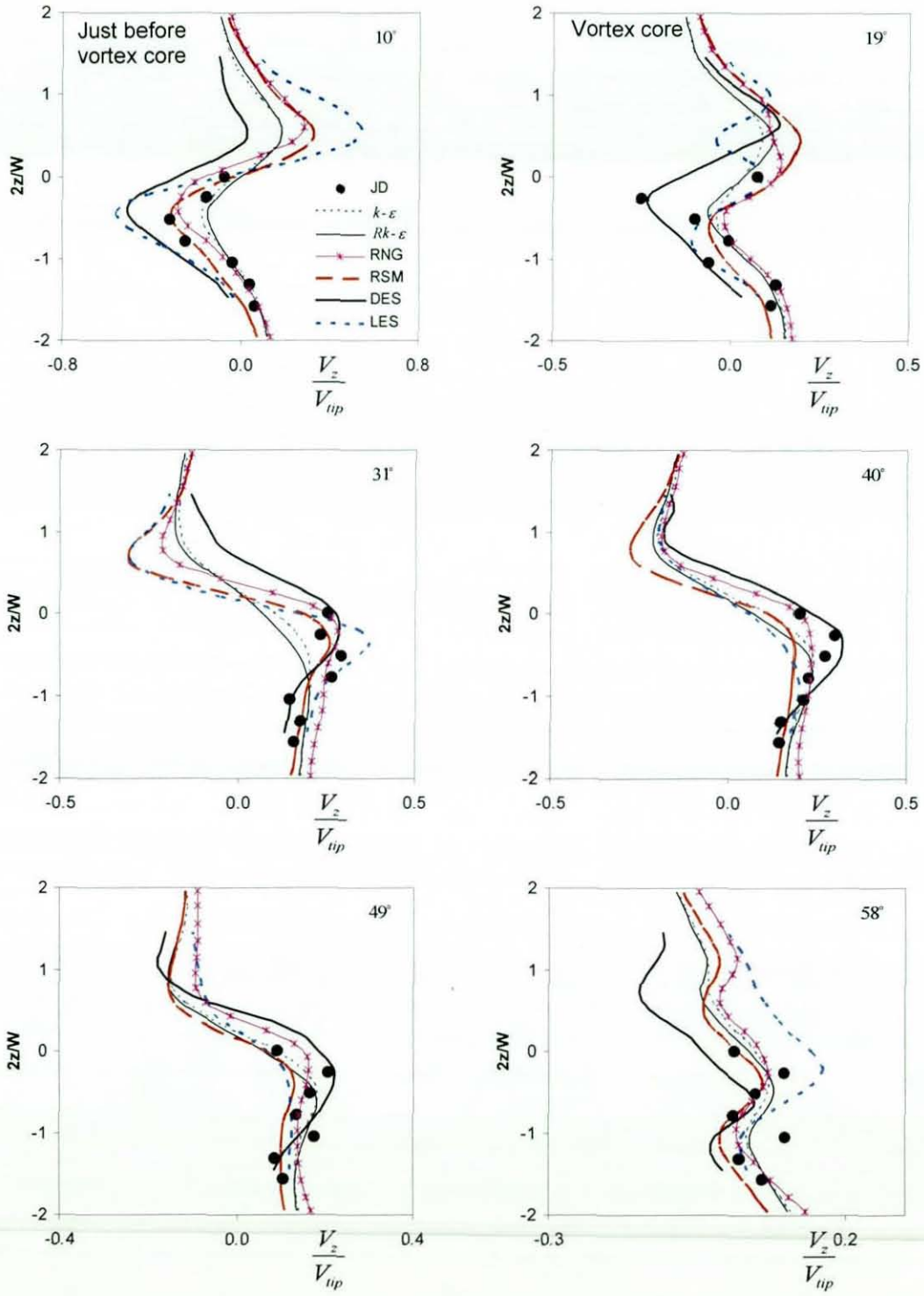

Figure 3-23: Prediction of the angle-resolved axial velocity at radial position $2r/D$ = 1.1 for different angle positions, JD corresponds to LDA data from Derksen *et al.* (1999)

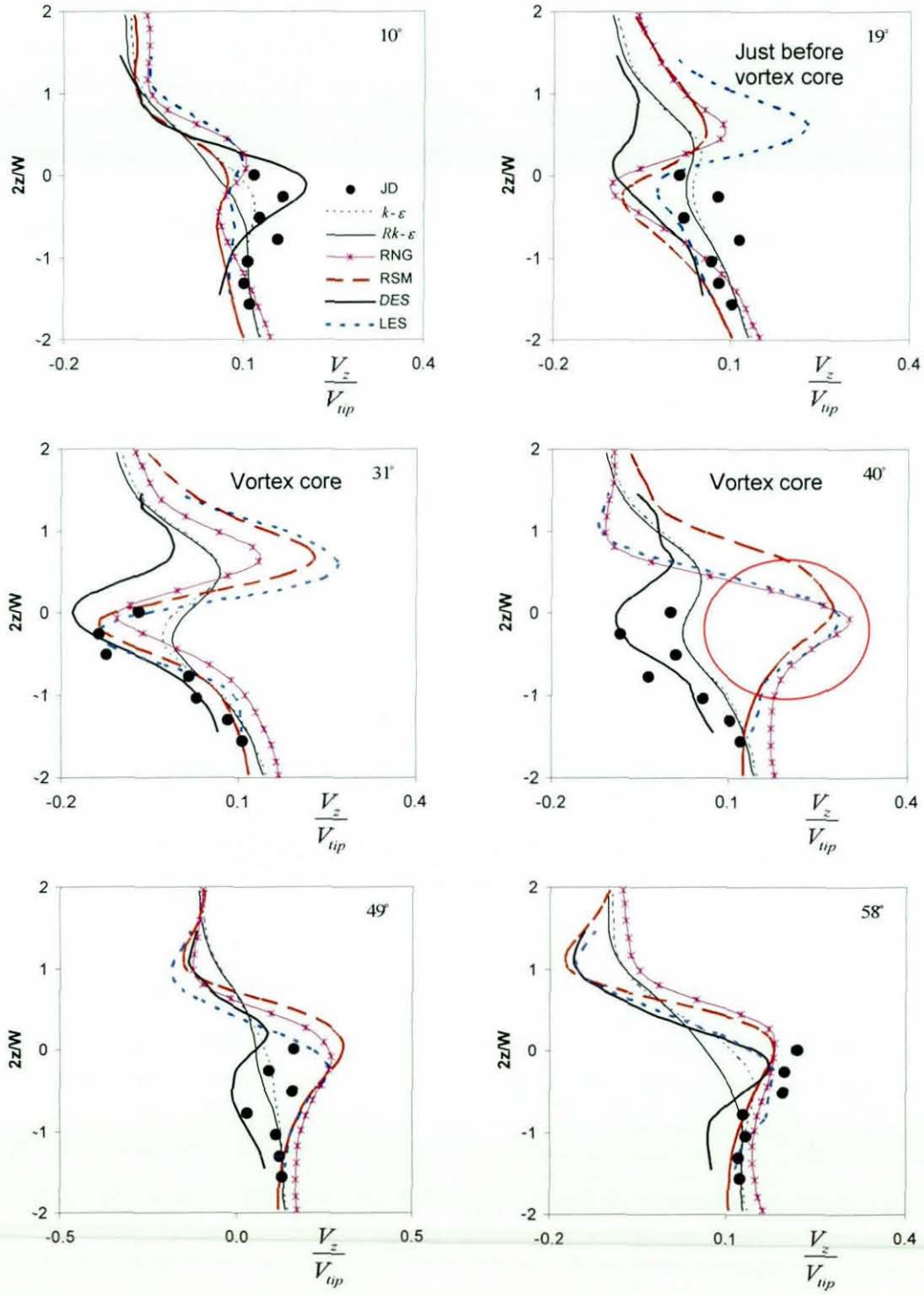

Figure 3-24: Prediction of the angle-resolved axial velocity at radial position $2r/D$ = 1.3 for different angle positions, JD corresponds to LDA data from Derksen *et al.* (1999)

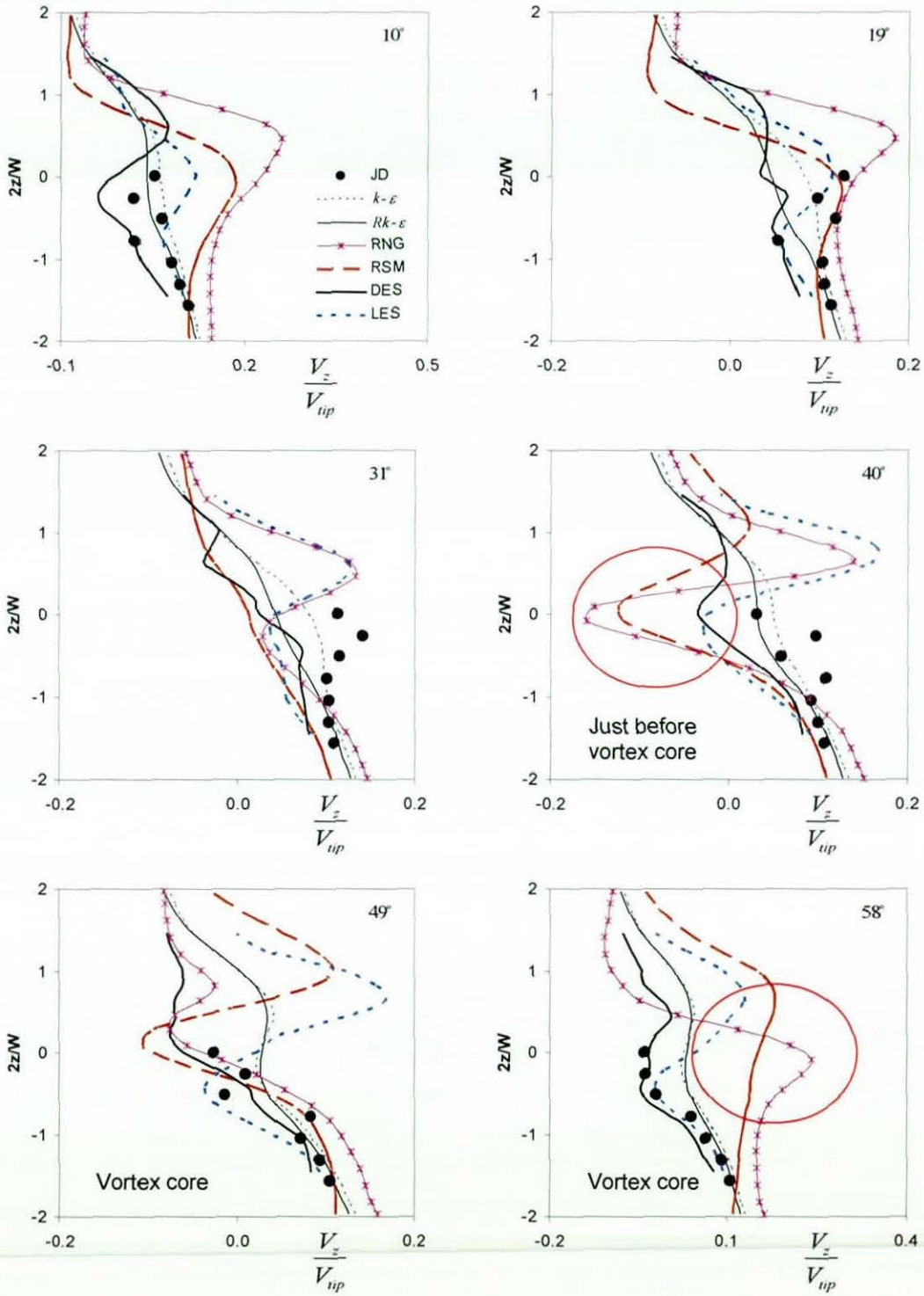

Figure 3-25: Prediction of the angle-resolved axial velocity at radial position $2r/D$ = 1.52 for different angle positions, JD corresponds to LDA data from Derksen *et al.* (1999)

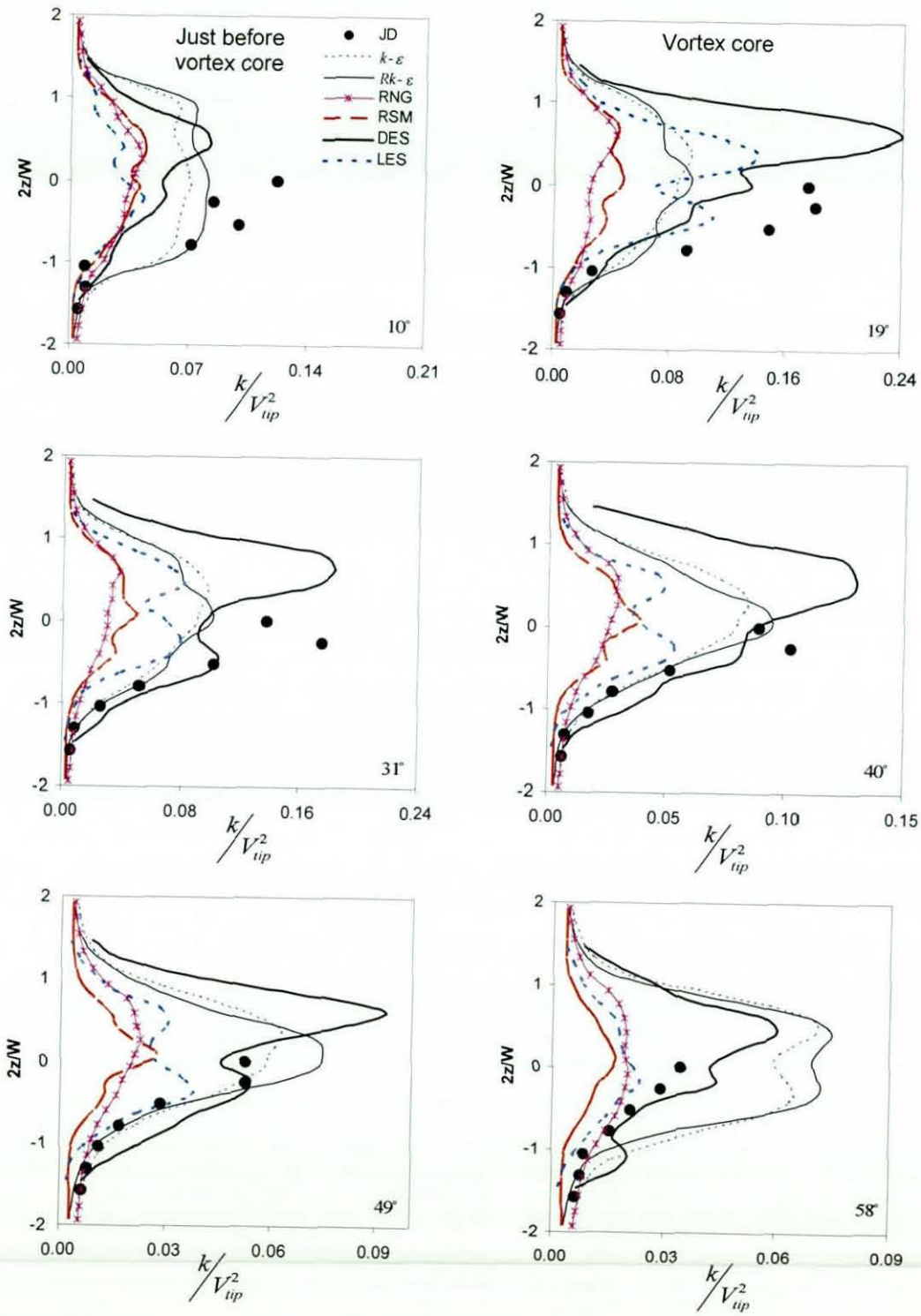

Figure 3-26: Prediction of the angle-resolved turbulent kinetic energy, $k_{ran}(\theta)$, at radial position $2r/D$ = 1.1 for different angle positions, JD corresponds to LDA data from Derksen *et al.* (1999)

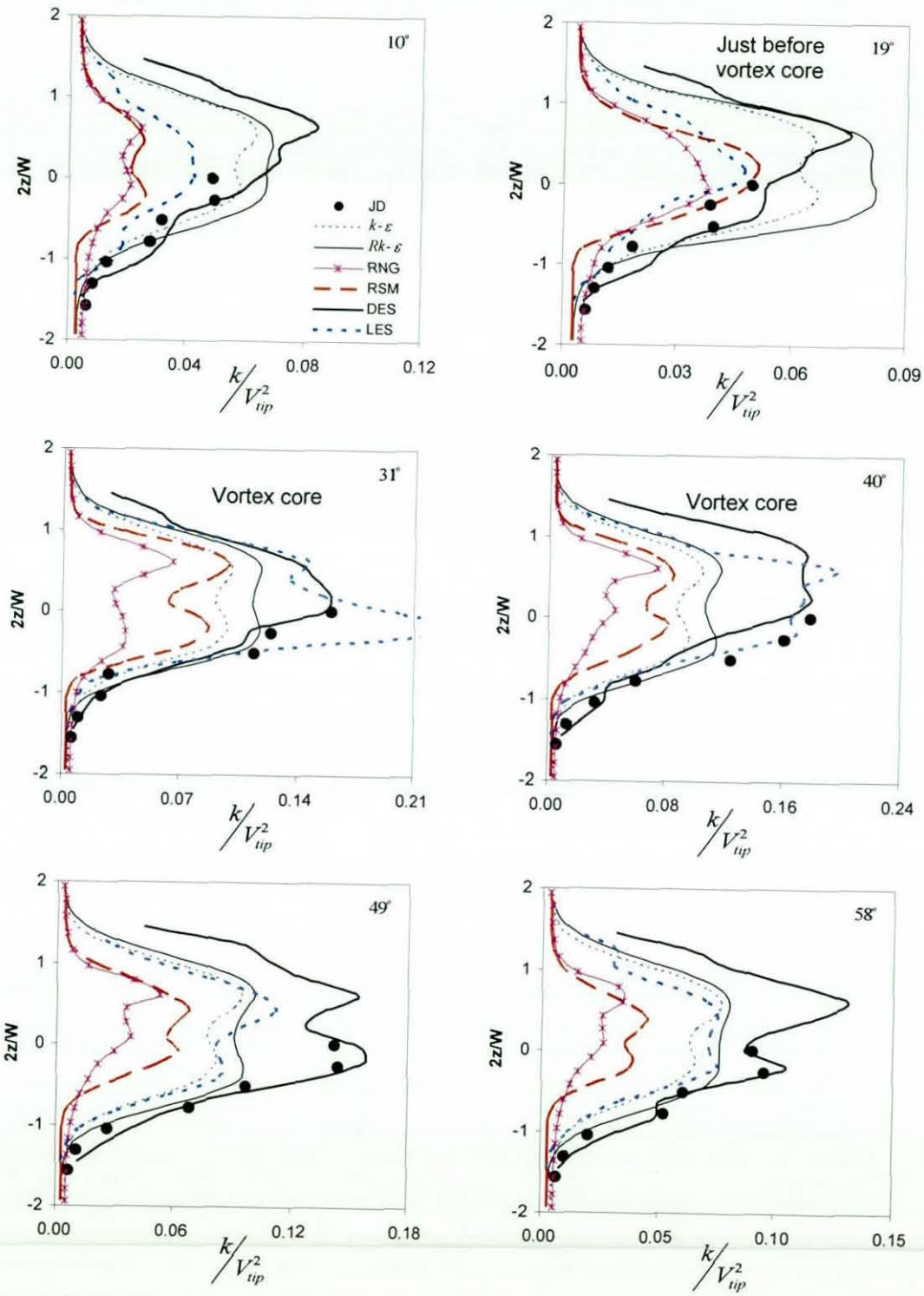

Figure 3-27: Prediction of the angle-resolved turbulent kinetic energy, $k_{ran}(\theta)$, at radial position $2r/D$ = 1.3 for different angle positions, JD corresponds to LDA data from Derksen *et al.* (1999)

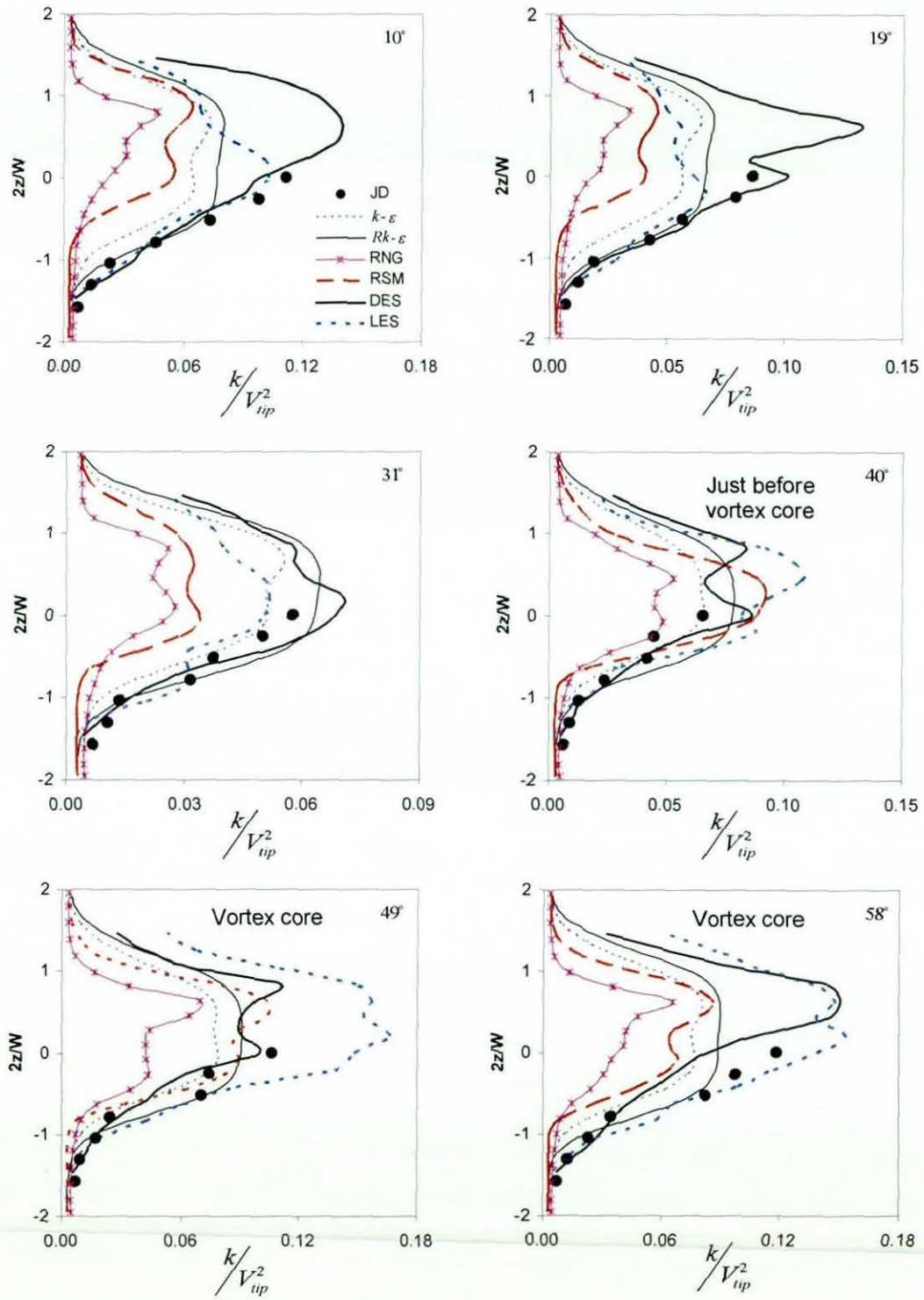

Figure 3-28: Prediction of the angle-resolved turbulent kinetic energy, $k_{ran}(\theta)$, at radial position $2r/D$ = 1.52 for different angle positions, JD corresponds to LDA data from Derksen *et al.* (1999)

and Rk-ε models for the angle-resolved tangential velocity are much closer to Derksen *et al.*'s (1999) measurements, whilst both RSM and RNG gave much poorer predictions. The V_θ are predicted well within the centre region of the vortex core when the DES, k-ε and Rk-ε models are employed but predictions by RNG, LES and RSM are not very good.

Predictions of angle-resolved radial velocity are also affected by the vortex core in a similar fashion to the angle-resolved tangential velocity as shown in Figs. 3-20 to 3-22. Of the turbulence models tested, DES was found to have the upper hand in predicting the angle-resolved radial velocity. However, predictions of the Rk-ε and k-ε were also in close agreement with the experimental measurements. Predictions by RNG, LES and RSM are not outstanding, especially just before and within the vortex core as shown in Fig. 3-22 (at 49° and 58°).

Figs. 3-23 to 3-25 show the prediction of angle-resolved axial velocities. All models seem able to reproduce correctly the detailed features of the angle-averaged axial velocities near to the impeller (see Fig. 3-23). There is not much difference between the angle-resolved axial velocities predicted using the k-ε and Rk-ε model. Predictions of these models are in reasonably good agreement with the experimental data, although on occasion there is a minor discrepancy in their predictions of the axial velocities near the impeller centreline (z = 0) (see Fig. 3-24 at 31° and Fig. 3-25 at 49°). Predictions of the RSM and RNG models are also quite good near the impeller, but give a poor prediction away from impeller, as shown in Fig. 3-24 at 40° and 49° and Fig. 3-25 at 58° where both models fail to predict the correct trend of the axial velocity. Both the RSM and RNG models are also struggling to predict the angle-resolved tangential and radial velocities in these positions, which may contribute to the poor predictions of the axial velocity. The LES also suffer similar drawbacks to the RSM model in this work, because the flow around the boundary layer is not resolved properly and that affects the flow field development around the impeller discharge region. The DES prediction of the angle-resolved axial velocity is also not uniformly good, e.g. see Fig. 3-24 at 40° and 49°, but overall the DES model is the most consistent model for predicting the angle-resolved axial velocity.

The angle-resolved values of the random turbulent kinetic energy can be obtained from:

$$k_{ran}(\theta) = \frac{1}{2}\left(\left\langle u_i^2 \right\rangle_\theta - \left\langle u_i \right\rangle_\theta^2\right) \tag{3.30}$$

where $\langle\ \rangle_\theta$ denotes the average value at angular position θ. It is well known that predictions of the k-ε model, and its variants, for the turbulence kinetic energy at positions far from impeller are in much better agreement with experimental measurements, as the turbulence becomes more isotropic. However, they are consistently reported to under-predict the turbulence kinetic energy close to the impeller, especially in the discharge region. CFD predictions of $k_{ran}(\theta)$ are shown in Figs. 3-26 to 3-28. Predictions of $k_{ran}(\theta)$ by the k-ε model in this study are also consistent with the previous findings in section 3.5.1; the predicted $k_{ran}(\theta)$ values at 2r/D = 1.52 are closer to Derksen *et al.*'s data than those at 2r/D = 1.1. In contrast with the angle-resolved tangential velocity, the prediction of $k_{ran}(\theta)$ is not affected by the position of vortex core. The position from the impeller seems to be more important factor for $k_{ran}(\theta)$ predictions in stirred tanks, showing that the wake behind the blade induces a highly anisotropic flow and at points far away from impeller the flow tends to be more isotropic. Both Rk-ε and k-ε model gives a better prediction of $k_{ran}(\theta)$ compared to RSM and RNG, although the RSM prediction improves at positions away from the impeller ($2r/D$ = 1.52), it is still not any better than the k-ε or Rk-ε models. DES has much success in predicting the $k_{ran}(\theta)$, as it is consistently shown to be superior compared to RANS models in this study (see Figs. 3-26 to 3-28). The LES model still managed to predict the $k_{ran}(\theta)$ better than any of the RANS model, despite the problem with the eddies around the boundary layer not being properly resolved. As expected, the effect of the unresolved boundary layers on the LES prediction is only prominent close to the impeller blades.

Predictions of the angle-resolved ε were not analysed because there were no data available for comparison. Estimation using eq.(3.28), i.e. from k_{ran} is meaningless since the prediction pattern will follow the prediction of the angle-resolved turbulent kinetic energy.

3.5.4 Spectral analysis

The power spectrum of the instantaneous tangential velocity component was carried out to investigate if the turbulence was resolved some way into the inertial sub-range as is required by DES and LES. The power spectrum curve was produced by doing a Fast Fourier Transform (FFT) on the time-series data recorded from a point close to impeller tip. Fig. 3-29 depicts the power spectral density obtained at several locations in the tank, for the DES of the flow generated by a Rushton turbine. The energy spectrum of the axial velocity in the impeller discharge region, in Fig. 3-29, exhibits the (−5/3) slope typical of the inertial sub-range of turbulence in the range $f/N \approx$ 1-20, but then some part of the small scale turbulence (f/N > 20) is not fully resolved as expected. A finer grid would help to resolve the whole spectrum away from impeller, but then this is not affordable to run using a personal computer at high Reynolds number at the moment. The sharp peaks in the spectrum at f =18.52 Hz shown in Fig. 3-29(A) are associated with the passage of the blades at every 1/6th of an impeller revolution. The FFT result proves that the DES model can resolve the turbulence in stirred tanks some way into the inertial subrange.

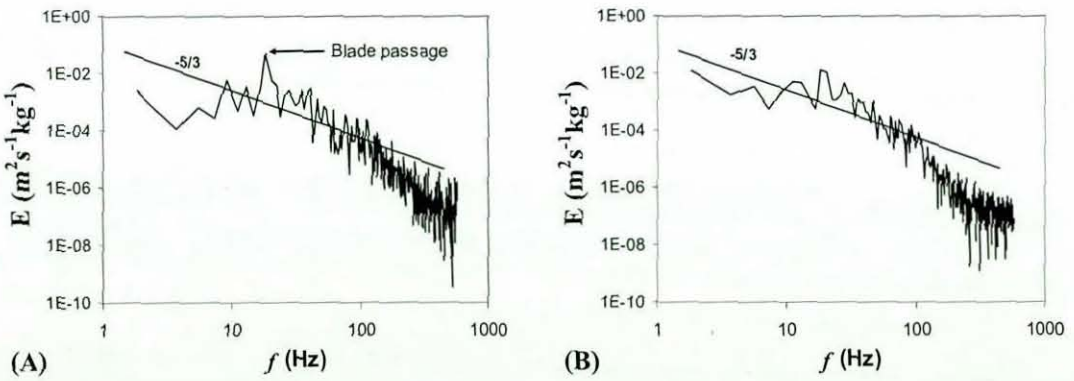

Figure 3-29: Power spectrum from the DES at $2z/W$ = -1.57 using the instantaneous tangential velocity for N = 3.14 rev/s, A) $2r/D$ = 1.1, B) $2r/D$ = 1.52

3.6 Prediction of the Power Number

The power number in a stirred tank can be estimated either by integrating the dissipation rate over the tank volume, or from a calculation of the moments acting on the shaft and impeller or baffles and tank wall. The calculated torque, Γ, is then related to the power input by;

$$P = 2\pi N\Gamma \tag{3.31}$$

Bujalski *et al.* (1987) showed experimentally that the power number in a stirred tank depended on the blade thickness, t, impeller diameter and tank diameter. Rutherford *et al.* (1996) also carried out an investigation of the influence of the blade thickness and the impeller diameter on the power number. Correlations obtained by these workers were presented in section 2.7.

Rutherford *et al.* (1996) carried out experimental measurements on the power number of Rushton turbines of different impeller thickness ($0.0082 < t/D < 0.034$) in a tank of $H = T = 0.294$ m. The power number at Re = 29 000 was 4.99, obtained from interpolation of Rutherford *et al.* (1996) data, for an impeller thickness of $t/D = 0.0204$ (very close to Derksen *et al.*'s geometry, $t/D = 0.0208$). Earlier, Yianneskis *et al.* (1987) reported $N_{p0} = 4.96$ for an exactly similar geometry to that used by Rutherford *et al.* (1996). Rutherford's and Bujalski's correlations give 5.25 and 4.94, respectively for the geometry evaluated in this work—the same geometry as used by Derksen *et al.* (1999).

The CFD predictions of the power number of a Rushton turbine are presented in Table 3-1. As expected the calculation using the moment method eq.(3.31) gives the better result compared to the ε integration methods, which lead to a large under-prediction (< 20%) of the experimental value. The reason for the under-prediction in the ε integration method is attributed to the under-prediction of the local ε value by the RANS model; although angle-averaged ε values were predicted well by k-ε near the impeller, they may be under-predicted in the other parts of the tank.

The power number estimated by the moment method gives much a closer value to published measurements (Rutherford *et al.* 1996; Yianneskis *et al.*, 1987), with an average error of less than 10%. The estimated power number from either shaft and impeller or baffle and tank wall should be similar, provided that angular momentum conservation is satisfied. Such evidence can be observed for the k-ε, Rk-ε, and RNG models, where isotropic turbulence is assumed and a steady-state solver is employed, but it is not quite the case for RSM and DES (see Table 3-1) which uses the non-isotropic turbulence assumption. In this case, it might be expected that calculation of the torque from the shaft and blades might be more reliable.

Table 3-1: Prediction of power number of a Rushton turbine

	Moment acting on impeller & shaft	Moment acting on wall & baffle	ε integration
k-ε	4.72	4.73	3.99
Rk-ε	4.76	4.74	3.85
RNG	4.96	4.96	3.05
RSM	4.81	5.04	3.13
DES	5.00	5.56	
LES	5.42	5.32	
Bujalski *et al.* (1987)*	4.94		
Rutherford *et al.* (1996)*	5.25		
Rutherford *et al.* (1996)	4.99		
Yianneskis *et al.* (1987)	4.87		

*Calculated from eq.(2.3) and eq.(2.4) described in chapter 2 using Derksen *et al.*'s (1999) dimensions

All the RANS models gave an almost similar value of power number either by calculating the moment on the wall and baffles or impeller and shaft; overall, calculations from the impeller and shaft were in better agreement with the experiments. Nevertheless, there is not a big difference among the predicted power numbers by any model tested in this study, suggesting that the choice of the turbulence model is not something crucial for power number estimation from the moment based methods.

3.7 Summary

Amongst the RANS models tested in this study, it can be concluded that the Rk-ε and k-ε prediction are the best for predicting either the angle-averaged or the angle-resolved turbulence kinetic energy induced by a Rushton turbine. RNG and RSM results are not an improvement, despite their need for greater computational effort and their difficulties with convergence. It is also important to note that the vortex core has a great influence on the prediction of the radial and tangential velocities, as elucidated in this work. This feature might be missed by previous researchers who have found that RANS turbulence models both under- or over-predicted the tangential velocity in a stirred tank. In fact both the radial and tangential velocities are predicted well by any RANS based turbulence model, except in the immediate vicinity of the trailing vortex core. In the case of a Rushton turbine, where the vortex core moves radially outward, the time-averaged tangential velocity can be well predicted by a RANS model.

Radial and axial positions of the lower and upper trailing vortex cores for a Rushton turbine have been successfully elucidated using RSM and DES models. Both trailing vortices were also predicted moving in the upward axial direction, in good agreement with measurements from the literature. The accuracy of power number predictions is not strongly affected by the choice of turbulence models. Instead, they were reasonably well predicted by any of the RANS or DES models used in this work, so long as the moment method was used.

Prediction of the turbulent kinetic energy very close to the impeller tip is also still an issue in a stirred tank; it is under-predicted by all of the RANS models. DES can predict the turbulent kinetic energy in the impeller discharge region much better than RANS, provided a sufficiently fine grid is applied. This study has uncovered a great potential for DES in predicting correctly the turbulent flows in a stirred tank. However, further attention to the modelling grid and perhaps some improvement to the DES model might be necessary, especially the turbulent viscosity model which is suspected of causing under-predictions of turbulent dissipation rates in the present work. This suggests that there is still room for improvement on the current DES model in order to get a better prediction of turbulent flows especially when a standard wall function is applied. The DES is also shown to work well for a coarser grid (y^+ ~ 20), where the LES fails to perform as well. The ability of DES to tolerate a coarser grid means a significant reduction in the computational effort for turbulent flow modelling in stirred tanks compared to a fully resolved LES solution.

DES and LES are of course better models for predicting turbulent flows in stirred tanks, but they are not yet affordable to solve on a personal computer in multiphase flow, especially when coupled with population balance modelling. Meanwhile, the RANS model, especially the Rk-ε model, is capable of yielding good predictions of the time-averaged turbulent kinetic energy and the mean velocities. In order for the developed two-phase model to be practical, a trade off must be made between prediction accuracy and computational expenses. Therefore, the Rk-ε model is employed for the gas-liquid stirred tank simulation in chapters 5 and 6 due to its relatively good prediction of the turbulent kinetic energy and dissipation rate, which is important in the modelling of bubble breakage and coalescence.

4 POPULATION BALANCE MODELLING

4.1 Overview

This chapter describes the population balance modelling framework used in the thesis. The population balance equations (PBE) and their common solution techniques are outlined. A derivation of the proposed solution for the PBE by means of the quadrature method of moments (QMOM) technique, by directly solving the set of differential algebraic equations (DAE) is presented and validated for simplified breakage, aggregation, nucleation, and growth problems. Results from the DAE-QMOM method are compared to (i) an analytical solution and (ii) the well-established method for solving QMOM via the product difference (PD) algorithm.

4.2 Introduction

The population balance framework has been accepted for some time as the most fundamental approach for modelling particulate, droplet or bubble dynamics in multiphase systems. A population balance is a powerful tool in evaluating the design of particulate related equipment such as crystallisers (e.g. Randolph and Larson, 1971), particularly when coupled with CFD software (e.g. Woo *et al.*, 2006; Gerstlauer *et al.*, 2002; Jaworski and Nienow, 2003; Wei *et al.*, 2001). Many solution techniques have been developed to solve the population balance equations, ranging from the simple standard method of moments (MOM), to the more advanced quadrature method of moments (QMOM) as direct numerical simulation approaches.

The standard method of moments is one of the most common methods of solving population balance equations. In the MOM, the PBE is transformed into a set of ordinary differential equations (ODEs) by multiplying the population balance equation by L^j in a length based PBE and integrating it, giving equations in terms of the moments (Randolph & Larson, 1971). The MOM is known as an efficient method to solve the population balance equation, but suffers from a closure problem for cases involving size-dependent growth, coalescence or aggregation processes. For that reason, the MOM is not directly applicable for

gas-liquid system, where bubble breakage and coalescence are dominating mechanisms.

The method of characteristics (MOCh) is another promising technique of solving the population balance equation as demonstrated by Lee *et al.* (2002). The MOCh for a first-order partial differential equation (PDE) determines the lines, called characteristic lines, along which the PDE reduce to set of ODEs. Once the ODEs are found, they can be solved easily and transformed into a solution for the original PDE. The MOCh has the advantage of solving the PDE directly for the particle size distribution with any required level of resolution along with the moments, however this method does not solve the closure problem. Therefore, the MOCh cannot be directly applied to model a system involving breakage and coalescence, such as in a gas-liquid dispersion.

Other classic solution techniques, such as the method of classes (MOC), are capable of solving the population balance equation for growth, nucleation, breakage, coalescence and aggregation processes. Although the term of 'size class' or 'sectional' have been used earlier by other authors e.g. Gillette (1972), Sutugin and Fuchs (1970), Tolfo (1977) and Gelbard *et al.* (1980), it is not until a detailed derivation of the MOC for particle growth, breakage and aggregation was introduced by Marchal *et al.* (1988) that the method becomes readily available for implementation. MOC has been applied to many problems involving the breakage and coalescence processes for gas-liquid dispersion (*e.g.* Venneker *et el.*, 2002; Chen *et al.*, 2004; Dhanasekharan *et al.*, 2005; Yeoh and Tu, 2005; Laakkonen *et al.*, 2007a). This method requires the whole particle size distribution (PSD) to be resolved into discrete size classes in order to get an accurate solution. The number of discretised equations increases with the number of size classes employed, and hence the solution for MOC can be numerically expensive to solve (Costa *et al.*, 2007), especially for multiple coordinate systems *e.g.* when coupled with three-dimensional CFD simulations.

McGraw (1997) proposed an attractive method for solving the population balance, namely the quadrature method of moments (QMOM), which utilises quadrature theory to avoid the closure problem with standard MOM simulations. The QMOM by McGraw (1997) is based on the product difference algorithm

(PD) of Gordon (1968). Application of QMOM has been extended into aggregation, coagulation and breakage systems by Wright *et al.* (2001), Rosner and Pyykonen (2002), Fan *et al.* (2004) and Marchisio *et al.* (2003). However, the PD algorithm is not always the best approach for computing the quadrature points from the moments of the particle size distribution (*e.g.* Lambin and Gaspard, 1982) because for a large number of moments, the computation is sensitive to small errors (*e.g.* Gautschi, 1994). Therefore, the applicability of QMOM is limited to no more than six quadrature points (Gordon, 1968) and even fewer for more complex cases such as diffusion-controlled growth with secondary nucleation.

Later, McGraw and Wright (2003) proposed a new method namely the Jacobian matrix transformation (JMT) method which avoids the use of the PD algorithm. This method is also based on the projection of the solution into the power moments, getting a set of equations for the evolution of the quadrature rule. The JMT method, however, still suffers from the problem of ill-conditioned, requiring the number of moments to be small (Dorao and Jakobsen 2006). The occurrence of singularities in the QMOM with PD or JMT is the consequence of using the power moments, thus making the calculation of population balance unfeasible for a higher number of moments and hence a higher number of quadrature points. Fan *et al.* (2004) proposed the direct quadrature method of moment (DQMOM) to avoid having to resort to the PD algorithm. The DQMOM defines a set of transport equations for the evolution of the quadrature rule in a similar manner to the JMT. The DQMOM can still be ill-conditioned for a higher number of moments because of the intrinsic problem of finding the roots of high order polynomials (Press *et al.*, 1992).

Recently, Alopaeus *et al.* (2006) proposed another solution, namely the fixed quadrature method of moment (FQMOM). This method exploits the zeros of orthogonal polynomials to find the quadrature points. Unlike the PD-QMOM which is restricted to an even number of moments (twice the number of the quadrature points), the FQMOM can be applied to any number of moments. The disadvantage of the FQMOM is that an optimized arbitrary constant must be established before it can be applied accurately for a specific problem. Finding

that optimised constant might be easy for simple cases where analytical solution is available, but can be difficult for more complex systems.

This work focuses on the simulation of gas-liquid dispersion in stirred tanks, where the dominant processes involve bubble breakage and coalescence. It is necessary to couple the computational fluid dynamics and population balance model for an accurate prediction of the performance of an aerated stirred tanks. Most of the previous studies involving gas-liquid dispersion employed the method of classes for prediction of bubble dynamics (e.g. Laakkonen *et al.*, 2007*a*; Chen *et al.*, 2004; Montante *et al.*, 2008). The QMOM is a more efficient method than the MOC because it requires less computational effort and is also capable of providing an accurate prediction of the moments, with a relatively small number of quadrature points. In contrast, the MOC requires a large number of size classes for an accurate prediction, thus resulting in a significant increase in computational effort. For that reason, the QMOM has been chosen to solve the population balance equations throughout this work. A detailed description of the QMOM for a gas-liquid system is presented in chapter 5, where the method is coupled to an Eulerian-Eulerian two-phase CFD model of flow in stirred tank.

Most of the currently available QMOM solutions are restricted to using a small number of moments. Although a small number of moments is enough to describe the particulate dynamics in simple cases, a larger number of moments might be required in other cases, especially when an inversion technique is applied to discover the particle size distribution. Diemer and Ehrman (2005) for example needed at least ten moments of the distribution to obtain acceptable reconstructions of the complete particle size distribution. Therefore, a better solution technique for the population balance that is capable of solving for higher order moments is needed. This chapter describes the possibility of solving the PBE via QMOM without resorting to the PD algorithm. A new solution technique for the QMOM is proposed, based on the simultaneous solution of the moment equations and quadrature approximation as a differential-algebraic equation (DAE) system. The result from the DAE-QMOM method is compared with the solution from the PD algorithm, as well as with analytical solutions.

4.3 Population Balance Equation

The dynamic population balance equation for a closed homogeneous system can be written with diameter as the internal coordinate as (Rod and Misek, 1982; Marchisio *et al.*, 2003):

$$\frac{\partial n(L)}{\partial t} = \underbrace{\int_L^\infty b(L,\lambda)a(\lambda)n(\lambda)\,\mathrm{d}\lambda}_{\text{birth due to breakage}} + \underbrace{\frac{L^2}{2}\int_0^L \frac{\beta\left(\left(L^3-\lambda^3\right)^{1/3},\lambda\right)n\left(\left(L^3+\lambda^3\right)^{1/3}\right)n(\lambda)}{\left(L^3-\lambda^3\right)^{2/3}}\,\mathrm{d}\lambda}_{\text{birth due to coalescence or aggregation}} \tag{4.1}$$

$$- \underbrace{a(L)n(L)}_{\text{death due to breakage}} - \underbrace{n(L)\int_0^\infty \beta(L,\lambda)n(\lambda)\,\mathrm{d}\lambda}_{\text{death due to coalescence or aggregation}} + \underbrace{\frac{\partial(G(L)n(L))}{\partial L}}_{\text{growth}} + \underbrace{\delta(L_0,L)B}_{\text{nucleation}}$$

where β, a, G, B, b, L_0 and δ are the aggregation kernel, breakage kernel, growth rate, nucleation rate, the daughter particle size distribution, size of the nuclei and the dirac delta function, respectively, whereas both L and λ are the particle characteristic length. The PBE in equation (4.1) can be further simplified using a moment transformation, where the k^{th} moments of the distribution, μ_k, is given by:

$$\mu_k = \int_0^\infty n(L)L^k\,\mathrm{d}L \tag{4.2}$$

Among the moments, only the lower order (i.e. zeroth to third) are important because they are related to the physical description of the particle size distribution i.e. μ_0 related to the total number of particles, μ_1 related to particle diameter, μ_2 related to particle surface area and μ_3 is related to particle volume. After the moment transformation the PBE of equation (4.1) is represented by the set of ODEs in terms of the moments (Hulburt and Katz, 1964; Randolph & Larson, 1988);

$$\frac{\mathrm{d}\mu_k}{\mathrm{d}t} = \underbrace{\int_0^\infty L^k\int_0^\infty a(\lambda)b(L,\lambda)n(\lambda)\,\mathrm{d}\lambda\,\mathrm{d}L}_{\text{birth due to breakage}} + \underbrace{\frac{1}{2}\int_0^\infty n(\lambda)\int_0^\infty \beta(L,\lambda)\left(L^3+\lambda^3\right)^{k/3}n(L)\,\mathrm{d}L\,\mathrm{d}\lambda}_{\text{birth due to coalescence or aggregation}}$$

$$- \underbrace{\int_0^\infty L^k a(L)n(L)\,\mathrm{d}L}_{\text{death due to breakage}} - \underbrace{\int_0^\infty L^k n(L)\int_0^\infty \beta(L,\lambda)n(\lambda)\,\mathrm{d}\lambda\,\mathrm{d}L}_{\text{death due to coalescence or aggregation}} \tag{4.3}$$

$$+ \underbrace{\int_0^\infty kL^{k-1}G(L)n(L)\,\mathrm{d}L}_{\text{growth}} + \underbrace{\delta(0,k)B}_{\text{nucleation}}$$

The moment equations represented by equation (4.3) are solvable for growth (except for size dependent growth problem) and nucleation problems using the standard method of moment technique, however it is not possible to solve the

breakage and coalescence terms due to the closure problem since the integrations cannot be written in term of the moments. Therefore, equation (4.3) needs to be transformed again into a quadrature method of moments formulation to eliminate the closure problem. The essence of the quadrature closure is to consider the number density $n(L)$ as a general weight function and to approximate the integrals that appear during the transformation of the PBE to moment equations in terms of a set of abscissas and weights. The quadrature method of moment employs a quadrature approximation (McGraw, 1997):

$$\mu_k = \int_0^{+\infty} n(L) L^k \, \mathrm{d}L \approx \sum_{i=1}^{N} w_i L_i^k \quad \text{for } k = 0, 1, 2, \ldots \tag{4.4}$$

where the w_i are the weights, L_i are the abscissas and N is the number of quadrature points. This quadrature approximation is exact if the function in eq.(4.4) is a polynomial up to the order of $2N$-1. After applying the quadrature rule the moment transformed PBE can be written as (Alopaeus *et al.*, 2006):

$$\begin{aligned} \frac{\mathrm{d}\mu_k}{\mathrm{d}t} = & \underbrace{\sum_{i=1}^{N} w_i a(L_i) b(k, L_i)}_{\text{birth due to breakage}} + \underbrace{\frac{1}{2} \sum_{i=1}^{N} w_i \sum_{j=1}^{N} w_j \left(L_i^3 + L_j^3\right)^{k/3} \beta(L_i, L_j)}_{\text{birth due to coalescence or aggregation}} - \underbrace{\sum_{i=1}^{N} w_i a(L_i) L_i^k}_{\text{death due to breakage}} \\ & \underbrace{- \sum_{i=1}^{N} w_i L_i^k \sum_{j=1}^{N} w_j \beta(L_i, L_j)}_{\text{death due to coalescence or aggregation}} + \underbrace{k \sum_{i=1}^{N} w_i L_i^{k-1} G(L_i)}_{\text{growth}} + \underbrace{\delta(0,k) B}_{\text{nucleation}} \end{aligned} \tag{4.5}$$

Now the closure problem has been eliminated, and hence the PBE in equation (4.5) is solvable by means of the quadrature method of moment by following the evolution of w_i and L_i, as well as μ_k. The moments are non-linearly related to the weights and abscissas by eqs.(4.4).

4.4 Numerical Techniques for QMOM

QMOM calculations require integration of the ODEs eq.(4.5) for k = 0 ... $2N$-1, alongside the non-linear algebraic eqs.(4.4). These equations may be numerically solved simultaneously as a set of DAEs. However, most of the QMOM solutions described in the literature were performed using the product difference algorithm of Gordon (1968) to solve eqs.(4.4). Solutions for the population balance equation via the PD-QMOM are well established for growth, nucleation, breakage and aggregation/coalescence. A variety of alternative methods are available to solve the QMOM, including FQMOM, JMT and

DQMOM (see section 4.2), however those techniques are not widely used. Therefore, the solution from the DAE-QMOM is only compared with the most common technique for QMOM, based on the PD algorithm. The first comparison is for a simplified case of diffusion-controlled growth only.

4.4.1 DAE-QMOM

The DAE method is an attractive alternative method for solving QMOM. The ODE equations (4.5) are generated from the moments equation while the algebraic equations (4.4) are obtained from the quadrature rule. The DAE-QMOM method is illustrated in this section using a diffusion-controlled growth model assuming the nucleation, breakage and coalescence or aggregation rates are zero. In diffusion-controlled growth model the growth rate is given by:

$$G(L)=\frac{G_0}{L} \tag{4.6}$$

where G_0 is a constant. The population balance equation written in the form of the quadrature approximation is given by:

$$\frac{d\mu_k}{dt}=k\sum_{i=1}^{N}G(L_i(t))L_i(t)^{k-1}w_i(t) \tag{4.7}$$

For the case of N quadrature points, the DAE-QMOM method needs $2N$ moments ODEs and another $2N$ algebraic equations before it can be solved. The first $2N$ moments are generated using the equation (4.7),

$$\begin{aligned}
&\frac{d\mu_0}{dt}=0\\
&\frac{d\mu_1}{dt}=\frac{G_0}{L_1}w_1+\frac{G_0}{L_2}w_2+\ldots+\frac{G_0}{L_N}w_N\\
&\vdots\\
&\frac{d\mu_{2N-1}}{dt}=(2N-1)\left(\frac{G_0}{L_1}L_1^{2N-2}w_1+\frac{G_0}{L_2}L_2^{2N-2}w_2+\ldots+\frac{G_0}{L_N}L_N^{2N-2}w_N\right)
\end{aligned} \tag{4.8}$$

The other $2N$ algebraic equations are generated using the quadrature approximation given by equation (4.4).

$$\begin{aligned}
&0=w_1+w_2+\ldots+w_N-\mu_0\\
&0=w_1L_1+w_2L_2+\ldots+w_NL_N-\mu_1\\
&\vdots\\
&0=w_1L_1^{2N-1}+w_2L_2^{2N-1}+\ldots+w_NL_N^{2N-1}-\mu_{2N-1}
\end{aligned} \tag{4.9}$$

Finally, the problem is represented by $4N$ equations containing $4N$ unknown made-up from $2N$ moments, N weights and N abscissas. Equations (4.8) to (4.9) together represent a semi-explicit DAE system which can be solved using standard DAE solution techniques and software. In semi-explicit form a generic DAE can be written as:

$$\dot{\vec{x}}(t) = f(\vec{x}, \vec{z}, t) \tag{4.10}$$

$$0 = g(\vec{x}, \vec{z}, t) \tag{4.11}$$

where the $\vec{x}(t)$ contains the differential variables and $\vec{z}(t)$ contains the algebraic variables. The ODE (equation (4-10)) for $\vec{x}(t)$ depends on additional algebraic variables $\vec{z}(t)$ and the solution is forced to satisfy the algebraic constraints (equation (4.11)) (Ascher and Petzold, 1998). In the case of QMOM $\vec{x}$ = [μ_0, μ_1, ..., μ_{2N-1}] and $\vec{z}$ = [w_1, w_1, ..., w_N, L_1, L_2, ..., L_N]. The semi-explicit system eqs.(4.12) and (4.13) can be written as:

$$\vec{M}(t, \vec{y})y' = \vec{F}(t, \vec{y}) \tag{4.12}$$

where M is a mass matrix and $y = \begin{pmatrix} x \\ z \end{pmatrix}$, $F = \begin{pmatrix} f \\ g \end{pmatrix}$. The mass matrix for the DAE in equations (4.10) and (4.11) is given by:

$$\vec{M} = \begin{pmatrix} I & 0 \\ 0 & 0 \end{pmatrix} \tag{4.13}$$

where I is the identity matrix of dimension n_x x n_x where n_x is the number of differential states. MATLAB is an efficient software tool for numerical computation and can be used readily for the solution of index 1 DAE problems of the type shown in eq.(4.12). The differential index of DAE is defined as the number of differentiations needed to transform the DAE into an explicit ODE. MATLAB can solve the DAE of index 1 via the *ode15s* or *ode23t* solvers (Shampine and Reichelt, 1997). In this work, the *ode15s* solver is employed to solve the DAE-QMOM. The *ode15s* is based on variant of the backward differentiation formula (BDF) called numerical differentiation formula (NDF) initially studied by Klopfenstein (1971) and Reiher (1978). According to Shampine and Reichelt (1997), many tactics adopted for *ode15s* resemble those found in the well known codes such as LSODE (Hindmarsh, 1980) and VODE (Brown *et al.*, 1989). It was developed to integrate stiff ODEs of the form of

eq.(4.12). The simplified Newton method is also implemented in *ode15s* to perform a correction to the current iteration (to satisfy the algebraic constraints), thus solving the DAE system. The requirement for the solution of the DAE system is the existence of a feasible initial condition for y_0, that is, if there is a vector such that $M(t_0, y_0)y' = F(t_0, y_0)$. The *ode15s* is implemented to detect automatically the DAE system and then to perform an automatic computation of consistent initial conditions for a robust computation. The DAE system might lead to instability on the solution, especially when a more complicated function is considered e.g. involving the breakage and coalescence kernels. To overcome such a problem it is necessary to provide the analytical Jacobian matrix. The Jacobian of the DAE system is defined as follows:

$$J = \begin{bmatrix} \frac{\partial f_1}{\partial x_1} & \frac{\partial f_1}{\partial x_2} & \frac{\partial f_1}{\partial x_3} & \cdots & \frac{\partial f_1}{\partial x_{4N}} \\ \frac{\partial f_2}{\partial x_1} & \frac{\partial f_2}{\partial x_2} & \frac{\partial f_2}{\partial x_3} & \cdots & \frac{\partial f_2}{\partial x_{4N}} \\ \vdots & \vdots & \vdots & \vdots\vdots & \vdots \\ \frac{\partial f_{4N}}{\partial x_1} & \frac{\partial f_{4N}}{\partial x_2} & \frac{\partial f_{4N}}{\partial x_3} & \cdots & \frac{\partial f_{4N}}{\partial x_{4N}} \end{bmatrix} \tag{4.14}$$

where f_1 to f_{2N} are the RHS of the differential moment equations, f_{2N+1} to f_{4N} are the RHS of the algebraic equations, x_1 to x_{2N} represent the moments, x_{2N+1} to x_{3N} are the weights and x_{3N+1} to x_{4N} are the abscissas. The Jacobian matrix for a given equation system can be generated using the symbolic computation facilities in MATLAB. If for example, N = 2, for the diffusion-controlled growth only case, then the Jacobian matrix, J, becomes:

$$J = \left[\begin{array}{cccc|cccc} 0 & 0 & 0 & 0 & 0 & 0 & 0 & 0 \\ 0 & 0 & 0 & 0 & \frac{G_0}{L_1} & \frac{G_0}{L_2} & \frac{-G_0}{L_1^2}w_1 & \frac{-G_0}{L_2^2}w_2 \\ 0 & 0 & 0 & 0 & 2G_0 & 2G_0 & 0 & 0 \\ 0 & 0 & 0 & 0 & 3G_0L_1 & 3G_0L_2 & 3G_0w_1 & 3G_0w_1 \\ \hline -1 & 0 & 0 & 0 & 1 & 1 & 0 & 0 \\ 0 & -1 & 0 & 0 & L_1 & L_2 & w_1 & w_2 \\ 0 & 0 & -1 & 0 & L_1^2 & L_2^2 & 2w_1L_1 & 2w_2L_2 \\ 0 & 0 & 0 & -1 & L_1^3 & L_2^3 & 3w_1L_1^2 & 3w_2L_2^2 \end{array}\right] \tag{4.15}$$

The Jacobian matrix can be divided into three major blocks. The first block, $J(1, 1)$ to $J(2N, 2N)$, contains the derivatives of the right hand sides of the moment equations with respect to the moments. This particular block will remain unchanged unless the LHS includes the moments. The second block, $J(1, 2N+1)$ to $J(2N, 4N)$, contains the derivatives of the RHS of the differential equations, with respect to the weights and abscissas. Therefore this block always changes whenever the mechanism change. The third block $J(2N+1, 1)$ to $J(4N, 4N)$ is derived from the algebraic equations. This block remains unchanged unless the number of quadrature points is altered.

4.4.2 PD-QMOM

The solution of the QMOM via the PD algorithm was first introduced by McGraw (1997) and has been further developed for aggregation and breakage by Marchisio *et al.* (2003). The PD algorithm is employed to calculate the weights and the abscissas from the moments in QMOM. The first step is the construction of a matrix P with components P_{ij} starting from the moments. The components in the first column of matrix P are:

$$P_{i,1} = \delta_{i1}, \qquad i = 1,...;2N+1 \tag{4.16}$$

where δ_{i1} is the Kronecker delta. The components in the second column of P are:

$$P_{i,2} = (-1)^{i-1} \mu_{i-1}, \qquad i = 1,...,2N+1 \tag{4.17}$$

The remaining components can be computed from an iterative equation as follows:

$$P_{i,j} = P_{1,j-1} P_{i+1,j-2} - P_{1,j-2} P_{i+1,j-1}, \qquad j = 3,...,2N+1 \text{ and } i = 1,...,2N+2-j \tag{4.18}$$

For example when $N = 2$ the matrix P becomes:

$$P = \begin{bmatrix} 1 & \mu_0 & \mu_1 & \mu_2 - \mu_1^2 & \mu_3\mu_1 - \mu_2^2 \\ 0 & -\mu_1 & -\mu_2 & -\mu_3 + \mu_2\mu_1 & 0 \\ 0 & \mu_2 & \mu_3 & 0 & 0 \\ 0 & -\mu_3 & 0 & 0 & 0 \\ 0 & 0 & 0 & 0 & 0 \end{bmatrix} \tag{4.19}$$

The coefficients of the continued fraction (α_j) are generated by setting the first element equal to zero ($\alpha_1 = 0$) and computing the others according to the

following recursive relationship:

$$\alpha_i = \frac{P_{1,i+1}}{P_{1,i}P_{1,i-1}}, \quad i = 2,...,2N \tag{4.20}$$

A symmetric tridiagonal matrix is then obtained from sums and products of α_i:

$$a_i = \alpha_{2i} + \alpha_{2i-1}, \qquad i = 1,...,2N-1 \tag{4.21}$$

and

$$b_i = -\sqrt{\alpha_{2i+1}\alpha_{2i-1}}, \qquad i = 1,...,2N-2 \tag{4.22}$$

where a_i and b_i are the diagonal and subdiagonal of the Jacobi matrix. Once the tridiagonal matrix is determined the abscissas and weights can be found by calculating the eigenvalues and eigenvectors of the tridiagonal matrix. The eigenvalues represent the abscissas and the weights can be found from:

$$w_j = \mu_0 \upsilon_{j1}^2 \tag{4.23}$$

where υ_{j1} is the first component of the j^{th} eigenvector. It should be noted that the elements of the eigenvectors should be normalised such that the norm of each eigenvector is 1.0. The eigenvalues and eigenvectors can be calculated numerically using the *eig* function in MATLAB.

4.5 Validation of QMOM Algorithm

The performance of the DAE-QMOM, is compared with the well-established PD-QMOM method and with a number of analytical solutions. Six cases were tested, namely (i) diffusion-controlled growth (see section 4.4.1), (ii) constant growth and primary nucleation, (iii) power-law growth, (iv) breakage, (v) constant aggregation kernel and (vi) sum aggregation kernel. In each case, except for the power-law growth, the initial size distribution was:

$$n_0(L) = 3L^2 \frac{N_0}{v_0} e^{-L^3/v_0} \tag{4.24}$$

where N_0 = 1 m^{-3} and v_0 = 1 m^3 or 0.001 m^3. The particle size distribution in eq.(4-24) is chosen because it has an analytical solution available from literature. Unless otherwise stated, the relative tolerance is set at 10^{-12} and the absolute tolerance at 10^{-10} for all cases tested in this work for both DAE-QMOM and PD-QMOM. The relative tolerance represents the error applies to all components of the solution vector, whereas the absolute tolerance applies to

individual components of the solution vector. The eliminated error in each integration step $err(i)$ for any state variable $x(i)$ in the solution vectors satisfies $err(i) \leq$ max(RelTol*abs($x(i)$), AbsTol(i)). A similar ODE solver (*ode15s*) is employed for both DAE-QMOM and PD-QMOM. All solutions in this chapter were solved for three quadrature points (6 moments). The error of the predicted moment is calculated as follows:

$$\%\,\text{error} = \frac{\left(\mu_{\text{analytical}} - \mu_{\text{calculated}}\right)}{\mu_{\text{analytical}}} \times 100 \tag{4.25}$$

4.5.1 Growth and nucleation examples

Case 1: Diffusion-controlled growth

The moment equations for the diffusion-controlled growth have been described in a previous section 4.4.1 (equations (4.6) to (4.8)). The initial distribution is given by equation (4.24) with N_0 = 1 m^{-3}, v_0 = 1 m^3 and G_0 = 0.01 m^2/s. The zeroth moment is the number density of particles per unit volume and can be obtained by integrating the initial distribution in equation (4.24) from zero to infinity. For growth only case, μ_0 will remain constant. Exact solutions are available for zeroth and even moments only given by McGraw, (1997) as:

$$\mu_0 = N_0 = constant \tag{4.26}$$

$$\mu_2 = 2G_0\mu_0 t + \mu_2(0) \tag{4.27}$$

$$\mu_4 = 4G_0^2\mu_0 t^2 + 4G_0\mu_2(0)t + \mu_4(0) \tag{4.28}$$

An analytical size distribution at any time t can be obtained from (Alopaeus *et al.*, 2006):

$$n(L) = \frac{3N_0}{v_0} L\sqrt{L^2 - 2G_0 t}\,\exp\left(-\frac{\left(L^2 - 2G_0 t\right)^{3/2}}{v_0}\right) \tag{4.29}$$

which then can be integrated numerically using the function *quadl* in Matlab to obtain the analytical solution for the odd moments. An analytical integration is not possible for equation (4.29) due to the presence of a discontinuity when $L^2 - 2G_0 t < 0$. Fig. 4-1 shows the plot of equation (4.29) at t = 1 s. The equation (4-29) returns an imaginary value at $L < \sqrt{2G_0 t}$ which result in a discontinuity. A numerical integration via *quadl* function at very small tolerance (function tolerance 10^{-12}) was employed to calculate the odd moments. The lower limit of

the *quadl* integration was set at $L = \sqrt{2G_0 t}$, the point where the discontinuity started.

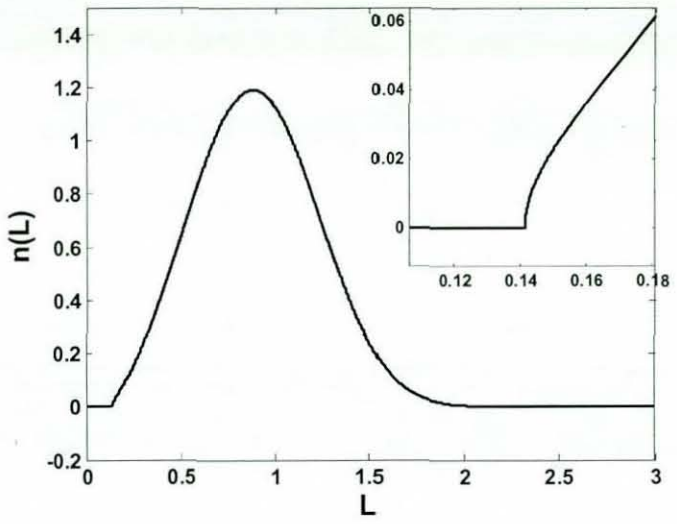

Figure 4-1: Discontinuity of equation (4.29) at t = 1 s, upper right is the enlarged view of the discontinuity

The moments for the diffusion-controlled growth were predicted remarkably well by both DAE and PD methods, with a small error (mostly less than 10^{-8}, see Fig. 4-2) for the zeroth and even moments where the exact analytical solution is available. There is no significant difference in the accuracy of the even moments predicted by the DAE-QMOM and PD-QMOM in this particular case except for a very small difference in the fourth moment. The error for the odd moments is significantly larger than for the even moments due to the fact that these are obtained from numerical integration of equation (4.29) and not from the exact solution. Evolutions of the first six moments are shown in Fig. 4-3. Each moment in Fig. 4-3 is normalised with their initial value ($\mu_{k,t}/\mu_{k,0}$). In this case where only growth is considered, the particles number density (zeroth moment) remain unchanged.

The DAE-QMOM and PD-QMOM were also tested to solve the diffusion-controlled growth at a looser tolerance for *ode15s* (absolute tolerance = relative tolerance = 10^{-6}) to further evaluate the robustness and accuracy of the proposed solution. Fig. 4-4 shows the relative error of the moment evolution from both DAE-QMOM and PD-QMOM. For the case of a looser tolerance, prediction of the moment evolution by DAE-QMOM and PD-QMOM did not

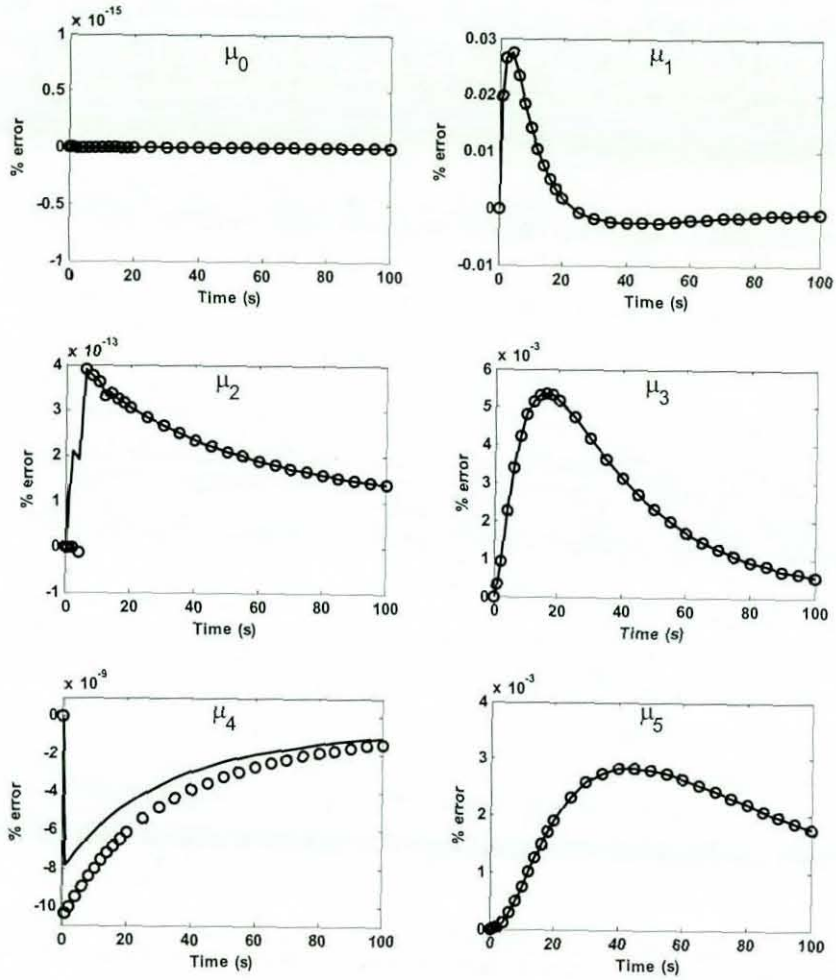

Figure 4-2: The error in the moments evolution for diffusion-controlled growth of DAE-QMOM (continuous line) and PD-QMOM (circles)

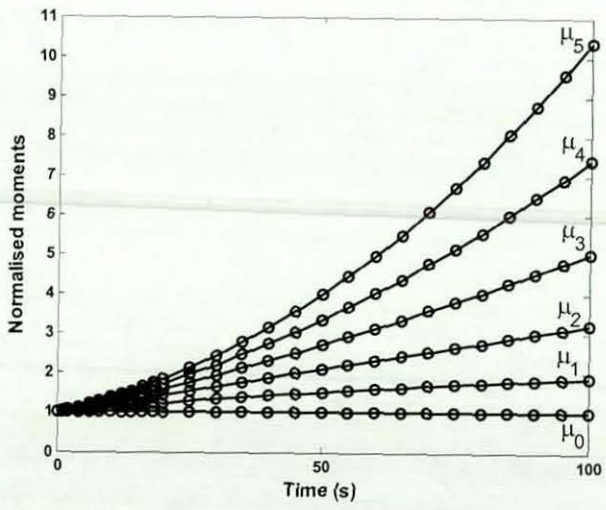

Figure 4-3: Moment evolution for diffusion-controlled growth from DAE-QMOM (circles), analytical solution (continuous line)

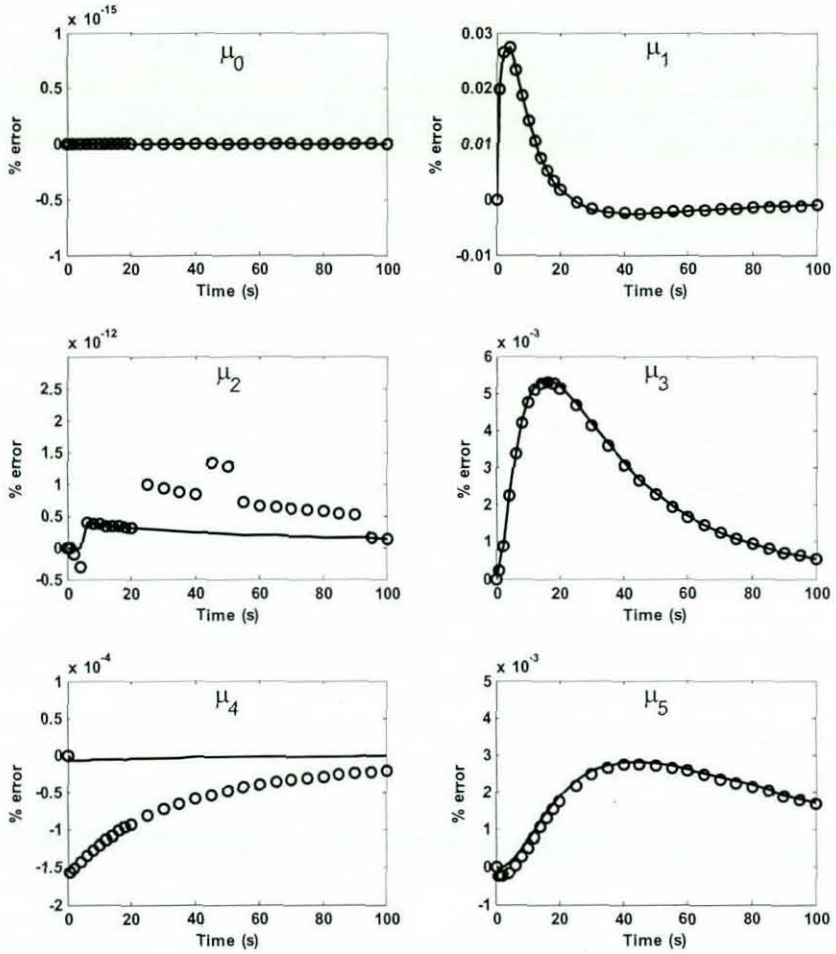

Figure 4-4: Error of moment evolution for diffusion-controlled growth from DAE-QMOM (continuous line) and PD-QMOM (circles) to the exact solution

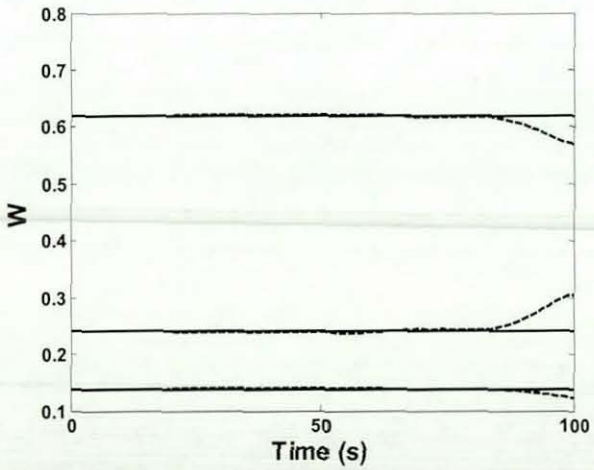

Figure 4-5: Evolution of weights at looser tolerance, DAE-QMOM (continuous line), PD-QMOM (dashed line)

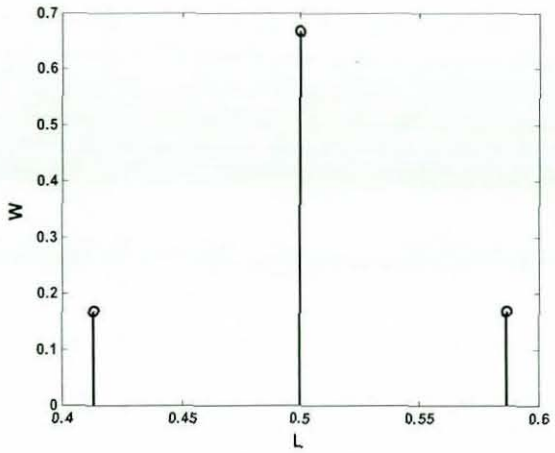

Figure 4-6: Weights for normal distribution function for three quadrature points ($\overline{L} = 0.5$ and $\sigma = 0.05$)

change much except for the fourth moment which was already showing some difference even for the tight tolerance. The error in the fourth moment shows that the accuracy of moments prediction in this case depends only on the tolerance setting because the magnitude of errors reflect the absolute tolerance applied. Fig. 4-5 shows the evolution of the weights from DAE-QMOM and PD-QMOM at the looser tolerance setting. For the case of growth only problem the weights should be constant because there is no change in the particle number density. The individual weights are conserved perfectly by DAE-QMOM at looser tolerance, however a significant error is observed in the case of the PD-QMOM method. There is no problem of conserving the weights at tight tolerance setting for both DAE-QMOM and PD-QMOM and therefore the results for weights evolution at tight tolerance are not shown. Even for the looser tolerance, the total weights are well conserved even if the individual weights are not. In some cases when the individual weights are not conserved, some of the weights actually become zero and thus they no longer contribute to the PD solution. In such cases, the PD algorithm has a singularity problem and is therefore no longer capable of solving the QMOM. The conservation of individual weights in QMOM is important to ensure the solution is robust and accurate. The weights are a crude approximation of the actual particle size distribution. In the case of normal distribution the abscissa of the middle weight is similar to the mean diameter and the other two weights have a similar value (see Fig. 4-6). The individual weights in the QMOM methods represent a unique solution and therefore should be

conserved perfectly in the growth only problem. This numerical evaluation has clearly demonstrated the robustness and accuracy of the DAE method compared to the PD algorithm in solving the population balance equations.

Case 2: Constant growth and primary nucleation

The next level of complication is to include nucleation, so that the number density of particle (μ_0) increases with time. The evolution of the zeroth moment for this case is given by:

$$\frac{d\mu_0}{dt} = B_0 \tag{4.30}$$

This particular case of constant growth rate, G, does not involve any closure problem and can be solved easily using the standard method of moments. The moments equation for this case for MOM is given as follows:

$$\begin{aligned} \frac{d\mu_0}{dt} &= B_0 \\ \frac{d\mu_k}{dt} &= k G \mu_{k-1} \quad k \geq 1 \end{aligned} \tag{4.31}$$

where in this case study B_0 = 0.1 $m^{-3}s^{-1}$. The initial distribution is again given by equation (4.24) with N_0 = 1 m^{-3}, v_0 = 1 m^3 and G = 0.01 m/s. The number of moments is not restricted for MOM and as many can be generated as are needed. A similar stiff ODE solver, *ode15s* from MATLAB was employed to solve the MOM for a proper comparison with the QMOM method. Furthermore, the analytical solution for this case can be derived easily and the first three moments are given as follows:

$$\begin{aligned} \mu_0(t) &= B_0 t + \mu_0(0) \\ \mu_1(t) &= GB_0 \frac{t^2}{2} + G\mu_0(0)t + \mu_1(0) \\ \mu_2(t) &= 2G^2 B_0 \frac{t^3}{3} + 2G^2 \mu_0(0)\frac{t^2}{2} + 2G\mu_1(0)t + \mu_2(0) \end{aligned} \tag{4.32}$$

The moments evolutions calculated using two different QMOM algorithms and the MOM are compared to the analytical solutions (equation (4.32)). Fig. 4-7 shows very small errors in the moments evolution calculated using two different QMOM algorithms and MOM. In this particular case the errors of the PD-QMOM and DAE-QMOM appear to be at similar magnitude. Prediction of the MOM was also found to be at similar accuracy to both QMOM solutions.

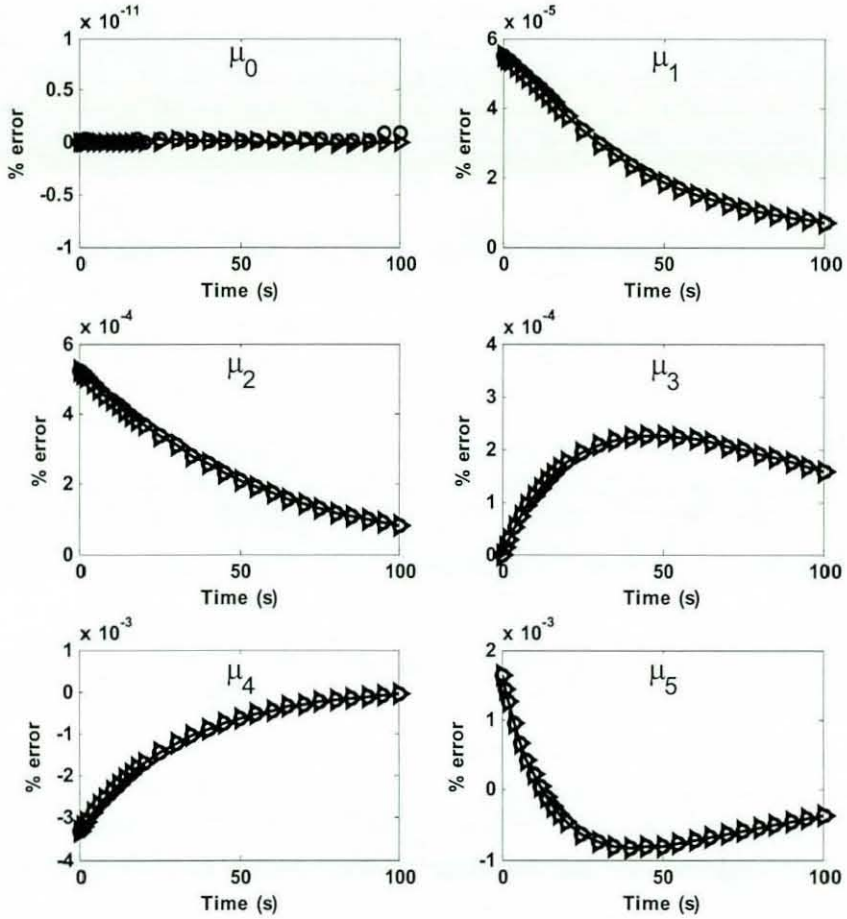

Figure 4-7: Comparison of error for the first six moments for primary nucleation and constant growth of DAE-QMOM (continuous line), PD-QMOM (circles) and MOM (triangles) compared with the analytical solution of eq.(4-32)

Case 3: Power-law growth

The power-law model is commonly applied for crystallization growth and mass transfer related problems. In the case evaluated in this work, a power-law growth model with the following relations without the nucleation term is considered.

$$G(L) = bL^p \tag{4.33}$$

where,

$$b = \frac{0.8^{1-p} - 0.3^{1-p}}{100(1-p)} \tag{4.34}$$

and p = 0.5 or -0.5. The case studied here is similar to those evaluated by Alopaeus *et al.* (2007) which was chosen due to availability of analytical solution from Alopaeus *et al.* (2007). However, the initial distribution is assumed to be a

normal distribution with mean size of $\overline{L} = 0.5$ m and a standard deviation $\sigma = 0.05$ m instead of eq.(4.24) in Alopaeus *et al.* (2007) work. An analytical size distribution at any time t for this particular case of power-law growth is given by:

$$n(L) = \frac{1}{\sqrt{2\pi}\sigma}\left(1 - \frac{(1-p)bt}{L^{1-p}}\right)^{p/(1-p)} \exp\left(-\frac{\left(\left(L^{1-p} - (1-p)bt\right)^{1/(1-p)} - \overline{L}\right)^2}{2\sigma^2}\right) \tag{4.35}$$

where $\overline{L}$ and σ are the initial mean diameter and standard deviation, respectively. A detailed derivation of the analytical solution for power-law growth is given in appendix A. Similar results were reported by Alopaeus *et al.* (2007) for eq.(4.24). The final analytical size distribution in equation (4.35) cannot be integrated analytically to obtain the exact moments due to a discontinuity in the function. However, equation (4.35) can be integrated numerically in MATLAB using the *quadl* solver to give an approximate value of the moments for comparison with the QMOM solution. The numerical integration employed a tight absolute tolerance of 10^{-12}. The relative tolerance used in the ODE integrations is set to 10^{-12} for both cases (p = 0.5 and p = -0.5), however it was necessary to reduce the absolute tolerance to 10^{-8} because the ODE integrator failed to solve the problem at a tighter tolerance.

The comparison of relative errors in the moment evolutions obtained using the DAE-QMOM and PD-QMOM methods for power law growth with p = 0.5 and p = -0.5 are presented in Figs. 4-8 and 4-9, respectively. In both cases the DAE-QMOM described the moment evolutions with a significantly lower relative error in most of the moments. For a negative value of p, the smaller particles grow faster than the bigger ones causing the particle size distribution to evolve as a shock wave (Alopaeus *et al.*, 2007), resulting in a major difficulty in conserving the individual weights (no nucleation in this case) generating the multiplicity problem in the solution from PD algorithm. Due to this singularity problem the correct solution cannot be found even for a tighter tolerance (see Fig. 4-10). As mentioned in the section for diffusion-controlled growth (section 4.5.1) the weights for a growth only problem should be perfectly conserved since there is no change in the total number of particles in the system.

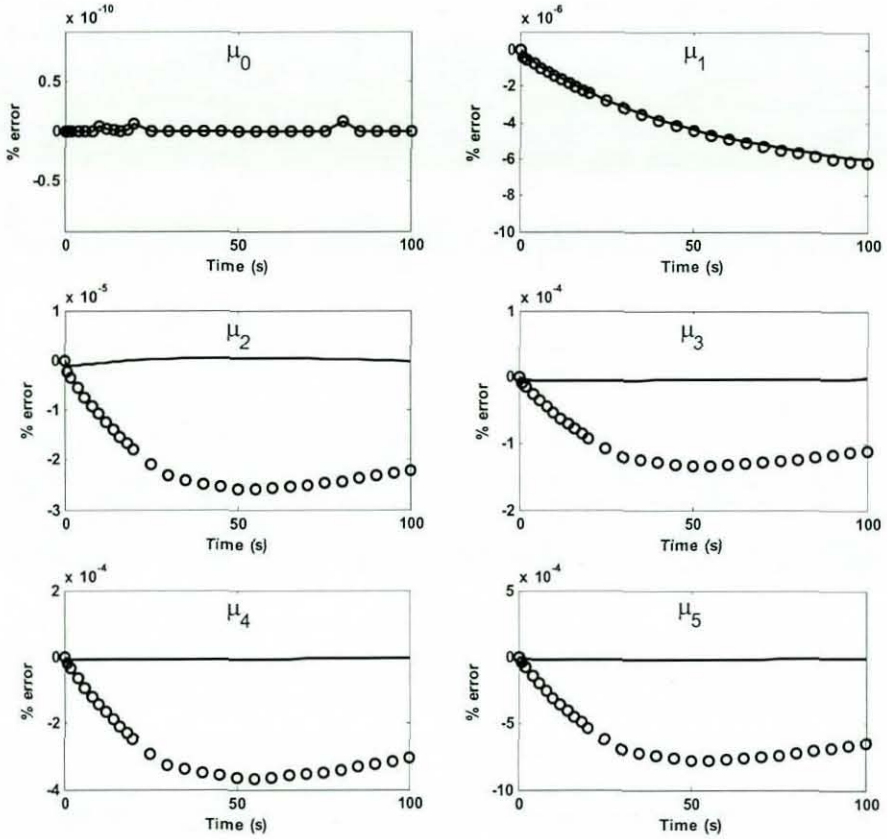

Figure 4-8: The relative errors of the first six moments for power law growth at p = 0.5 of DAE-QMOM (continuous line) and PD-QMOM (circle) to the analytical solution

The tests on using a loose (relative tolerance of 10^{-6} and absolute tolerance of 10^{-6}) and tight (relative tolerance of 10^{-12} and absolute tolerance of 10^{-8}) tolerance setting were carried out to assess the robustness of the new solution method. Figs. 4-10 and 4-11 show that the PD-QMOM fails to conserve the weights at tight tolerance and is even worse for the looser tolerance setting. In contrast, the DAE-QMOM conserves the weights at both looser and tight tolerance settings. For p = -0.5 shown in Fig. 4-10 the PD-QMOM solution becomes worse as time increases. The moments are computed as a product between the weights and abscissas, thus any problem in predicting the weights could translate into an error in the moment calculation. The moments may be predicted fairly well even if the weights are not predicted correctly because the PD-QMOM counteracts the change in the weights by altering the abscissas and forcing the moments to obey the quadrature rule. However, ill-condition may occur when one or more weights become zero because they no longer

contribute to the PD solution and when this happen the PD-QMOM stops providing any solution. Thus it is important to get a correct prediction of the weights to maintain a robustness of the solution process.

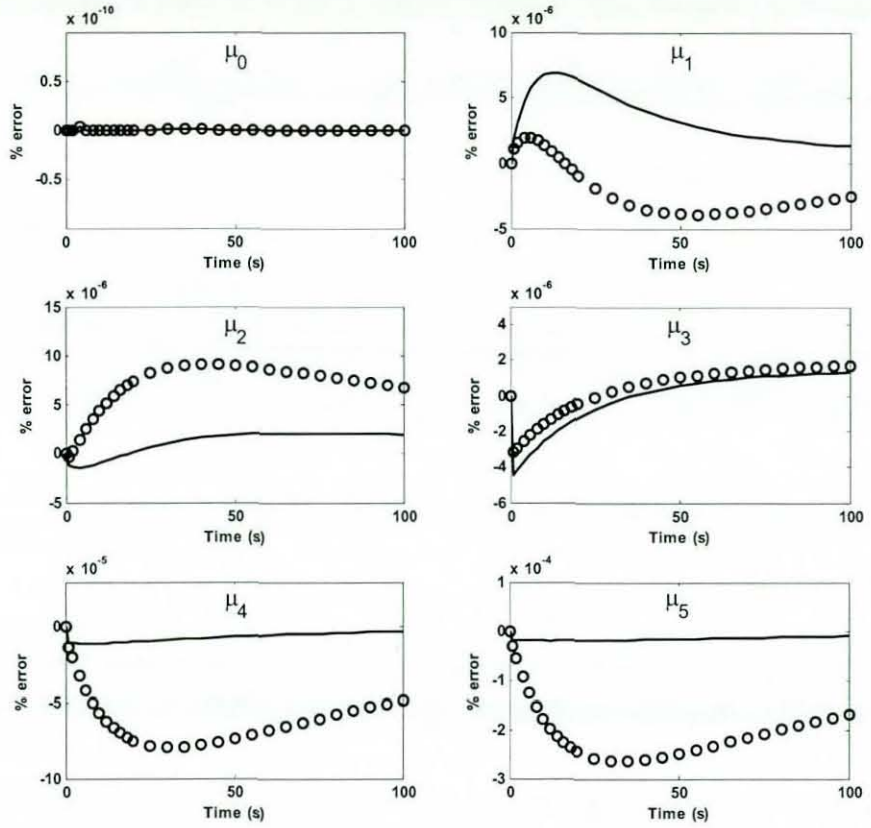

Figure 4-9: The relative errors of the first six moments for power-law growth at p = -0.5 of DAE-QMOM (continuous line) and PD-QMOM (circle) compared to the analytical solution

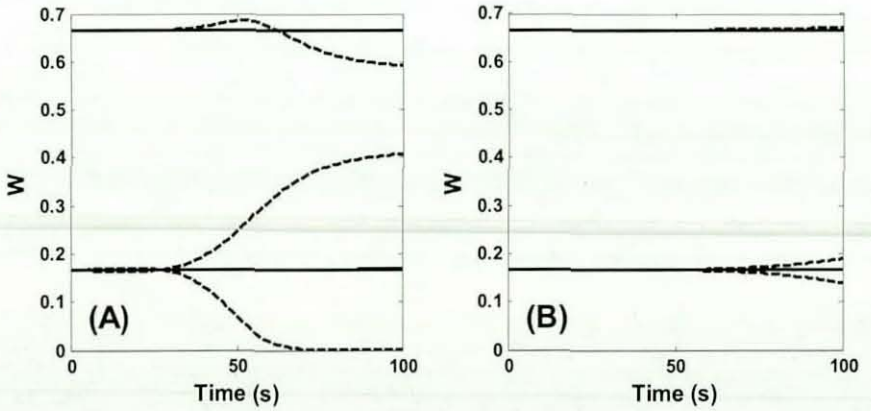

Figure 4-10: Evolution of the weights for power law growth at p = -0.5, DAE (*continuous line*) and PD (*dashed line*), A) Looser tolerance (relative tolerance of 10^{-6} and absolute tolerance of 10^{-6}), B) Tighter tolerance (relative tolerance of 10^{-12} and absolute tolerance of 10^{-8})

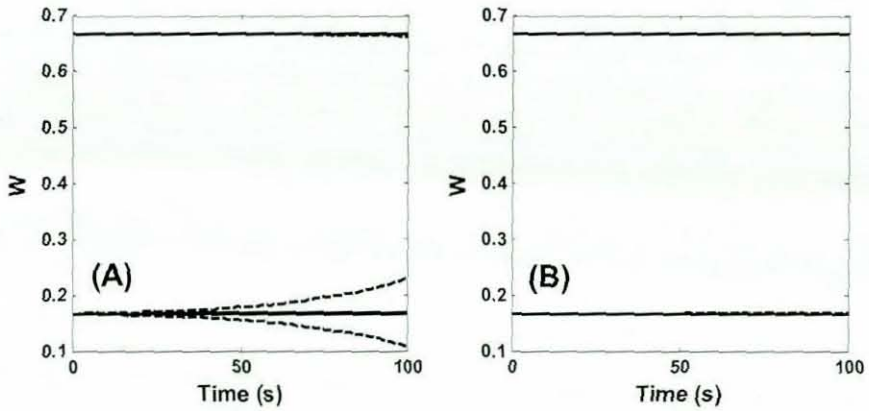

Figure 4-11: Evolution of the weights for power law growth at p = 0.5, DAE (continuous line) and PD (dashed line), A) Looser tolerance (relative tolerance of 10^{-6} and absolute tolerance of 10^{-6}), B) Tighter tolerance (relative tolerance of 10^{-12} and absolute tolerance of 10^{-8})

4.5.2 Aggregation kernel examples

The next stage of complication is aggregation (coalescence) which leads to changes in both the particle size distribution and the number density of particles. Two different aggregation kernels were tested, namely the constant and sum kernel. The initial distribution employed for both aggregation kernels was given by equation (4.24) with N_0 = 1 m^{-3} and v_0 = 0.001 m^3.

Case 4: Constant aggregation kernel

The constant aggregation kernel is given by:

$$\beta(L,\lambda)=1 \tag{4.36}$$

and in this case the breakage, growth and nucleation terms are set to zero. The analytical solutions for the moments for this case can be obtained from the following equation (Gelbard and Seinfeld, 1978):

$$\mu_k = \mu_{k0}\left(\frac{2}{2+N_0\beta(L,\lambda)t}\right)^{1-((k-1)/3)} \tag{4.37}$$

In Fig. 4-12, the numerical solutions using the DAE-QMOM and PD-QMOM methods are compared to the analytical solution for the first six moments. In this case the errors of both DAE-QMOM and PD-QMOM are similar. The third moment which is related to the total particle volume appears to be conserved very well in this case, as shown in Fig. 4-13. Each of the moments in Fig. 4-13 are normalised with their initial value ($\mu_{k,t}/\mu_{k,0}$). For aggregation only problem, the zeroth moment (representing the number of bubble per unit volume) is

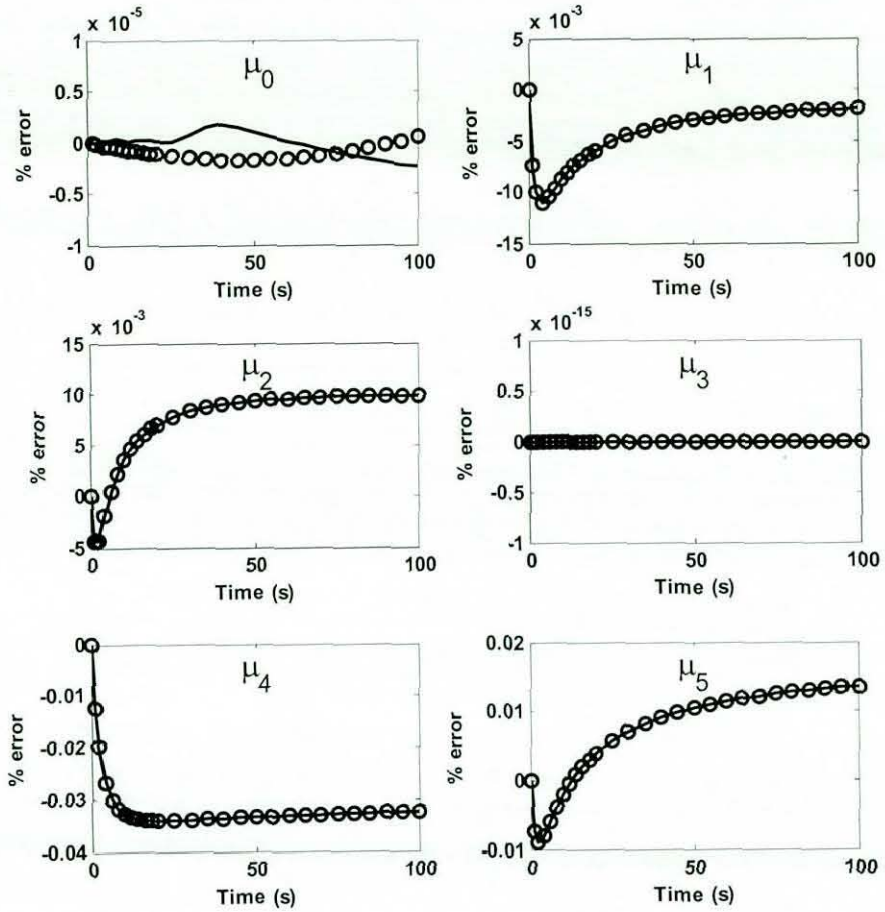

Figure 4-12: Comparison of errors for the first six moments for constant aggregation kernel using DAE-QMOM (continuous line) and PD-QMOM (circles) compared to the analytical solution of eq.(4.37)

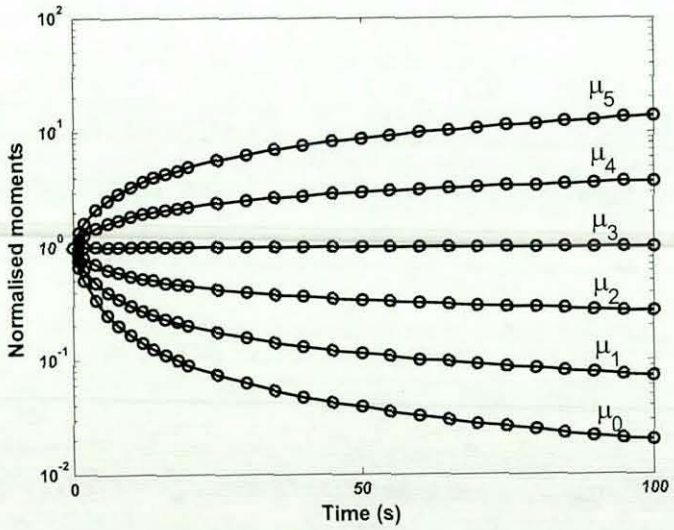

Figure 4-13: Moment evolution for constant aggregation kernel obtained from the exact solution (solid line) and the DAE-QMOM method (circles)

decreasing. The first moment, which represents the total particle diameter, the second moment, which is related to the total particle surface area are also decreasing due to aggregation. The total particle volume is represented by the third moment. For problems involving only aggregation and/or breakage, the third moment should be conserved, because there is no addition of new volume into the system. This is however not true for problems involving growth and/or nucleation, where the total volume of particle is changing.

Case 5: Sum aggregation kernel

The sum aggregation kernel (Melzak, 1953; Scott, 1968) is given by:

$$\beta(L,\lambda)=\left(L^3+\lambda^3\right) \tag{4.38}$$

For this case the analytical solution is only available for the zeroth moment which is given by:

$$\mu_0 = N_0 e^{-N_0 v_0 t} \tag{4.39}$$

The third moment is also conserved in this case. The percentage error for the zeroth moment is significantly smaller in the case of the DAE-QMOM method than for the PD-QMOM as shown in Fig. 4-14. Result from the example showed very little difference in prediction accuracy for both PD-QMOM and DAE-QMOM for aggregation kernel. Although, there is a very small difference in the prediction for the zeroth moment, but the difference is too small (less than 10^{-6}) to concern about and may not be significant considering the error for other moments is larger than 10^{-3} except for the μ_3 which is perfectly conserved.

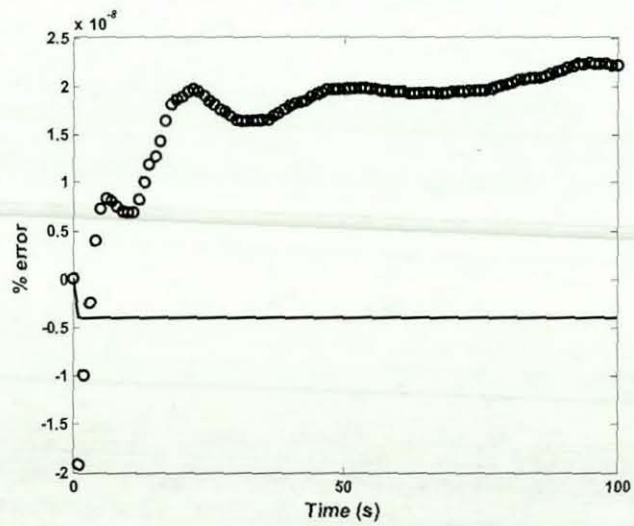

Figure 4-14: Comparison of errors for the zeroth moment for sum aggregation kernel using the DAE-QMOM (continuous line) and PD-QMOM methods (circles)

4.5.3 Breakage kernel

For the breakage case, the breakage kernel was assumed to be proportional to the particle volume:

$$g(L) = L^3 \tag{4.40}$$

The uniform breakage function is assumed which gives uniform probability of all fragment sizes:

$$b(L,\lambda) = \frac{6L^2}{\lambda^3} \tag{4.41}$$

The daughter particle distribution function, $b(L,\lambda)$, determines the number and size of the daughter particle, L, after the breakage event of particle size λ. For the uniform breakage function, the binary breakage with similar particle size is assumed.

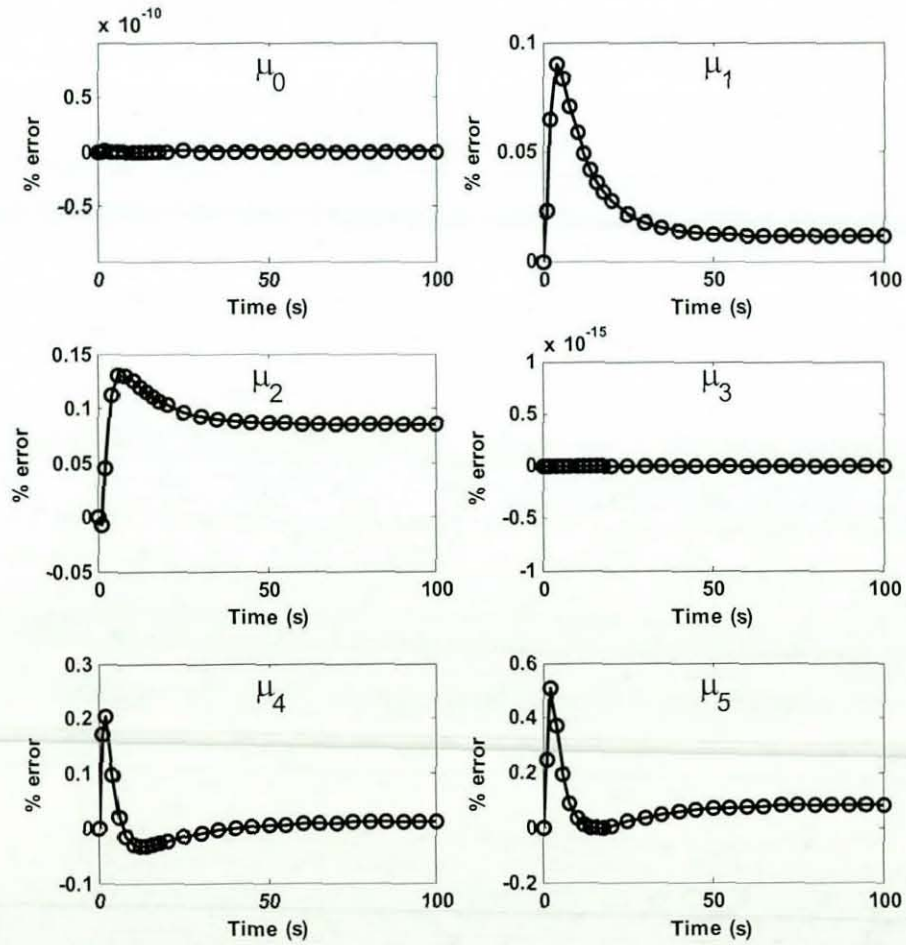

Figure 4-15: Comparison of error for the first six moments for proportional to volume breakage kernel obtained using the DAE-QMOM method (continuous line) and PD-QMOM method (circles)

In this case the aggregation, growth and nucleation terms are set to zero. The initial particle distribution is given by equation (4.24) with N_0 = 1 m^{-3} and v_0 = 1 m^3. In this case the analytical solution at any time t is given by (e.g. Hounslow *et al.* 2001):

$$n(L) = 3L^2(1+t)^2 e^{-L^3(1+t)} \tag{4.42}$$

which then can be integrated analytically using the *int* function in MATLAB to obtain the exact moments. The analytical integration was performed with the limits from zero to infinity. As shown in Fig. 4-15 the errors from both the DAE-QMOM and PD-QMOM in this case are small of order ~0.1% or less and similar. The third moment is also well conserved, as shown in Fig. 4-16. The profiles for the evolution of the normalised moments for the breakage kernel (Fig. 4-16) are the reverse of those for the aggregation kernel in Fig. 4-13. For this breakage-only problem, the first three moments increase steadily as the large particles break into smaller particles. It is clear from the test for breakage only case that there is nothing to choose between both the DAE-QMOM and PD-QMOM in this case since both method yielded similar accuracy.

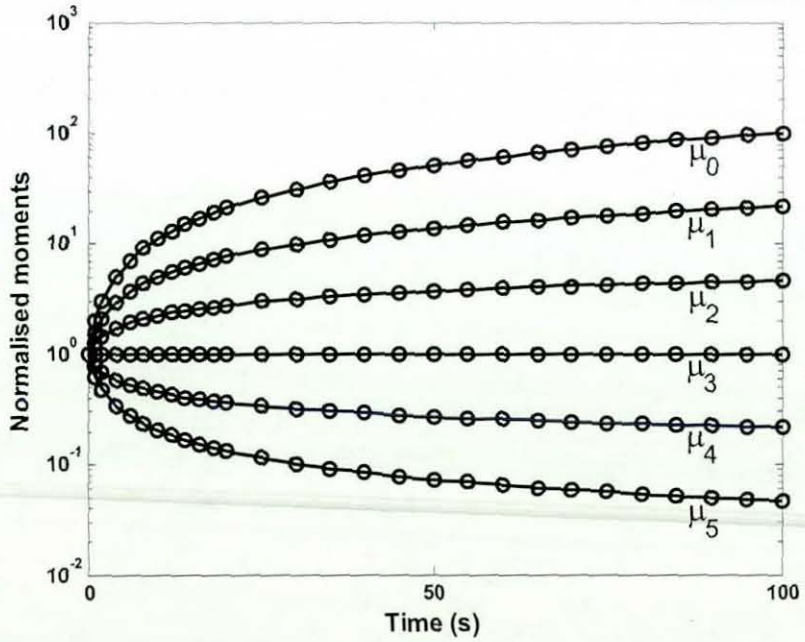

Figure 4-16: Moment evolution for proportional to volume breakage kernel using the DAE-QMOM method (solid line) and the exact solution (circles)

4.6 Comparison of Computational Effort for PD-QMOM and DAE-QMOM

Apart from the prediction accuracy, the performance of the newly introduced QMOM solution, DAE-QMOM, in terms of CPU time is also compared to the existing PD-QMOM method. The test was carried out by employing a similar ODE solver (*ode15s*) and tolerance (similar to those applied for cases 1 to 6) for both PD and DAE algorithms. The comparison of the CPU times for the various PBE solutions is shown in Table 4-1. The DAE-QMOM is more than three times faster than the existing solution via PD-QMOM for constant aggregation and growth with a primary nucleation problems. For the breakage and diffusion-controlled growth problems, the DAE-QMOM is shown to be at least twice as fast as the PD-QMOM. It is also interesting to note that the DAE-QMOM provides a slightly faster solution than the MOM for constant growth with primary nucleation. This test confirms that it is possible to speed-up the computational time of the PBE at least by two times with the new method. In the case of the power-law growth with p = -0.5 the solution time using the PD-QMOM appears to be faster than the DAE-QMOM method. However in this case the PD-QMOM method yields consistently larger errors than the DAE-QMOM and fails to conserve the weights even at tight tolerance setting. Therefore, the computation time of PD-QMOM in this test cannot be compared to the DAE-QMOM solution. For power-law growth with p = 0.5, the DAE-QMOM provides a slightly faster solution than the PD-QMOM, however in this particular case the difference is not very significant.

Table 4-1: Comparison of the CPU time in second for different solution methods for the population balance equation

PBE solution	Diffusion-controlled growth	Constant growth and primary nucleation	Power-law growth		Aggregation - constant	Breakage - proportional to volume
			p = 0.5	p = -0.5		
DAE	0.781	0.516	0.406	1.630	0.609	1.875
PD	1.375	1.703	0.435	Fails	3.188	3.547
MOM		0.562				

4.7 Summary

A new QMOM method for solving the population balance equation was proposed, which solves simultaneously the differential equations for the moments and the system of nonlinear equations resulted from the quadrature approximation as a differential algebraic system. Solution from the proposed method is compared to the product difference based QMOM. Both methods have been validated against the analytical solution for growth, nucleation, breakage and coalescence. The results indicate that both methods are capable of predicting accurately the moment evolutions in all cases tested in this study. This validation exercise has confirmed a correct implementation of the population balance model. This can be used as a basis to implement the real breakage and coalescence kernels suitable for gas-liquid dispersions.

The new numerical solution for QMOM via the DAE method has been demonstrated to be more robust and accurate than the PD algorithm in some cases, especially for growth only problems. The DAE-QMOM has a mathematically simpler formulation eliminating the additional complexity related to the product difference algorithm, providing a more robust solution framework. The only downside of the DAE-QMOM at present is the lack of an automatic Jacobian generator in the DAE solver. At present the Jacobian elements are computed symbolically in software like MATLAB or MAPLE and then included manually within the DAE-QMOM algorithm. However, the use of DAE solvers with automatic differentiation would make the DAE-QMOM much simpler to implement than the PD-QMOM. At present, commercial software like MATLAB can perform a symbolic computation but the DAE-QMOM implementation requires a simultaneous symbolic and numerical evaluation repeatedly and thus requires more complicated implementation in MATLAB at present. Apart from being able to provide a more accurate solution, the DAE-QMOM also provides a faster solution than both PD-QMOM and MOM for all cases evaluated in this work, assessed from the CPU times required to perform the calculation.

It is necessary to solve the population balance simultaneously with the equation for the fluid flow to get a better description of the multiphase flow. The simultaneous modelling approach would require the DAE-QMOM to be implemented within the CFD software. However, currently the DAE-QMOM

cannot be implemented in commercial CFD software unless DAE solvers would become available within the CFD software. On the other hand, a well established PD-QMOM is capable of yielding similarly accurate predictions as DAE-QMOM for the breakage and coalescence problems. Implementation of the PD-QMOM is also quite straightforward in FLUENT, as it can be implemented as a user defined scalar utilising the available ODE solver. For these reasons, the PD-QMOM is employed for further development of population balance modelling of gas-liquid dispersion instead of the DAE-QMOM.

5 THREE-WAY COUPLING SIMULATION OF A GAS-LIQUID STIRRED TANK USING A MULTI-COMPARTMENT POPULATION BALANCE MODEL

5.1 Overview

This chapter discusses the development of a population balance model for gas-liquid dispersion in stirred tanks. Theories related to multiphase simulation, multi-compartment population balance modelling (PBM), as well as the bubble breakage and coalescence kernel are outlined. At first, a single compartment PBM for gas-liquid dispersion is developed and tested. The single compartment model is then extended to a multi-compartment model for aerated stirred tanks simulation. Due to lack of experimental data, the local turbulent dissipation rate, the local gas hold-up and the inter-compartment gas fluxes were obtained from a gas-liquid CFD simulation. Results from the multi-compartment PBM are compared to the experimental data from Laakkonen *et al.* (2007a). In the following chapter, these methods will be extended to a fully coupled CFD-PBM simulation of gas-liquid mass transfer in a stirred vessel.

5.2 Introduction

Gas-liquid stirred tanks are often used in fine-chemicals manufacturing, and biochemical fermentations. Many efforts have been devoted to investigate the performance of aerated stirred tanks experimentally (e.g. Lu and Ju, 1987; Bakker *et al.*, 1994a; Barigou and Greaves, 1992; Morud and Hjertager, 1996; Laakkonen *et al.*, 2005b; Deen, 2001; Aubin *et al.*, 2004b; Montante *et al.*, 2007) or via numerical simulation (e.g. Morud and Hjertager, 1996; Deen, 2001; Khopkar and Ranade, 2006; Sun *et al.*, 2005; Wang *et al.*, 2006; Scargiali *et al.*, 2007; Zhang *et al.*, 2008; Lane *et al.*, 2005; Kerdouss *et al.*, 2006; Venneker *et al.*, 2002; Laakkonen *et al.*, 2006a, 2006b, 2007a, 2007b; and Moilanen *et al.*, 2008). A detailed review of the measurement techniques commonly employed for gas-liquid stirred tank is outlined previously in chapter 2. However, a comprehensive method for modelling aerated stirred tanks has not yet been fully established due to the fluid dynamics complexity of the turbulent gas-liquid flow which is further complicated by bubble coalescence and break-up events.

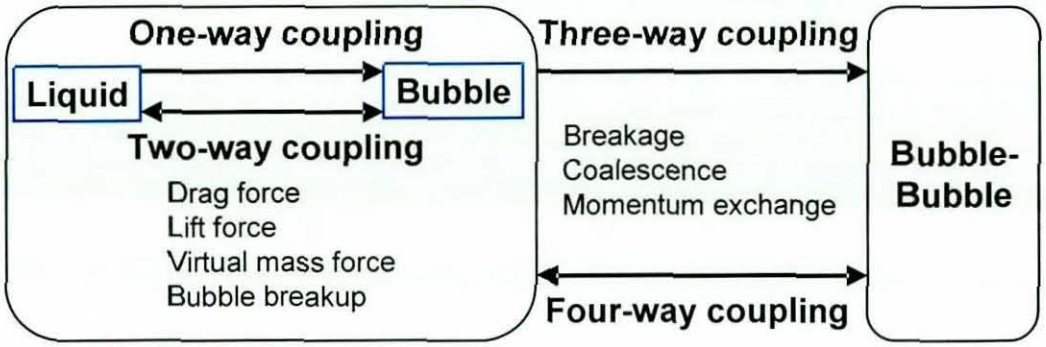

Figure 5-1: Illustration of phase coupling in gas-liquid modelling

Fig. 5-1 illustrates the various ways of phase coupling usually considered for gas-liquid modelling. Earlier work on aerated stirred tanks modelling was carried out using a one-way coupling method. In a one-way coupling simulation, it is assumed that the gas phase motion is affected by the liquid flow, but not vice-versa; a simulation of the single phase flow is carried out first until convergence is reached, and then the bubble motion is tracked later using the calculated liquid flow field (see Fig. 5-1). Some of the earlier work of this kind was by Bakker and Van den Akker (1994a) who employed the impeller boundary condition method to model the impeller motion. Models for bubble break-up and coalescence were also incorporated using a population density method. It is possible to obtain a bubble mean diameter using a population density method, but not the bubble size distribution. They managed to obtain a fair agreement with experimental data on bubble size and gas hold-up. The most advanced one-way coupling simulation to have been performed so far may be the one reported by Venneker *et al.* (2002), which solved the population balance using the liquid flow-field from a single phase simulation. They reported a good prediction of gas hold-up, but the bubble size prediction was not reported. However, simulation using one-way coupling is not thought to be an appropriate method, as the gas-liquid interactions and the liquid aeration height are not considered. Therefore, such a modelling approach may not be applicable when the aeration height is not known, thus limiting its application as a design tool.

Most of the published works related to gas-liquid stirred tank simulation were performed using two-way coupling simulations (via the Eulerian-Eulerian method) using an assumed constant bubble size throughout the tank (e.g. Khopkar and Ranade, 2006; Sun *et al.*, 2005; Wang *et al.*, 2006; Morud and

Hjertager, 1996; Deen *et al.*, 2002; Scargiali *et al.*, 2007). In this method flows from both phases contribute to the gas-liquid dispersion inside the tank (see Fig. 5-1). The bubble-bubble interactions and breakage events are not considered in this method and hence was deemed not good for gas-liquid stirred tank simulations, where in general the bubble size can be non-uniform in space.

Alternatively, the bubble-bubble interaction may be considered in a separate population balance model using the flow field information (flow rate, ε and α_g) obtained from a two-way coupling simulation i.e. multi-compartment modelling. For the multi-compartment modelling, the whole tank volume has to be divided into several smaller well-mixed compartments. The gas hold-up, ε and α_g for each compartment is assumed to be constant and are taken as a volume average value in each compartment from the CFD simulation. This method called a three-way coupling (see Fig. 5-1) will allow prediction of local bubble size. However the effect of the local bubble size on the gas-liquid flow field is not taken into account. There are many papers published concerning multi-compartment simulations (e.g. Zahradnik *et al.* (2001); Hristov *et al.*, 2001; Alves *et al.*, 2002; Alopaeus *et al.*, 1999) but in most cases the inter-compartment flow field is not obtained from two-way coupled CFD simulations. In the case where the flow field is obtained from experimental measurements, the multi-compartment model can be considered as a four-way coupling because the measured flow field was already affected by the local bubble size. In some cases, e.g. Alves *et al.* (2002) and Alopaeus *et al.* (1999), the flow field was obtained using a simple correlation assuming the velocity magnitude during aeration is ~30% less than for the single phase flow whereas the turbulent dissipation rate was obtained from the power number. Such a model cannot be considered as a proper three-way coupling simulation. Laakkonen *et al.* (2006a; 2006b, 2007a) has performed a three-way coupling simulation utilising the PBM via the method of classes and they reported a good prediction of the local bubble size. However, no previous three-way coupling stirred tank simulations have been performed using the QMOM and this is the objective of this chapter.

Four-way coupling simulation considers all the two-way coupling, bubble-bubble interaction and effect of the local bubble size on the two-phase flow field (see

Fig. 5-1). The only possible way of performing the four-way coupling simulation is by implementing the PBM within the CFD code. Simulation using a four-way coupling will be discussed in the next chapter 6.

The first part of this chapter focuses on the development and validation of a single compartment population balance model based on the quadrature method of moments (QMOM) for a system involving bubble break-up and coalescence. A sensitivity study concerning the number of quadrature approximation points used for QMOM and their effect on the prediction accuracy is evaluated. The effects of the turbulence dissipation rate, gas hold-up and the initial bubble size on the final bubble size are also studied. In the second part of the work the single compartment is extended to a multi-compartment model for simulation of gas-liquid stirred tanks. The exchange flows between compartments, the local gas hold-up and the local energy dissipation rates are estimated from separate Eulerian-Eulerian CFD calculations conducted assuming a uniform bubble size. Results from the multi-compartment model are then compared with the experimental measurements of Laakkonen *et al.* (2007a).

5.3 CFD Approach for Gas-Liquid Stirred Tanks

5.3.1 CFD modelling of two-phase flow

The Eulerian-Eulerian approach is employed for gas-liquid stirred tanks simulation in this work, whereby the continuous and disperse phases are considered as interpenetrating media, identified by their local volume fractions. The derivation of the conservation equations by ensemble-averaging the local instantaneous balance for each phase was first proposed by Anderson and Jackson (1967). The volume fractions sum to unity and are governed by the following continuity equations:

$$\frac{\partial}{\partial t}(\alpha_l \rho_l) + \nabla \cdot (\alpha_l \rho_l \vec{u}_l) = 0 \qquad (5.1)$$

where α_l is the liquid volume fraction, ρ_l is the density, and $\vec{u}_l$ is the velocity of the liquid phase. The mass transferred between phases is negligibly small and hence is not included in the right hand-side of eq.(5.1). A similar equation is solved for the volume fraction of the gas phase by replacing the subscript l with g for gas. It has to be noted that the form shown in eq.(5.1) is only applicable

when Favre' averaging is applied. A brief review about different averaging methods for the continuity and momentum equations in two-phase flow is given by e.g. Lane *et al.* (2002) and Scargiali *et al.* (2007). According to Lane *et al.* (2002) the precise form of eq.(5.1) can vary depending on the averaging method applied. For instance, Favre averaging which is used by FLUENT is density-weighted whereas Reynolds averaging which is applied by other CFD code i.e. CFX employs a time-averaging method. Favre averaging method yields a more exact form with no additional turbulent dispersion term introduced in the continuity equation, whereas Reynolds averaging needs an additional term in the continuity equation for turbulent dispersion. The momentum balance for the liquid phase is:

$$\frac{\partial}{\partial t}\left(\alpha_l \rho_l \vec{u}_l\right) + \nabla \cdot \left(\alpha_l \rho_l \vec{u}_l \vec{u}_l\right) = -\alpha_l \nabla P + \nabla \cdot \bar{\bar{\tau}}_l + \vec{F}_{\mathrm{lg}} + \alpha_l \rho_l \vec{g} + \vec{F}_{lift,l} + \vec{F}_{vm,l} \tag{5.2}$$

where $\bar{\bar{\tau}}_l$ is the liquid phase stress-strain tensor, $\vec{F}_{lift,l}$ is a lift force, $\vec{g}$ is the acceleration due to gravity, $\vec{F}_{vm,l}$ is the virtual mass force and a similar equation is solved for the gas phase. $\vec{F}_{\mathrm{lg}}$ is the interaction force per unit volume of mixture between phases due to drag. As pointed out by Scargiali *et al.* (2007) the effects of the virtual mass and lift forces are almost negligible, despite a significant increase in computational expenses and convergence difficulties. Scargiali *et al.* (2007) found a minimal increase of the overall gas hold-up from 4.36% to 4.60% and from 4.36% to 4.67%, by adding the effects of virtual mass and lift force, respectively. They concluded that the effect of the drag force largely predominates in aerated stirred tanks. The virtual mass and lift force were also omitted by many previous studies, e.g. Bakker and Van Den Akker, 1994a; Morud and Hjertager, 1996; Lane *et al.*, 2002; Kerdouss *et al.*, 2006. It was therefore decided not to include the effects of the virtual mass and lift force in this work. Hence, $\vec{F}_{\mathrm{lg}}$ is represented by a simple interaction term for the drag force, given by:

$$\vec{F}_{\mathrm{lg}} = -\frac{3\alpha_g \alpha_l \rho_l C_D \left|\vec{u}_g - \vec{u}_l\right| \left(\vec{u}_g - \vec{u}_l\right)}{4 d_b} \tag{5.3}$$

where C_D is the drag coefficient and d_b is the Sauter mean bubble diameter.

The drag model employed has a significant effect on the flow field of the aerated flow, as it is related directly to the bubble terminal rise velocity. In this chapter the standard FLUENT drag model of Schiller and Naumann (1935) is used.

$$C_D = \max\left(\frac{24}{\mathrm{Re}_b}\left(1+0.15\,\mathrm{Re}_b^{0.687}\right),\ 0.44\right) \tag{5.4}$$

where $Re_b = \rho u_{slip} d_b / \mu$ is the bubble Reynolds number. The slip velocity, u_{slip}, is given by:

$$u_{slip} = \left|\vec{u}_g - \vec{u}_l\right| \tag{5.5}$$

The Schiller and Naumann drag model is best suited for a spherical bubble, i.e. in air-water for a bubble with a diameter smaller than 3 mm. This is considered appropriate since a uniform bubble size of 2 mm is employed throughout the simulation in this chapter. Previous experimental measurement by Laakkonen *et al.* (2005b) and (2007a) reported bubbles size from 1 mm near the impeller vicinity to 3 mm in the bulk region for the same tank. For that reason, a uniform bubble diameter of 2 mm was chosen as an approximate average bubble size in the tank. Simulations using a more comprehensive drag model will be presented and discussed in the four-way coupling CFD-PBM simulation in the next chapter 6.

5.3.2 Modelling of turbulence

The turbulence modelling uses the two-phase realizable k–ε model, in which both k and ε are allowed to have different values for each phase. The transport equations for the two-phase k-ε model are given in the Fluent manual (2005) and the standard values (similar to the one in section 3.4.2) of the model parameters have been applied. The realizable k-ε is considered to be a better model than the standard k-ε for stirred tank flows (Fluent, 2005), as it better accounts for flow features such as strong streamline curvature, vortices and rotation. A detailed comparison of the performance of the realizable k-ε and the standard k-ε model in predicting the single phase fluid flow in a stirred tank has been presented previously in section 3.5. Both the realizable k-ε and the standard k-ε model predict the mean flow field excellently, but the realizable k-ε

give a slightly better prediction of the turbulence quantities than the standard k-ε model. The realizable k-ε differs from the standard k-ε model in two important ways: first it has a new formulation of the turbulent viscosity and second it employs a new transport equation for the dissipation rate incorporating different model constants. Details about this model are given in section 3.4.2.

5.3.3 Modelling of bubble breakage and coalescence

The QMOM is employed to solve the PBM and predict the evolution of the moments of the bubble size distribution. For breakage and coalescence only, the QMOM equation for the k^{th} moment of a single well-mixed system is given by:

$$\frac{d\mu_k}{dt} = \underbrace{\sum_{i=1}^{N} w_i a(L_i) b(k, L_i)}_{\text{birth due to breakage}} + \underbrace{\frac{1}{2}\sum_{i=1}^{N} w_i \sum_{j=1}^{N} w_j \left(L_i^3 + L_j^3\right)^{k/3} \beta(L_i, L_j)}_{\text{birth due to coalescence}} \\ \underbrace{-\sum_{i=1}^{N} w_i a(L_i) L_i^k}_{\text{death due to breakage}} \underbrace{-\sum_{i=1}^{N} w_i L_i^k \sum_{j=1}^{N} w_j \beta(L_i, L_j)}_{\text{death due to coalescence}} \tag{5.6}$$

where $\beta(L_i, L_j)$, $a(L_i)$ and $b(k, L_i)$ are the coalescence kernel, breakage kernel and daughter bubble distribution function, respectively. Full details of the QMOM are elaborated in section 4.3. In this implementation, the solution for the weights (w) and abscissas (L) from the moments was obtained using the product difference algorithm (see section 4.4.2) of Gordon (1968).

There are many breakage and coalescence kernels available for bubbly flow, but they are essentially written in a similar form, except for some minor differences in the model constants or assumptions. The Prince and Blanch (1990) model is commonly applied and has been shown to give a good prediction of bubble sizes in bubble columns (e.g. Shimizu *et al.*, 2000; Podila *et al.*, 2007). Some researchers (e.g. Chen *et al.*, 2005; Bordel *et al.*, 2006; Podila *et al.*, 2007) made a comparison of the prediction of various kernels combinations including those proposed by Prince and Blanch (1990), Luo and Svendsen (1996), Luo (1993), Chesters (1991), Martinez-Bazan *et al.* (1999) and Lehr *et al.* (2002). Their findings suggest that there is no great difference between the mean velocities, gas hold-up and bubble Sauter mean diameter predicted by using different kernels although, there are some differences in the

predicted bubble size distribution. The Luo and Svendsen (1996) breakup kernel was found to generate excessively small and large bubbles, due to its U-shaped daughter bubble distribution function (Podila *et al.*, 2007). Podila *et al.* also pointed out the problem of the Luo (1993) coalescence kernel, which tends to yield large bubbles due to its high coalescence rates. Laakkonen *et al.* (2007a) and Moilanen *et al.* (2008) employed a modified version of Prince and Blanch's (1990) model for their work on gas-liquid stirred tanks, and they reported good agreement with experimental measurements in stirred tanks with operating volumes of 14L and 200L and aeration numbers ranging from 0.001 to 0.039. Laakkonen *et al.* (2007a) compared the prediction of two different kernels i.e. Lehr *et al.* (2002) and a modified version of the Prince and Blanch models. Their findings suggest that Lehr's model tends to under-predict the local bubble size in gas-liquid stirred tanks, even though it has been reported to produce an excellent prediction for bubble columns (Lehr *et al.*, 2002). Based on these previous studies, the original Prince and Blanch (1990) model has been employed to predict the bubble dynamics in this work.

Coalescence kernel

The bubble coalescence kernel, $\beta(L_i, L_j)$, is given as a product of the collision frequency $\omega(L_i, L_j)$ and the bubble collision efficiency $\Lambda(L_i, L_j)$ (Prince and Blanch, 1990).

$$\beta(L_i, L_j) = \Lambda(L_i, L_j)\omega(L_i, L_j) \tag{5.7}$$

Bubble collisions may occur due to a variety of mechanisms, *e.g.* Prince and Blanch (1990) consider collisions arising from turbulence, buoyancy and laminar shear. In turbulent flow, bubble collisions are driven mainly by random motion of bubbles due to turbulent eddies. Bubbles of different sizes also have different rise velocities which may lead to collision. Furthermore there is also a possibility for bubbles from a high liquid velocity region to collide with bubbles in slower section of the velocity field, especially when there is a large velocity gradient in the mean flow. Thus, the bubble collision frequency for a Newtonian fluid can be modelled following the approach proposed by Prince and Blanch (1990):

$$\omega(L_i,L_j)=\underbrace{\pi\left(\frac{L_i}{2}+\frac{L_j}{2}\right)^2\left[u_t^2(L_i)+u_t^2(L_j)\right]^{0.5}}_{turbulent}+\underbrace{\pi\left(\frac{L_i}{2}+\frac{L_j}{2}\right)^2\left|u_\infty(L_i)-u_\infty(L_j)\right|}_{bouyancy} \tag{5.8}$$

where $u_t(L_i)$ is the turbulent velocity in the inertial range of isotropic turbulence (Rotta, 1972)

$$u_t(L_i)=1.4\varepsilon^{1/3}L_i^{1/3} \tag{5.9}$$

and $u_\infty(L_i)$ is the rise velocity of bubble given as a function of bubble size (e.g. using the method by Clift *et al.*, 1978).

$$u_\infty(L_i)=\left(2.14\frac{\sigma}{\rho_l L_i}+0.505gL_i\right)^{0.5} \tag{5.10}$$

The laminar shear effect is not included in this work as it is not significant for a Newtonian fluid operating within the fully turbulent regime. This work deals with an air-water system in stirred tank with Reynolds number of 85856 and gas superficial velocity of 0.3 cm/s. The effect of laminar shear was also found to be insignificant by Alexiadis *et al.* (2004) who performed a CFD-PBM of gas-stirred ladle with superficial velocities ranging from 8.5 to 50.5 cm/s.

The bubble collision efficiency, $\Lambda(L_i,L_j)$, is the probability of coalescence during a bubble-bubble collision between sizes L_i and L_j. According to Prince and Blanch (1990), coalescence of two bubbles in turbulent flows occurs in three steps which is collision, film draining and film rupture. First, bubbles collide and a small amount of liquid film separating the bubbles is trapped between the bubble boundaries. The liquid then drains until the liquid film separating the bubbles reaches the critical thickness and finally the film rupture occurs resulting in coalescence. The first step involves the bubble collisions which means the coalescence mechanism is very much dependent on the collision rate. However, not all bubbles collision lead to bubble coalescence and the collision efficiency must be known to determine whether a given collision will result in coalescence. Coalescence only occurs if two bubbles remain in contact for a sufficient period of time for the liquid film between them to thin to the critical thickness necessary for rupture (Prince and Blanch, 1990). For Prince and Blanch's model, the bubble collision efficiency is given as a function of film drainage and bubble-bubble contact times:

$$\Lambda(L_i, L_j) = \exp\left(\frac{-\ln(h_o/h_f)\sqrt{(L_{ij}/2)^3 \rho_l / 16\sigma}}{(L_{ij}/2)^{2/3} / \varepsilon^{1/3}} \right) \tag{5.11}$$

where $L_{ij} = 2(1/L_i + 1/L_j)^{-1}$, h_o is the initial film thickness and h_f is the final thickness at which the film rupture occur. A value of 10^{-4} m for h_o and a value of 10^{-8} m for h_f from Prince and Blanch (1990) was used throughout this work.

Breakage kernel

Prince and Blanch (1990) considered the bubble break-up to be caused by collisions with turbulent eddies of sizes equal to, or smaller than, the bubble size. They argued that eddies smaller than 0.2 times the bubble diameter are unlikely to contribute significantly to the overall break-up rate and set the lower limit of the effective turbulent eddies as $0.2L$. Further discussion regarding the validity of this assumption is given in section 6.4.4. They considered only eddies having a velocity larger than the critical velocity, u_{ci}, where the disruptive force due to the momentum of the eddy and the cohesive force due to surface tension balance each other. The break-up rate is given as a product of the collision rate of bubbles with turbulent eddies, θ_{ie}, and the break-up efficiency, κ_i. According to Prince and Blanch (1990), the bubble break-up rate is given by the expression:

$$a(L_i) = \theta_{ie} \kappa_i \tag{5.12}$$

The collision rate of bubbles with turbulent eddies is given by Kennard (1938):

$$\theta_{ie} = n_i n_e S_{ie} \left(u_t(L_i)^2 + u_t(L_e)^2 \right)^{0.5} \tag{5.13}$$

where n_i, n_e and S_{ie} are the number of bubbles per unit volume, number of eddies per unit volume and collision cross-sectional area, respectively. The $u_t(L_i)$ is the turbulent velocity in the inertial range of isotropic turbulence given by eq.(5.9); and the eddy velocity, $u_t(L_e)$, of eddy size L_e is also calculated from eq.(5.9). The eddy size may be expressed using Kolmogorov's (1941) theory of isotropic turbulence as $L_e = (\nu_l^3/\varepsilon)^{1/4}$.

The break-up efficiency, κ_i, is given by (Kennard, 1938; Prince and Blanch, 1990):

$$\kappa_i = \exp\left(u_{ci}^2 / u_t \left(L_e\right)^2\right) \tag{5.14}$$

where the u_{ci} is the critical eddy velocity necessary to break a bubble of diameter L_i, given by Shimizu *et al.* (2000).

$$u_{ci} = \left(\frac{\sigma}{L_i \rho_L}\right)^{0.5} \tag{5.15}$$

Prince and Blanch's (1990) break-up model does not include the daughter bubble size distribution. In QMOM, the daughter bubble distribution function, $b(k, L_i)$, determines the corresponding moments of the daughter particles L_i formed after any breakage event. Here, a uniform breakage function was selected with binary breakage to form similar particle sizes.

$$b(k, L_i) = L_i^k \frac{6}{k+3} \tag{5.16}$$

There is a high possibility of non-binary breakage for liquid-liquid systems where the internal viscosity of the dispersed phase can lead to multiple daughter drops (Andersson and Andersson, 2006). However, the assumption of binary break-up is considered valid for bubbles, since the air viscosity is low and thus the bubbles cannot form an extremely elongated shape (e.g. as for liquid-liquid drops) which favours a non-binary breakage. Furthermore, a recent study by Andersson and Andersson (2006) revealed that more than 95% of bubble break-ups involved binary breakage.

5.4 Gas-liquid Modelling via QMOM for a Single Compartment

The validation tests in section 4.5 show the QMOM algorithm works well for aggregation, breakage, growth and nucleation problems. However, the algorithm has not yet been tested for a real problem involving a gas-liquid problem with bubble coalescence and break-up occur simultaneously. It is necessary to test the QMOM algorithm with real coalescence and break-up kernels for gas-liquid dispersion before further development can be initiated. In this section, a sensitivity study for a QMOM to different numbers of quadrature approximation is performed besides studying the response of developed model to the changes in gas hold-up, turbulence dissipation rate and initial bubble size.

A multiphase flow in a bubble column with a superficial gas velocity of 0.12 m/s from Degaleesan (1997) was considered for the single compartment simulation. Gas is sparged into the column through a perforated plate with 0.33 mm diameter holes. The bubble column has a cylindrical shape with diameter of 0.19 m. Degaleesan (1997) observed an overall gas hold-up about 29% (the initial water level was 0.96 m and the aerated water level is 1.24 m) and the mean turbulence dissipation rate may be roughly estimated equal to gv_g = 1.18 m^2/s^3.

Table 5-1: Comparison of QMOM results obtained for different quadrature points, N, for ε = 1.18 m^2/s^3, Lognormal distribution parameter (d_{mean} initial = 5 mm, σ_d = 0.2)

N	2	3	4	5	Pohorecki	Wilkinson
Initial L_i (cm)	0.393 0.588	0.352 0.500 0.710	0.324 0.448 0.605 0.836	0.303 0.411 0.542 0.714 0.969		
Initial w_i (n/cm^3)	2.516 1.374	1.342 2.315 0.233	0.685 2.358 0.822 0.025	0.350 1.965 1.410 0.164 0.002		
d_{32} (cm)	0.410	0.413	0.412	0.412	0.36	0.44
CPU time (s)	4.20	16.30	46.87	102.86		
% excess time compare to N = 2	0.00%	287.70%	1014.66%	2346.39%		
% relative error compare to N = 5	0.54%	0.24%	0.01%	0.00%		

In this case, a single compartment population balance model is employed assuming a steady-state, well-mixed and homogeneous system. Both bubble break-up and coalescence were modelled using the Prince and Blanch (1990) model. The initial bubble size distribution was assumed to be lognormal with geometric mean diameter 5 mm and standard deviation of 0.2. The gas in flow and out flow from the compartment was omitted in this particular case because the main objective of this section was to test the response of developed model to the changes in gas hold-up, turbulence dissipation rate and initial bubble size. The PD-QMOM is employed to solve the simultaneous bubble break-up and coalescence problem in this bubble column. The ODE integrations were conducted by setting both the relative and the absolute tolerances equal to 10^{-8}.

All solutions presented in this chapter were solved using the *ode113* integrator in MATLAB. The maximum simulation time was set to t = 30 s because a steady-state moment evolution can be achieved in less than 1 s (see Fig. 5-3).

Correlations to estimate the mean bubble size are often related to liquid surface tension (σ), liquid density (ρ_l), liquid viscosity (μ_l) and gas superficial velocity (v_{sg}). Some correlations include the gas density (ρ_g) and gravity (g) as well, such as the one proposed by Wilkinson (1991):

$$d_{32} = 3g^{-0.44}\sigma^{0.34}\mu_l^{0.22}\rho_l^{-0.45}\rho_g^{-0.11}v_{sg}^{-0.02} \tag{5.17}$$

Another correlation for bubble size was proposed by Pohorecki *et al.* (2005):

$$d_{32} = 0.289\sigma^{0.442}\mu_l^{-0.048}\rho_l^{-0.552}v_{sg}^{-0.124} \tag{5.18}$$

Both correlations work with S.I. unit and give similar mean bubble sizes, i.e. 4.4 mm for Wilkinson and 3.6 mm for Pohorecki. The PBM equations were solved using a different number of quadrature approximation ranging from two to five. Table 5-1 shows the predicted and calculated bubble Sauter mean diameter, d_{32}, for the bubble column. The PBM predictions are in fair agreement with the values calculated from the correlations of Wilkinson (1990) and Pohorecki *et al.* (2005) in equation (5.17) and (5.18), respectively. The predicted bubble size also did not vary significantly with the number of quadrature points used. Marchisio *et al.* (2003) also has evaluated the effect of quadrature points on the global error, and they concluded that a higher number of quadrature approximation decreases the overall error. However, they also noted that higher number of quadrature approximation does not always reduce the prediction error in certain aggregation and breakage problems. Marchisio *et al.* (2003) also found that there was no significant gain in QMOM prediction accuracy beyond three quadrature points. A similar conclusion can also be drawn from the result in Table 5-1, where the prediction of d_{32} from two and five quadrature points did not differ appreciably. It is also interesting to note that calculations for greater number of quadrature points (i.e. 5) require significantly higher computational effort, (more than 2000% compared to those with only two quadrature points), but produce less than 0.6% gain in prediction accuracy. Consequently, it was not considered necessary to solve the QMOM with higher number of quadrature points (i.e. more than 3) because the gain in accuracy is almost insignificant.

Table 5-2: Comparison of QMOM result obtained at different d_{mean} initial, ε and α_g for three quadrature points

Case	5.1	5.2	5.3	5.4	5.5	5.6	5.7	5.8
Initial L_i (cm)	0.155	0.352	0.155	0.352	0.155	0.352	0.155	0.352
	0.220	0.500	0.220	0.500	0.220	0.500	0.220	0.500
	0.312	0.710	0.312	0.710	0.312	0.710	0.312	0.710
Initial w_i (n/cm^3)	15.752	1.342	15.752	1.342	8.879	0.756	8.879	0.756
	27.182	2.315	27.182	2.315	15.321	1.305	15.321	1.305
	2.731	0.233	2.731	0.233	1.539	0.131	1.539	0.131
ε (m^2/s^3)	1.18	1.18	2.4	2.4	1.18	1.18	2.4	2.4
α_g	0.23	0.23	0.23	0.23	0.11	0.11	0.11	0.11
d_{mean} initial (cm)	0.22	0.5	0.22	0.5	0.22	0.5	0.22	0.5
d_{32} (cm)	0.41	0.41	0.30	0.30	0.37	0.37	0.26	0.26
CPU time (s)	16.54	16.30	26.15	25.68	12.96	13.13	21.23	21.21

Apart from the previous test, some runs using a higher turbulence dissipation rate (2.4 m^2/s^3), smaller initial bubble size (2.2 mm) and lower gas hold-up have also been carried out to test the algorithm for any possible dependencies on those three variables. In these tests the PD-QMOM with three quadrature points was employed. Results for these runs are shown in Table 5-2. As expected a higher turbulence dissipation rate promotes a breakage dominated mechanism thus results in a smaller mean bubble size. Another important feature of gas-liquid dispersion is that the steady-state bubble size should not depend on the initial size distribution, and should only depend on the turbulence dissipation rate and gas hold-up. Results from the test in Table 5-2 (see cases 5.1 and 5.2) are in good agreement with this theoretical framework. It can be seen that the final bubble size for different initial bubble size converged to the exactly similar value (compare cases 5.1 and 5.2 or 5.3 and 5.4 or 5.5 and 5.6 or 5.7 and 5.8 in Table 5-2).

The gas hold-up was reduced by half from 0.23 to 0.11 to evaluate the effect of this variable on the final bubble size (runs 5.5 to 5.8 in Table 5-2). The turbulence dissipation rate was set similar to the previous test (1.18 m^2/s^3) to enable a proper comparison. By definition the sum of the QMOM weights is equivalent to the number of bubbles per unit volume. Assuming a spherical bubble, volume of gas, V_g, from the abscissas and weights may be estimated from,

$$V_{g,QMOM} = \sum_{i=1} \frac{1}{6} \pi V_T w_i L_i^3 \tag{5.19}$$

where V_T is the total dispersion volume. The gas volume in the whole system may also be obtained from,

$$V_{g,system} = \alpha_g V_T \tag{5.20}$$

The third moment μ_3 is related to α_g by the following relation:

$$\alpha_g = \sum_{i=1} \frac{1}{6} \pi w_i L_i^3 = \frac{\pi}{6} \mu_3 \tag{5.21}$$

Assuming an initial lognormal bubble distribution with mean bubble size of 2.2 mm and standard deviation of 0.2, the initial bubble size distribution as shown in Fig. 5-2 (continuous line) may be obtained. The moments can be obtained from the following equations:

$$\mu_k = \exp\left(k\mu + k^2\sigma^2/2\right) \tag{5.22}$$

where μ_k, k, μ and σ are the moments, order of moments, arithmetic mean and arithmetic standard deviation, respectively. The moments are then used to obtain a set of abscissas and weights (see Fig. 5-2 bar plot) using the PD algorithm (see section 4.4.2). However, the initial weights obtained from lognormal distribution are normalised so that $\mu_0 = \sum w_i = 1$, and thus have to be adjusted to match the gas hold-up using both equations (5.19) and (5.20) because the PBM calculations need μ_0 equal to number of bubbles per unit volume of dispersion. Example of the weights adjustment may be better appreciated by looking at Table 5-3. After adjustment the gas volume obtained from the moments match exactly the value calculated from the gas hold-up. The same method was applied for all PBM calculations in this chapter.

Table 5-3: Scaling the QMOM weights according to gas volume fraction

L_i	w_i	$V_{g,QMOM} = \sum_{i=1} \frac{1}{6} \pi V_T w_i L_i^3$	$f = \frac{\alpha_g V_T}{\sum \frac{\pi}{6} V_T w_i L_i^3}$	$w_{i,adj} = w_i f$	$V_{g,system} = \alpha_g V_T$	$V_{g,QMOM} = \sum_{i=1} \frac{1}{6} \pi V_T w_{i,adj} L_i^3$
(cm)	-	(cm^3)	-	(n/cm^3)	(cm^3)	(cm^3)
0.15	0.34	0.005	45.66	15.75	7938.80	7938.80
0.22	0.60			27.18		
0.31	0.06			2.73		

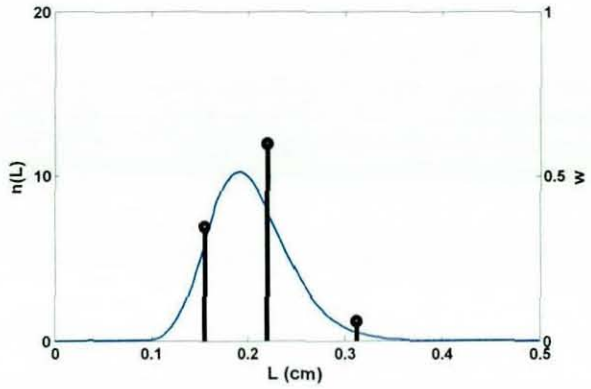

Figure 5-2: Example of initial bubble distribution for lognormal function with d_{mean} = 2.2 mm, σ_d = 0.2 mm), continuous line (bubble size distribution), Bar plot (weights and abscissas obtained using PD algorithm)

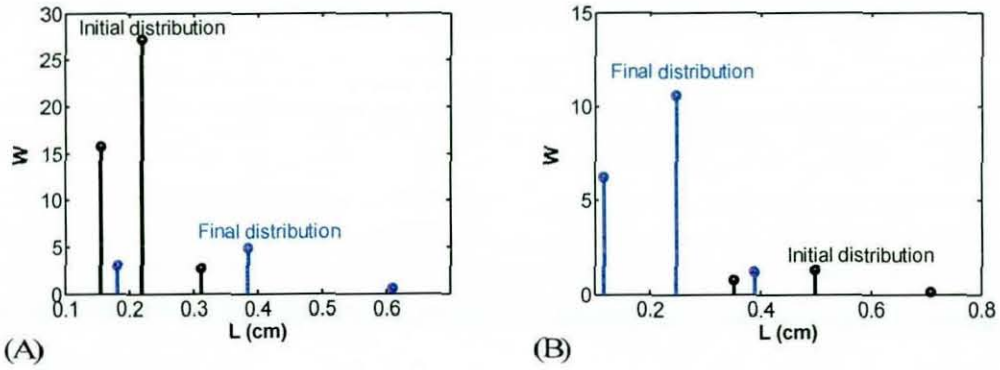

Figure 5-3: Initial (t = 0 s) and final (t = 30 s) bubbe size distribution, A) Coalescence dominated case 5.1, ε = 1.18 m^2/s^3, Lognormal distribution parameter (d_{mean} initial = 2.2 mm, σ_d = 0.2), B) Breakage dominating case 5.8, ε = 2.4 m^2/s^3, Lognormal distribution parameter (d_{mean} initial = 5 mm, σ_d = 0.2)

The effect of the gas hold-up on the final bubble size is presented in Table 5-2 (see cases 5.1, 5.2, 5.5 and 5.6). It shows that the final stable bubble size increases with increasing gas hold-up. This is due to higher probability of bubble-bubble collisions at higher gas hold-up, which results in more coalescence events taking place. The bubble-eddy collisions may also increase with gas hold-up but their rate is much slower than the coalescence processes since the break-up kernel depend upon L_i (eq. 5.13) compared L_i^2 in the coalescence kernel (eq. 5.8). The combination of a higher turbulence dissipation rate and a lower gas hold-up produces even smaller bubbles, as shown in Table 5-2 (see cases 5.7 and 5.8). This test proves that the present algorithm is capable of predicting qualitatively, the evolution of the mean bubble

size in a gas-liquid dispersion, with respect to the change in turbulence dissipation rate, gas hold-up and initial bubble size.

In the case where coalescence is the dominant mechanism, the final bubble size distribution appears to be broader than the initial distribution (Fig. 5-3A). The opposite can be observed when break-up is the dominant mechanism as shown in Fig. 5-3B.

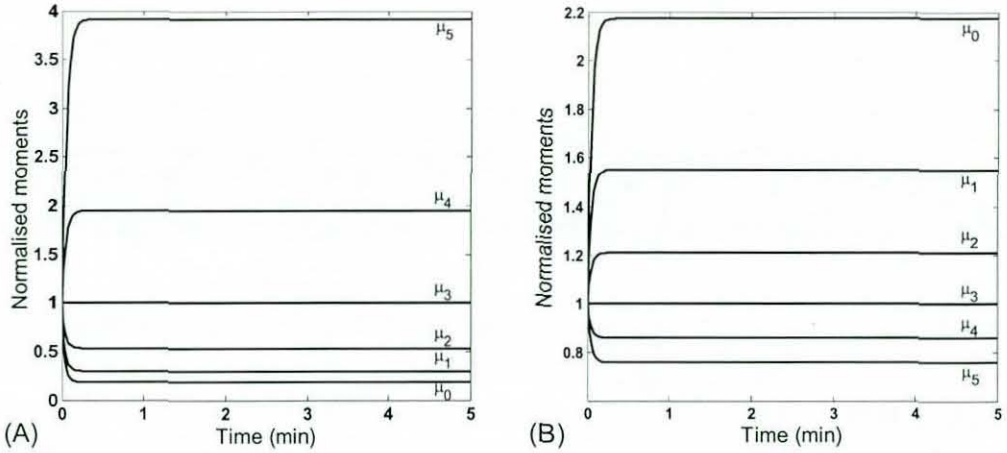

Figure 5-4: Moments evolution for bubble coalescence and breakage problem, A) Coalescence dominating case 5.1, ε = 1.18 m^2/s^3, Lognormal distribution parameter (d_{mean} initial = 2.2 mm, σ_d = 0.2), B) Breakage dominating case 5.2, ε = 1.18 m^2/s^3, Lognormal distribution parameter (d_{mean} initial = 5 mm, σ_d = 0.2)

Fig. 5-4 shows the evolution of moments obtained from QMOM with three quadrature points. The initial mean bubble size was set at 5 mm for Fig. 5-4A and 2.2 mm for Fig. 5-4B. The turbulence dissipation rate for both cases was set at 1.18 m^2/s^3. The third moment which is related to the total bubble volume appears to be perfectly conserved in both cases as it should be for breakage and coalescence only problems. In Fig. 5-4A, the first three moments which are related to total number of bubbles, total bubble diameter and total bubble surface area are increasing, because the large initial bubble size favours the break-up mechanism. The opposite can be observed in Fig. 5-4B where the initial bubble size is smaller, thus creating a condition favourable for coalescence.

It is clear from these simulation exercises that the QMOM algorithm can predict the bubble Sauter mean diameter in good agreement with published correlations for the air-water system. The developed PBM algorithm is also

capable to respond well with various settings, representing either a coalescence or break-up dominating system. Therefore, the present algorithm is used as a basis for development of a multi-compartment population balance model and then a User Defined Function (UDF) for aerated stirred tanks.

5.5 Multi-compartment Modelling

The multi-compartment model is a trade-off between the ideal mixing assumption of section 5.4 and the coupled CFD-PBM of chapter 6. For a stirred tank, the vessel is divided into a number of homogeneous and well-mixed compartments. The non-homogeneous behaviour of the stirred tank is accounted by the different values of the turbulent dissipation rate and inter-compartment flow which can be obtained from either measurements or CFD simulations. The connectivity between each compartment is determined by the flow direction obtained from CFD simulation or experiment. The inter-compartment flow eventually yields a different bubble size in each compartment due to the in and out flow of bubble from and to the neighbouring compartment beside the effect of the local turbulent dissipation rates and gas hold-up. The gas inflow to the compartment may have a different bubble size and hence affecting the local bubble size. The same applies to the gas outflow from the compartment which reduces the local bubble density thus affecting the local bubble size. Of course the multi-compartment models are not capable of providing as high resolution as CFD, however they require far less computational effort. Therefore, the multi-compartment model applies best to the cases where local conditions (i.e. local bubble size) in the tank are of interest at lower computational expense.

Multi-compartmental models have been applied in many studies to investigate the local gas-liquid hydrodynamics in aerated stirred tanks (Vasconcelos *et al.* 1995; Vrábel *et al.* 2000; Vlaev *et al.* 2000; Zahradnik *et al.* 2001; Hristov *et al.* 2001; Alves *et al.* 2002; Laakkonen *et al.*, 2006a; 2007a). Most of the earlier studies (Vasconcelos *et al.* 1995; Vrábel *et al.* 2000; Vlaev *et al.* 2000; Zahradnik *et al.* 2001) employed a constant bubble size throughout the tanks. Alves *et al.* (2002) employed the population bubble density method for prediction of local bubble size, and they reported a good agreement with

experimentally measured bubble sizes. Recently, Laakkonen *et al.* (2006a; 2007a) has implemented the population balance model (using the method of classes) in a multi-compartment model of a gas-liquid stirred tank. They reported good agreement for the local bubble size predicted by the multi-compartment model, CFD-PBM and experimental measurement, but only by adjusting the constants in the breakage and coalescence kernels. Further discussion regarding the bubble size modelling in aerated stirred tank is outlined in section 6.2. In this chapter, the local turbulence dissipation rate, the local gas hold-up and the inter-compartment fluxes were obtained from a gas-liquid CFD simulation due to lack of detailed experimental data.

5.5.1 Modelling of Gas-Liquid Stirred Tank

An aerated stirred tank agitated by a Rushton turbine, with operating volumes of 14L, as used by Laakkonen *et al.* (2007a), was considered for the multi-compartment modelling in this chapter. Detailed dimensions of the case considered in this chapter are given in Table 5-4. The case considered in this chapter operates within the fully dispersed regime ($N > N_{CD}$) which is relevant to a better gas dispersion. Gas was injected through a sparger ring at a flow rate of 0.7 VVM which is treated as a continuous source of gas (velocity inlet) in the CFD simulation. The two-phase CFD simulation was performed using an Eulerian-Eulerian approach for the multiphase modelling and the impeller movement was modelled using the multiple reference frame technique. The turbulence was modelled using the two-phase realizable k-ε model. Transient solvers with a second-order spatial interpolation scheme were also applied for the final simulation in order to minimise the amount of numerical diffusion. The transient solver is employed in this work because it is impossible to use the steady-state solver for gas-liquid stirred tanks when the Eulerian-Eulerian is used and moreover the PBM also needs the transient solver. The iteration residual was set to fall below 1×10^{-4} at each time step to achieve good convergence. The volume average of the gas void fraction in the rotating zone (impeller region) was used as a monitor variable to assess when the steady-state had been obtained; the iterations in the transient simulation were only halted once a constant value was obtained. An example of the volume fraction evolution for a CFD simulation is shown in Fig. 5-5.

The CFD simulation was performed assuming a uniform bubble diameter of d_{32} = 2 mm throughout the tank. As mentioned earlier in section 5.3.1, the bubble size selection for CFD simulation was chosen based on Laakkonen *et al.* (2007a) and (2005b) work on the same tank. The interphase drag coefficient was estimated using the standard Schiller-Naumann drag model (Schiller and Naumann, 1935). Of course a better drag model which considers the distorted bubble may be implemented as user defined function within the CFD code (see section 6.3.1), but in this chapter the CFD simulation was solved using the default FLUENT model. A detailed four-way coupling simulation will be discussed further in chapter 6. Moreover, there is only a little difference between the drag coefficients for bubble less than 3 mm. The CFD and multi-compartment model were solved separately (the local bubble size obtained from the multi-compartment model was not passed back to the CFD simulation), thus there is not much benefit of using the more comprehensive drag model.

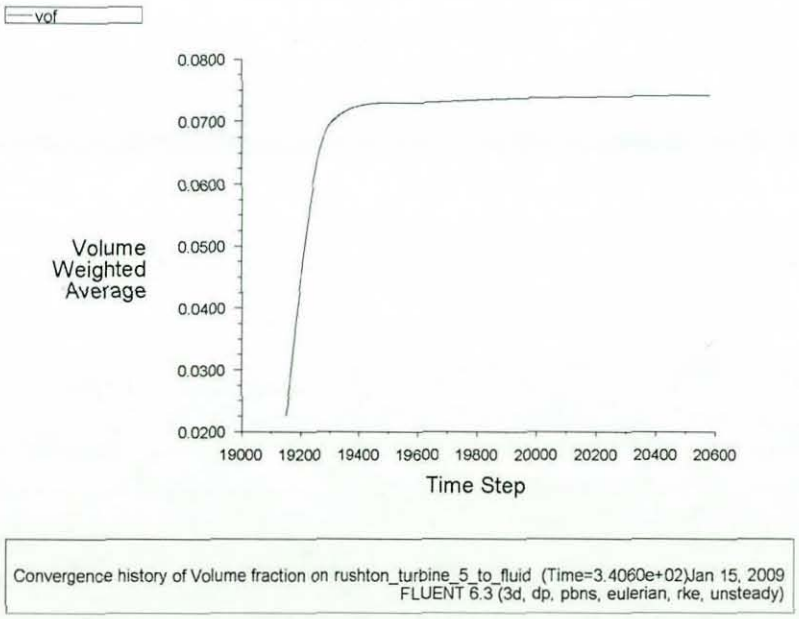

Figure 5-5: Evolution of the average gas hold-up in the impeller region, each time step = 0.005 s

The CFD simulation was performed using a half-tank domain consisting of about 225k hexahedral elements (structured mesh) shown in Fig. 5-6B. The structured mesh is less prone to the numerical diffusion errors and also reduces the memory size requirement compared to the unstructured tetrahedral elements (Tu *et al.*, 2007). A finer mesh was employed around the impeller with

up to 11 nodes placed along the impeller blade height in order to resolve the trailing vortex core, which is vital for a correct prediction of turbulence in stirred tanks. According to Derksen *et al.* (1999), a grid with eight or less nodes along the impeller blade height may not be able to resolve the vortex core structure correctly and hence can give errors in the predicted mean flow field. A grid refinement is also employed in the impeller discharge region because up to 80% of the turbulence is dissipated within the impeller swept volume and the impeller outflow region (Derksen and van den Akker, 1999). For that reason, a grid sensitivity study must consider a refinement in these highly turbulent regions and should not be based on the total number of grid cells count.

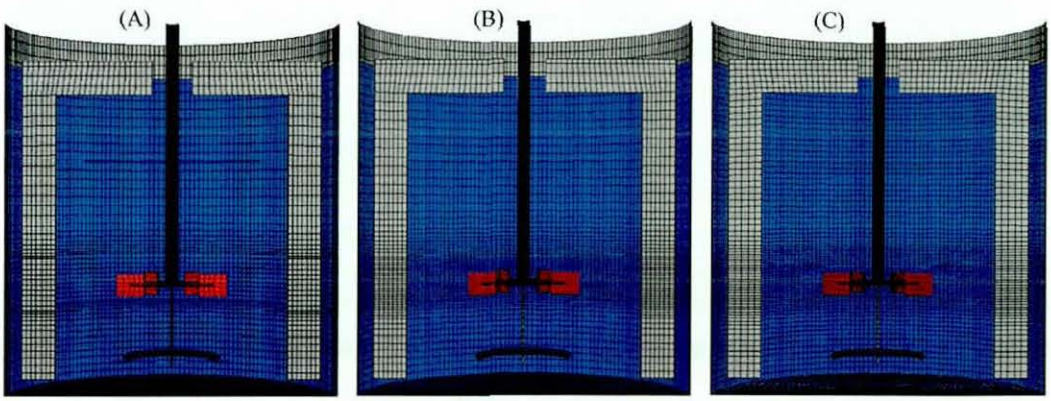

Figure 5-6: Computational grid showing tank wall and its internal for Laakkonen *et al.*'s geometry, A) coarse, B) intermediate, C) fine

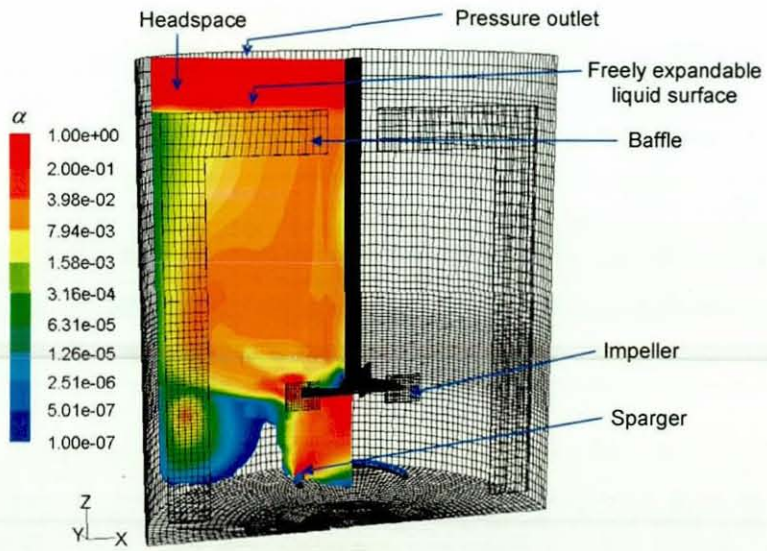

Figure 5-7: Boundary condition of gas-liquid stirred tank simulation. Also shown is the instantaneous contour of gas hold-up

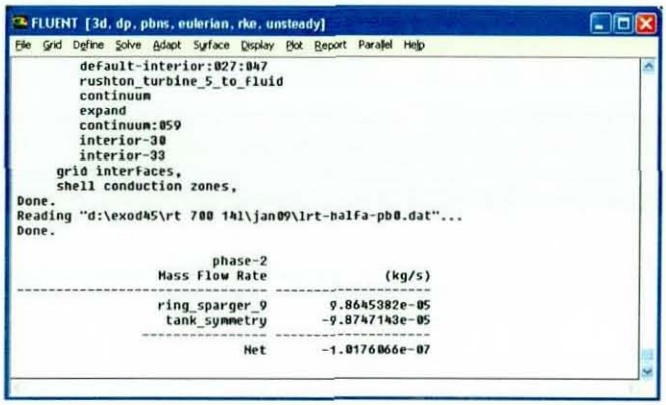

Figure 5-8: Evaluation of the instantaneous gas fluxes leaving (from top surface) and entering (at sparger) the tanks for case 5.5

The stirred tank grid was prepared with a headspace to accommodate the liquid expansion due to aeration. The liquid surface was modelled as a freely expandable liquid surface and the top of the headspace region was set as a pressure outlet (see Fig. 5-7). The mass balance between the gas outflow at the outlet boundary (above the headspace region) and the gas inflow at the sparger was satisfied; Fig. 5-8 shows that the mass balance agreed to within 0.1%.

A grid sensitivity study was performed on Laakkonen's geometry prior to the final grid selection using three different meshes: coarse (165k), intermediate (225k) and fine (335k). The CFD setup (for models employed and boundary conditions) for grid sensitivity study was set exactly the same as the main simulation except the use of different grid densities. The grids employed for the sensitivity study are shown in Figs. 5-5A to 5-5C. The main differences between the three grids are the number of nodes placed at impeller blade height; 6 nodes for the coarse grid, 11 nodes for the intermediate grid and 13 nodes for the fine grid. It was found that a domain consisting of 225k cells yielded a grid independent solution (see Fig. 5-9). Comparison was made using the tangential velocity, turbulent kinetic energy and the turbulent dissipation rate because they are the hardest to predict as observed from earlier study for the single phase stirred tank in chapter 3. Fig. 5-9 shows, that the coarser grid under-predicts the liquid and gas phase tangential velocities by around 30% (see Figs. 5-9A and 5-9B). An even greater under-prediction (up to 70%) can be observed for the turbulence quantities in Figs. 5-9C and 5-9D. This is due to failure to resolve the

trailing vortex core by a coarser grid with just 6 nodes placed along the impeller blade height. Only a very little difference (less than 5%) between the gas and liquid phase tangential velocities was obtained using the intermediate and the fine grids. Predictions of the turbulence quantities also show less than 10% difference and thus confirming the suitability of the prepared grid to produce a relatively grid independent solution.

Table 5-4: Geometry of the stirred tanks employed for the model validation

Reference	Laakkonen *et al.* (2007a)
$T = H$ (m)	0.26
D (m)	$T/3$
Baffle (m)	$T/10$
Tank type	Flat bottomed
Impeller type	Standard RDT
W (m)	$0.2D$
L_D (m)	$0.25D$
C (m)	$T/3$
Sparger type	Ring
Sparger diameter Ds (m)	$0.8D$
Q_g (m^3/s)	1.6×10^{-4}
Fl_g	0.022
Fr	1.19
Re	85856
N (rpm)	700
N_{CD} (rpm)	548.7
Flow regimes	Fully dispersed
Grid	225k
	Fig. 5-5B
d_{32} for CFD const. d_b (mm)	2.0

Predictions of the gas hold-up and turbulent dissipation rate from the CFD simulation are shown in Figs. 5-7 and 5-10. A fully dispersed flow pattern can be observed with the gas circulating around the lower circulation loop. There are regions of lower gas hold-up near the tank bottom. Experimental observations often made through the tank wall, indicate in this region bubbles to be fairly well dispersed (circulating near the tank bottom). This feature was expected considering $N > N_{CD}$ (estimated using eq.(2.12)) and has been reproduced fairly successfully by the CFD simulation. The gassed power number may be estimated from the torque acting on the impeller and shaft (eq. 3.31) from CFD simulation, whereas the single phase power number may be estimated following Bujalski *et al.* (1987) given by eq.(2.3) described earlier in section 2.7. The relative power number, P_g/P_0, from CFD simulation was 0.42

which is in close agreement to the value estimated using Smith (2006) correlations (eq.(2.5)) of 0.45. Results from the two-way coupling CFD simulations show that at least the general mean flow, gas hold-up and aerated power number were predicted reasonably well and thus the CFD results may be employed as a basis for the multi-compartment modelling. More extensive studies on the gas-liquid mean velocities, turbulence, power number and gas hold-up will be discussed in chapter 6.

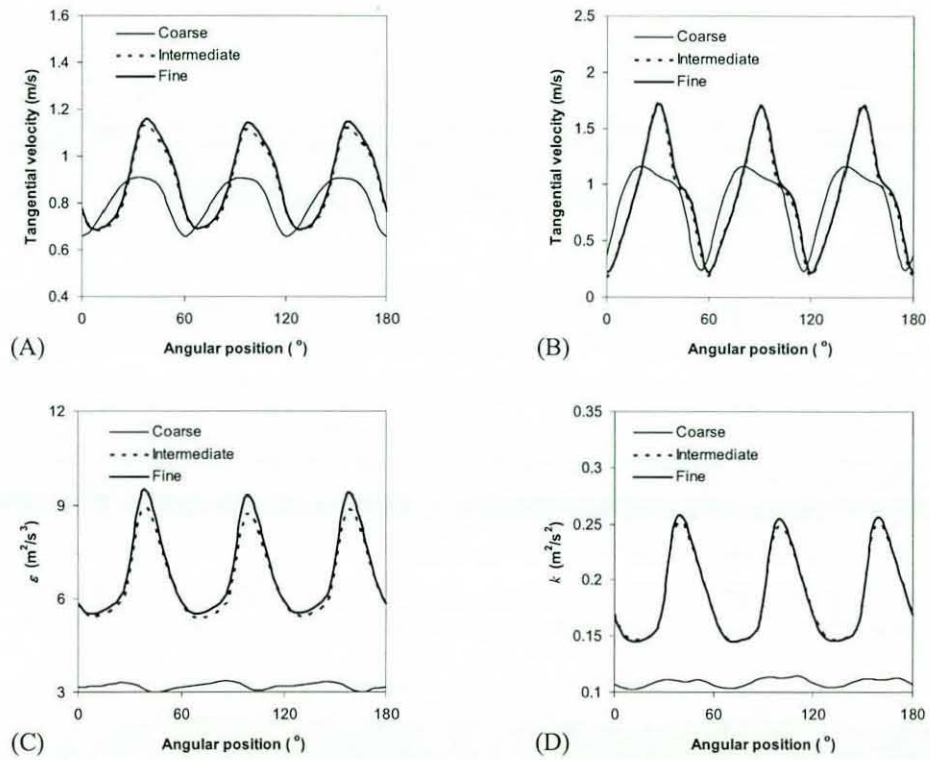

Figure 5-9: Result from grid analysis at z = 0 with respect to the impeller and r/R = 0.37 (N = 513 rpm and Q_g = 0.7 VVM), A) liquid tangential velocity, B) gas tangential velocity, C) ε of the liquid phase, D) k of the liquid phase

5.5.2 Implementation of the multi-compartment model

The simulation result from the grid shown in Fig. 5-6B cannot be used directly for the multi-compartment study because the grid is not separated into a number of compartments. For the purpose of this study, a new mesh of the vessel consisting of 12 compartments was prepared based on the CFD predicted flow patterns. Then the result obtained using the grid shown in Fig. 5-5B was interpolated into the new mesh for easier data interpretation. The compartments were prepared in a way that only one flow direction was allowed at each interface dividing the two compartments. Fig. 5-11A shows the vector

map of the gas flow from CFD simulation which is taken as a basis to construct the compartments in Fig. 5-11B. It can be seen that, the criteria of only one flow direction for each compartment interface was satisfied except for compartments 2 and 3 but manual adjustment were made to satisfy the inter-compartment mass balance. The liquid turbulence dissipation rates and the inter compartment gas flow rates were obtained from averaging the detailed CFD results azimuthally over compartment volumes or areas, respectively. The gas flows between the compartments are obtained by reporting the fluxes (mass flow rate) through each interface in the CFD simulation. The gas flow rates to and from each compartment do not exactly balance (with difference up to 10^{-6} kg/s) possibly due to interpolation error and the fact that the CFD result is obtained from a transient simulation. Therefore, the inter-compartment flows were adjusted (balanced) manually in order to make the multi-compartment model satisfy the gas mass balance exactly. A multi-compartment simulation without balanced inter-compartment flow rates would result in a different distribution of third moments (related to gas hold-up by eq.(5.21)) to those from CFD simulation. It was made clear from the test performed for a single compartment in section 5.4 that the third moments should be preserved, unless there is a change to the local gas-hold up.

Table 5-5: Parameter for the multi-compartment PBM

Compartment	Volume (cm^3)	α_g x 100	ε (m^2/s^3)	Gas flow direction	Gas flow rate (cm^3/s)	Gas flow direction	Gas flow rate (cm^3/s)
1	635.85	7.56	11.35	q_{11to12}	28.08	q_{6to7}	0.00
2	1502.22	1.16	2.57	q_{9to12}	57.78	q_{2to8}	108.48
3	552.35	1.56	0.40	q_{10to11}	25.47	q_{2to9}	46.36
4	394.21	0.07	0.05	q_{8to10}	41.23	q_{8to9}	67.25
5	863.14	0.02	0.12	q_{9to11}	55.83	q_{1to12}	6.21
6	2425.29	0.00	0.05	q_{2to3}	3.33	q_{1to2}	154.84
7	1043.64	1.53	0.06	q_{4to2}	3.33	q_{7to1}	161.05
8	1370.65	1.44	0.29	q_{3to4}	2.92	q_{out12}	92.07
9	977.86	3.92	0.05	q_{3to5}	0.41	q_{out11}	53.22
10	1938.08	0.47	0.06	q_{4to7}	0.00	q_{out10}	15.76
11	1378.62	2.14	0.06	q_{6to4}	0.41	q_{spr}	161.05
12	2427.41	3.72	0.03	q_{5to6}	0.41		

The number density of bubbles in each compartment was determined by the gas hold-up i.e. volume averaged gas hold-up for each compartment. The initial bubble size distributions at each compartment were assumed to follow the

lognormal distribution with a geometric mean diameter of 2 mm and standard deviation of 0.2 mm. Calculation for the bubble number density in each compartment was performed following the method described earlier in section 5.4 using the information of gas hold-up from CFD simulation. The turbulence dissipation rates and inter-compartment gas flow rates are given in Table 5-5.

The sparger is modelled as a constant source of bubbles (a nucleation term) with uniform diameter of 5.5 mm, following the experimental measurements by Laakkonen *et al.* (2007a). The gas flow rate of 1.6×10^{-4} m^3/s (0.7 *VVM*) was set to match Laakkonen's experiment. Table 5.6 shows the rate of the moments introduction in sparger (compartment no. 7) is calculated using the eq.(3.23).

$$S_{\text{sparger},k} = \frac{6 q_{spr} L^{k-3}}{\pi \sqrt{V_7}} \tag{3.23}$$

Table 5-6: Rate of moments introduction at sparger

$S_{\text{sparger},0}$ ($/m^3s$)	1771417.33
$S_{\text{sparger},1}$ (m/m^3s)	9742.80
$S_{\text{sparger},2}$ (m^2/m^3s)	53.59
$S_{\text{sparger},3}$ (m^3/m^3s)	0.29

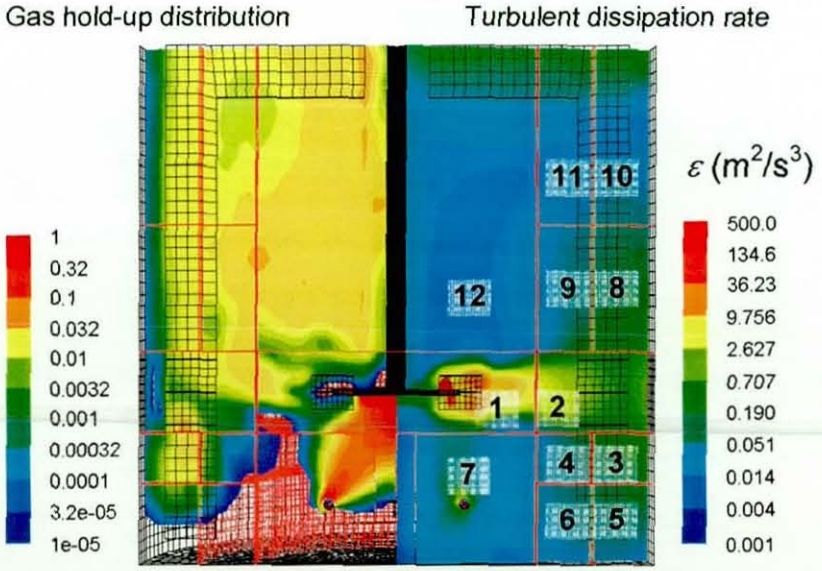

Figure 5-10: Contour of α_g and liquid ε (m^2/s^3) after interpolation to the 12 block mesh, the number at each block represent the compartment number

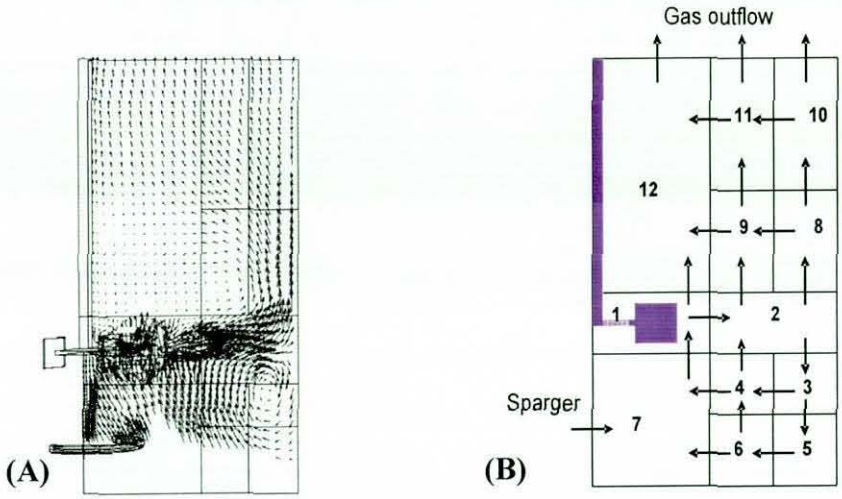

Figure 5-11: A) Gas velocity vector in between two baffles obtained from CFD simulation, B) Compartment connectivity for half of the tank based on inter-compartmental gas flow rate. Symmetry around the impeller axis is assumed.

The gas flow leaving at the top of the tank is also taken into consideration in the multi-compartment model. The flow rate of gas leaving at top liquid surface from CFD simulation is 161.1 cm^3/s is also adjusted to match the gas inflow at the sparger. The multi-compartment model is developed based on the compartmental flow connectivity from CFD simulation shown in Table 5-5 and Fig. 5-11. The multi-compartment moment equations are given as follows:

$$\frac{\partial \mu_{1,k}}{\partial t} = \frac{1}{V_1}\left[\frac{q_{7\text{to}1}\mu_{7,k}}{\alpha_7} - \left(q_{1\text{to}2} + q_{1\text{to}12}\right)\frac{\mu_{1,k}}{\alpha_1}\right] + B - D \tag{5.24}$$

$$\frac{\partial \mu_{2,k}}{\partial t} = \frac{1}{V_2}\left[\frac{q_{1\text{to}2}\mu_{1,k}}{\alpha_1} + \frac{q_{4\text{to}2}\mu_{4,k}}{\alpha_4} - \left(q_{2\text{to}3} + q_{2\text{to}8} + q_{2\text{to}9}\right)\frac{\mu_{2,k}}{\alpha_2}\right] + B - D \tag{5.25}$$

$$\frac{\partial \mu_{3,k}}{\partial t} = \frac{1}{V_3}\left[\frac{q_{2\text{to}3}\mu_{2,k}}{\alpha_2} - \left(q_{3\text{to}4} + q_{3\text{to}5}\right)\frac{\mu_{3,k}}{\alpha_3}\right] + B - D \tag{5.26}$$

$$\frac{\partial \mu_{4,k}}{\partial t} = \frac{1}{V_4}\left[\frac{q_{3\text{to}4}\mu_{3,k}}{\alpha_3} + \frac{q_{6\text{to}4}\mu_{6,k}}{\alpha_6} - \left(q_{4\text{to}2} + q_{4\text{to}7}\right)\frac{\mu_{4,k}}{\alpha_4}\right] + B - D \tag{5.27}$$

$$\frac{\partial \mu_{5,k}}{\partial t} = \frac{1}{V_5}\left[\frac{q_{3\text{to}5}\mu_{3,k}}{\alpha_3} - \frac{q_{5\text{to}6}\mu_{5,k}}{\alpha_5}\right] + B - D \tag{5.28}$$

$$\frac{\partial \mu_{6,k}}{\partial t} = \frac{1}{V_6}\left[\frac{q_{5\text{to}6}\mu_{5,k}}{\alpha_5} - \left(q_{6\text{to}4} + q_{6\text{to}7}\right)\frac{\mu_{6,k}}{\alpha_6}\right] + B - D \tag{5.29}$$

$$\frac{\partial \mu_{7,k}}{\partial t} = \frac{1}{V_7}\left[\frac{q_{6\text{to}7}\mu_{6,k}}{\alpha_6} + \frac{q_{4\text{to}7}\mu_{4,k}}{\alpha_4} - \frac{q_{7\text{to}1}\mu_{7,k}}{\alpha_7}\right] + B - D + S_{\text{sparger},k} \tag{5.30}$$

$$\frac{\partial \mu_{8,k}}{\partial t} = \frac{1}{V_8}\left[\frac{q_{2\text{to}8}\mu_{2,k}}{\alpha_2} - \left(q_{8\text{to}9} + q_{8\text{to}10}\right)\frac{\mu_{8,k}}{\alpha_8}\right] + B - D \tag{5.31}$$

$$\frac{\partial \mu_{9,k}}{\partial t} = \frac{1}{V_9}\left[\frac{q_{2\text{to}9}\mu_{2,k}}{\alpha_2} + \frac{q_{8\text{to}9}\mu_{8,k}}{\alpha_8} - \left(q_{9\text{to}12} + q_{9\text{to}11}\right)\frac{\mu_{9,k}}{\alpha_9}\right] + B - D \tag{5.32}$$

$$\frac{\partial \mu_{10,k}}{\partial t} = \frac{1}{V_{10}}\left[\frac{q_{8\text{to}10}\mu_{8,k}}{\alpha_8} - \left(q_{10\text{to}11} + q_{\text{out}10}\right)\frac{\mu_{10,k}}{\alpha_{10}}\right] + B - D \tag{5.33}$$

$$\frac{\partial \mu_{11,k}}{\partial t} = \frac{1}{V_{11}}\left[\frac{q_{9\text{to}11}\mu_{9,k}}{\alpha_9} + \frac{q_{10\text{to}11}\mu_{10,k}}{\alpha_{10}} - \left(q_{11\text{to}12} + q_{\text{out}11}\right)\frac{\mu_{11,k}}{\alpha_{11}}\right] + B - D \tag{5.34}$$

$$\frac{\partial \mu_{12,k}}{\partial t} = \frac{1}{V_{12}}\left[\frac{q_{11\text{to}12}\mu_{11,k}}{\alpha_{11}} + \frac{q_{9\text{to}12}\mu_{9,k}}{\alpha_9} + \frac{q_{1\text{to}12}\mu_{1,k}}{\alpha_1} - \left(q_{\text{out}12}\right)\frac{\mu_{12,k}}{\alpha_{12}}\right] + B - D \tag{5.35}$$

where B and D are the birth and death due to breakage and coalescence, similar to those in single compartment model; see eq.(5.6). The bubble breakage and coalescence terms were obtained from Prince and Blanch's (1990) model described earlier in section 5.3. The multi-compartment population balance was implemented using the PD-QMOM in MATLAB; the ODE integrations were conducted with absolute and relative tolerances set at 10^{-8} for all solutions. The multi-compartment model represented by eqs. 5.24 to 5.35 was solved using the *ode113* solver in MATLAB. The simulations took about 5 minutes (wall clock) to complete on a GENIE workstation fitted with two dual-core 3.8 GHz Xeon processors and 3 GB RAM.

5.5.3 Prediction of Local Bubble Size

The local bubble Sauter diameter is an important variable as it affects the momentum exchange in the fluid hydrodynamics. The bubble Sauter mean diameter can be obtained from the population balance as the ratio of the third moment to the second moment (μ_3/μ_2). Results from the multi-compartment model are compared to the experimental measurements and CFD-PBM simulations of Laakkonen *et al.* (2007a). The bubble size evolution in each compartment is shown in Fig. 5-12. It shows the steady-state bubble size can be attained within 10 seconds. This is because only the inter-compartmental

moment balances are calculated for this simulation but not the inter-compartmental mass balances, which were already fixed from the CFD simulation. As it was shown earlier for the single compartment study, the steady-state bubble sizes in each compartment can be achieved within a second. However, for the case of multi-compartment PBM, the moment evolution in the neighbouring compartments can affect the evolution of the moments in another compartment, which explains why the bubble size evolution took up to 5 second to achieve a steady-state bubble size for this case.

Fig. 5-13 shows the prediction of the local steady-state bubble size via the multi-compartment population balance model. The results show some qualitative agreement to Laakkonen *et al.*'s experimental data and CFD-PBM simulation. There are discrepancies on bubble size prediction in some compartments, e.g. no. 3, where d_{32} is slightly larger than the value measured by Laakkonen *et al.* (2007a). Predictions of the multi-compartment model in this work were also in fair agreement to the CFD-PBM predictions from Laakkonen *et al.* (2007a). Mainly the discrepancy occurs in the lower circulation loop where d_{32} is over-predicted by the current model. This may be due to the small uniform bubble size (2 mm throughout the tank) employed for the initial CFD simulation which led to a higher gas hold-up around the lower circulation loop than would be obtained in reality. It can be observed from the Fig. 5-13 that the assumption of bubble size around 2 mm is only valid around the impeller and to some extent in the upper circulation loop but certainly not for lower circulation loop. It was found from the single compartment study in section 5.4 that higher gas hold-up led to a larger bubble size especially in regions of lower turbulence dissipation rate. Nevertheless the multi-compartment simulation has successfully reproduced the correct distribution of local bubble size inside the tank with the smallest bubble around the impeller region and the largest in the bulk flow of the upper circulation loop. The former is due to a higher turbulence dissipation rate around the impeller region (see Table 5-5). This finding is in agreement with the experimental measurements by Barigou and Greaves (1992) and Laakkonen *et al.* (2005b) who also observed a smaller bubble size around the impeller region.

There is also a concern about the CFD simulation as it was performed using a constant bubble size assumption. Such an assumption is certainly not valid in a

stirred tank where the turbulence dissipation rate gradient is very high especially around the impeller region. The mean bubble size should be significantly smaller around the impeller region compared to the bulk region, as evidenced in the multi-compartment results. The bubble size can affect the prediction of turbulent flows, gas void fraction and the gas flow rate which is required for the multi-compartment modelling. Therefore, the error from the original CFD simulation can severely affect the results of the multi-compartment modelling. This issue will be addressed in the next chapter 6, where the population balance is implemented as a UDF in a CFD simulation, so that four-way coupling can be achieved. The aim is to solve the CFD with PBM together, and thus the problem of an assumed uniform bubble size can be eliminated. Nevertheless, the multi-compartment model is capable of yielding a reasonably accurate prediction of the local bubble size, despite all its simplifications.

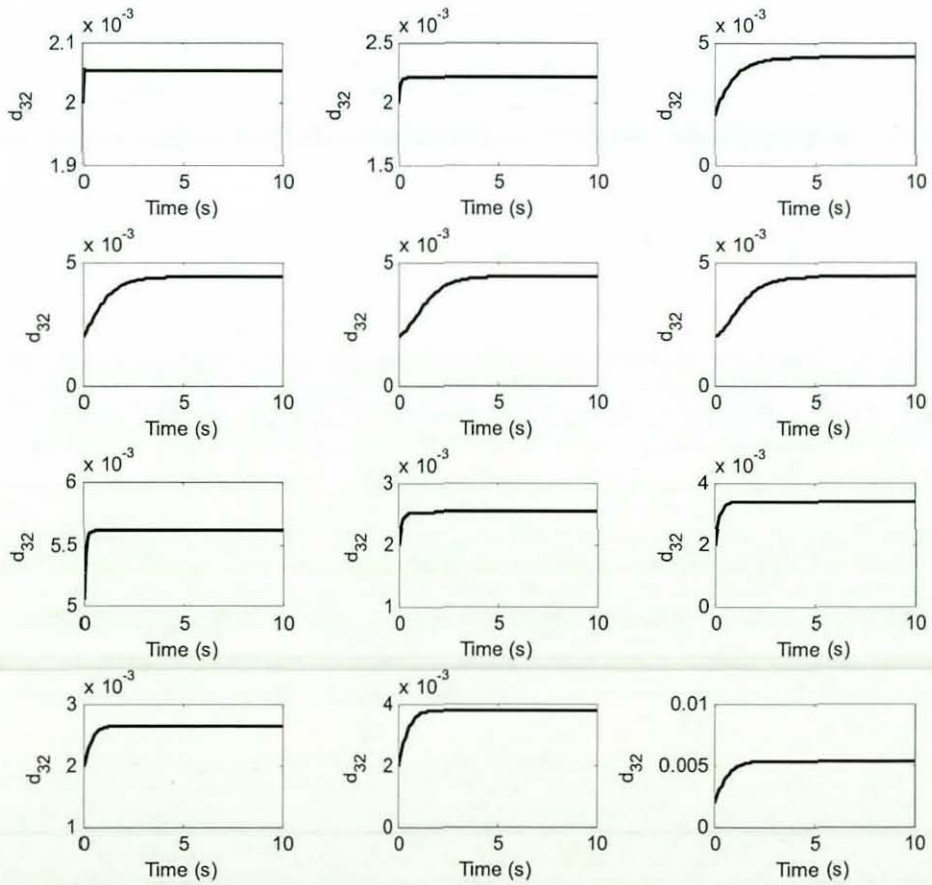

Figure 5-12: Evolution of the Sauter mean bubble size d_{32} (m) at each compartment

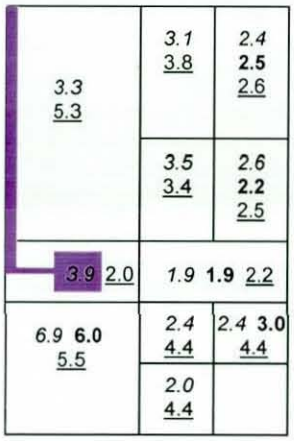

Figure 5-13: Prediction of local bubble size (d_{32}) italic font (CFD-PBM MUSIG Laakkonen *et al.*, 2007a), bold font (Laakkonen *et al.* (2007a) experiment), underlined font (this work)

The gas hold-up is one of the important mass transfer parameters in gas-liquid stirred tanks. The gas hold-up in each compartment is related to the third moment and may be estimated using eq.(5.21). The gas hold-up obtained from multi-compartment PBM is compared to the result from CFD simulation in Table 5-7. The prediction shows an excellent agreement between the multi-compartment model and the CFD predictions which means that the third moment is perfectly conserved during the simulation, further confirming the correct implementation of the multi-compartment model.

Table 5-7: Comparison between the gas hold-up from CFD simulation and the value obtained from multi-compartment simulation

Compartment	Multi-compartment $\alpha_g = \pi\mu_3/6$ x 100	CFD simulation α_g x 100
1	7.56	7.56
2	1.16	1.16
3	1.56	1.56
4	0.07	0.07
5	0.02	0.02
6	0.00	0.00
7	1.53	1.53
8	1.44	1.44
9	3.92	3.92
10	0.47	0.47
11	2.14	2.14
12	3.72	3.72

5.6 Summary

A test using a single compartment model has demonstrated the capability of the PD-QMOM algorithm, with realistic breakage and coalescence kernels, to predict the bubble size evolution in a homogeneous gas-liquid flow. The prediction from the single compartment population balance model shows a reasonable agreement with the Sauter mean bubble sizes obtained from empirical correlations. The algorithm also responded well to changes in the turbulence dissipation rate and the initial bubble size distribution. The results suggest that the final bubble size is only affected by the turbulence dissipation rate and local gas hold-up, but is not affected by the initial bubble size.

The single compartment population balance is used as a basis for the multi-compartment model development. The local turbulence dissipation rate and gas flow rates were obtained from a two-phase CFD simulation due to lack of experimental data. Despite the uniform bubble size assumption for the CFD simulation, the multi-compartment population balance model still yielded a reasonable prediction of the local bubble size compared to the experimental measurement by Laakkonen *et al.* (2007a). However, there were some discrepancies in the bubble size prediction in some compartments which might have resulted from the uniform bubble size assumption in CFD simulation which affected prediction of the gas hold-up. Further refinement of the compartmental procedure may be necessary to obtain a better prediction of the local bubble sizes. The issue related to bubble-hydrodynamics coupling will be addressed in the next chapter, where the four-way coupling CFD-PBM is employed.

6 CFD AND POPULATION BALANCE MODELLING OF GAS-LIQUID STIRRED TANKS

6.1 Overview

A combined computational fluid dynamics and population balance model (PBM) approach has been applied to simulate gas-liquid stirred tanks agitated by a Rushton turbine and CD-6. The multiphase simulations were realised via an Eulerian-Eulerian two-fluid model and the drag coefficient of spherical and distorted bubbles was modelled using the Ishii-Zuber equations. The effect of the void fraction on the drag coefficient was modelled using the correlation by Behzadi *et al.* (2004). The local bubble size distribution was obtained by solving the PBM using the quadrature method of moments. The local volumetric mass transfer coefficient, k_La, was estimated using both the Higbie penetration theory and the surface renewal model. Results from the CFD-PBM simulation were compared against experimental measurements from the literature and also with the CFD simulations solved using a monodispersed bubble size. After validation, the model was then used to evaluate the effect of scale-up of the mass transfer rate in a gas-liquid stirred tank agitated either by a Rushton turbine or CD-6 impeller.

6.2 Introduction

There are many industrial processes that involve gas-liquid dispersion in stirred tanks, *e.g.* in fine-chemicals manufacturing, or in biochemical fermentations. For economic and safety reasons, reliable models are needed for the scale-up and design of such reactors. One of the most important problems in modelling gas-liquid dispersions is the prediction of bubble size and volumetric mass transfer coefficient. Bubbles in gas-liquid stirred tanks may experience coalescence and breakage depending on the local turbulent dissipation rate (related to the agitation speed) and gas hold-up (related to the aeration rate). Equilibrium of these breakage and coalescence events determines the bubble sizes and thus the gas-liquid interfacial area. Therefore, poor predictions of the bubble sizes may result in a poor prediction of the mass transfer rate. As shown experimentally by many researchers (*e.g.* Montante *et al.*, 2008; Barigou and

Greaves, 1992; Laakkonen *et al.* 2005b; 2007a) the distribution of bubble sizes varies inside the stirred tank depending on the spatial position. Generally, bubble sizes around the impeller discharge stream are the smallest, due to breakage caused by high local energy dissipation rates. Furthermore, knowledge of bubble sizes is necessary in a two-phase CFD model to calculate momentum exchange by, for example drag. Hence, the population balance, phase continuity and momentum equations are coupled and in principle should be solved simultaneously. In addition, local bubble sizes and the local gas volume fraction are required for the calculation of the interfacial area, which is an important variable in designing an aerated stirred tank to achieve a required rate of gas-liquid mass transfer.

Many modelling studies on gas-liquid stirred tanks have been performed in recent years, mostly using a uniform, mono-dispersed bubble size throughout the tank (e.g. Khopkar and Ranade, 2006; Sun *et al.*, 2005; Wang *et al.*, 2006; Morud and Hjertager, 1996; Deen *et al.*, 2002; Scargiali *et al.*, 2007). Generally, the CFD predictions of gas hold-up and mean velocities are in fair agreement with experimental data, except around the impeller discharge stream. Previous studies have applied a variety of methods to improve the predictions with uniform bubble sizes, such as grid refinement, different drag laws and various turbulence models, but without complete success. Deen *et al.* (2001) evaluated the effects of different drag laws and grid refinement and found good predictions of the mean radial velocity, but poor predictions of the gas axial velocity. Others, such as Sun *et al.* (2005) and Wang *et al.* (2006), employed a k-ε-Ap turbulence model without complete success in predicting the two-phase flow. The k-ε-Ap model differs from the ordinary k-ε model because it has an additional algebraic term for the gas turbulent viscosity from Hinze and Tchen (Hinze, 1956). Scargiali *et al.* (2007) studied the influence of the turbulent dispersion force, virtual mass, grid refinement and the prescribed bubble size on the holdup in a gas-liquid flow. They concluded that the grid size may significantly affect the prediction, but the effects of the turbulent dispersion force and virtual mass were not very significant in determining the distribution of gas holdup. Khopkar and Ranade (2006) studied a gas-liquid stirred tank operating in different flow regimes and obtained reasonable prediction of the gas hold-up and gassed

power number, but only by employing the turbulent drag correlations by Brucato *et al.* (1998): their work showed over-prediction of gas hold-ups around the lower and upper circulation loop, especially near the top liquid surface (see Fig. 6-1). Further discussion regarding the effect of turbulent flow on the drag coefficient is given in the following section 5.3.1.

Whereas it is possible to predict correctly the mean flow field in a single phase stirred tank using any RANS based turbulence model (as was shown earlier in section 3.5.1), this performance has not yet been replicated for gas-liquid stirred tanks. The common practice of employing a uniform bubble size throughout the tanks is suspected to be the main reason for the poor prediction of two-phase flows in stirred tanks. Of course, other factors such as the drag model for distorted and dense bubbles, turbulent drag laws, lift and other forces also cannot be ruled out. However, their effects appear to be secondary compared to that of an assumed uniform bubble size, due to the predominant momentum exchange mechanism of inter-phase drag coefficient, which directly affects the prediction of the local mean velocities and gas hold-up.

The simplest method of predicting the local bubble size was to implement a correlation, e.g. by Calderbank (1958) in eq.(2.17), within the CFD code utilising the local turbulent dissipation rate and local gas hold-up. Recently, this method has been employed by Zhang *et al.* (2008) combined with LES. They did not show an excellent prediction of the liquid mean velocities and local gas hold-up despite employing a LES. In fact, such method is rather a crude way of predicting the local bubble size since the original correlation has been developed assuming tank-averaged quantities: i.e. the overall hold-up, mean d_{32} and power per unit volume. The probability and rate of bubble-bubble and bubble-eddy collisions are also not considered in this method.

Another method to predict the local bubble sizes was performed using the population bubble density model (BDM) and a one-way coupled approach, *e.g.* as in the model of Bakker and Van den Akker (1994a). In recent years, a coupled CFD-BDM has been employed to predict the local bubble size in gas-liquid stirred tanks by Lane *et al.* (2002, 2005), Kerdouss *et al.* (2006) and Moilanen *et al.* (2008). In most cases, the BDM is reported to give a satisfactory

prediction of the local bubble size, but only by adjusting some of the empirical constants within the model. This practice is thought to be inappropriate because the model is unlikely to be fully predictive and hence cannot be applied to cases where experimental data are not available. Lane *et al.* (2005), for example, introduced a correction factor of up to 3.5 for the turbulence dissipation rate, whilst Kerdouss *et al.* (2006) adjusted constants in the breakage and coalescence term in order to get good agreement with measurements reported by Alves *et al.* (2002). Lane *et al.* (2005) argue correctly that the turbulence dissipation rate is not predicted well by the RANS k-ε turbulence model. However, the correction factor that was applied is too large, considering the under-prediction of the turbulence dissipation rate by k-ε model is only around 30% (Ducoste and Clark, 1999). The k-ε model was also shown to give a reasonable prediction of the turbulent dissipation rate in the immediate vicinity of the impeller blade in section 3.5.1 (see Fig. 3-8). The formulation of the BDM itself is also questionable, since proper bubble breakage and coalescence kernels are not included. Instead all equations related to the bubble size are lumped together as a function of the critical Weber number and energy dissipation rate, without considering the probability and rate of bubble-bubble and bubble-eddy collisions. As a consequence, the BDM is not thought to be a fully predictive model for simulation of gas-liquid dispersions in stirred vessels.

A full PBM has been employed to predict the local bubble size in stirred tanks, mostly using a discretisation based on the method of classes (MOC). Venneker *et al.* (2001) performed a one-way coupled PBM via the MOC for a stirred tank bioreactor. Recently, a coupled CFD-PBM simulation using the MOC also has been performed by Montante *et al.* (2008), Moilanen *et al.* (2008) and Kerdouss *et al.* (2008). A comparison between the local bubble sizes predicted using the BDM and MOC by Moilanen *et al.* (2008) show a good agreement with their experimental measurements, but only by introducing some adjustable constants to the breakage and coalescence kernels. These authors generally show reasonable agreement for the predicted and measured local bubble size, but only by adjusting some of the model constants within the breakage and coalescence kernels. A fully predictive model should not require the tuning of model parameters for each case considered. A downside of the MOC is its

computational demand, since it often requires more than 30 classes to get a good level of accuracy in the prediction of the evolution of the moments of the bubble size distribution.

The quadrature method of moments (QMOM) is based on solving equations for the moments of the bubble size distribution; the quadrature approximation overcomes the difficulties in obtaining a closed form solution for the population balance equations involving breakage and coalescence. Details of the QMOM were discussed previously in section 4.3. The QMOM requires considerably less computational effort than the MOC and also is capable of providing an accurate prediction of the moments with a relatively small number of quadrature points. Hence it is suitable for coupling with CFD simulations of the two-phase hydrodynamics. The QMOM has been applied previously to breakage and aggregation problems in a pseudo-homogeneous single phase flow (*e.g.* Marchisio *et al.*, 2003). Recently, Petitti *et al.* (2007) have employed the QMOM to solve the bubble dynamics for a gas-liquid dispersion in a stirred tank. In their work, bubble coalescence is not considered and only a simple breakage kernel is employed, instead of one based on the physics of bubble breakup. No comparisons with experimental measurement were presented by Petitti *et al.* (2007). In the interest of reduced computational effort, the QMOM method was selected to solve the population balance equation for bubble dynamics in aerated stirred tanks in this work.

This chapter focuses on the development of a modelling approach for gas-liquid stirred tanks. For an initial comparison, the CFD simulation was performed assuming a constant bubble size throughout the tank. A coupled CFD-PBM was then performed to account for the spatially non-uniform bubble sizes inside the tank. The CFD prediction of the two-phase flow field was compared to experiments by Deen (2001), whereas the results using the CFD-PBM approach were compared against measurements by Laakkonen *et al.* (2007a and b). Predictions of the local gas hold-up were compared to experimental measurements by Bombac *et al.* (1997). A discussion of the experimental measurements used by these workers was previously presented in section 2.5. Finally, the influence of scale-up to the mass transfer in gas-liquid stirred tank agitated by either a Rushton turbine or a CD-6 impeller is carried out.

6.3 Modelling Approach for Gas-Liquid Stirred Tanks

6.3.1 CFD modelling of two-phase flow

The gas-liquid stirred tank simulation is performed using the Eulerian-Eulerian approach described earlier in chapter 5. However, unlike the standard FLUENT model used for the previous chapter, modifications were made to the drag model, besides having the PBM implemented within FLUENT, thus enabling a four-way coupled simulation.

The drag model employed has a significant effect on the flow field of the aerated flow, as it is related directly to the bubble terminal rise velocity. Bubbles have a tendency to form a non-spherical shape, especially those with a diameter > 3 mm. Therefore, the drag model of Ishii and Zuber (1979) was selected in this work, as it takes into account the drag of distorted bubbles:

$$C_D = \max\left(\frac{24}{\mathrm{Re}_b}\left(1+0.15\,\mathrm{Re}_b^{0.687}\right),\ \min\left(\frac{2}{3}\sqrt{E_O},8/3\right)\right) \tag{6.1}$$

where the $Re_b = \rho u_{slip} d_b/\mu$ and $E_O = g\Delta\rho d_b^2/\sigma$ are the bubble Reynolds number and Eotvos number, respectively. The slip velocity, u_{slip}, is given by:

$$u_{slip} = \left|\vec{u}_g - \vec{u}_l\right| \tag{6.2}$$

The drag for the ellipsoidal bubble regime is dependent on the bubble shape through the Eotvos number, which represents the ratio of gravitational to surface tension forces; for the spherical cap regime the drag coefficient is approximately 8/3. The cap regime may not be a significant issue in gas-liquid stirred tanks at lower aeration rates, operating under fully dispersed or loaded regimes. However, the Ishii and Zuber drag model was implemented without any changes; the cap-regime equation will not be activated unless the bubble size becomes larger than 10.9 mm in air-water system. The effect of the local bubble volume fraction on the drag coefficient was estimated using Behzadi *et al.*'s (2003) correlation as follows:

$$C_{D,dense} = C_D\left(e^{3.64\alpha} + \alpha^{0.864}\right) \tag{6.3}$$

where C_D is the drag coefficient for an isolated bubble estimated using eq.(6.1), whereas $C_{D,dense}$ is for the dense dispersion of bubbles. The drag model

described above is not available as a standard option in FLUENT and hence it has been implemented via a user-defined subroutine.

Turbulent flow is known to affect the drag of the particles in solid-liquid flow in stirred tanks, from the experimental observations by Schwartzberg and Treybal (1968), who measured the particle velocities in baffled stirred tanks using streak photography. They observed a reduction in particle settling velocity by 30 to 50% compared to their observations made in a stagnant liquid. A similar finding was also reported by Nienow and Bartlett (1974), who measured the settling velocities of 2.3 mm NaCl particles in a stirred vessel also via streak photography. Further work by Kuboi *et al.* (1974) using a high-speed cine-photography technique, Nouri and Whitelaw (1992) using a LDA and Brucato *et al.* (1998) using a pair of photo-diodes and laser beams, also reported similar findings -- increases in drag coefficient for particles under turbulent flow. Unfortunately, there is no published work related to the influence of turbulence on the bubble drag in gas-liquid flows.

Several authors e.g. Khopkar and Ranade (2006) and Lane *et al.* (2002) employed the drag correction model for particles moving through turbulent flow by Brucato *et al.* (1998) for gas-liquid stirred tank simulation. Brucato *et al.* (1998) proposed a drag correction for particles in turbulent flow as a function of the volume average value of the bubble size and the Kolmogorov microscale. Brucato *et al.*'s (1998) correlation may not be applicable to gas-liquid stirred tanks; furthermore the Kolmogorov microscale in a stirred tank is not uniform in space, unlike the Taylor-Couette flow for which the correlation was originally derived. Moreover, Brucato *et al.*'s correlation was developed for a solid-liquid flow rather than a bubbly flow. Both Khopkar and Ranade (2006) and Lane *et al.* (2005) reported a fair prediction of the local gas hold-up despite a constant bubble size employed throughout the tank by Khopkar and Ranade (2006). It is not known if the Brucato *et al.*'s correlation is responsible to the over-prediction (by 30 to 50%) of gas hold-ups around the upper circulation loops in Khopkar and Ranade's (2006) work (see Fig. 6-1). Lane *et al.* (2002) also concluded the pattern of predicted gas hold-up is not correct when Brucato *et al.*'s correlation is employed; too high a gas hold-up is obtained within the lower circulation loop. Therefore, the drag correction due to turbulent flow has not been included in

this work, due to lack of reliable data and correlations available from the literature.

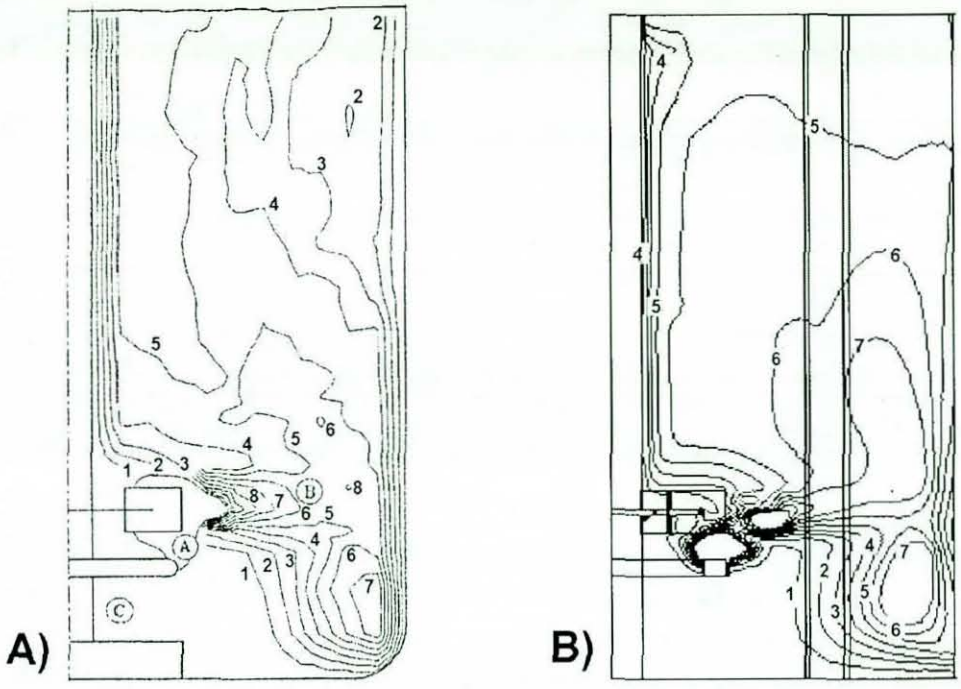

Figure 6-1: Distribution of the local gas hold-up (%) 12° behind the baffle, A) Experimental measurements by Bombac *et al.* (1997), B) Prediction by Khopkar and Ranade (2006)

It is also important to consider the formation of the gas cavities behind the impeller blades. According to Lane *et al.* (2005), it is possible to model the gas cavity in the Eulerian-Eulerian framework, providing a certain modification is made to the interphase exchange coefficient: the drag coefficient is set to turn into that for isolated bubble when the void fraction is greater than 0.7, *i.e.* the cavity behind the blade behaves in a manner similar to an isolated bubble, rather than the dense bubble case. An attempt to implement the dense drag bubble model within the cavity region has been tested, resulting in the disappearance of the bubble cavity behind the blade (see Fig. 6-2) and an over-prediction of the relative gassed power number by more than 20% from 0.45 (from Smith's (2006) correlation) to 0.55. Significant increases in the radial velocity were also observed (see Fig. 6-2B). However, this issue has been successfully addressed by disabling the dense drag model around the cavity i.e. setting the model to calculate the drag for isolated bubble when the local volume fraction exceeded 0.7.

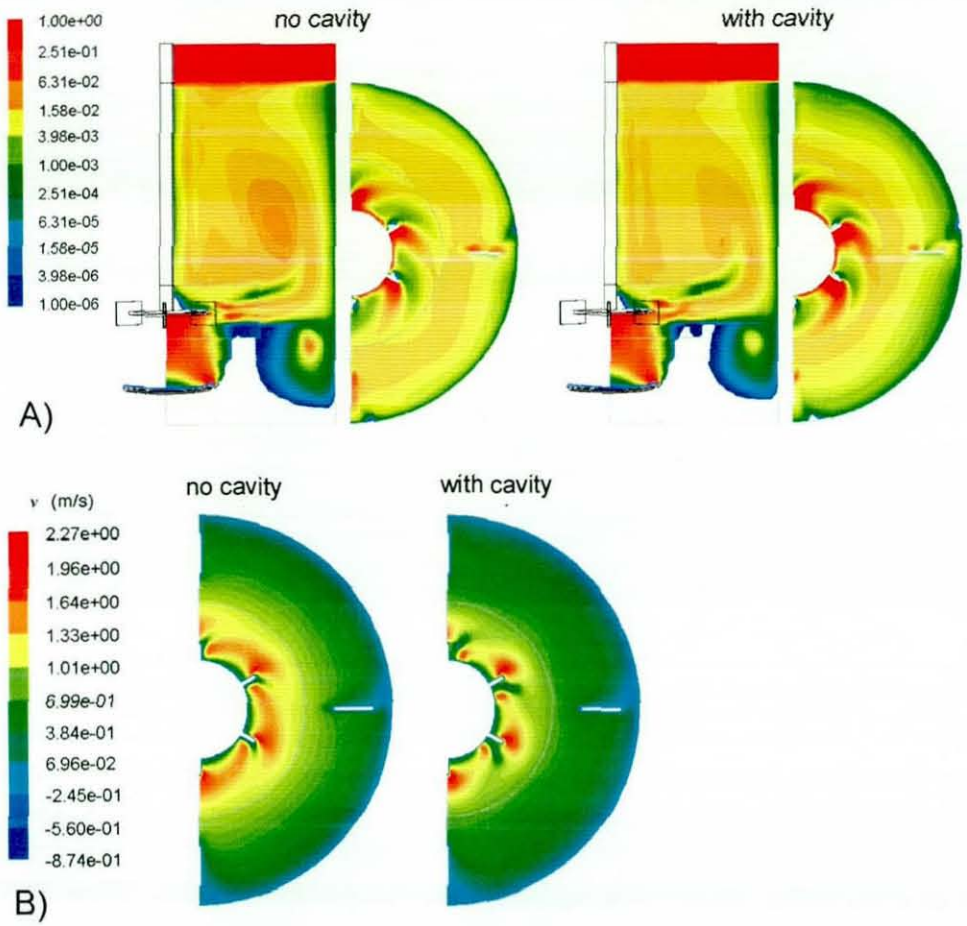

Figure 6-2: Effect of the cavity model, no cavity employed the dense drag law whereas with cavity used an isolated bubble drag model for α > 0.7, A) instantaneous gas hold-up at impeller level and at 30° mid way between two baffles, B) radial velocity at impeller level

6.3.2 Modelling of turbulence

The turbulence modelling uses the two-phase realizable k–ε model, in which both k and ε are allowed to have different values for each phase. The transport equations for the two-phase k-ε model are given in the Fluent manual (2005) and the standard values (similar to the one in section 3.4.2) of the model parameters have been applied. The realizable k-ε is considered to be a better model than the standard k-ε for stirred tank flows (Fluent, 2005), as it better accounts for flow features such as strong streamline curvature, vortices and rotation. Detailed comparisons on the performance of the realizable k-ε and the standard k-ε model in predicting the fluid flow in a stirred tank have been presented previously in section 3.5. Both the realizable k-ε and the standard k-ε model predict the mean flow field excellently, but the realizable k-ε gives a

slightly better prediction of the turbulence quantities than the standard k-ε model. The realizable k-ε differs from the standard k-ε model in two important ways: first it has a new formulation of the turbulent viscosity and second it employs a new transport equation for the dissipation rate incorporating different model constants. Details about this model were given in section 3.4.2.

6.3.3 Modelling of bubble breakage and coalescence

The QMOM is employed to solve the PBM and predict the evolution of the moments of the bubble size distribution. Full details of the QMOM were elaborated earlier in section 4.3 whereas the breakage and coalescence is described in section 5.3.3. An earlier assessment in section 5.4 shows only a mere 0.6% relative difference between the result obtained using two and five quadrature points despite over 2000% increase in CPU time. Therefore, a QMOM based on two quadrature points was applied for the CFD-PBM simulations to minimise computational cost.

The population balance model was solved using user-defined scalars to represent the moments, weights and abscissas and was implemented in FLUENT via a user-defined subroutine. The transport equation for a scalar, ϕ, in multiphase flow is given by:

$$\frac{\partial \alpha_g \rho_g \phi_{g,k}}{\partial t} + \nabla \cdot \left(\alpha_g \rho_g \vec{u}_g \phi_{g,k} - \alpha_g \Gamma_{g,k} \nabla \phi_{g,k} \right) = B_{g,k} - D_{g,k} + S_{g,k} \tag{6.4}$$

where $B_{g,k}$ and $D_{g,k}$ are the birth and death terms for bubble breakage and coalescence. All the breakage and coalescence kernels (see section 5.3.3) were implemented without adjusting any of the model constants. The $S_{g,k}$ term accounts for a bubble source in the system, i.e. the sparger. $B_{g,k}$, $D_{g,k}$ and $S_{g,k}$ have units consistent with the moments. The sparger is treated as a constant source of fresh bubbles. In this work, the sparger is assumed to produce continuously bubbles of size of 2 mm by fixing the moments at the sparger boundary. The scalars are per unit mass of phase g (air) whereas moments are per unit volume of dispersion. Thus the scalars have to be multiplied with the air density and local gas hold-up in order to make the units consistent. Large difference in the order of magnitude between the zeroth (10^8 m^{-3}) and the third (10^0 m^3/m^3) moments also cause a numerical difficulty within the FLUENT

solver. This problem has been overcame by making the scalars have almost similar order of magnitude (i.e. by multiplying by fixed number i.e. 10^{-3} for the μ_0 and 10^4 for the μ_3) before they are passed into the FLUENT solver; the same correction is applied again (dividing the scalars with the similar value used earlier) before the scalars are passed into the product difference algorithm to cancel the earlier correction. The corrections are necessary because the product difference algorithm only works with the actual moments. The user-defined subroutine was compiled within the commercial CFD code, FLUENT 6.3 and was available as an add-on program after the compilation; hence a fully coupled CFD-PBM simulation could be performed.

6.3.4 Modelling of k_La and oxygen transfer rate

Many empirical scale-up rules and correlations have been developed to calculate the volumetric mass transfer coefficient, k_La, in aerated stirred tanks. However, the vast majority of the existing correlations are only capable of calculating the average k_La value in the tank and not the local values. Information about the local k_La is important in the study of gas-liquid stirred tanks to identify the occurrence of 'dead zones', where very little mass transfer occurs. These dead zones are unwanted in aerobic bioreactors because the micro-organism needs dissolved oxygen for respiration and for production of the desired product. Lack of dissolved oxygen may reduce the yield of the desired product; for example yeast is more likely to produce vinegar under aerobic conditions, whilst producing alcohol in anaerobic condition. Ideally, achieving a uniform k_La and uniform driving force is desirable during scale-up of aerated stirred tanks. Whilst this maybe the case for laboratory scale stirred tanks, it is not always true for larger scale tanks, which can suffer from zones of oxygen depletion, particularly where there is an oxygen sink, *e.g.* through chemical reaction.

Assuming a spherical bubble shape, the local interfacial area per unit volume may be calculated from

$$a = \sum_i \pi L_i^2 w_i \tag{6.5}$$

where L_i is the bubble size and w_i is number of bubbles of size L_i per unit volume of dispersion. The bubble sizes and numbers of bubble used in the

calculation of the interfacial area were obtained from the CFD-PBM simulation, directly from the weights and abscissas used in the QMOM. Bubbles with diameters greater than around 3 mm (for air-water) are ellipsoidal with an aspect ratio (ratio of the major to minor axis of an oblate spheroid) which may be calculated as a function of the Eotvos number from the correlation of Wellek *et al.* (1966)

$$R = 1 + 0.163E_O^{0.757} \tag{6.6}$$

which was developed originally for liquid–liquid dispersions. Guet *et al.* (2005) compared eq.(6.6) with their experimental measurements obtained using a four-point optical fibre probe and reported that Wellek *et al.*'s (1996) correlation is also applicable for bubbles. In this work the interfacial area for small bubble (L_i ≤ 1 mm) was estimated from eq.(6.5), whilst bigger bubbles (L_i > 1 mm) were assumed to be oblate spheroids and their surface area was calculated using R from eq.(6.6). Bubbles smaller than one millimetre were modelled as a sphere because they are more likely to form spherical shape (Montante *et al.*, 2006). The bubble diameter, L_i, obtained from QMOM is assumed to be an equivalent diameter of an oblate spheroid with major and minor axis of r_1 and r_2, respectively.

$$L_i = 2\left(r_1^2 r_2\right)^{1/3} \tag{6.7}$$

The surface volume of the oblate may be calculated from:

$$S = 2\pi r_1^2 + \pi \frac{r_2^2}{e} \ln\left(\frac{1+e}{1-e}\right) \tag{6.8}$$

where the e is the eccentricity of the oblate calculated from the following relations.

$$e = \sqrt{1 - \frac{r_2^2}{r_1^2}} \tag{6.9}$$

Even larger bubbles (L_i > 5 mm) may not form perfect oblate ellipsoids in turbulent flow, but nonetheless, eq.(6.6) is a step towards improved bubble shape prediction.

Higbie's (1935) penetration theory results in an average mass transfer coefficient for each bubble size given by:

$$k_{L,i} = \frac{2}{\sqrt{\pi}}\sqrt{\frac{D_l u_{slip}}{L_i}} \tag{6.10}$$

where u_{slip} and are the bubble slip velocity and diffusion coefficient, respectively. Higbie's model assumes a constant contact time between fluid element and the bubble interface which is characterised by the L_i/u_{slip}. The slip velocity can be obtained from the difference in phase velocities from an Eulerian-Eulerian two-fluid CFD simulation. Thus local values of k_La were calculated from:

$$k_L a = 2\left(\pi D_l u_{slip}\right)^{0.5} \sum_i L_i^{1.5} w_i \tag{6.11}$$

Danckwerts (1951) suggested a refinement of the penetration model by assuming that k_L is related to the average surface renewal rate resulting from exposure of the bubble interface to turbulent eddies with a variable contact time. Danckwerts formulated the surface renewal model as follows:

$$k_L = \sqrt{D_l s} \tag{6.12}$$

where s is the fractional rate of surface-element replacement. Lamont and Scott (1970) assumed that the small scale turbulent motion, which extends from smallest viscous motion to inertial ones, affects the rate of mass transfer. Consequently, s can be calculated using Kolmogorov's theory of isotropic turbulence. They suggested the eddy cell model as follows:

$$k_L = K D_l^{0.5}\left(\frac{\varepsilon_l}{\nu_l}\right)^{0.25} \tag{6.13}$$

where ε_l is the turbulence dissipation rate in the liquid phase, ν_l is the liquid dynamic viscosity and K = 0.4 is the model constant. Combining k_L and a gives another equation for calculating the volumetric mass transfer coefficient:

$$k_L a = K\pi D_l^{0.5}\left(\frac{\varepsilon_l}{\nu_l}\right)^{0.25} \sum_i L_i^2 w_i \tag{6.14}$$

The local oxygen transfer rate (per unit volume) can be estimated from the following relations once the local k_La has been determined,

$$N_o = k_L a(C_o^* - C_o) - r_o \tag{6.15}$$

where C_o^* is the oxygen solubility in the liquid phase, C_o is the oxygen concentration in the liquid phase and r_o is the specific oxygen consumption rate. The transport equation for dissolved oxygen mass fraction was also solved as a

user-defined scalar implemented within a user-defined subroutine, with the sink terms given in the right hand side of eq.(6.15) above. The transport equation for oxygen transfer rate is given as follow:

$$\frac{\partial \alpha_l \rho_l \phi_l}{\partial t} + \nabla \cdot \left(\alpha_l \rho_l \vec{u}_l \phi_l - \alpha_l \Gamma_l \nabla \phi_l\right) = \alpha_l \left(k_L a \left(C_o^* - \rho_l \phi_l\right) - r_o\right) \qquad (6.16)$$

6.3.5 Tank Geometry and Modelling Strategy

Four scales of aerated stirred tanks containing a Rushton turbine, with operating volumes of 8.6L, 14L, 152L and 200L, studied by Deen (2001), Bombac *et al.* (1997), Laakkonen *et al.* (2007a) and Laakkonen *et al.* (2007b) were considered for the initial model validation. One of the cases considered in this chapter (case 6.2) is the same as the one used in the previous chapter (section 5.5.1), but a four-way coupling simulation is performed in this chapter instead of two-way coupling in the previous chapter. Tank with operating volumes up to 1500L were also evaluated for the scale-up studies. Apart from the Rushton turbine, simulation using a CD-6 impeller was also performed for three different tanks size i.e. 14L, 200L and 1500L mainly for the scale-up study. The CD-6 is a concave impeller produced commercially by Chemineer and has been extensively studied experimentally by many researchers *e.g.* Myers et al. (1999); Smith *et al.* (2001); Paglianti *et al.* (2008). A brief description about the CD-6 impeller is also given in chapter 2 (see section 2.4). Detailed dimensions of each case considered in this chapter are given in Tables 6-1 and 6-2. All cases considered in this chapter operate either in the fully dispersed regimes or loaded regimes (see Figs. 6-4 to 6-6). These two regimes are relevant to a better gas dispersion in gas-liquid stirred tanks and thus better mass transfer. Details about the flow regimes transition have been discussed earlier in section 2.7. Case 6.4 shown in Fig. 6-4 falls just below the fully dispersed regime line, but according to Bombac *et al.*'s (1997) experiment the vessel is indeed operating in the fully dispersed regime. This is due to the location and size of sparger employed by Bombac *et al.* (1997), which is very close to the impeller and has a diameter equal to the impeller. This arrangement is favourable for immediate gas dispersion by the impeller. Effects of the impeller dimension and position to the gas-liquid flow in stirred tank have been described earlier in section 2.3.

The boundary conditions were set similar the ones described earlier in section 5.5.1 (see Fig. 5-6). Following the grid analysis performed in the previous chapter, all grids prepared in this chapter were set to have around 225k to 267k for the smaller tanks (8.6L to 200L) and up to 311k for the bigger tanks (1500L). A minimum of 11 nodes were placed along the impeller blade height for Rushton turbine which is critical to resolve the highly turbulent region around the impeller. A much higher grid density was employed for the CD-6 impeller (up to 18 nodes at impeller blade height) due to the impeller surface curvature. All simulations were performed using a half-tank grid made of 100% hexahedral elements which is desired for a better prediction accuracy and minimum numerical diffusion.

First, a two-phase CFD simulation was performed assuming a uniform bubble diameter throughout the tank. Barigou and Greaves (1992) performed a detailed measurement of the bubble size on a gas-liquid stirred tank agitated by a Rushton turbine operating at the aeration rate ranged from Fl_g = 0.015 to 0.06. Their experimental data indicate that the bubble size is not spatially uniform inside the tank, with around 1 mm at impeller vicinity and up to 4.5 mm in the bulk region. Therefore for the cases with unknown bubble size distribution a uniform bubble of 3.5 mm was applied for the initial simulation of the tanks up to 200L, whereas for the bigger tanks (1500L) the initial simulation was performed using a 5 mm bubble. Bubble sizes for case 5.2 and 5.3 are known from Laakkonen *et al.* (2007a) experiment, which was then used for the initial simulation. Case 6.5 has the same tank size and similar operating conditions to case 5.2 except with a different impeller type; hence a similar bubble size was employed for the initial simulation of both cases.

The interphase drag coefficient was estimated using the standard Schiller-Naumann drag model (Schiller and Naumann, 1935). The impeller movement was modelled using the multiple reference frame technique and the Eulerian-Eulerian approach was employed for the multiphase modelling. The turbulence was modelled using the two-phase realizable k-ε model. Transient solvers with a second-order spatial interpolation scheme were also applied for the final simulation in order to minimise the amount of numerical diffusion. The transient solver was employed in this work because it was impossible to use the steady-

state solver for a gas-liquid stirred tanks when the Eulerian-Eulerian model was used, moreover the PBM also needs a transient solver. The iteration residual was set to fall below 1×10^{-4} at each time step to achieve good convergence. The volume average of the gas void fraction at the rotating zone (impeller region) was also monitored and the iterations in the transient simulation were only halted once a constant value was observed. Some examples of the volume fraction and the Sauter mean diameter evolution for a CFD-PBM simulation are shown in Fig. 6-7. At first, (from point a to b) the CFD simulation is solved alternately with the PBM, where either one of the solvers is turned-off at a particular period. The reason for doing this is to control the stability of the simulation. The effect of the PBM is to pass the bubble Sauter mean diameter to the CFD simulation, when the CFD solver is enabled. At a certain stage (point b), when the bubble size evolution had reached a stable point, a combined CFD-PBM was then performed until a pseudo-steady solution was achieved. Once the steady solution was achieved (at point c) a second-order discretisation was applied and further simulation was performed alternately until a pseudo-steady solution was achieved. For the second-order simulation, it was not possible to run the fully coupled CFD-PBM mode because the model was prone to diverge when the fully coupled simulation was enabled. Technically both the fully coupled CFD-PBM and the alternate CFD-PBM approach would converge to similar result in the end of the simulation, but the alternate approach would take much longer time to be completed compared to the fully coupled approach.

The PBM was initialised using a set of moments with the d_{32} corresponding to a certain bubble size (1.9 mm for the 152L and 14L tanks, 3.6 mm for the 8.6L and 152L and 200L tanks and 5.1 mm for the 1500L tank) as shown in Tables 6-1 and 6-2. The initial bubble sizes were assumed to follow a lognormal distribution with a standard deviation of 0.1. The initial bubble size has no effect on the final bubble size (refer to section 5.4) because the bubble size will evolve according to the local gas hold-up and turbulent dissipation rate; a larger initial bubble size was employed for the larger tanks to speed up the computations. It has to be noted that the initial bubble size employed for the CFD simulation with constant bubble size throughout the tank need not be similar to the initial d_{32}

from the initial moments. This is because, the PBM is not activated at first for the initial CFD simulation until a crude approximation of the local gas hold-up and turbulent dissipation rate distribution were available (estimated using the CFD with constant bubble size). After the initial CFD simulation, the PBM can be activated and each scalar is initialised using the value shown in Tables 6-1 and 6-2. The sparger is treated as a continuous source of bubble with size of 3.1 mm which was determined by the corresponding scalars (given in Table 6-3). The rates of moments flowing from the sparger are determined by the gas inlet velocity.

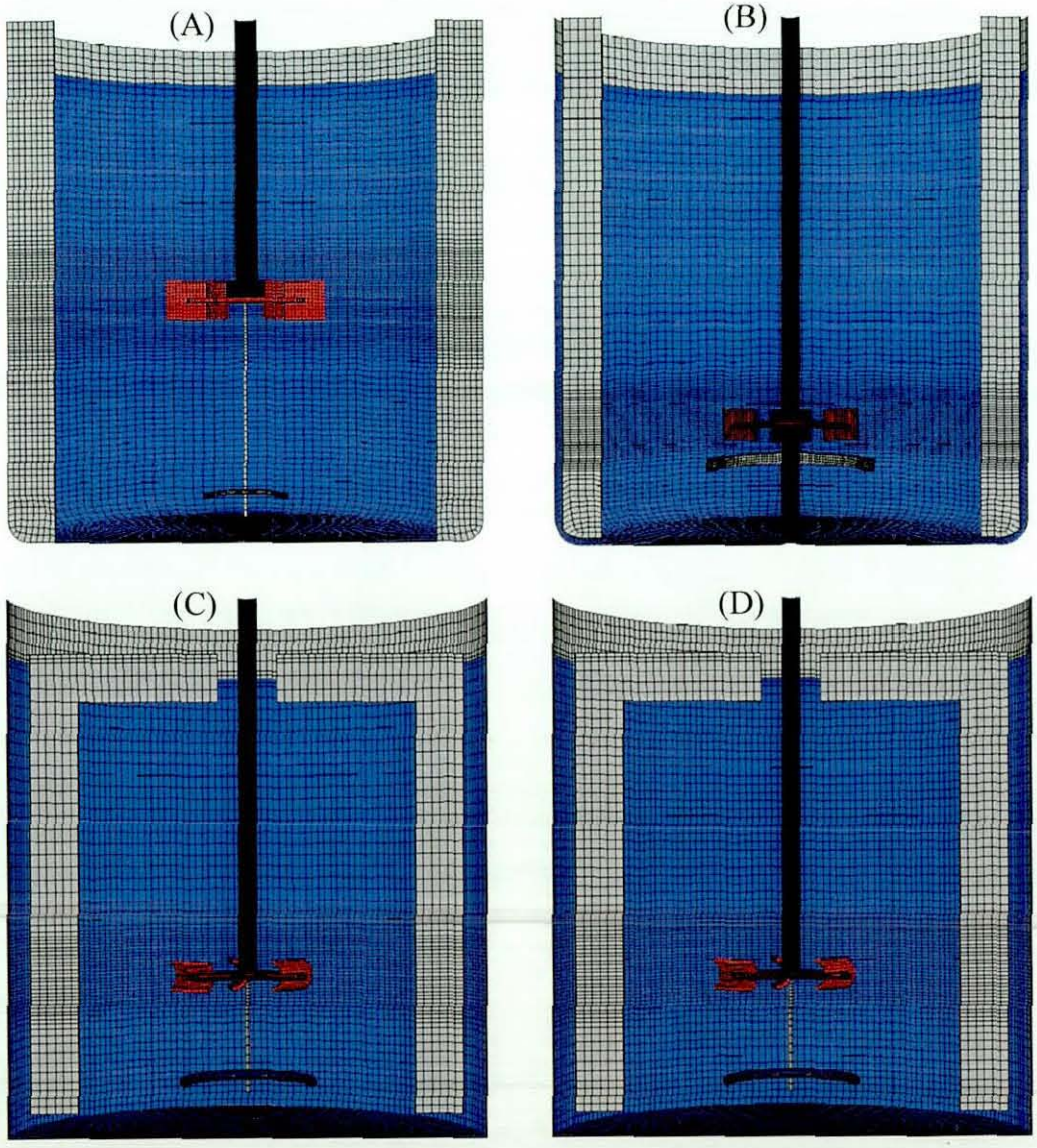

Figure 6-3: Computational grid showing tank wall and its internal, A) Deen's geometry, B) Bombac *et al.*'s geometry, C) CD-6 (intermediate), D) CD-6 (fine)

Table 6-1: Geometry of the stirred tanks employed for the model validation

Case	6.1	6.2	6.3	6.4	6.5
Reference	Deen *et al.* (2002)	Laakkonen *et al.* (2007a)	Laakkonen *et al.* (2007a)	Bombac *et al.* (1997)	-
$T = H$ (m)	0.222	0.26	0.63	0.44	0.26
D (m)	$T/3$	$T/3$	$T/3$	$T/3$	$T/3$
Baffle (m)	$T/10$	$T/10$	$T/10$	$T/10$	$T/10$
Tank type	Dished bottomed	Flat bottomed	Flat bottomed	Dished bottomed	Flat bottomed
Impeller type	Generic RDT	Standard RDT	Standard RDT	Standard RDT	CD-6
W (m)	$0.25D$	$0.2D$	$0.2D$	$0.2D$	$0.2D$
L_D (m)	$0.25D$	$0.25D$	$0.25D$	$0.25D$	$0.25D$
C (m)	$T/2$	$T/3$	$T/3$	$T/4$	$T/3$
Sparger type	Ring	Ring	Ring	Ring	Ring
Sparger diameter Ds (m)	$0.18D$	$0.8D$	$0.8D$	D	D
Q_g (m^3/s)	7.2×10^{-5}	1.6×10^{-4}	2.3×10^{-3}	5.6×10^{-4}	1.6×10^{-4}
Fl_g	0.030	0.022	0.038	0.029	0.021
Fr	0.27	1.19	0.90	0.59	1.21
Re	32692	85856	285221	134131	89047
N (rpm)	360	700	390	376	698
N_{CD} (rpm)	538.7	548.7	379.2	408.8	197.8
Flow regimes	Loaded	Fully dispersed	Fully dispersed	Fully dispersed	Fully dispersed
Grid	267k	225k	225k	242k	253k
	Fig. 5-3E	Fig. 5-3B	Fig. 5-3B	Fig. 5-3D	Fig. 5-3F
d_{32} for CFD const. d_b (mm)	3.5	2.0	3.0	3.5	2.0
Initial scalars (same everywhere inside the tank)	$\phi_{g,0}$ = 35300977	$\phi_{g,0}$ = 216712661	Same as case 6.1	Same as case 6.2	Same as case 6.2
	$\phi_{g,1}$ = 123538.78	$\phi_{g,1}$ = 41419.97			
	$\phi_{g,2}$ = 436.68	$\phi_{g,2}$ = 799.58			
	$\phi_{g,3}$ = 1.56	$\phi_{g,3}$ = 1.56			
	d_{32} = 3.5 mm	d_{32} = 1.9 mm			

Table 6-2: Geometry of the stirred tanks employed for the scale-up study

Case	6.6	6.7	6.8	6.9	6.10	6.11	6.12	6.13
$T = H$ (m)	0.63	0.63	0.63	1.24	0.63	0.63	0.63	1.24
D (m)	$T/3$	$T/3$	$T/3$	$T/3$	$T/3$	$T/3$	$T/3$	$T/3$
Baffle (m)	$T/10$	$T/10$	$T/10$	$T/10$	$T/10$	$T/10$	$T/10$	$T/10$
Tank type	All cases considered for the scale-up studies uses flat bottomed tank.							
Impeller type	RDT	RDT	RDT	RDT	CD-6	CD-6	CD-6	CD-6
W (m)	$0.2D$	$0.2D$	$0.2D$	$0.2D$	$0.2D$	$0.2D$	$0.2D$	$0.2D$
L_D (m)	$0.25D$	$0.25D$	$0.25D$	$0.25D$	$0.25D$	$0.25D$	$0.25D$	$0.25D$
C (m)	$T/3$	$T/3$	$T/3$	$T/3$	$T/3$	$T/3$	$T/3$	$T/3$
Sparger type	Ring	Ring	Ring	Ring	Ring	Ring	Ring	Ring
Sparger diameter Ds (m)	$0.8D$	$0.8D$	$0.8D$	$0.8D$	$0.8D$	$0.8D$	$0.8D$	$0.8D$
Q_g (m^3/s)	9.5×10^{-4}	1.2×10^{-3}	2.3×10^{-3}	1.8×10^{-2}	9.5×10^{-4}	1.3×10^{-3}	2.3×10^{-3}	1.8×10^{-2}
Fl_g	0.0171	0.0217	0.0384	0.0598	0.0153	0.0205	0.0361	0.0581
Fr	0.76	0.80	0.89	0.72	0.87	0.89	0.91	0.72
Re	261507	267521	282618	703276	287877	290555	294767	714857
N (rpm)	357.6	365.8	386.4	248.2	378.5	382.0	387.6	246.4
N_{CD} (rpm)	317.7	334.6	379.2	289.2	100.3	116.8	156.1	133.8
Flow regimes	Fully dispersed	Fully dispersed	Fully dispersed	Large cavities	All CD-6 cases operates under fully dispersed regime			
Grid	267k Fig. 5-3B	225k Fig. 5-3B	225k Fig. 5-3B	308k Fig. 5-3C	253k Fig. 5-3F	253k Fig. 5-3F	253k Fig. 5-3F	311k Fig. 5-3G
d_{32} for CFD const. d_b (mm)	3.5	3.5	3.5	5.0	3.5	3.5	3.5	5.0
Initial scalars (same everywhere inside the tank)	$\phi_{g,0}$ = 35300977 $\phi_{g,1}$ = 123538.78 $\phi_{g,2}$ = 436.68 $\phi_{g,3}$ = 1.56 d_{32} = 3.5 mm	Same as case 6.6	Same as case 6.6	$\phi_{g,0}$ = 12104021 $\phi_{g,1}$ = 60519.96 $\phi_{g,2}$ = 305.64 $\phi_{g,3}$ = 1.56 d_{32} = 5.1 mm	Same as case 6.6	Same as case 6.6	Same as case 6.6	Same as case 6.9

Both RDT and CD-6 refer to standard impeller.

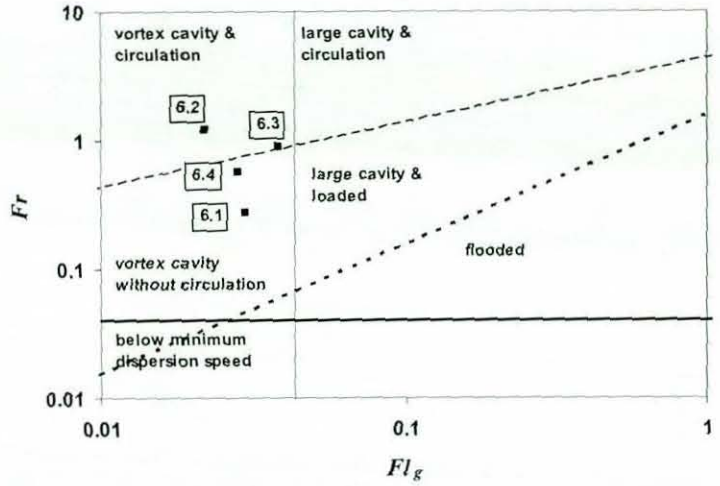

Figure 6-4: Flow map of the RDT used for the validation study

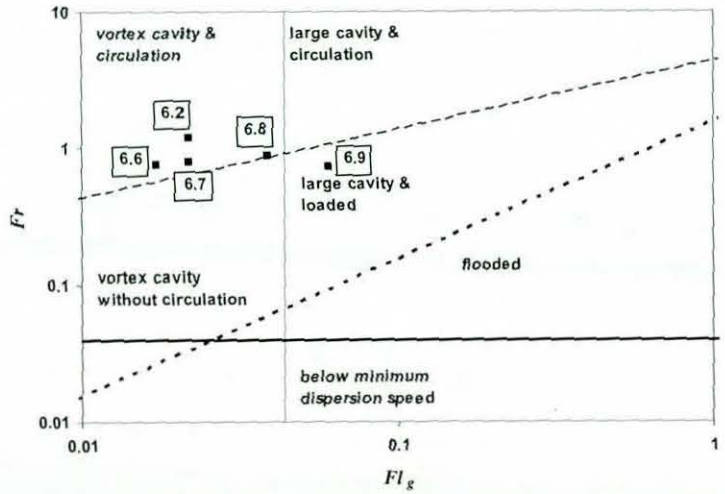

Figure 6-5: Flow map of the cases considered for RDT scale-up study

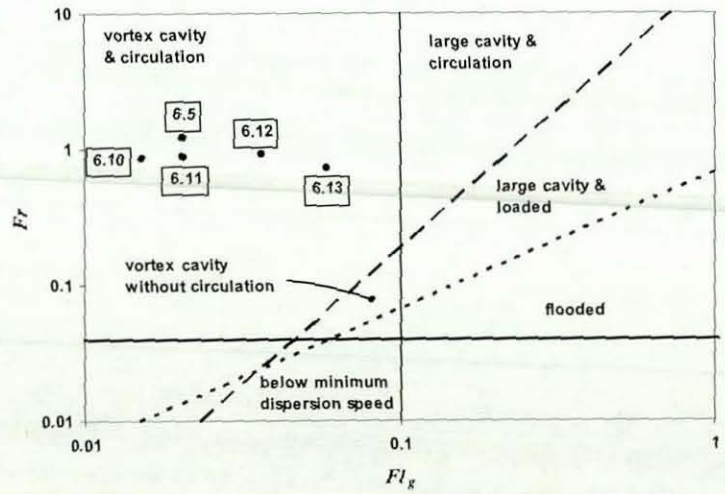

Figure 6-6: Flow map of the cases considered for CD-6 scale-up study

Table 6-3: Scalars at sparger for all cases studied in this chapter

Scalars at sparger
$S_{\phi,0}$ = 56072916
$S_{\phi,1}$ = 168182.54
$S_{\phi,2}$ = 509.51
$S_{\phi,3}$ = 1.56
d_{32} = 3.1 mm

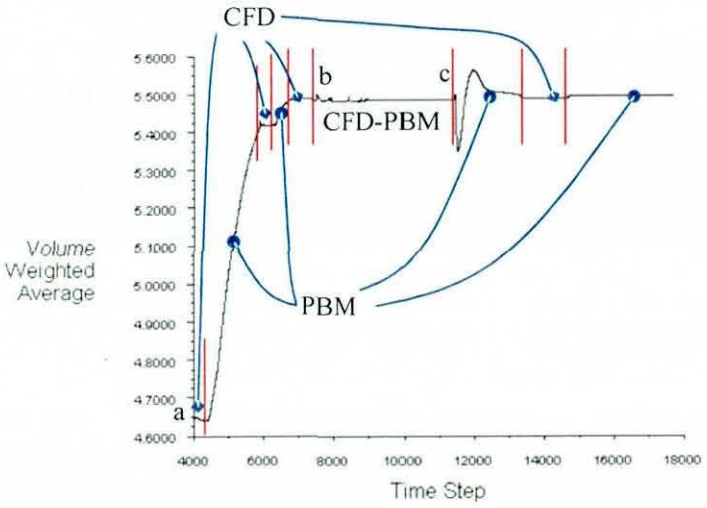

(A)

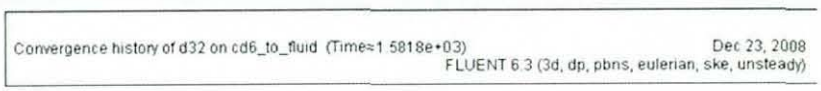

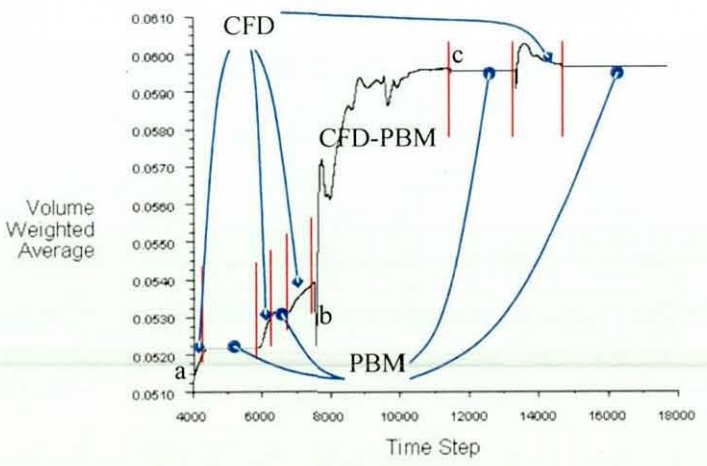

(B)

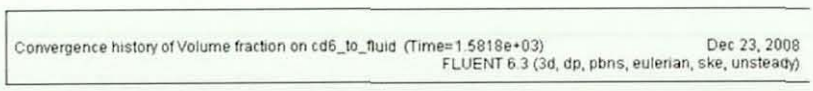

Figure 6-7: Evolution of the volume averaged d_{32} (A) and gas hold-up (B) at the impeller region for case 6.11. Time step for the CFD simulation is 0.005 s and 0.001 s for both the PBM and CFD-PBM simulation.

6.4 Results and Discussions

6.4.1 Prediction of the Gas-Liquid Hydrodynamics

First, the CFD simulations were validated against experimental data using the two-phase PIV measurements reported by Deen (2001) for a stirred tank with Fl_g = 0.0296. Deen (2001) added 4 g of NaCl per litre to the water in their experiment in order to make a non-coalescing system. Details of the geometry and operating parameters of Deen's tank are given in Table 6-1 (case 6.1). The initial simulation using a constant bubble size is required before a coupled CFD-PBM simulation can be performed. Therefore, a realistic initial bubble size of 3.5 mm was employed throughout the tank for the initial simulation. It has to be noted that this initial bubble size does not really matter in the end of the CFD-PBM simulation, as the final bubble size will be determined by the local gas hold-up and the local turbulent dissipation rate. The bubbles were assumed to be spherical and the Schiller and Naumann (1935) drag model was employed to estimate the drag coefficient. The CFD results were time-averaged over all blade angles and compared with Deen's (2001) PIV measurements. For easier comparison, the results for the mean velocities and turbulent kinetic energy were normalised using the V_{tip} and V_{tip}^2, respectively. Despite the assumption of a constant bubble size and spherical bubbles, the predictions (marked as CFD constant) shown in Figs. 6-8 to 6-10 are reasonably close to the experimental data, except for the axial gas velocity. The differences can be explained by the neglect of bubble coalescence and break-up caused by the turbulent flow induced by the rotating impeller. These mechanisms are not considered in the case where a uniform bubble size is assumed throughout the tank.

A simulation using a non-uniform bubble size was next performed to evaluate these effects on the CFD predictions. The local bubble sizes were estimated using the population balance model, which tracks the moments of the bubble size distribution. The local Sauter mean diameters, obtained from the ratio of the third and second moments, were then passed into the CFD simulation and used for the two-phase flow modelling. The CFD-PBM simulations were performed using two different drag models: (i) the hard sphere drag model of Schiller and Naumann (1935) (a default FLUENT model) marked as CFD-PBM-SN and (ii) another that takes into account the drag of distorted bubbles (Ishii

and Zuber, 1979) and dense bubble effect (Behzadi *et al.*, 2003) marked as CFD-PBM-IZ. Predictions of the CFD-PBM model were slightly better than the one with a constant bubble size. Although there is not much improvement when the CFD-PBM and spherical drag model (CFD-PBM-SN) is employed. There is a little improvement observed when the distorted bubble drag model is considered (CFD-PBM-IZ) however ultimate success was not achieved. Improvement of the CFD prediction is due to the fact that the effect of local bubble sizes on the two-phase flow is mainly via the inter-phase exchange coefficient, which depends on the drag model. The Schiller-Naumann model is suitable for spherical rigid bubbles, but in comparison, the Ishii-Zuber model predicts drag coefficients for the spherical, ellipse and cap bubble regime. Predictions of the mean axial and radial velocities in the liquid phase (Fig. 6-8) are much better than those of the gas phase (Fig. 6-10). The result suggest that the local bubble size plays only a small role in the prediction of liquid mean velocities, as it can be observed in Fig. 6-8 there is no significant difference between the prediction by CFD-PBM-SN and CFD with constant bubble size. There is some improvement especially for the mean axial liquid velocity when the distorted drag model is considered (see Fig. 6-10) however ultimate success was not achieved.

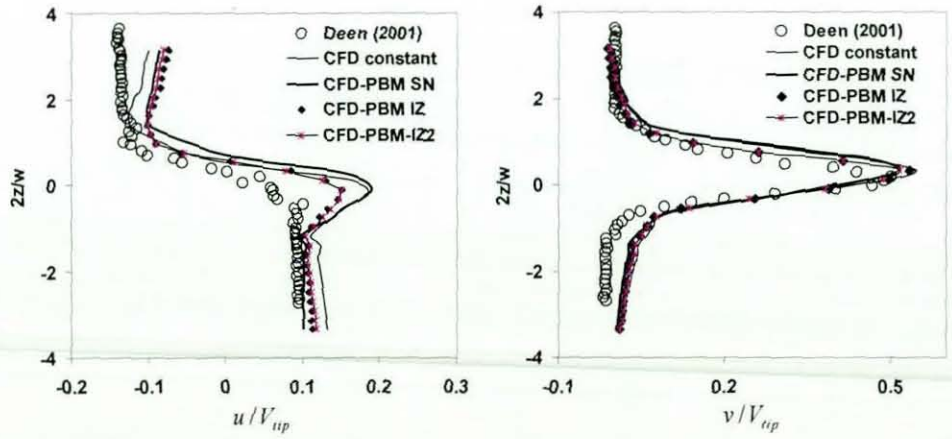

Figure 6-8: Prediction of liquid phase axial (u) and radial (v) velocity at normalised radial position (radial position, r over tank radius, R) r/R = 0.37. CFD constant (constant bubble size and Schiller-Naumann drag), CFD-PBM-SN (CFD-PBM with Schiller-Naumann drag), CFD-PBM-IZ (CFD-PBM with Ishii-Zuber drag), CFD-PBM-IZ2 (CFD-PBM with reduced coalescence rate and Ishii-Zuber drag). Data points adopted from Deen (2001).

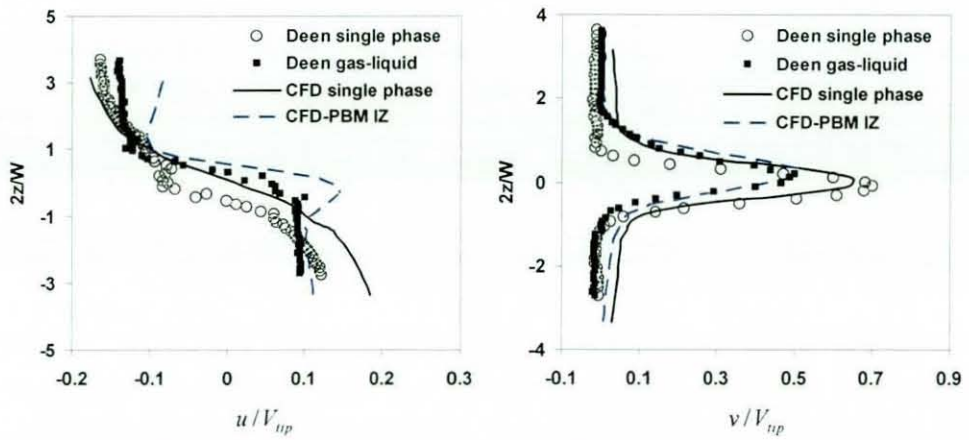

Figure 6-9: Comparison between the liquid phase axial (u) and radial velocity (v) for single phase and gas-liquid stirred tank at r/R = 0.37. Experimental data obtained from Deen (2001).

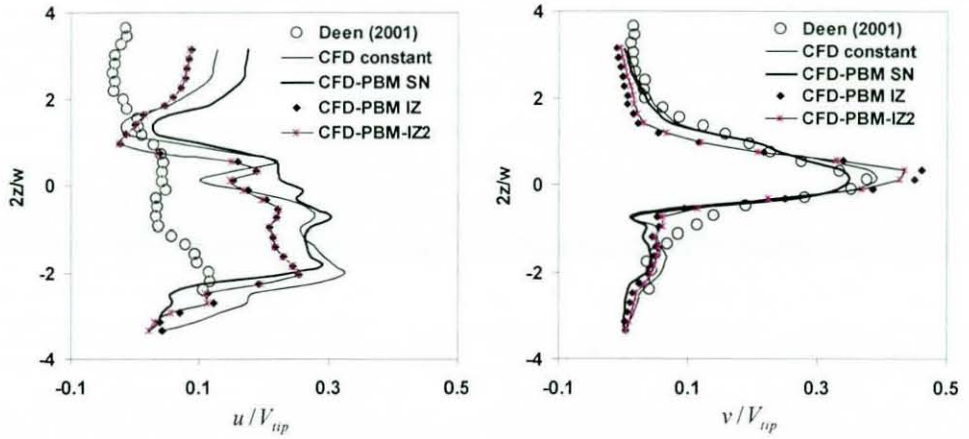

Figure 6-10: Prediction of gas phase axial (u) and radial velocity (v) at r/R = 0.37. Experimental data is adopted from Deen (2001).

Predictions of the gas mean velocities (see Fig. 6-10) are not as good as the liquid velocities, as shown in Fig. 6-8 especially for the axial velocities. Unlike the liquid phase radial velocity, the effect of the bubble size shows some influence on the prediction of the mean radial gas velocity (see Fig. 6-10). Prediction of radial gas velocity is surprisingly much better by the CFD model with constant bubble size, although predictions of axial gas velocity prove otherwise. This phenomenon may be due to the 4 grams per litre NaCl added to the system in order to create the non-coalescing system by Deen (2001). Although a non-coalescing agent (NaCl) were added to the system by Deen (2001), it may not be possible to prevent the coalescence completely. The

breakage events induced by the impeller rotation will also contribute towards smaller bubbles. This problem has not been considered in the present model which is only valid for the bubbly flow where coalescence and breakage can take place together i.e. in tap water. It may be assumed that addition of NaCl will affect the coalescence kernel by reducing the collision efficiency by let say 50%. For this case only, the collision efficiency was multiplied with a constant equal to 0.5 in order to evaluate the sensitivity of the PBM to the reduced coalescence rate and also as an attempt to mimic the reduced coalescing effects when NaCl was added to the system (results from this case are marked as CFD-PBM-IZ2). This study does not imply that the PBM kernels should be fitted in this way, but it represents a simple method to evaluate the effect of a lower coalescence rate in the PBM. Of course, a proper method of formulating the kernels should be carried out experimentally, such as is described by Martinez-Bazan *et al.* (1999). A NaCl addition may change the initial and final film thickness responsible for the bubble coalescence. As expected, the bubble size reduces when the coalescence efficiency is reduced by 50% (see Fig. 6-11). The PBM simulation is not sensitive towards the collision efficiency, as it can be observed from Figs. 6-11B and 6-11C that reduction of collision efficiency by 50% only yielded a marginal change in the local bubble size. This small change in bubble size (3.8 mm to 3.3 mm around the impeller zone) does not seem to change the predictions of the mean velocities as is shown in Figs. 6-8 and 6-10 (see CFD-PBM-IZ and CFD-PBM-IZ2).

Previous work by Deen (2001) also shows a large over-prediction of the mean gas axial velocity. Deen (2001) considered drag for a distorted bubble, virtual mass and lift force in their work but a monodispersed bubble size distribution was employed throughout the tank. Montante *et al.* (2008) recently showed a reasonable prediction of the mean gas velocities in stirred tanks using a CFD-PBM method. However, the d_{32} in their work was under predicted by as much as 50%, which undoubtedly affected the gas axial velocity. Recently, Zhang *et al.* (2008) showed correct prediction of the gas mean velocities using a combination of LES and Brucato *et al.*'s (1998) correction for the particle drag coefficient in turbulence flow. However, Lane *et al.* (2002) has pointed out that Brucato *et al.*'s drag model led to a wrong prediction of gas hold-up distribution;

higher gas hold-up near the bottom of the tank. The local bubble size was predicted correctly by Lane *et al.* (2002) using a bubble density method. This issue may be addressed by taking into consideration the drag correction due to turbulent flow, which is not considered in this work due to lack of suitable correlations and experimental data available in the literature. The turbulent corrections may increase the drag coefficient by 20 to 30% which would decrease the axial gas velocities and move them closer to the experimental values.

Fig. 6-9 shows the predicted mean liquid velocities of the single and two phase flow using a single phase simulation and the CFD-PBM-IZ. The CFD predictions of the radial velocity show a good agreement with Deen (2001). The reduced velocities during the aeration condition were also predicted correctly. Predictions of the mean axial velocity are not as good as the radial velocity, nevertheless the overall trend of the liquid axial velocity with and without aeration were predicted correctly.

The predicted gas hold-up distribution shown in Fig. 6-12 shows clearly the loaded regime pattern which is in agreement with the flow regime map (see case 6.1 in Fig. 6-4). There is some influence of the local bubble size on the predicted gas hold-up (compare Fig. 6-12A to Fig. 6-12B) but the effect is not as significant as the drag coefficient (compare Figs. 6-12A and 6-12B to Figs. 6-12C and 6-12D). Difference between the gas hold-up distributions predicted by reduced coalescence rate (Fig. 6-12D) and the one with the default Prince and Blanch (1990) model (Fig. 6-12C) is not significant due to a minimal differences in the predicted bubble size (~ 1 mm) as shown in Fig. 6-11 (B and C). More quantitative comparison between the predicted local gas hold-up will be discussed further in section 6.4.3. The effect of the drag coefficient on the local bubble size distribution is also visible in Figs. 6-11A and 6-11B which show a larger bubble when drag for distorted bubbles is considered. This is due to a higher gas hold-up which will translate into higher numbers of bubble per unit volume and thus higher chance for coalescence to occur.

Predictions of the axial gas velocity in Fig. 6-13 shows more influence induced by the drag coefficient than the local bubble size, as it shows little significant

difference between the case with constant bubble size (Fig. 6-13A) and the CFD-PBM-SN (Fig. 6-13B). These two cases employed the same Schiller-Naumann drag model. The gas axial velocities are much lower when the drag for distorted bubble is applied (Figs. 6-13C and 6-13D) due to much higher drag force induced by the non-spherical bubbles. The liquid axial velocity is not significantly affected by either the bubble size or the drag coefficient except in the impeller vicinity (Fig. 6-14) which resulted from the higher gas axial velocity in that region. Prediction of the radial gas and liquid velocities are also affected significantly by the drag model applied as can be seen in Figs. 6-15 and 6-16. Very low radial gas velocities around the impeller vicinity can be seen in Fig. 6-15 due to the fact that this is a gas cavity region which is shown to have almost 100% gas hold-up in Fig. 6-12. A similar conclusion was also suggested by Scargiali *et al.* (2007) who studied separately the effect of bubble size and drag coefficient in a gas-liquid stirred tank. Scargiali *et al.* (2007) concluded that the drag force is the most dominant interfacial force in gas-liquid stirred tanks.

Deen (2001) performed a measurement of the rms velocities fluctuations for the single phase and gas-liquid flow via 2D PIV. They performed a PIV measurement for the gas-liquid flow using two cameras, i.e. one for the liquid velocities and another one for the gas velocities (bubble). A pseudo-isotropic assumption (Zhou and Kresta, 1996) may be employed to estimate the turbulent kinetic energy in the case when only two velocities components are available.

$$k = \frac{4}{3}\left(u'^2 + v'^2\right) \tag{6.17}$$

Although eq.(6.17) assumed a pseudo-isotropic turbulence flow, they do not imply the turbulent to be isotropic because the u' and v' can vary quite significantly (Khan *et al.*, 2005). Previous work by e.g. Khan *et al.* (2005) and Zhou and Kresta (1996) shows that eq.(6.17) can give a good estimate of the turbulent kinetic energy. Khan *et al.* (2005) for instance shows a good reproduction of the distribution and magnitude of the turbulent kinetic energy measured by 3D PIV using eq.(6.17) and 2D PIV data.

Fig. 6-17 shows the predicted random turbulent kinetic energy for the single phase and multiphase flow. Equations related to definition of $\overline{k_{ran}}$ and k_{tot} were

described earlier in section 3.5.1. For the single phase flow the $\overline{k_{ran}}$ was predicted reasonably well although the double peak trend was not reproduced correctly. This is due to the isotropic assumption of turbulent viscosity in the RANS model (Rk-ε). A similar finding was also observed from a single phase study in chapter 3 earlier. However, it is not possible to compare the prediction of k_{tot} because the impeller position for the multiple reference frame model is fixed at a particular position during the simulation. The k_{tot} calculation requires a full tank simulation and sliding mesh method (discussed in section 3.5.1) which is not performed in this chapter due to its computational demand, especially when the two-phase model and population balance modelling is used. However, it is thought that the turbulent kinetic energy has been predicted reasonably well in this work, considering a reasonable prediction of $\overline{k_{ran}}$.

Previous work by Lu and Ju (1987) and Deen (2001) showed a reduction in the velocities fluctuations magnitude (corresponding to reduced turbulent kinetic energy) under aerated conditions. The reason behind this phenomenon is that some energy is absorbed by the secondary phase. The reductions of $\overline{k_{ran}}$ in stirred tank under aeration also have been reproduced correctly in this work (see Fig. 6-17A). Unfortunately, further comparison cannot be made for the liquid phase $\overline{k_{ran}}$ in Fig. 6-17A because the measurements of the angle-resolved liquid phase velocity fluctuation were not presented by Deen (2001). However, comparisons of the gas phase $\overline{k_{ran}}$ in Fig. 6-17B shows a fair agreement to Deen (2001). The effect of the bubble size and drag coefficient on the predicted turbulent kinetic energy is not significant (see Fig. 6-17B). It is also interesting to note that the $\overline{k_{ran}}$ for gas and liquid phase is essentially similar despite the separate turbulent viscosities for both phases in the two-phase Rk-ε model (see Fig. 6-17A). Recently, Montante *et al.* (2008) also reported a similar finding from their PIV measurements in aerated stirred tank at low gas loading (0.2 VVM). Montante *et al.* concluded that liquid phase turbulence flow (velocities fluctuation) may be used as a benchmark for gas-liquid modelling. Some discrepancies in the predictions may also be due to the inherent issue in Rk-ε model which assume an isotropic turbulent viscosity.

Limitations of the Eulerian-Eulerian model which utilises the d_{32} instead of the real bubble size distribution may also affect the predictions. In reality the bubble sizes at any given point inside the tank cannot be represented by a single bubble size because the local bubble size changes with time and these different bubble sizes have a different magnitude of forces acting to them. The local bubble size distribution at any given time inside the tank is better appreciated by looking at the experimental measurement e.g. by Laakkonen *et al.* (2005b). The effect of the various bubble sizes has not been taken into account in Eulerian-Eulerian model, nevertheless the CFD-PBM predictions are reasonable despite this simplification.

Fig. 6-18 shows a reduction in the predicted turbulent dissipation rate by about a quarter during aeration, compared to its value for single phase flow. This trend is similar to the predicted mean velocities and turbulent kinetic energy shown earlier in Figs. 6-9 and 6-17. Reduction in the mean velocities under gassing condition translates into lower velocity fluctuations which mean lower turbulent kinetic energy and turbulent dissipation rate. Under gassing conditions some energy from the liquid phase is used to disperse the secondary phase especially to overcome the interfacial force i.e. the drag force. Prediction of the turbulent dissipation rate is not affected significantly by the drag model employed, as can be observed from Fig. 6-18: the predictions of CFD-PBM-SN are quite similar to those of CFD-PBM-IZ. However, the local bubble sizes seem to affect the location of the peak turbulent dissipation rate as they are shifted up when a constant bubble size is employed. The local bubble size near the impeller discharge is slightly smaller than the one employed for a constant bubble size (3.5 mm) simulation and thus more inclined to produce higher radial flow at impeller level (see Fig. 6-15 and 6-16), because smaller bubbles tend to follow the liquid flow. Therefore a peak turbulent dissipation rate closer to the impeller level is more likely to be observed when the CFD-PBM model is employed. The estimated value of ε is much lower than those from the CFD predictions because of the assumptions that the length scale $\Lambda = W/2$ which is not necessarily valid for a stirred tank. For instance, experimental measurements by Khan *et al.* (2004) shows the length scales vary from $0.3W$ to $1.1W$ throughout the tank.

The two-phase mean velocities and turbulent kinetic energy have been predicted fairly well despite the simplification i.e. by employing a half-tank MRF model, RANS Rk-ε and Eulerian-Eulerian model. Any CFD-PBM simulations employed in the remainder of this chapter refer to the CFD-PBM-IZ due to its better prediction than the CFD-PBM-SN.

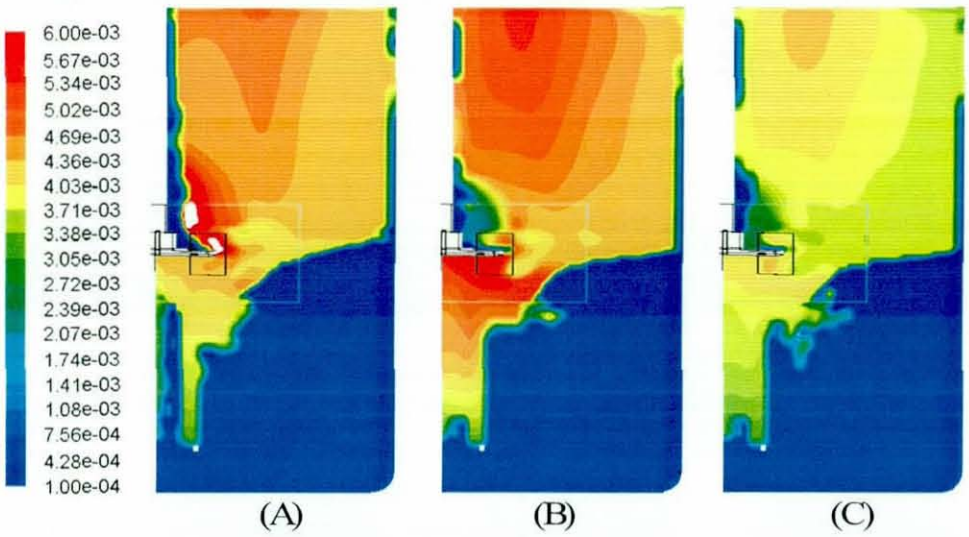

Figure 6-11: Prediction of local bubble size (d_{32}, m) for case 6.1, A) CFD-PBM-SN, B) CFD-PBM-IZ and C) CFD-PBM-IZ2

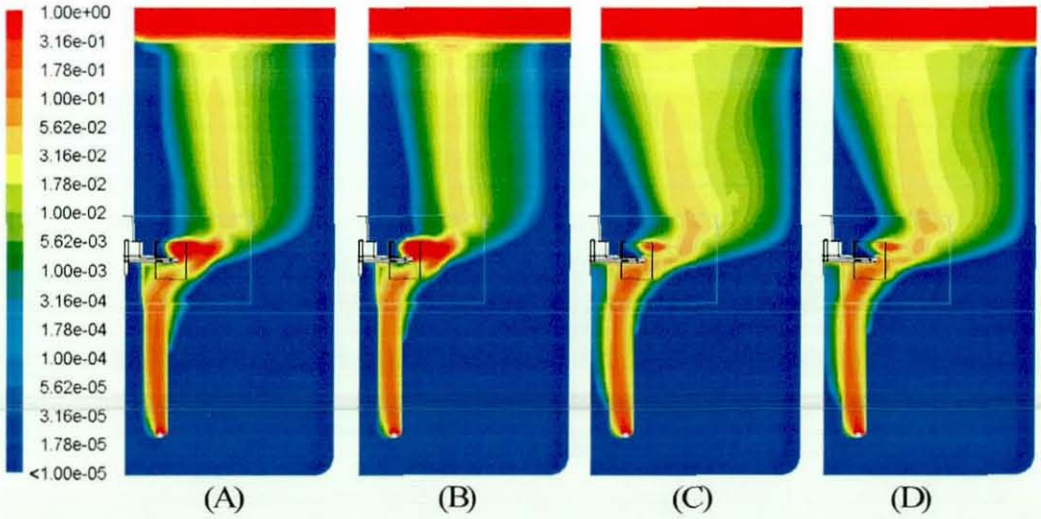

Figure 6-12: Prediction of gas hold-up distribution for case 6.1, A) Constant bubble size, B) CFD-PBM-SN, C) CFD-PBM-IZ and D) CFD-PBM-IZ2

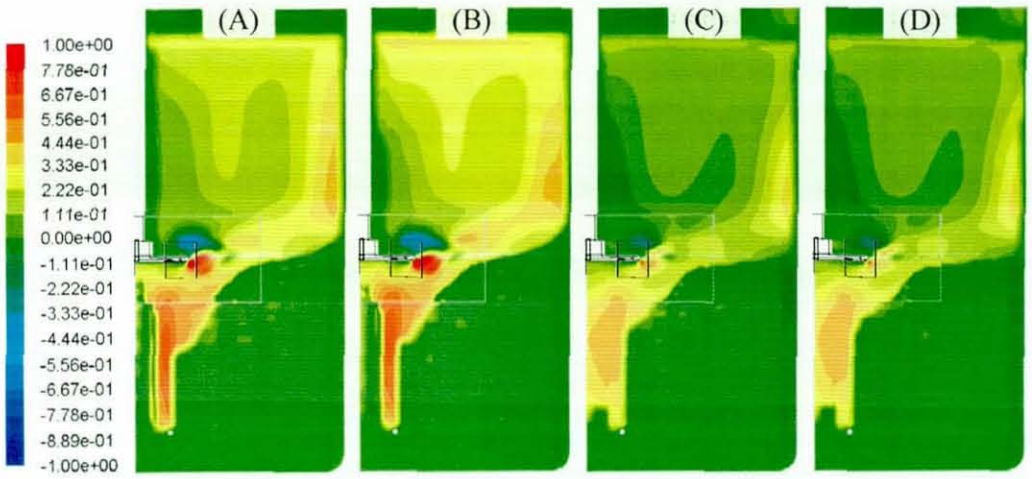

Figure 6-13: Prediction of axial gas velocities (m/s) for case 6.1, A) Constant bubble size, B) CFD-PBM-SN, C) CFD-PBM-IZ and D) CFD-PBM-IZ2

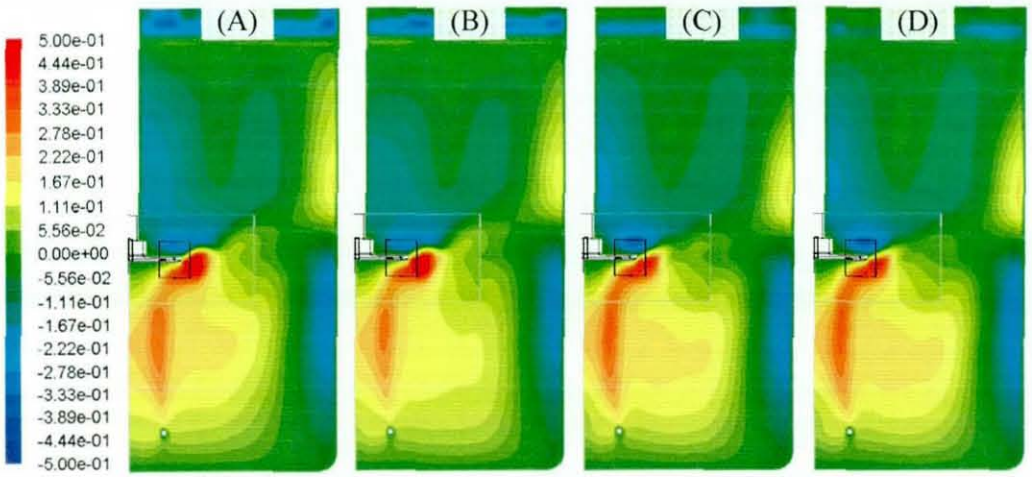

Figure 6-14: Prediction of axial liquid velocities (m/s) for case 6.1, A) Constant bubble size, B) CFD-PBM-SN, C) CFD-PBM-IZ and D) CFD-PBM-IZ2

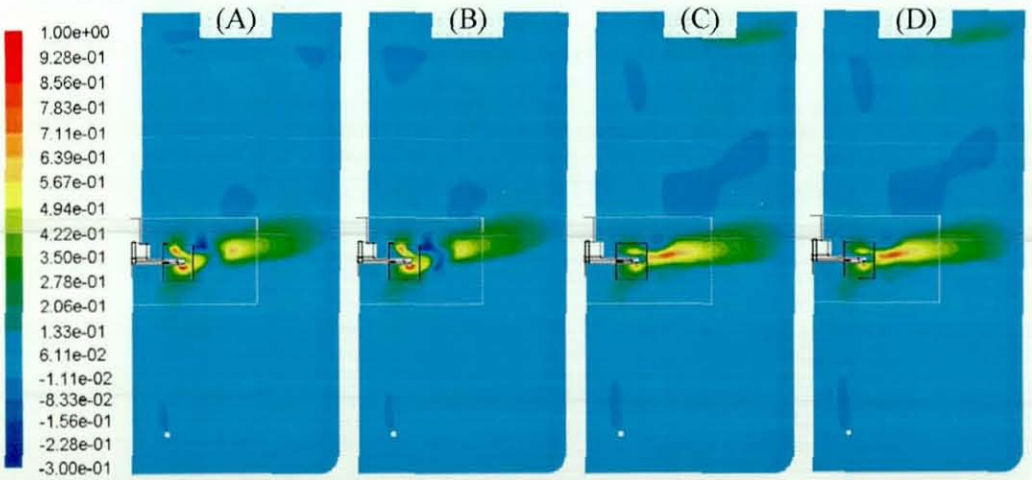

Figure 6-15: Prediction of radial gas velocities (m/s) for case 6.1, A) Constant bubble size, B) CFD-PBM-SN, C) CFD-PBM-IZ and D) CFD-PBM-IZ2

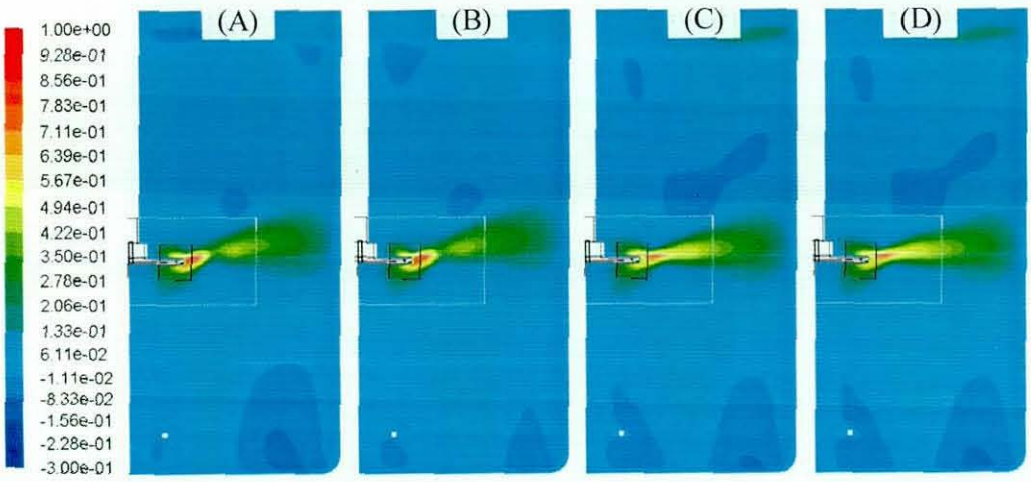

Figure 6-16: Prediction of radial liquid velocities (m/s) for case 6.1, A) Constant bubble size, B) CFD-PBM-SN, C) CFD-PBM-IZ and D) CFD-PBM-IZ2

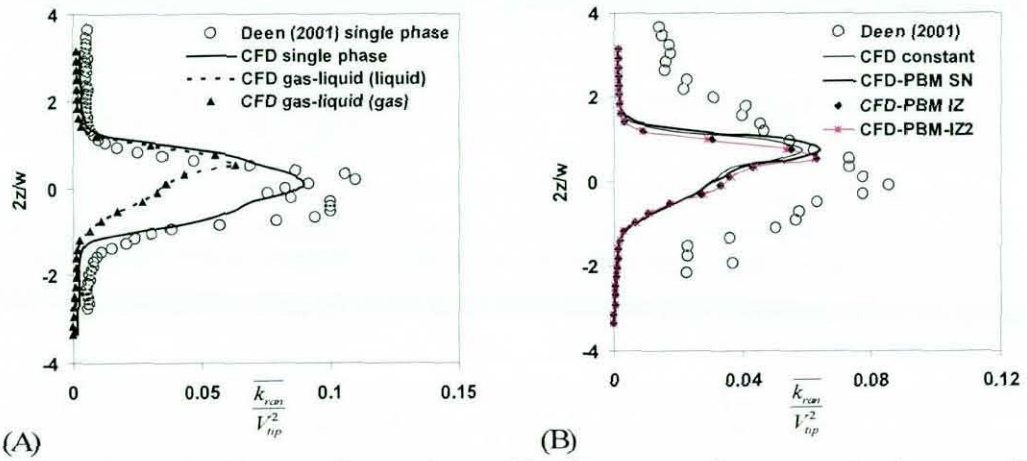

(A) (B)

Figure 6-17: Prediction of turbulence kinetic energy for geometry in case 6.1, A) single phase, B) gas-liquid system (gas phase). Experimental data obtained from Deen (2001).

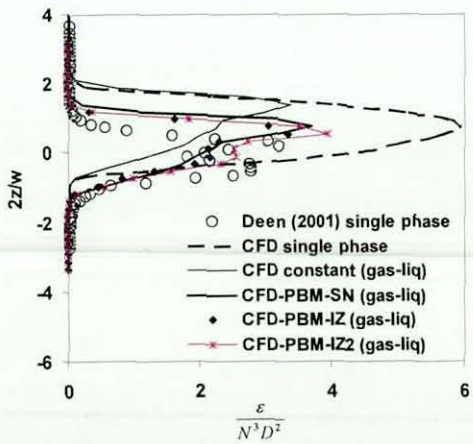

Figure 6-18: Comparison between the turbulent dissipation rate for single phase and gas-liquid stirred tank (case 6.1). Data points estimated using eq.(3.28) and Deen (2001) measurement.

6.4.2 Prediction of the Aerated Power Number

Prediction of the gassed power input by integrating the dissipation rate over the tank volume is known to provide an underestimate of the power input. P_g may also be estimated from the moment acting on the shaft and impeller or baffles and tank wall combined with eq.(3.31). In this work P_g was calculated using the moment acting on the impeller and shaft, because it was shown previously in section 3.6 to produce a more reliable prediction than the moment acting on baffle and wall. However, the P_g estimated using the ε integrations are also presented for further discussion related to the effect of the under-prediction of ε on the mass transfer prediction.

Many correlations are available for calculating the gassed and ungassed power number of stirred tanks agitated by a Rushton turbine and some of them are discussed earlier within section 2.7. Myers *et al.* (1999) performed extensive experiments in single phase and aerated stirred tanks fitted with either a Rushton type impeller, a CD-6 impeller or a BT-6 impeller; they reported the P_g/P_0 of a Rushton turbine drops significantly compared to that of a CD-6 or BT-6 impeller on gassing. In this study the CFD predictions were compared with measured P_g/P_0 obtained by Myers *et al.* (1999) for the CD-6 impeller, and using eq.(2.5) for the standard Rushton turbine, together with eq.(2.3) described earlier in section 2.7. Deen (2001) employed a Rushton type impeller with the blade width equal to its length (see Table 6-1). From experimental measurement, Deen (2001) observed the N_{p0} = 6.0 and the N_{pg} = 3.8, respectively. Thus Smith's (2006) correlation is not employed for Deen's geometry (case 6.1) due to the non-standard impeller dimension; instead the CFD prediction is compared directly to Deen (2001) measurement.

Effect of the uniform bubble size on the prediction of the power number is assessed by comparing the P_g/P_0 from the CFD simulation with a uniform bubble size and the one with CFD-PBM. Unless otherwise mentioned, the CFD simulation with the uniform bubble size throughout the tank was solved with the Schiller-Naumann drag model without a dense bubble effect (default FLUENT model). The P_g/P_0 ratio is shown to be predicted reasonably well using the assumption of a constant bubble sizes throughout the tank (see Table 6-4). There is a small improvement in the prediction of P_g/P_0 when a non-uniform

bubble size is employed using the CFD-PBM method as can be seen for cases 6.1 to 6.5. This is due to the changes in the distribution of gas hold-up, mean velocities and turbulent dissipation rates when the CFD-PBM-IZ is employed. The effect of the drag model and local bubble sizes on the two-phase mean velocities and turbulence flow have been discussed earlier in section 5.4.1.

There is some discrepancy between the predicted relative power number from the CFD simulations and Smith's correlation for case 6.4 (see Table 6-4). In fact, Smith's (2006) correlation is only shown to have a good prediction of the relative power number in the range from 0.3 to 0.6 (Smith 2006), whilst some discrepancy is shown when it applied outside this range. This finding is also supported by Cui *et al.* (1996) who proposed two different correlations for a different flow regime arguing that the Fl_g alone is not sufficient to describe the value of P_g/P_0. Although Smith (2006) has considered an other dimensionless number, Fr, in his correlations at eq.(2.5), it still seems to have a limitation. Previous work by Khopkar and Ranade (2006) on the same case (Khopkar and Ranade (2006) performed a CFD simulation of Bombac *et al.*'s (1997) geometry and operating conditions) give the value of P_g/P_0 = 0.66 from their CFD simulation employing a monodisperse bubble size. The effect of the uniform bubble size is not evaluated for the cases employed for scale-up studies (cases 6.6 to 6.13) because it is thought that the model had been validated enough using cases 6.1 to 6.5. An initial simulation using a constant bubble size is not needed for the scale-up study; instead they are initialised using the result from an earlier simulation rather than starting from zero initialisation. This approach also helps to speed up the computation by starting from an almost correct gas hold-up and bubble size distribution. Moreover, there is a little motivation of running the uniform bubble simulation for the scale-up study because a proper calculation of the mass transfer can only be performed via a CFD-PBM simulation.

Prediction of the P_g/P_0 for the other cases (case 6.6 to 6.13 were set for scale-up study) were also reasonably close to the values obtained from Smith (2006) correlations for the Rushton turbine and Myers *et al.* (1999) measurement for the CD-6 impeller. Overall, the results suggest that the P_g/P_0 can be predicted reasonably well using the uniform bubble size assumption with bubble size

close to the experimental mean values. However, the CFD-PBM method is a more suitable approach for predicting the relative power number in cases when the mean bubble size is not known beforehand.

6.4.3 Prediction of Local Gas Hold-up

Bombac *et al.* (1997) has carried out detailed measurements of gas hold-up in a stirred tank agitated by a Rushton turbine using a resistivity probe. They carried out the gas hold-up measurements at an azimuthal position 12° behind the baffle in 190 different point nodes. The local gas hold-up distributions from Bombac *et al.*'s (1997) measurement are depicted in Fig. 6-19A showing a fully dispersed regime with gas circulating over the lower and upper circulation loops. Recently, Scargiali *et al.* (2007) and Khopkar and Ranade (2006) have performed CFD simulations for this case using a constant bubble size of 3 mm throughout the tank. The main difference between the two works is that Khopkar and Ranade (2006) considered the effect of turbulence on the bubble drag using Brucato *et al.*'s (1998) correlation, whereas Scargiali *et al.* (2007) neglect this term citing a lack of reliable data and correlations in the literature for a bubbly flow. Predictions by Khopkar and Ranade (2006) in Fig. 6-19B were reasonably good in the lower circulation loop, but unable to predict accurately the gas hold-up distribution above the impeller especially closer to the liquid surface. Meanwhile Scargiali *et al.* (2007) were unable to predict correctly the gas hold-up distribution in the lower and upper circulation loops, as well as near the liquid surface (see Fig. 6-19C). The poor prediction of gas hold-up distribution by both Khopkar and Ranade (2006) and Scargiali *et al.* (2007) may be due to the application of a constant bubble size throughout the tank in their work. As discussed previously in section 5.3.1, Khopkar and Ranade's (2006) prediction may also be affected by the turbulent correction for drag coefficient they employed which consider an average value of the Kolmogorov microscale over for the whole tank.

Comparison between Bombac *et al.*'s (1997) measurements and the CFD simulation is shown in Fig. 6-19. The CFD-PBM-IZ prediction (Fig. 6-19E) shows a better agreement with the measured local hold-up than those from a CFD simulation with a monodispersed bubble size (d_{32} = 3.5 mm) as shown in

Table 6-4: Prediction of the relative power number

Case	Q_g (m^3)	*P_g/V (W/m^3)	V (m^3)	Fl_g	VVM	v_g (cm/s)	N (rpm)	Relative power number (P_g/P_0)			
								Smith (2006) Myers *et al.* (1999) Deen (2001)	ε integral CFD-PBM-IZ	CFD const. d_b	Torque CFD-PBM-IZ
6.1	7.2×10^{-5}	210.4	0.0086	0.030	0.50	0.19	360	0.63	0.31	0.52	0.59
6.2	1.6×10^{-4}	1174.7	0.014	0.022	0.70	0.30	700	0.45	0.28	0.41	0.45
6.3	2.3×10^{-3}	1205.8	0.2	0.038	0.70	0.74	390	0.42	0.29	0.38	0.43
6.4**	5.6×10^{-4}	660.8	0.071	0.026	0.48	0.35	376	0.49	0.49	0.58	0.68
6.5	1.6×10^{-4}	1174.7	0.014	0.021	0.7	0.30	698	0.71	0.29	0.75	0.69
6.6	9.5×10^{-4}	1174.7	0.2	0.017	0.29	0.30	357.6	0.53	0.29	-	0.50
6.7	1.2×10^{-3}	1174.7	0.2	0.022	0.37	0.39	365.8	0.49	0.30	-	0.47
6.8	2.3×10^{-3}	1174.7	0.2	0.038	0.70	0.74	386.4	0.42	0.25	-	0.43
6.9	1.8×10^{-2}	1174.7	1.5	0.060	0.70	1.45	248.2	0.39	0.17	-	0.39
6.10	9.5×10^{-4}	1174.7	0.2	0.015	0.29	0.30	378.5	0.73	0.31	-	0.68
6.11	1.3×10^{-3}	1174.7	0.2	0.021	0.39	0.39	382.0	0.71	0.31	-	0.68
6.12	2.3×10^{-3}	1174.7	0.2	0.036	0.70	0.74	387.6	0.68	0.28	-	0.62
6.13	1.8×10^{-2}	1174.7	1.5	0.058	0.70	1.45	246.4	0.71	0.28	-	0.64

* The P_g/V is estimated using the value at column no 9 which is either taken from Smith (2006) correlations, Myers *et al.* (1999) or Deen (2001).

** The monodisperse bubble size simulation is performed with consideration of a dense bubble function in eq.(5.5) for a fair comparison between the predicted local gas hold-up with those modelled using the CFD-PBM-IZ.

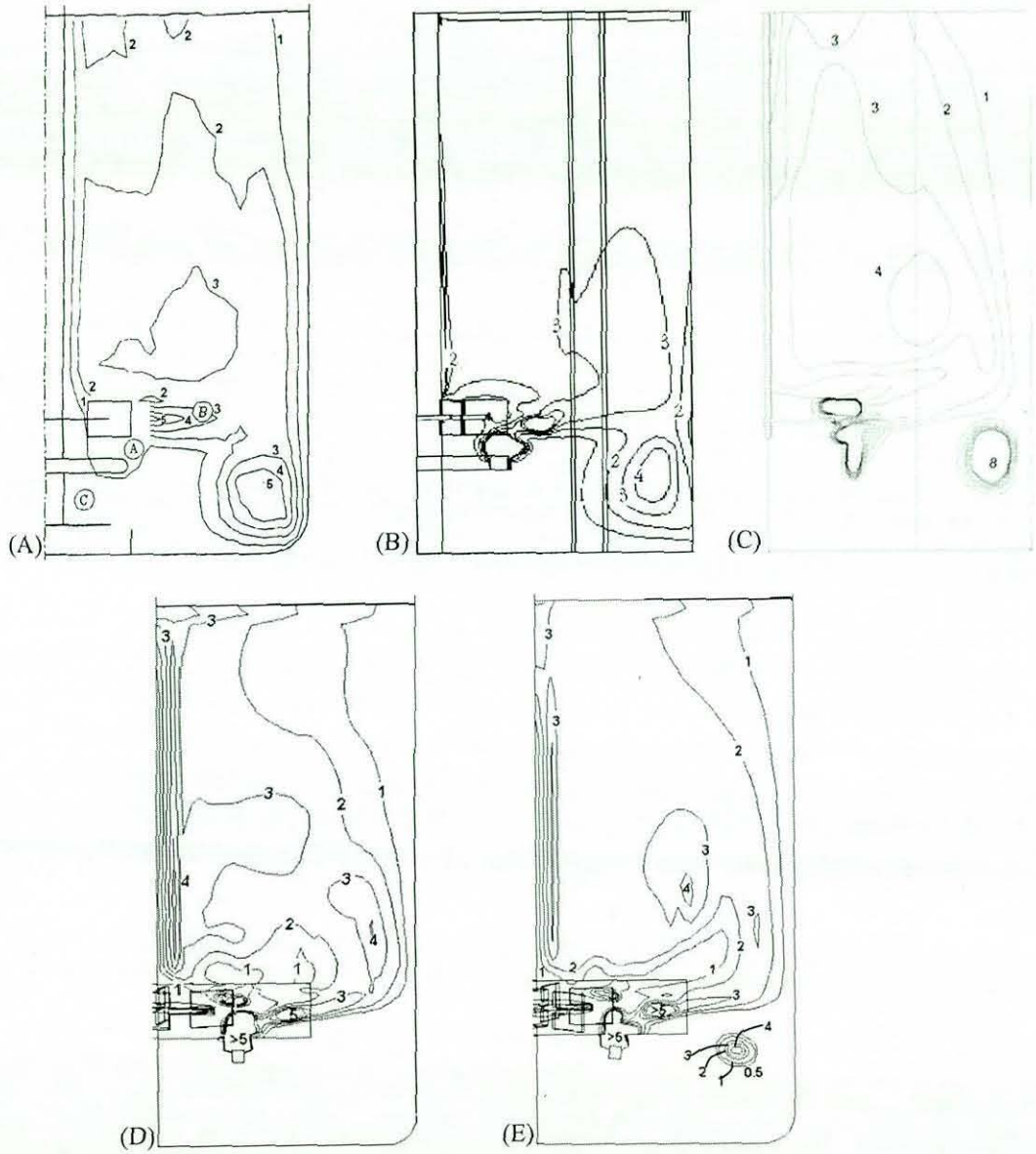

Figure 6-19: Prediction of gas hold-up (%), A) Bombac *et al.* (1997), B) Constant bubble size d_{32} = 3 mm by Khopkar and Ranade (2006), C) Constant bubble size d_{32} = 3 mm by Scargiali et al. (2007), D) Constant bubble size d_{32} = 3.5 mm (this work), E) CFD-PBM (this work)

Fig. 6-19D. The higher gas hold-ups in the impeller discharge are also predicted pretty well, compared to those obtained experimentally. Gas is present around the lower circulation loop, which indicates a complete dispersion regime has been correctly reproduced by the CFD-PBM-IZ simulation, however the local hold-up is under-predicted compared to Bombac *et al.*'s (1997) measurement. Omission of the effect of turbulence on the drag coefficient is thought to be the main reason for this under-prediction. Similar conclusions were also drawn by

Lane *et al.* (2002) who studied the gas-liquid stirred tank using a combined CFD and the bubble density method. Lane *et al.* (2002) found a significant change in their result when the drag correction due to turbulent by Brucato *et al.* (1998) was employed. However, Brucato *et al.*'s drag correction cause a wrong distribution of the gas hold-up; higher gas hold-up in the lower circulation loop compared to the measured value. As mentioned in section 5.3.1, Brucato *et al.*'s model is formulated for solid-liquid system and thus may not be suitable for bubbly flow. Prediction of the CFD-PBM model in this work may be improved if the effect of turbulence on the drag coefficient is taken into account. However there is no drag correction due to turbulent available for bubbles available from the literature at present.

The pattern of the gas hold-up above the impeller region is not predicted correctly, but nevertheless the predictions are closer to Bombac *et al.*'s measurements. Gas hold-up near the top surface is also predicted well by the CFD-PBM method which shows values of around 2%, similar to those from Bombac *et al.*'s measurements. A slightly higher gas hold-up (3%) is shown in Fig. 6-19D for the case with constant bubble size, due to the fact that bubble size should be much bigger near the liquid surface due to coalescence process (see Fig. 6-20). Essentially, the bubble size stays almost the same above the impeller near the liquid surface, but is not affected by the liquid upper circulation loop as much as the flow just above the impeller (see Fig. 6-21). The gas and liquid phase velocity vectors shown in Fig. 6-21 demonstrate this effect clearly. A weak gas recirculation can be observed just above the impeller (Fig. 6-21A) where a strong liquid recirculation occurs (Fig. 6-21B), whereas no gas circulation occurs near the top liquid surface due to reduced (or no) liquid circulation in that region. Consequently, the bubble rise velocity near the top surface is greater than those just above the impeller (see Fig. 6-21A). Scargiali *et al.* (2007) also over-predicted the gas hold-up near the top surface by up to 50% (3% compared to 2% from Bombac *et al.*'s measurement) in their work which also employed a monodisperse bubble size throughout the tank (Fig. 6-19C).

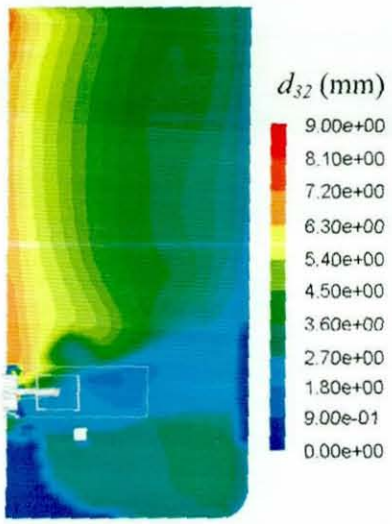

Figure 6-20: Distribution of sauter mean bubble diameter for case 6.4

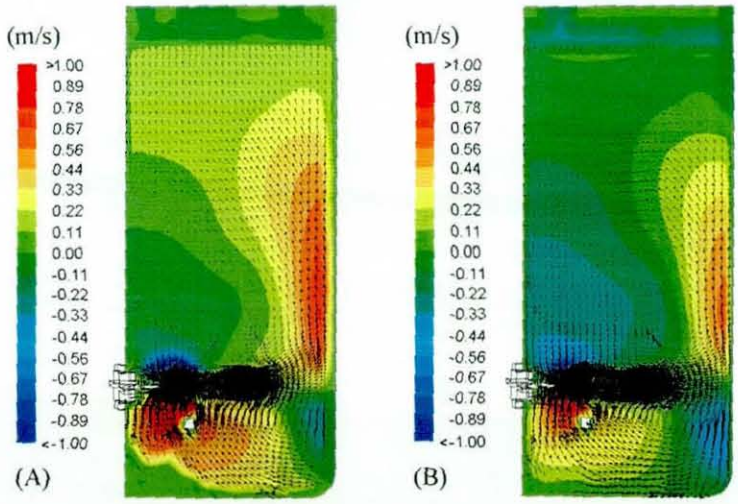

Figure 6-21: Vector plot for case 6.4 the background is contour of axial velocity, A) gas phase vector and axial gas velocity, B) liquid phase vector and axial liquid velocity

There are notable differences between the gas hold-up distributions obtained using CFD simulations with a monodispersed bubble size by Khopkar and Ranade (2006), Scargiali *et al.* (2007) and the one from this work (Figs. 6-19B, 6-19C and 6-19C) due to the different model used to calculate the interfacial force. Khopkar and Ranade (2006) for instance employed the drag correction due to turbulent by Brucato *et al.* (1998). It is not explicitly clear which drag model is employed by Scargiali *et al.* (2007) however they employed a Reynolds averaged two-phase model which tend to have a different treatment

for the interfacial force modelling. The present work employed a Favre averaged two-phase model (standard FLUENT two-phase model). A brief description regarding to this different averaging method was outlined earlier in section 5.3.1. The differences arises from the two averaging technique relate mostly to modelling of turbulent dispersion and interphase forces and thus may affect significantly prediction of gas hold-up distribution (Lane *et al.*, 2002).

There are still some discrepancies in the predicted gas hold-up using the CFD-PBM method because of many other issues such as the limitations of turbulence model and the inherent problem in Eulerian-Eulerian method which utilise the Sauter mean diameter instead of the real bubble size distribution. The bubble sizes at any given point inside the tank cannot be represented by a single bubble size because the local bubble size changes with time and these different bubble sizes have a different magnitude of forces acting to them. The local bubble size distribution at any given time inside the tank is better appreciated by looking at the experimental measurement by e.g. by Barigou and Greaves (1991), Lu and Wu (2001), Alves *et al.* (2004) and Laakkonen *et al.* (2005b). The value obtained from experiment is in fact a combination of effect of the different bubble size from the overall distribution and these may not be captured correctly by the Eulerian-Eulerian model employed in this work. Nevertheless prediction of the local gas hold-up is reasonably accurate despite the simplification. Moreover, the CFD-PBM result is better than those obtained using a constant bubble size by Scargiali *et al.* (2007) shown in Fig. 6-19C. The gas hold-up distribution in the upper region of the tank also shows a better agreement with Bombac *et al.*'s (1997) measurement in Fig. 6-19A; and an improvement compared to those from Khopkar and Ranade (2006) in Fig. 6-19B. As discussed earlier in chapter 5, the influence of the virtual mass and lift force to the gas hold-up prediction may not be significant (Scargiali *et al.*, 2007), despite adding convergence difficulties and increasing the computational demand. Further improvement to the prediction accuracy may also be obtained if the drag correction due to turbulence is considered. However, the model in this current form is more accessible computationally and hence more practical as a design tool.

6.4.4 Prediction of Local Bubble Size

CFD-PBM simulations were performed using a user-defined subroutine compiled within FLUENT. The Prince and Blanch (1990) breakage and coalescence kernels were employed to predict the bubble dynamics throughout the tank. The volume-average Sauter mean diameter, d_{32}, in the impeller region was used as a convergence indicator in these simulations (see Fig. 6-7). For each case (with grid consisting of around 250k cells), the overall simulation process takes at least three weeks of iterations to complete using a Genie workstation fitted with two dual-core Xeon 3.8 GHz processors and 3 gigabyte of RAM.

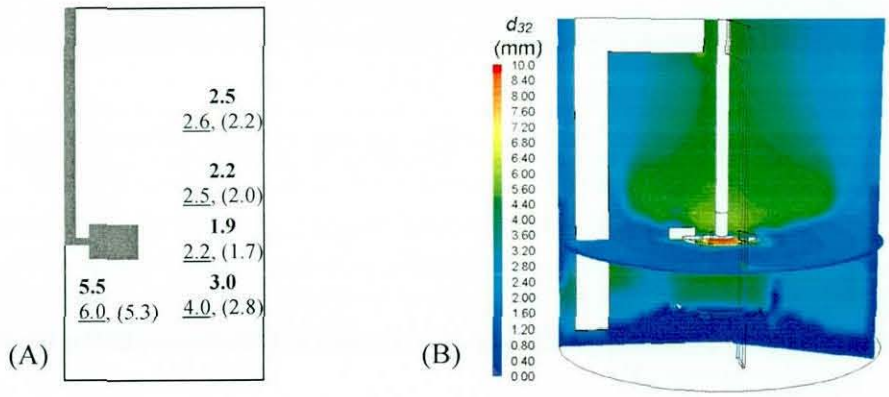

Figure 6-22: Prediction of local Sauter mean bubble diameter (mm) for case 5.2: RDT, 14 L tank, N = 700 rpm, Q_g = 0.7 *VVM*. A) Laakkonen *et al.* (2007a) measurement (bold), CFD-PBM (bracket), Multi-compartment (underlined), B) Contour map of Sauter mean diameter

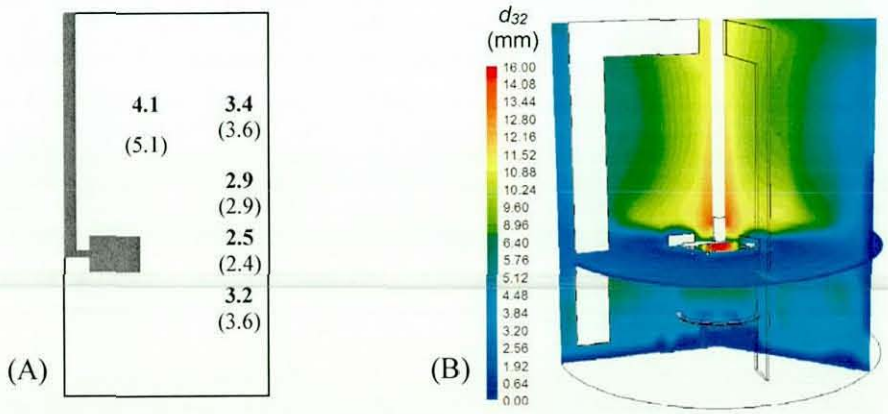

Figure 6-23: Prediction of local Sauter mean bubble diameter (mm) for case 5.3: RDT, 200 L tank, N = 390 rpm, Q_g = 0.7 *VVM*. A) Laakkonen *et al.* (2007a) measurement (bold), this work (bracket), B) Contour map of Sauter mean diameter

Figures 6.22 and 6.23 show that the local bubble sizes predicted by the CFD-PBM simulation for both the smaller and the larger tanks are in good agreement with the experiments by Laakkonen *et al.* (2007a). The smallest bubbles can be observed around the impeller, where the dissipation rates are a maximum, whereas the largest bubbles are found below the impeller, just above the sparger, due to the combination of a high void fraction and low dissipation rates. Some discrepancies in the local bubble size predictions can be observed in the bulk region for the bigger tank, possibly due to the well-known under-prediction of the energy dissipation rates by the k-ε model combined with under-prediction of local gas hold-up around the lower circulation loop. It was known from single compartment study in section 5.4 that the evolution of the bubble size depends mainly on the dissipation rates and the gas void fraction. However, the effect of ε on the local d_{32} predictions is thought to be minimal since the kinetics of the breakage and coalescence depend on ε^c, where |c| is small (0.25 or 0.33). Thus a 30% error in ε gives rise to <10% error in the kinetic rate. The predictions of the gas hold-up may also be compromised by the omission of drag correction due to turbulent flow in the previous section 6.4.3, and thus may affect the prediction of local bubble sizes.

Fig. 6-24 shows distributions of the breakage kernel, the turbulent dissipation rate in the liquid phase, the smaller QMOM abscissa, the coalescence kernel, first weight of QMOM and the gas volume fraction distribution. It is clear from Fig. 6-24A that bubble breakage mainly occurs around the impeller discharge stream, where the turbulent dissipation rate is sufficiently high (see Fig. 6-24B), whereas in the bulk region the breakage kernel is closer to zero indicating minimal (or no) breakage events. The Prince and Blanch (1990) breakage kernel given by eq.(5.13) assumes that only eddies with size larger than $0.2L_i$ are effective for breakage. This assumption may be reasonable for gas-liquid stirred tank because the smaller bubble size is well below 1 mm (~ L_i = 0.28 mm) as shown in Fig. 6-24C. The sub-millimetre bubble is more stable and less likely to be affected by breakage events. The distribution of the breakage kernel shown in Fig. 6-24A also shows the expected distribution i.e. higher breakage around the impeller discharge stream. Thus, it may be concluded that Prince

and Blanch's (1990) assumption of only eddies with size larger than $0.2L_i$ is effective for breakage may be acceptable for gas-liquid stirred tank.

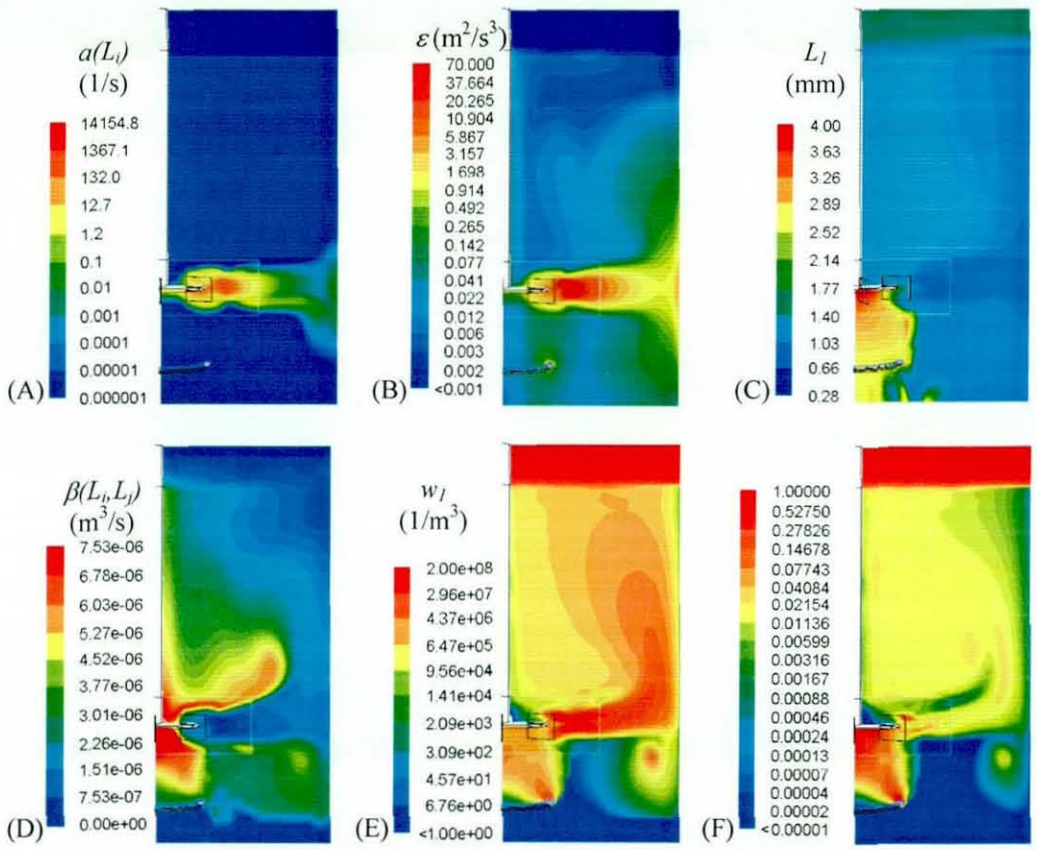

Figure 6-24: Result from CFD-PBM-IZ simulation for case 6.2. A) Breakage kernel, B) Turbulent dissipation rate of liquid phase, C) The smaller QMOM abscissa, D) Coalescence kernel, E) weight of QMOM, F) Gas volume fraction

The coalescence kernel results (see Fig. 6-24D) need much complicated explanation since they are affected by combination of local bubble size and local gas hold-up. The bubble collision frequency in eq.(5.8) is proportional to the L_i^2 which means larger bubbles have more tendency to coalesce. The moments equation for coalescence event also had a proportional relation to the square of the gas hold-up characterised by w_i^2 (number of bubbles per unit volume). Relations between the local gas hold-up and the QMOM weight is much better understood by looking at Figs. 6-24E and 6-24F which show much high value of w_i at locations of high gas hold-ups. Distribution of the QMOM weight is not exactly similar to the gas hold-up because the calculation of weight is also depending on the local abscissa (bubble size); nevertheless the weight

has approximately similar distribution to the gas hold-up. A higher value of the coalescence kernel is spotted at locations with a higher value for both L_i and w_i, such as below the impeller (above the sparger) and within the upper and lower circulation loops.

The CFD-PBM approach is also capable of responding to changes in operating conditions. For instance, case 6.1, which considers a lower impeller speed, produces larger bubbles compared to case 6.2, where the impeller speed is much higher (see Table 6-1). However, the value reported in Table 6-5 is a bit misleading since the volume averaged bubble size also considered the region that has no bubble thus resulting in a smaller bubble size for the case 6.1 than it should be; case 6.1 operates in the loaded regime. Comparison might be fair for cases operating in similar flow regimes because in that way the proportion of the tank with zero gas fraction remains at about the same level. A systematic comparison cannot be made between cases 6.1 and 6.4 with cases 6.2 and 6.3 because of several reasons. Firstly, case 6.1 operates under the loaded regime and has a different sparger size and impeller dimension compared to cases 6.2 and 6.3. Secondly, case 6.4 uses large sparger placed immediately below the impeller and such an arrangement will not cause air accumulation below the impeller disk as in cases 6.2 and 6.3. The air accumulations below the impeller disk cause formation of larger bubbles. A fair comparison may be obtained by comparing results from cases 6.2, 6.3, 6.5, 6.6 and 6.7. According to Calderbank's (1958) correlations, eq.(2.17), the d_{32} is proportional to $(P_g/V)^{-0.4}\alpha^{0.5}$. Laakkonen *et al.* (2005a) obtained a fair agreement between Calderbank's (1958) correlations and their experimental measurement for air-water stirred tank. The volume averaged d_{32} plotted against $(P_g/V)^{-0.4}\alpha^{0.5}$ in Fig. 6-25 shows a good correlation between the bubble size and $(P_g/V)^{-0.4}\alpha^{0.5}$ for an aerated stirred tank agitated with a Rushton turbine. The constant obtained from this correlation is not similar to those from Calderbank's correlation in eq.(2.17) because Calderbank (1958) generated the fit using a non-metric unit while all units employed for this study were SI. Nevertheless, this finding has further confirmed the result from CFD-PBM approach. The correlation is also not dependent on the impeller type, as is shown in Fig. 6-26 where the correlation is essentially similar for Rushton turbine and the CD-6. The best fit line for the CD-

6 impeller is much closer to the case 5.13 in Fig. 6-26 than the case 5.9 in Fig. 6-25 for the Rushton turbine, which eventually led to the difference in the line slope. Theoretically the bubble size should remain the same irrespective of the impeller type if ε (related to P_g/V) and α remain constant as was shown earlier in section 5.4. Findings from this work in Figs. 6-25 and 6-26 also suggest a similar conclusion.

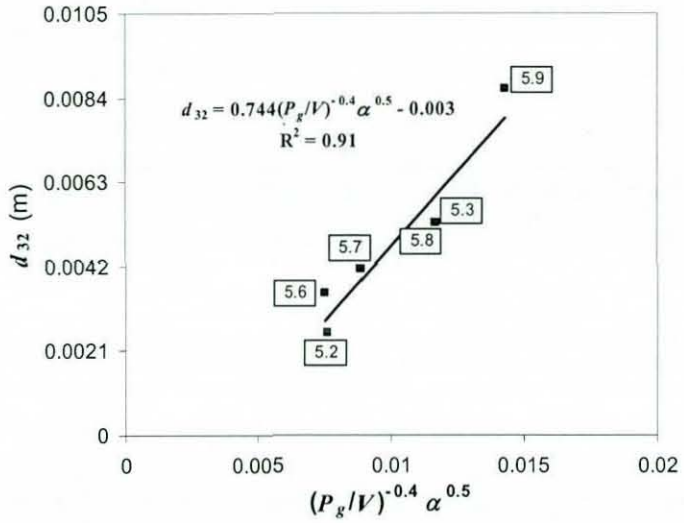

Figure 6-25: Plot of averaged bubble size from CFD-PBM against $(P_g/V)^{-0.4}\alpha^{0.5}$ for stirred tank agitated by a Rushton turbine. The numbers represent the case number in Tables 6-1 and 6-2

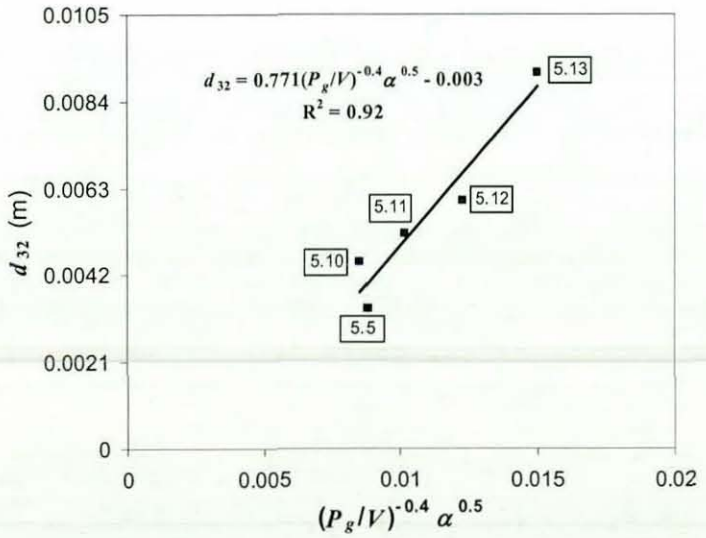

Figure 6-26: Plot of averaged bubble size from CFD-PBM against $(P_g/V)^{-0.4}\alpha^{0.5}$ for stirred tank agitated by a CD-6 impeller. The numbers represent the case number in Tables 6-1 and 6-2

6.4.5 Prediction of Mass Transfer Coefficient

Having obtained the local bubble size from the CFD-PBM simulation, the local k_La can be estimated using Higbie's penetration theory or the surface renewal model of Danckwerts. For the smaller tank (14L) the penetration theory gave a significantly higher value of k_La (see Fig. 6-27A) due to its sensitivity towards the smaller bubble sizes. In contrast, for the bigger tanks (200L and 1500L), the Danckwerts model gave slightly higher k_La values around the impeller region. Similar trends were also found for the evolution of the oxygen transfer rate in Fig. 6-28 and the $\langle k_La \rangle$ values in Table 6-5 (compare cases 6.5, 6.8 and 6.9). In eq.(6.11) for Higbie's model the $k_La \propto L_i^{1.5}$ whereas for Danckwerts model in eq.(6.14) the $k_La \propto L_i^2$. So for a small bubble, say a 1 mm bubble, the difference in k_La caused by the bubble size alone for Higbie's model is about 30 times ($0.001^{1.5}/0.001^2$) larger than the Danckwerts model. However, the k_La estimated from both models did not differ by a magnitude of 30 because of the different assumptions for calculating the contact time. The contact time is assumed constant for Higbie's model which is characterised by d_i/u_{slip}, whilst Danckwerts' model assumes a variable contact time depending upon the rate of eddy renewal at surface of the bubble expressed as $(\varepsilon_l/\nu_l)^{0.5}$. The differences between the k_La estimated by these two different methods appear to be minimal and both can be employed to predict the mass transfer in gas-liquid stirred tanks with reasonable accuracy.

The maximum local k_La values for the larger tank (Figs. 6-27B and 6-27C) were significantly smaller (roughly 40% less) than for the smaller tank (Fig. 6-27A), due to the bigger mean bubble size (see Table 6-5), which consequently reduced the interfacial area. However, the volume averaged k_La shown in Table 6-5 for a constant P_g/V and VVM indicates a much higher value due to a much higher aeration number for the bigger tanks compared to the smaller tank when VVM is kept constant. The local k_La contour map also revealed a large dead zone in the bottom region of the tank due to the poor gas dispersion produced by the Rushton turbine. All cases considered in this chapter are operating at impeller speed higher than the critical speed for full dispersion, N_{CD}, except for

case 6.1 (see Tables 6-1 and 6-2). However, the model at present cannot predict the gas hold-up in the lower circulation loop accurately, as discussed in section 6.4.3. It is not possible to discuss further the effect of gas hold-up on the predicted mass transfer coefficient at this stage due to lack of experimental data for comparison but further explanation will be elaborated when comparing the predicted and measured $\langle k_L a \rangle$.

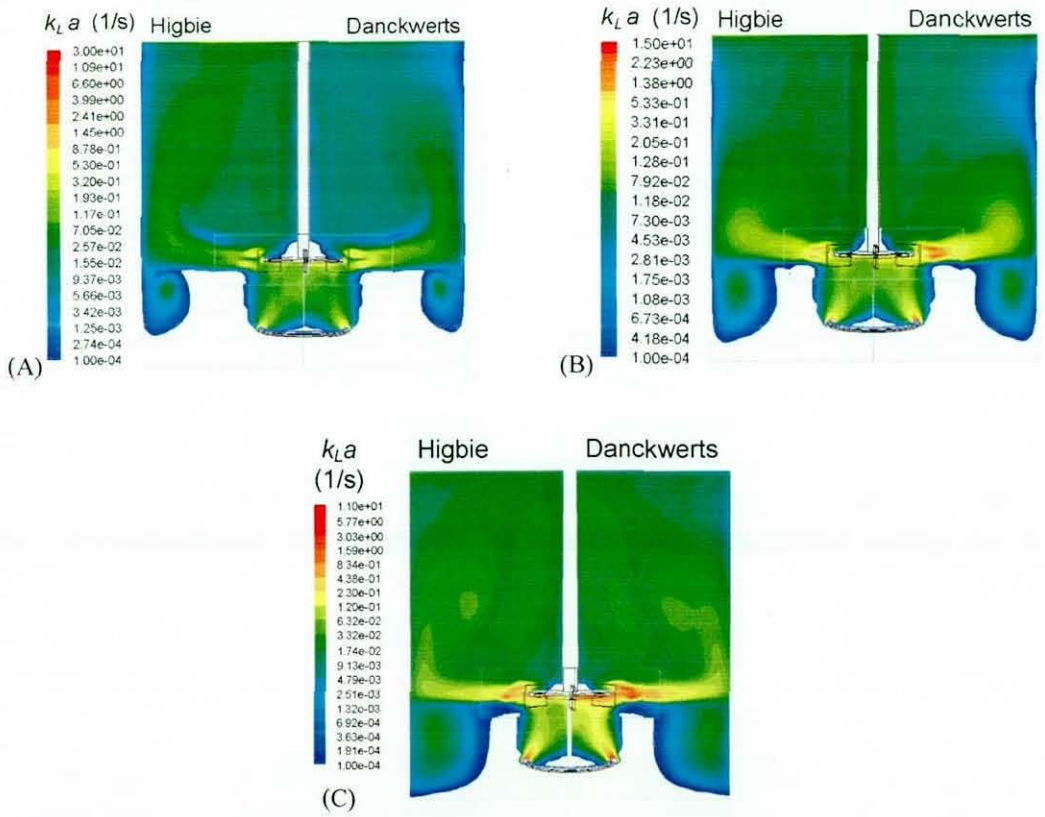

Figure 6-27: Prediction of local $k_L a$ with a RDT. A) 14 L tank (case 6.2), B) 200 L tank (case 6.8), C) 1500 L tank (case 6.9)

By analogy with experimental measurements, which often assume a well-mixed liquid phase, a representative of global value, $\langle k_L a \rangle$ was estimated by monitoring the oxygen concentration at any position inside the tank throughout the simulation, from

$$\ln\left(\frac{C_o^* - C_o(t)}{C_o^* - C_o(0)}\right) = -\langle k_L a \rangle t \tag{6.18}$$

where C_o^* and $C_0(t)$ are the oxygen solubility in water and the oxygen concentration in a specific location at any time t, respectively. This is not to say

that the oxygen concentration in the vessel is well-mixed; the method simply allows a comparison with experimental data which have been analysed in the similar way. According to Grenville and Nienow (2004), a correlation for mixing time to reach the 95% homogeneity for all impellers at all the scales may be estimated as follow:

$$\theta_{95} = \frac{5.2}{N_p^{1/3} N} \left(\frac{T}{D} \right)^2 \tag{6.19}$$

where N_p, N, D and T is the power number, impeller speed, impeller diameter and tank diameter, respectively. This correlation gives mixing time values ranging from 3.2 s to 9.1 s for case 6.2 and 6.9. The $1/\langle k_L a \rangle$ values for case 6.2 and 6.9 are 43.5 and 37 s respectively, which is about one order of magnitude greater, confirming the perfect mixing assumption employed in this work. It has to be noted that eq.(6.18) is only valid for a poorly soluble gas such as oxygen in water, where the liquid-phase mass transfer resistance is dominant over the gas-phase mass transfer. Values of $\langle k_L a \rangle$ were obtained from the slopes of the graphs obtained by plotting the left hand side of eq.(6.18) against time. Fig. 6-29 shows the evolution of the dissolved oxygen concentration, $C_0(t)$, calculated using the Higbie and Danckwerts methods, respectively. The $C_0(t)$ were obtained from a point placed at impeller discharge. The predicted $C_0(t)$ profile is in fair agreement with the experimental measurement from Laakkonen *et al.* (2007b) especially when an oblate spheroid shape is considered for the bigger bubbles. As expected, the discrepancy is much bigger when bubbles assumed to have a spherical shape throughout the tank which may not be correct for diameters > 1 mm. As mentioned by Montante *et al.* (2006), no bubble appeared completely in a spherical shape from their photographic observations in stirred tanks, except for the bubbles smaller than 1 mm. Due to its better prediction of the $C_0(t)$ evolution, the combined spherical and oblate spheroid model is applied for the remainder of this work.

The discrepancy of the $C_0(t)$ prediction may be introduced by the under-prediction of gas hold-up mentioned earlier in section 6.4.3. Under-prediction of gas hold-up yielded a smaller bubble size because it reduces the probability of bubble-bubble collisions which often led to bubble coalescence. The predicted

local bubble sizes in the impeller discharge stream where most of the mass transfer occur are slightly smaller (see Figs. 6-22 and 6-23) than those observed experimentally by Laakkonen *et al.* (2007a). However, these slight under-prediction of local bubble sizes may not result in over-prediction of the mass transfer coefficient because the mass transfer coefficient is affected by both the gas hold-up and bubble size. Thus, the effect of the smaller bubble on the mass transfer coefficient is balanced by the lower gas hold-up. Nevertheless, predictions of mass transfer by the CFD-PBM model are reasonable despite it being compromised by under-prediction of the gas hold-up.

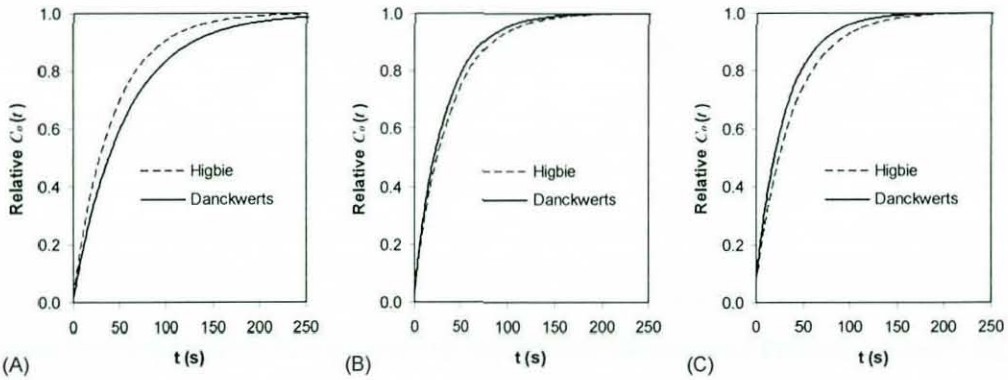

Figure 6-28: Comparison between the $C_0(t)$ evolution calculated using two different method at impeller level for tank agitated with RDT at constant P_g/V and VVM. Relative $C_0(t)$ is $C_o(t)/C_o^*$. a) case 6.2, b) case 6.8, c) case 5.9

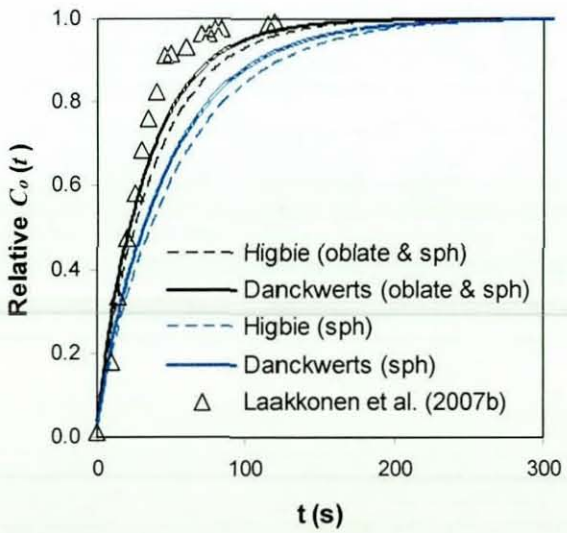

Figure 6-29: Prediction of $C_0(t)$ evolution for case 6.3 at impeller level, N = 390 rpm and Q_g = 0.7 VVM. Data points from Laakkonen *et al.* (2007b).

Higbie's method is found to have a slightly faster oxygen transfer rate than the Danckwerts's method for a smaller vessel (see Fig. 6-28A), where the mean number bubble size (d_{10}) is less than 1.5 mm, but the opposite happens for the larger vessels (see Figs. 6-28B and 6-28B) when the d_{10} is larger than 2 mm. This is also reflected in the calculated values of the $\langle k_L a \rangle$ shown in Table 6-5, for cases 6.2, 6.8 and 6.9. As explained earlier both models have a different sensitivity towards a different bubble size with the Higbie's model more sensitive to the smaller bubbles (~ 1 mm).

The $C_0(t)$ evolution was recorded at three different locations inside the tank namely the dead zone below the sparger, the impeller region and bulk region above the impeller. Only a small amount of variation was found between the $\langle k_L a \rangle$ values estimated using these $C_0(t)$ evolutions (see Fig. 6-30), hence the remaining discussion focuses only on the data recorded at impeller discharge, where the majority of experimental measurements are usually made. In eq.(6.18), and often in experimental measurements of the mass transfer coefficient, it is assumed that the dissolved oxygen concentration, $C_0(t)$ is uniform. Results from the CFD-PBM simulations suggests that this assumption is applicable for the lab and pilot scale gas-liquid vessels shown in Figs. 6-31 and 6.32, without the presence of an oxygen sink (*i.e.* a reaction or micro-organism respiration). There is a little difference between the evolution of oxygen concentrations for 14L and 1500L tanks except there is a visibly lower

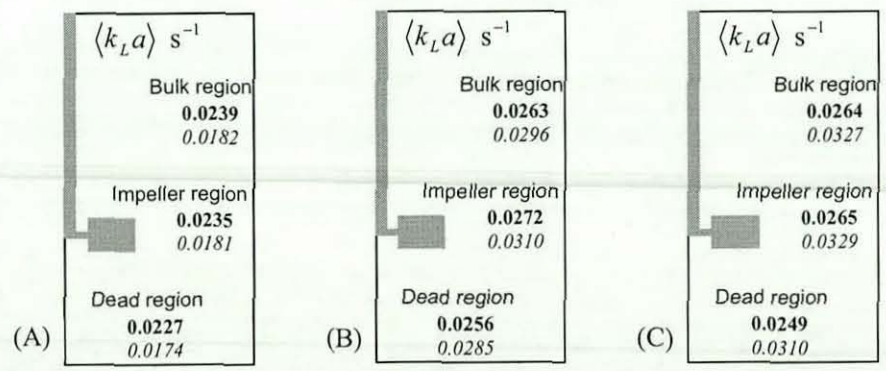

Figure 6-30: Comparison between the $\langle k_L a \rangle$ estimated using the $C_0(t)$ evolution obtained at different position inside the tank at constant P_g/V and VVM, A) Case, B) case 6.8, C) case 6.9. Higbie's method (bold font), Danckwerts's method (italic font)

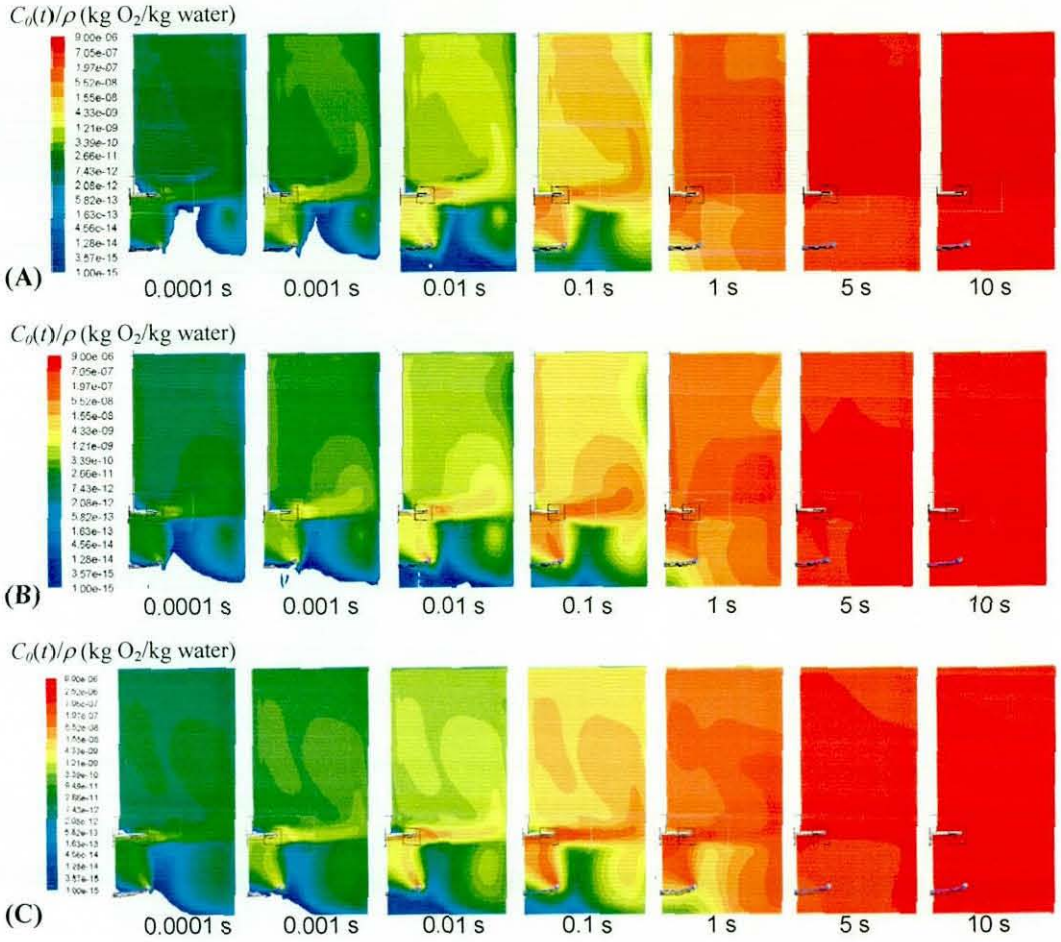

Figure 6-31: Evolution of oxygen concentration in aerated stirred tank agitated with a RDT operating at the same P_g/V and VVM. The mass transfer coefficient estimated using Higbie's model. A) 14 L case 6.2, B) 200L case 6.8, C) 1500L case 6.9

oxygen concentration below the sparger for the bigger tanks (200L and 1500L) at 1 second. However, there is little difference in the oxygen concentration contour after 5 second. The region below the sparger is also known for its poor mixing and was indicated as a dead region (see Fig. 6-27) which is due to absence of gas circulation in this region (see Figs. 6-24F). Assumption of a uniform $C_0(t)$ may not be valid in a gas-liquid bioreactor, even at small scale, depending on the local rate of consumption of dissolved oxygen. In such a case, the $C_0(t)$ may fall towards zero within dead regions leading to a severe mass transfer limitation. The well-mixed assumption is also less likely to be correct with increasing scale of operations (Schuetze and Hengstler, 2006), especially when dealing with industrially sized vessels. Thus in practice, the $C_0(t)$ may be non-uniform, being almost saturated in some locations where there

is a high local k_La, and having a low $C_0(t)$ in regions with poor gas dispersion. It may be concluded that simple volume averages of k_La from CFD simulations, without knowledge of their correlation with local driving forces, are of little practical use; they would tend to be larger than the $\langle k_La \rangle$ values obtained by experiment, or from eq.(6.18). However, a CFD calculation which solves the oxygen transport equation, coupled with local values of k_La takes this effect into account, and can serve as a more correct framework for the design and scale-up of aerated stirred tanks than methods that use eq.(6.18) with volume averaged quantities.

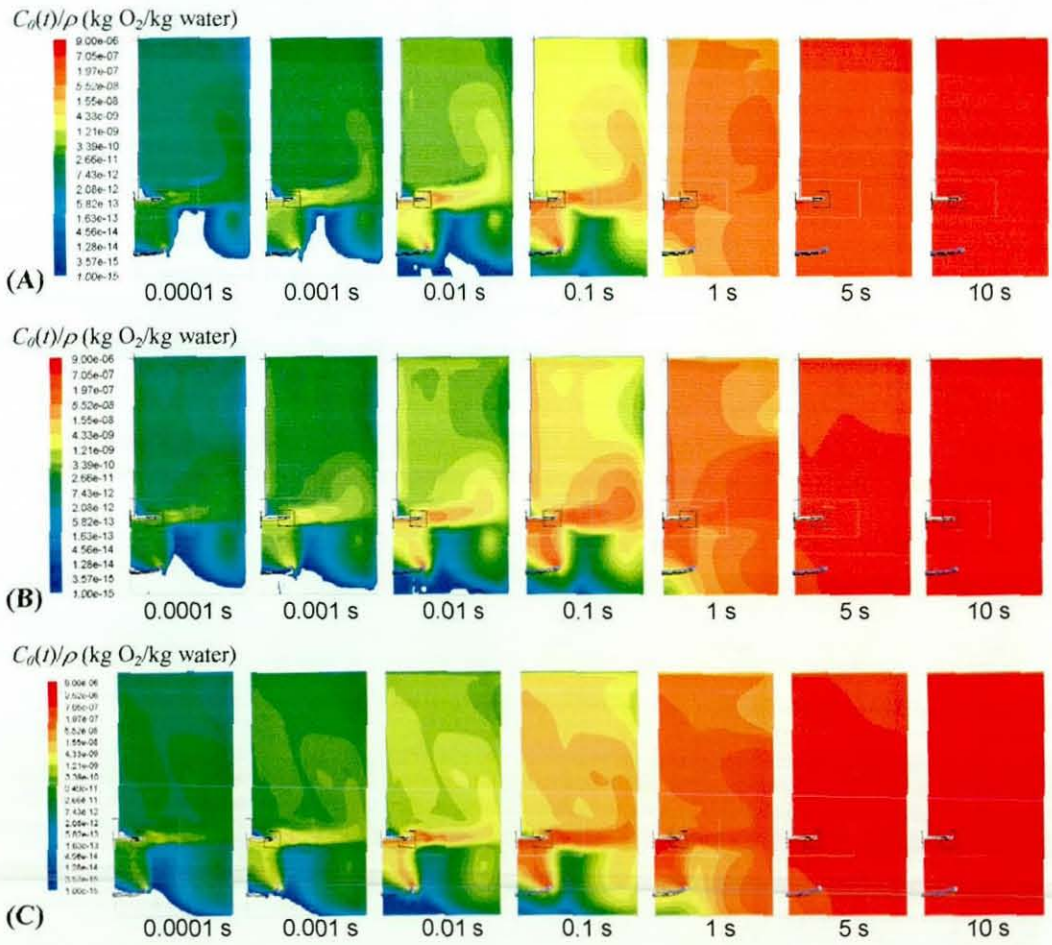

Figure 6-32: Evolution of oxygen concentration in aerated stirred tank agitated with a RDT operating at the same P_g/V and VVM. The mass transfer coefficient estimated using Danckwerts's model. A) 14 L case 6.2, B) 200L case 6.8, C) 1500L case 6.9

Volumetric mass transfer coefficients, $\langle k_La \rangle$, for air-water stirred tanks might be estimated from a correlation as a function of P_g/V and superficial velocity such

as the one given in chapter 2 (see eq. 2.20). One of those correlations suggested by van't Riet was said to be applicable for a vessel of volume ranging from 2 to 2600 L and for P_g/V ranging from 500 to 10000 W/m^3 with an accuracy of approximately 20-40% (van't Riet, 1979). Comparison between the $\langle k_L a \rangle$ estimated using eq.(2.20) and the CFD-PBM model evaluated in this work (using the $C_0(t)$ evolution at the impeller region) is presented in Table 6-5. The relative error from the $\langle k_L a \rangle$ value obtained from eq.(2.20) and the CFD simulations ranged from 3% to 56%, with a larger error for the bigger vessel i.e. cases 6.9 and 6.13. Correlations such as eq.(2.20) are known to be problematic when applied to tanks of different size from that of the original experiments. For instance, Garcia-Cortes *et al.* (2004) reported a deviation up to 18% from their experimental measurements in a 5 L tank; earlier Zhu *et al.* (2001) reported about a 20% discrepancy for a 120 L tank. There is also a concern about the CFD prediction knowing the poor prediction of ε by the k-ε turbulence model, as is indicated by the prediction of the gassed power number from the ε integration in Table 6-4. However, as was discussed previously in section 6.4.4, the effect of ε on the bubble size is thought to be minimal since the kinetics of the breakage and coalescence depend on ε^c, where |c| is small. Although ε may not be predicted accurately in some regions inside the tank, the k-ε model appears to predict ε satisfactorily around the impeller region, as shown in Fig. 3-8 for the single phase stirred tank. Application of a uniform scaling factor for local values of ε, e.g. as used by Lane *et al.* (2005), may then lead to an overestimate of ε in regions of high breakage rate and hence was not considered appropriate in the current work.

The $\langle k_L a \rangle$ obtained from eq.(6.18) is also consistently shown to be somewhat smaller than the volume averaged $k_L a$ (see Table 6-5). These two quantities are in fact a different measure of the mass transfer coefficient. As stated earlier (see description of eq.(6.18)) $\langle k_L a \rangle$ takes into account the effect of the driving force on the overall mass transfer rate, whereas the volume-averaged $k_L a$ value does not.

6.4.6 Comparison of the Mass Transfer Rates in Aerated Stirred Tanks Agitated by a Rushton Turbine and a CD-6 Impeller

Comparison between the gas dispersion performances of the CD-6 impeller and the Rushton turbine have been evaluated experimentally by many researchers e.g. Bakker and Benz (1996); Myers *et al.* (1999); Zhu *et al.* (2001); Smith *et al.* (2001); Paglianti *et al.* (2008). Most of the previous experimental work deals with gassed power drop and the volumetric mass transfer coefficient. Much earlier works on concave impellers, e.g. by Warmoeskerken and Smith (1989) also exist but the impellers used in their work showed only limited similarity to the CD-6 design. Generally, the CD-6 impeller is known to maintain a high value of P_g/P_0 but has a slightly lower mass transfer coefficient compared to the Rushton turbine at the same P_g/V.

CFD studies of concave type impellers are quite rare in the literature. Bakker and Benz (1996) presented a study of gas-liquid stirred tank agitated with multiple CD-6 impellers, but no comparisons were made to experimental measurements. Vlaev *et al.* (2004) performed a CFD simulation on a single phase stirred tank agitated with either a Rushton turbine, a shallow and a deep concave blade design. Their study shows higher pressure difference at the surface of impeller blade for Rushton turbine than the concave impeller which explains the higher power number for the Rushton turbine compared to the concave impeller. No comparison was made to experimental measurements in Vlaev *et al.*'s work. Khopkar *et al.* (2004) performed CFD simulation of a single phase and an aerated stirred tank agitated by a Scaba (concave type) impeller. They presented a fair prediction of the single phase mean velocities and turbulent kinetic energy compared to their PIV measurement. Khopkar *et al.* (2004) also made a limited comparison for the gas-liquid prediction by comparing qualitatively the measured mean velocity vectors to the CFD prediction. They also compared the vorticity magnitude behind the impeller blade for a Rushton turbine and a Scaba impeller, but no comparisons were made for the size of gas cavity. Recently, Min *et al.* (2008) performed a CFD-PBM study of aerated stirred tank agitated by a combination of two axial impellers and a BT-6 impeller (concave type). They employed the method of classes available within the CFX code (MUSIG) to solve the population balance equation in their work. They managed to obtain a good prediction of the axial

gas hold-up profile compared to their experimental measurement. From this brief review it is clear that no comprehensive CFD study has been performed to compare the performance of both the Rushton turbine (conventional impeller) and the CD-6 impeller (advanced gas-liquid impeller). It is of great interest to evaluate the predicting capability of the CFD-PBM model for an advanced impeller such as the CD-6. Thus a detail comparisons was performed in this work for a CD-6 impeller and a Rushton turbine operating at similar P_g/V, v_g and VVM (cases 6.2 and 6.5).

Fig. 6-33 shows the predicted gas hold-up for aerated stirred tanks agitated by a Rushton turbine and a CD-6 impeller. The CFD-PBM result managed to reproduce correctly the experimentally observed smaller gas cavity for the CD-6 impeller compared to the Rushton turbine which is responsible for the smaller reduction in aerated power number for the CD-6 impeller. Predictions of aerated power number have been discussed previously in section 6.4.2. The CFD result also shows a slightly higher gas fraction for the CD-6 impeller especially in the bulk region above the impeller.

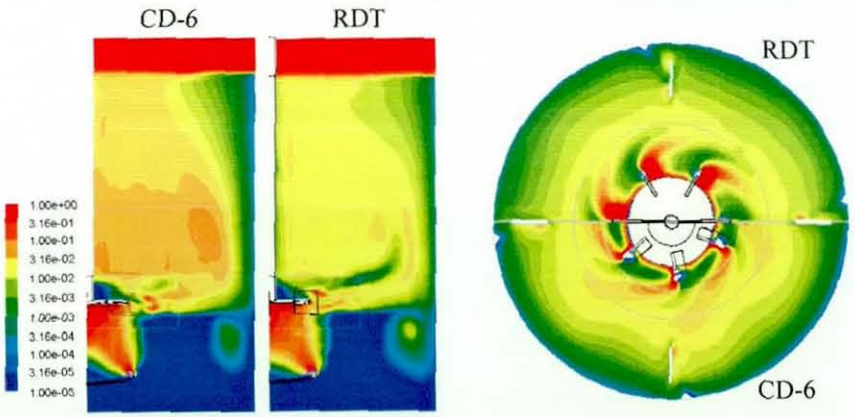

Figure 6-33: Comparison between the predicted local gas hold-up for aerated stirred tank agitated with RDT (case 6.2) and CD-6 (case 6.5), both operating at the same P_g/V, v_g and VVM

The CD-6 impeller shows much lower turbulent kinetic energy than the Rushton turbine (see Fig. 6-34) due to a higher reduction in power number and formation of much larger gas cavity by the Rushton turbine. The CFD-PBM predictions in this study are in agreement with Kovac *et al.*'s (2001) who found a lower turbulent kinetic energy for the Scaba impeller (comparable to CD-6) compared to the Rushton turbine from experimental measurement. For a single phase flow

the CD-6 has a turbulent power number around 3 whilst the Rushton turbine has around 5. During aeration the power number for CD-6 reduces by about 30% whereas up to 70% reduction is observed for the Rushton turbine due to formation of gas cavity discussed earlier. This gas cavity which is moving along the trailing vortices behind the impeller blade tends to have a more random flow and hence much higher turbulent kinetic energy. Similar distributions are also shown for the turbulence dissipation rate in Fig. 6-35 which shows much lower ε_{max} values for the CD-6 compared to the Rushton turbine.

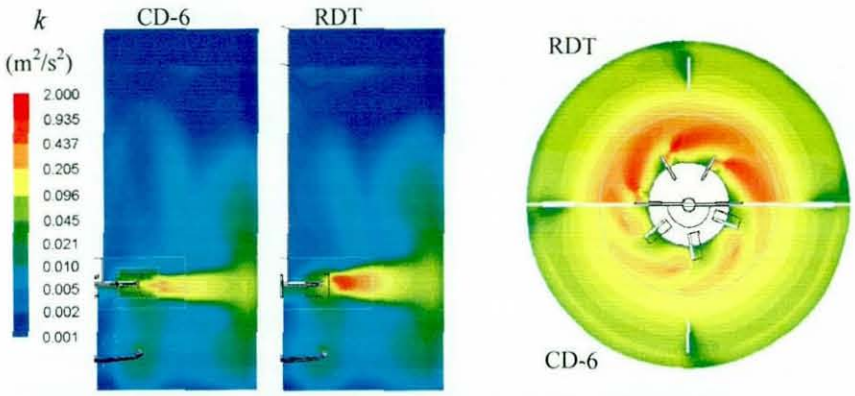

Figure 6-34: Comparison between the predicted liquid phase local turbulent kinetic energy for aerated stirred tank agitated with RDT (case 6.2) and CD-6 (case 6.5), both operating at the same P_g/V, v_g and VVM

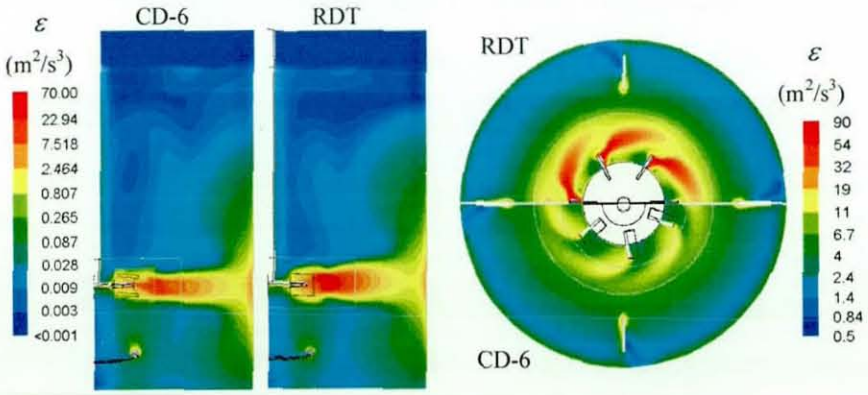

Figure 6-35: Comparison between the predicted liquid phase local turbulent dissipation rate for aerated stirred tank agitated with RDT (case 6.2) and CD-6 (case 6.5), both operating at the same P_g/V, v_g and VVM

Fig. 6-36 shows the contour map of local bubble size for the tank with a Rushton turbine and a CD-6 impeller. Both the mean number bubble size and the Sauter mean diameter for the tank agitated by CD-6 impeller are shown to be much larger than in the case of the Rushton turbine due to the combination

of higher gas hold-up and lower turbulence dissipation rate for the CD-6 impeller. Higher gas hold-ups favour bubble coalescence events because they increase the chances of bubble-bubble collision. On the other hand, lower turbulence dissipation rates reduce the breakage rate; the equilibrium between these higher coalescence rates and the lower break-up rates for the CD-6 impeller result in bigger bubbles.

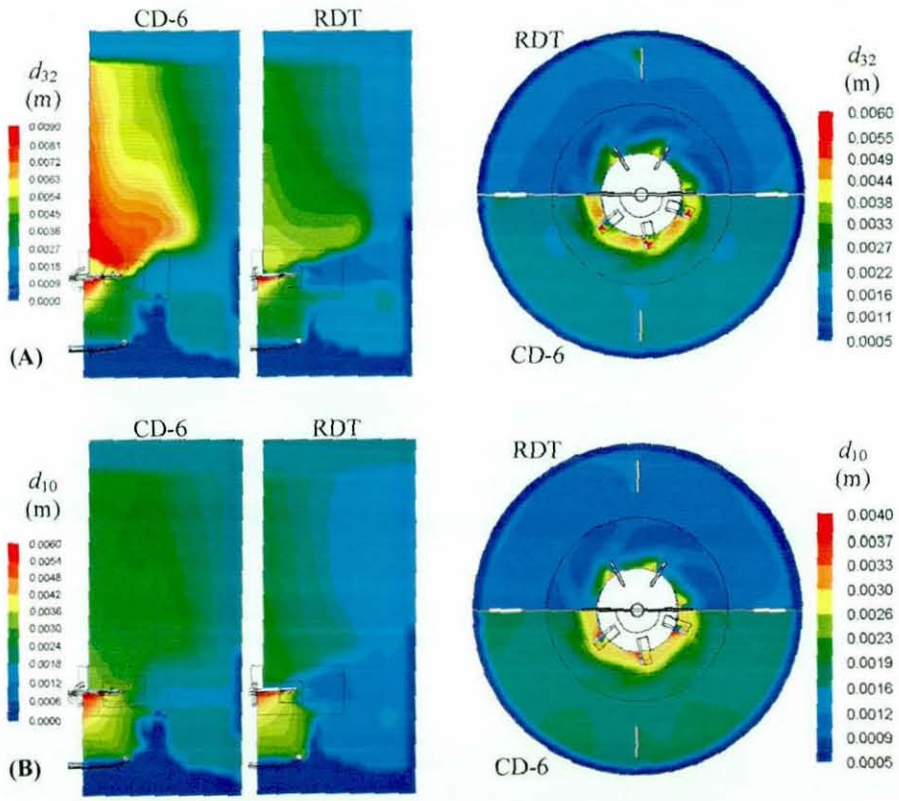

Figure 6-36: Comparison between the predicted local bubble size for aerated stirred tank agitated with RDT (case 6.2) and CD-6 (case 6.8) both operating at the same P_g/V, v_g and VVM, A) Sauter mean diameter, B) Mean number diameter

Consequently, these bigger bubble sizes yielded a much lower value of local k_La as shown in Fig. 6-37 compared to the values for the Rushton turbine in Fig. 6-27. This is due to the lower interfacial area resulting from the bigger bubbles. Reduction of the local k_La is also reflected in the lower values of the predicted $\langle k_La \rangle$ for CD-6 impeller in Table 6-5 and the oxygen transfer rate in Figs. 6-38 and 6-39. In addition to the comparison for the small tank (14L), the results obtained from 200L and 1500L tanks are also presented in Figs. 6-38 and 6-39.

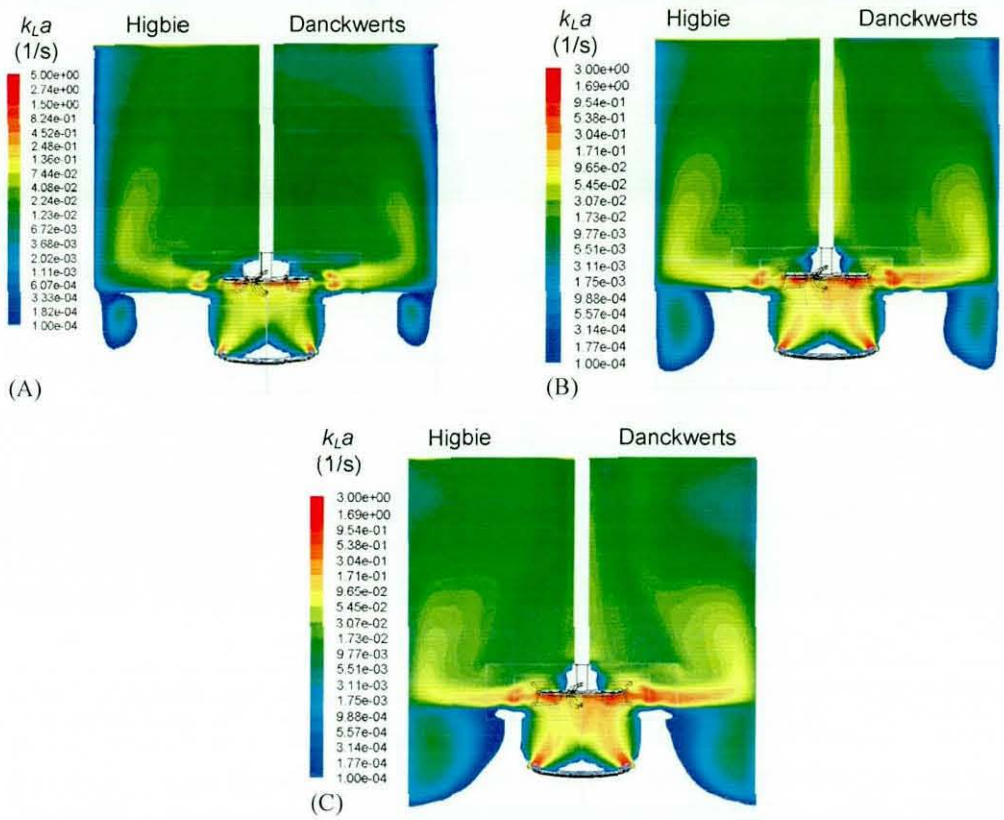

Figure 6-37: Prediction of local k_La with a CD-6. A) 14 L tank (case 6.5), B) 200 L tank (case 6.12), C) 1500 L tank (case 6.13)

Results for the bigger tanks also follow the trend of the smaller tanks except the difference between the CD-6 and the Rushton turbine is much smaller for the 1500L tank. This phenomenon can be explained by calculating the effect of the mean bubble size (d_{10} in Table 6-5) on the local k_La. For Danckwerts' model, the $k_La \propto L_i^2$, which means for the smaller tank (cases 6.2 and 6.5), where the mean bubble size is 1.3 mm and 2.0 mm respectively, the difference caused by the bubble size alone is around 60%. Whereas for the bigger tank (cases 6.9 and 6.13), where the mean bubble size is 3.5 mm and 4.2 mm respectively, the differences caused by the bubble size is just around 30%. Similar trends were observed for Higbie's model where the $k_La \propto L_i^{1.5}$, which translate to about 50% difference in k_La for the smaller tank and around 20% difference for the bigger tank, considering effect of bubble size alone. Of course the bubble size is not the only factor affecting the local k_La, as these value are affected by the local gas hold-up as well, which is why the difference in the predicted $\langle k_La \rangle$ is not as much as 10%.

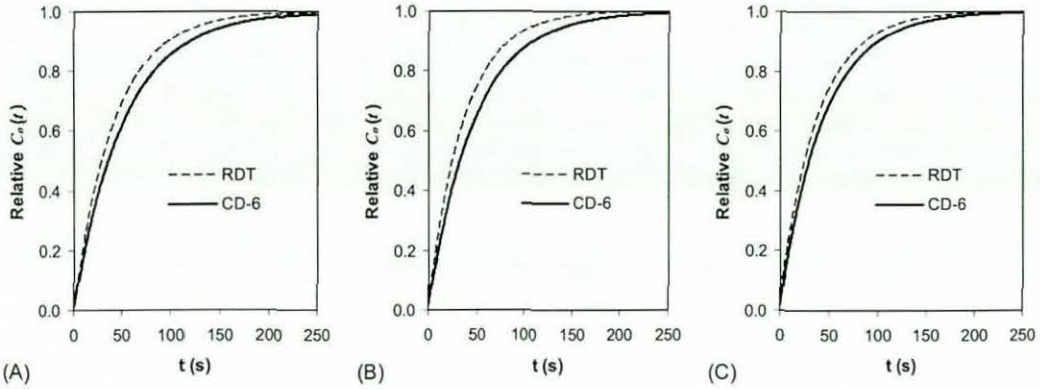

Figure 6-38: Comparison between the oxygen transfer rate calculated using Higbie's method for aerated stirred tank agitated with RDT and CD6 operating at the same P_g/V and VVM, A) cases 6.2 and 6.5, B) cases 6.8 and 6.12, C) cases 6.9 and 6.13

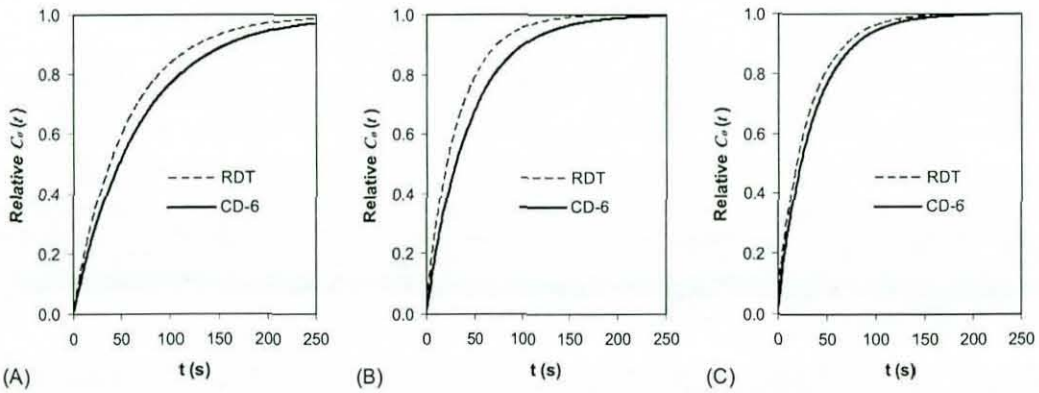

Figure 6-39: Comparison between the oxygen transfer rate calculated using Danckwerts's method for aerated stirred tank agitated with RDT and CD6 operating at the same P_g/V and VVM, A) cases 6.2 and 6.5, B) cases 6.8 and 6.12, C) cases 6.9 and 6.13

6.4.7 Assessment of the Influence of Scale-up on the Mass Transfer Rate in Aerated Stirred Tanks

This section focuses on the scale-up study of gas-liquid stirred tanks, especially from the perspective of the mass transfer rate. Correct prediction of the $\langle k_L a \rangle$ is a crucial step in the design, operation and scale-up of bioreactors (Ochoa and Gomez, 2009). Scale-up is a part of the commercialisation process which involves a change in production capacity from a laboratory scale study to a pilot or production scale. The main aim for gas-liquid stirred tanks i.e. bioreactor scale-up is to achieve a similar performance such as the growth rate and product yield, for both the production and laboratory scales. Theoretically, the performance of the bigger tank could match the smaller one (lab scale vessel) if

the production rate can be maintained in the bigger vessel. However, in most cases the production rate in aerated bioreactors is hampered by poor mass transfer, mainly the oxygen transfer from gas to the liquid phase. It has been proven experimentally for aerobic fermentation that the production rate in the bigger vessel can match those in a smaller vessel if the mass transfer rate can be maintained (e.g. Flores *et al.*, 1997; Shukla *et al.*, 2001; Bandaiphet and Prasertsan, 2006; Islam *et al.*, 2008). However, details about the operating variables such as the P_g/V, Fl_g, VVM and v_g needed to achieve a repeatable successful scale-up are not described in the above-mentioned work. Thus the scale-up study without information about its operating variable is of little practical use because they cannot be used for design purpose.

Oldshue (1966) performed a scale-up of gas-liquid stirred tank from 2L to 20L. Oldshue (1966) studied the effect of conserving a single variable such as P_g/V, impeller Reynolds number, impeller speed and impeller tip speed to the $\langle k_L a \rangle$ for a gas-liquid stirred tank of 2L and 20L. Oldshue's findings suggest that it is impossible to maintain all the parameters in the same ratio to one another for a successful scale-up. Figueiredo and Calderbank (1979) studied geometrically similar tanks with operating volumes of 43L and 600L and their findings suggest a successful scale-up may not be achieved by keeping the combination of P_g/V and v_g or P_g/V and VVM constant. Their findings suggest that the $\langle k_L a \rangle$ decreases with increasing tank size when constant P_g/V and v_g are applied; whereas the $\langle k_L a \rangle$ increases with increasing tank size when constant P_g/V and VVM are employed. Their study implies that the constant P_g/V and VVM criterion is a more conservative scale-up approach. Garcia-Ochoa and Gomez (2009) provided a detail review on the scale-up of gas-liquid bioreactors from the oxygen transfer rate perspective. Their reviews cover both the measurement techniques for oxygen transfer rate and volumetric mass transfer coefficient. They also provide a brief review about previous scale-up studies on aerated stirred tank. They concluded none of the available scale-up approaches i.e. constant P_g/V, oxygen transfer rate, k_La and shear rate can be used as a sole general method because their success depends on the process conditions. They concluded the constant oxygen transfer rate method is the most suitable

scale-up approach for aerobic fermentation based on the results reported in the literature e.g. Flores *et al.*, 1997; Shukla *et al.*, 2001; Bandaiphet and Prasertsan, 2006; Islam *et al.*, 2008. Most of the previous scale-up studies deal with conventional gas dispersion impellers such as the Rushton turbine. It is of great interest to evaluate the scale-up approach for the advanced gas dispersion impeller such as the CD-6 which is capable of handling higher gas loading and has lower gassed power drop compared to Rushton turbine.

Recently, CFD-PBM has been employed to predict the mass transfer in gas-liquid bioreactors by several authors (e.g. Dhanashekaran *et al.*, 2005; Laakkonen *et al.*, 2006a). Dhanashekaran employed a CFD-PBM simulation to predict the mass transfer coefficient in an airlift reactor, where the solution of the population balance equation was provided by method of classes. They reported a fair agreement compared to the experimental measurements from Kawase and Hashimoto (1996) despite using a standard drag model (Schiller-Naumann, 1935). Laakkonen *et al.* (2006a) performed a simulation and experimental study on xanthan fermentation in aerated stirred tank bioreactor. They employed a population balance modelling solved via method of classes for the bubble dynamics modelling. The two-phase modelling was realised with an Eulerian-Eulerian model, the k-ε turbulence model and a drag model suitable for spherical and distorted bubble was also considered. The reaction kinetics for xanthan fermentation were modelled according to Garcia-Ochoa *et al.* (2000) and the mass transfer modelling was via Higbie's (1935) model. Laakkonen *et al.* (2006a) managed to obtain a good prediction of the bubble size, mass transfer coefficient and gassed power number for the two different tank size (194L and 640L) considered in their work. Thus CFD-PBM was employed in this work following the previous work by Dhanashekaran *et al.* (2005) and Laakkonen *et al.* (2006a). However, solution for the population balance equation in this work is provided by the QMOM described previously in sections 4.3 and 5.3.3 instead of the method of classes.

The effect of scale-up on the mass transfer rate in gas liquid stirred tanks with the operating volume ranging from 14L to 1500L was evaluated. It is impossible to keep all quantities constant at different scales, but it is feasible to maintain a couple of variables *i.e.* a combination of P_g/V and either Fl_g, VVM or v_g. It is

generally accepted that constant P_g/V should be maintained, since it directly affects the local energy dissipation rate, which is the key hydrodynamic variable in the breakage and coalescence kernels. Three combinations of scale-up approaches were applied going from the 14L to the 1500L vessels, namely constant P_g/V and either Fl_g, VVM or v_g. Table 6-5 shows that for all three cases (6.2, 6.6, 6.7, 6.8 and 6.9) for RDT and (6.5, 6.10, 6.11, 6.12 and 6.13) for CD-6 impeller, approximately the same values of the global $\langle k_L a \rangle$ were obtained from the CFD-PBM calculation which is also reflected in the $C_0(t)$ evolution shown in Figs. 6-40 and 6-41. None of the scale-up approaches considered in this work could maintain the $\langle k_L a \rangle$ perfectly. If Higbie's model is employed for the evaluation purpose, a similar $\langle k_L a \rangle$ level is more likely to be achieved by keeping the P_g/V and VVM constant for RDT, *i.e.* this rule provides a more conservative design. If the Danckwerts model is used, fixing the P_g/V and Fl_g constant may be able to yield a similar $\langle k_L a \rangle$ level. Maintaining constant v_g gave a slight reduction in $\langle k_L a \rangle$ whereas constant VVM led to slight increase. This finding is in agreement with experimental observations by Figueiredo and Calderbank (1979) who studied geometrically similar tanks of 43L and 600L agitated by a Rushton turbine. At constant P_g/V, the bubble sizes and number per unit volume (L_i and w_i from QMOM) only depend on the local gas hold-up. Considering only the effect of bubble size and gas hold-up in eq.(6.11) for Higbie model the $k_L a \propto L_i^{1.5} w_i$ whereas for Danckwerts model in eq.(6.14) the $k_L a \propto L_i^2 w_i$. Using a simple analogy taking the L_i as d_{10} and w_i as α from Table 6-5, it is clear that the effect of gas hold-up outweighs the effect of smaller bubble in the case of constant v_g by about 1.5 times for constant Fl_g and 3.6 times higher for constant VVM if the Higbie model is considered. Even the larger effect of α is observed when Danckwerts model eq.(6.14) is employed with up to 2.4 times higher $\langle k_L a \rangle$ for constant Fl_g compared to constant v_g and 17.4% higher $\langle k_L a \rangle$ for constant VVM. A similar conclusion may also drawn from the tank agitated by CD-6 impeller as shown in Fig. 6-41 and Table 6-5 (compare cases 6.5, 6.10, 6.11, 6.12 and 6.13). In all cases studied for the scale-up studies, there is a good chance of obtaining a similar $\langle k_L a \rangle$ level by fixing the

P_g/V and Fl_g but even higher $\langle k_L a \rangle$ may be achieved by keeping the P_g/V and VVM constant. The CFD predictions shown here give around a 3-56% lower $\langle k_L a \rangle$ value for Higbie and Danckwerts models compared to correlations by van Riet (1979), but this is within the likely experimental error of the empirical correlations.

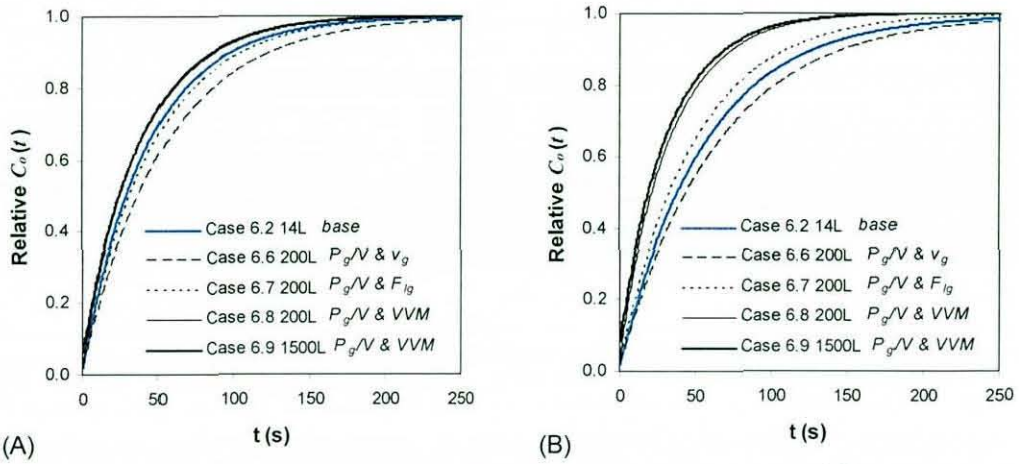

Figure 6-40: Comparison between the $C_0(t)$ evolution for a different scale-up approach of a tank agitated by RDT, a) Higbie's Method (6.8 and 6.9 overlap), b) Danckwerts's method

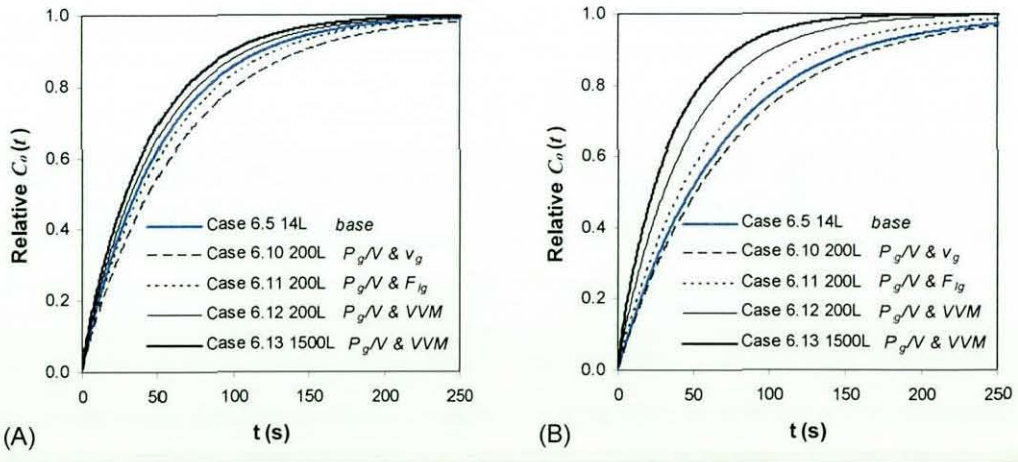

Figure 6-41: Comparison between the $C_0(t)$ evolution for a different scale-up approach of a tank agitated by CD-6, a) Higbie's Method, b) Danckwerts's method

Table 6-5: Evaluation of the scale-up effect to the mass transfer coefficient in aerated stirred tanks

Case	Impeller	Scale-up parameter	V (L)	P_g/P_0		α	$\bar{d}_{32}$ / $\bar{d}_{10}$	$\langle k_L a \rangle$ Van't Riet (1979)	Volume averaged $k_L a$ (1/s)		$\langle k_L a \rangle$ eq.(5.32) (1/s)	
				Smith (2006) Myers *et al.* (1999)	CFD-PBM	(mm)	(mm)	(1/s)	Higbie	Danckwerts	Higbie	Danckwerts
6.2	RDT	Base case	14	0.45	0.45	1.68	2.5 1.3	0.024	0.031	0.026	0.023	0.018
6.6	RDT	P_g/V and v_g	200	0.53	0.50	1.63	3.5 1.6	0.024	0.022	0.019	0.018	0.015
6.7	RDT	P_g/V and Fl_g	200	0.49	0.47	2.26	4.1 1.7	0.028	0.026	0.025	0.022	0.021
6.8	RDT	P_g/V and VVM	200	0.42	0.43	3.95	5.3 2.1	0.038	0.033	0.038	0.027	0.031
6.9	RDT	P_g/V and VVM	1500	0.39	0.39	5.86	8.6 3.5	0.053	0.035	0.044	0.027	0.033
6.5	CD-6	Base case	14	0.71	0.69	2.25	3.4 2.0	0.024	0.021	0.016	0.019	0.015
6.10	CD-6	P_g/V and v_g	200	0.73	0.68	2.11	4.5 2.1	0.024	0.016	0.015	0.016	0.013
6.11	CD-6	P_g/V and Fl_g	200	0.71	0.68	2.97	5.2 2.4	0.028	0.019	0.019	0.018	0.017
6.12	CD-6	P_g/V and VVM	200	0.68	0.62	4.32	6.0 2.8	0.038	0.024	0.026	0.021	0.023
6.13	CD-6	P_g/V and VVM	1500	0.71	0.64	6.46	9.1 4.2	0.053	0.027	0.035	0.023	0.029

6.5 Summary

A comprehensive method via CFD-PBM for modelling aerated stirred tanks has been developed. The CFD-PBM method with a drag model suitable for spherical and distorted bubbles is shown to be a better approach for modelling the gas-liquid flows in stirred tanks, than simply assuming a uniform bubble size. The power number, local bubble sizes, gas hold-up, dissolved oxygen concentration and the mean velocities of the two-phase flow have been predicted satisfactorily in correspondence with experimental data taken from the literature. The CFD-PBM models are also able to reproduce correctly the reduction in the mean velocities magnitude during aeration. The predicted bubble size shows good correlation to $(P_g/V)^{-0.4}\alpha^{0.5}$ which is in agreement with the earlier study by Calderbank (1958). The mass transfer calculation considering an oblate spheroid bubble shape is also shown to be a much better approach than an assumption of a spherical bubble. There is no significant difference between the $\langle k_L a \rangle$ estimated using the $C_0(t)$ evolution at the impeller region, compared to those obtained at other spatial positions, for the sizes of tank studied in this work (up to 1500L). Higbie's model gave a higher $\langle k_L a \rangle$ value than the Danckwerts model for the smaller tank due to its sensitivity towards the smaller bubbles, but the opposite happens for the bigger tanks. The $\langle k_L a \rangle$ predicted using the correlation, such as eq.(2.20), which suggest a dependence on P_g/V and v_g must be used with care because they may not be applicable for vessels of a different size to those from which the original correlation was derived.

The CFD-PBM model also managed to reproduce correctly the trend of lower $\langle k_L a \rangle$ and gassed power number for the CD-6 impeller compared to Rushton turbine. Detail mechanisms behind this phenomenon are also elucidated by comparing the prediction from CFD-PBM simulation on the gas hold-up, bubble sizes and the turbulence quantity. At constant P_g/V and VVM, the difference between the $\langle k_L a \rangle$ for the tank agitated by RDT and CD-6 is quite significant for the smaller tank (14L), but the difference become less significant for the bigger tanks (1500L). This event can be explained by the smaller contribution of the

bubble size to k_La for larger tanks when the mean number bubble size becomes greater than 3 mm.

The scale-up of gas-liquid stirred tanks remains a very challenging task. For the small scale-up factor used here (linear scaling by x2.4, or volume scaling by x14), all three rules gave approximately similar $\langle k_La \rangle$ values. The most conservative approach was to keep both the P_g/V and VVM constant, which in the CFD-PBM computations discussed here led to a slightly larger value of $\langle k_La \rangle$ at larger scale; in contrast, constant P_g/V and v_g led to a slight reduction in the rate of mass transfer at larger scale which is in agreement with the findings by Figueiredo and Calderbank (1979) from experimental measurement. Results from studies of even larger tanks (1500 L linear scaling by x4.8, or volume scaling by x107) further confirm the higher $\langle k_La \rangle$ value when the P_g/V and VVM is fixed. Results from the CFD-PBM simulation also suggest a similar scale-up rule may be applicable for advanced gas dispersion impellers such as the CD-6, which yielded a similar scale-up trend to those of Rushton turbine.

7 CONCLUSIONS AND RECOMMENDATIONS

7.1 Conclusions

In this study, computational methods have been applied to investigate the fluid mechanics of single phase and gas-liquid stirred tanks. Most of the work deals with CFD simulations; however, development and implementation of a population balance model are also studied. The aim of this study is to produce a modelling method with improved capabilities, which may be used in designing, troubleshooting and scaling-up of gas-liquid stirred tanks. This chapter summarises the main findings and considers the extent to which the original aim has been achieved.

Results from the single phase CFD study showed that any of the tested turbulence models can predict correctly the time-averaged mean velocities, but only a few models (i.e. DES, k-ε and Rk-ε) can predict the turbulence quantities reasonably well. However, none of the RANS models can predict accurately the angle-resolved mean velocities, especially just before the centroid of the trailing vortex core. The RANS models also fail to predict the angle-resolved turbulence quantities correctly. The DES model shows much better predictions of the angle-resolved mean velocities and turbulence quantities, compared to any of the RANS models. However, the DES model employed in this work cannot predict the turbulence dissipation rate correctly (under-predicted by up to 75%) and thus may require further refinement i.e. by having a variable turbulent viscosity parameter (C_{Des}), in a way similar to Lily's (1992) model for LES, which evolved according to the information provided by the resolved velocity field, instead of constant C_{Des} in the present model. Apart from that the DES also required more than 10 times longer computational time than the RANS model and thus may not be a practical choice for design, scale-up and troubleshooting tools, especially for multiphase systems. Due to the above-mentioned reasons the Rk-ε was employed for the gas-liquid stirred tank simulations instead of DES. Nevertheless, this study has revealed a great potential of DES for predicting the turbulence quantities in stirred tanks and its ability to work with a standard wall

functions means a significant reduction of computational demand compared to LES.

Radial and axial positions of the lower and upper trailing vortex cores for Rushton turbine have been successfully reproduced numerically using RSM and DES models. Both trailing vortices were also predicted moving in the upward axial direction, in good agreement with the presented measurements from the literature. The accuracy of the power number predictions is not strongly affected by the choice of turbulence models. Instead, they were reasonably well predicted by any of the RANS or DES models used in this work, as long as the moment method was used. Volume integration of the dissipation rate under-predicted the power number by more than 20%.

With the aim of developing a fully coupled CFD and population balance model (PBM) for gas-liquid stirred tanks, various PBM solutions methods were investigated. The quadrature method of moment (QMOM) was found to be a computationally efficient solution approach for PBMs. A new numerical solution for the QMOM via a simultaneous solution of the differential equations resulting from the moment transformation and the system of nonlinear equations obtained from the quadrature approximation has been proposed using a differential-algebraic equation (DAE) formulation, based on exiting DAEsolvers. Simulations have demonstrated that the proposed DAE_QMOM method is more robust and accurate than the product-difference (PD) algorithm in most cases, especially for growth only problems. The DAE-QMOM has a mathematically simpler formulation eliminating the additional complexity related to the product difference algorithm, providing a more robust solution framework. The only downside of the DAE-QMOM at present is the lack of an automatic Jacobian generator in the DAE solver. At present, the Jacobian elements are computed symbolically in MATLAB and then included manually within the DAE-QMOM algorithm. However, the use of DAE solvers with automatic differentiation would make the DAE-QMOM much simpler to implement than the PD-QMOM. However, currently it is impossible to implement the DAE-QMOM within FLUENT due to the lack of suitable DAE solver in the CFD code, and thus the PD-QMOM was implemented instead, since it has a similar prediction accuracy as DAE-QMOM for breakage and coalescence problems.

A test using a single compartment model with realistic breakage and coalescence kernels has demonstrated the capability of the PD-QMOM algorithm, , to predict the bubble size evolution in a homogeneous gas-liquid flow. The prediction from the single compartment population balance model showed a reasonable agreement with the Sauter mean bubble sizes obtained from empirical correlations. The algorithm also responded well to changes in the turbulence dissipation rate and the initial bubble size distribution. The results suggest that the final bubble size is only affected by the turbulence dissipation rate and local gas hold-up, but is not affected by the initial bubble size.

A three-way coupling method which combines both two-way coupling CFD simulation and the population balance modelling could provide a satisfactory prediction of local bubble sizes in aerated stirred tanks provided a reasonable bubble size is employed for the initial CFD simulation. However, prediction of this method is strongly affected by the choice of bubble size in the CFD simulation and hence may not be the best method for predicting the bubble size for aerated stirred tanks.

A comprehensive method via CFD-PBM for modelling aerated stirred tanks considering the drag model for spherical and distorted bubbles together with a correction for dense gas dispersions has been developed. Predictions from the developed model are shown to be better for modelling the gas-liquid flows in stirred tanks, than simply assuming a uniform bubble size. The power number, local bubble sizes, gas hold-up, dissolved oxygen concentration and the mean velocities of the two-phase flow have been predicted satisfactorily in correspondence with experimental data taken from the literature. The CFD-PBM models are also capable to reproduce correctly the reduction in the mean velocities magnitude following aeration.

The mass transfer calculation considering an oblate spheroid bubble shape for bubbles bigger than 1 mm is also shown to be a much better approach than the ones with a spherical bubble. There is no significant difference between the mean mass transfer coefficient $\langle k_L a \rangle$ estimated using the dissolved oxygen ($C_0(t)$) evolution at the impeller region, compared to those obtained at other spatial positions, for the sizes of tank studied in this work (up to 1500L). Higbie's

model gave a higher $\langle k_L a \rangle$ value than the Danckwerts model for the smaller tank, due to its sensitivity towards the smaller bubble, but the opposite occurs for the bigger tanks. The $\langle k_L a \rangle$ predicted using a correlation, such as by van't Riet (1979), which suggest a dependence on P_g/V and v_g must be used with care because they may not be applicable for vessels of a different size to those from which the original correlation was derived.

The CFD-PBM model also reproduced correctly the trend of lower $\langle k_L a \rangle$ and smaller gassed power drop for the CD-6 impeller compared to Rushton turbine. Detailed mechanisms behind this phenomenon are also elucidated by comparing the prediction from the CFD-PBM simulations for the gas hold-up, bubble sizes and the turbulence quantities. At constant P_g/V and VVM, the difference between the $\langle k_L a \rangle$ for the tank agitated by RDT and CD-6 is quite significant for the smaller tank (14L) but it becomes less pronounced for the larger scale tanks (1500L) due to a much smaller difference between the bubble interfacial area for bigger bubbles.

Three scale-up rules, namely a constant P_g/V combined with either constant Fl_g, v_g and VVM were studied numerically using the CFD-PBM method developed in this work. The results suggest that a successful scale-up may be achieved by keeping the P_g/V and VVM constant. This method can lead to a slightly higher $\langle k_L a \rangle$ with increasing scale representing the most conservative approach. In contrast, constant P_g/V and v_g led to a slight reduction in the rate of mass transfer at larger scale, which is in agreement to the findings by Figueiredo and Calderbank (1979) from their experimental measurements. Results from a study of even larger tanks (1500 L linear scaling by x4.8, or volume scaling by x107) further confirmed the higher $\langle k_L a \rangle$ value when the P_g/V and VVM are fixed during scale-up. Results from the CFD-PBM simulation also suggest a similar scale-up rule may be applicable for advanced gas dispersion impeller such as CD-6 which yielded a similar scale-up trend to those of the Rushton turbine.

However, the volumetric mass transfer coefficient still assumes that $C^* - C_0(t)$ is uniform in space. This assumption becomes less likely at industrial scale

(Schutze and Hengstler, 2006) and hence the whole concept of calculating the overall mass transfer rate from a single point $C_0(t)$ evolution becomes questionable. The real strength of the CFD-PBM is that it can take into account varying driving forces and varying k_La values inside the tank, which is critical for its design, scale-up and troubleshooting.

7.2 Recommendations

The model developed from this work needs further refinement, especially on the interfacial force modelling which is at present does not include the effect of turbulence on the drag coefficient, virtual mass and lift forces. Of the many simplifications employed in this work, omission of turbulent drag coefficient due to lack of data and correlations available in the literature is potentially the most important issue because drag coefficient is known to increase with up to 50% for particles in the condition of intense turbulence (Schwartzberg and Treybal, 1968). An alternative solution may be provided by employing a drag model for solid particles subject to background turbulence. Such a model may not be able to give an accurate prediction, but it may be a better solution than not considering them at all. The virtual mass and lift forces are not thought to affect the model prediction significantly.

A better turbulence model such as DES, LES or even DNS combined with sliding mesh method could be a positive development for the current model. A multiple-size Eulerian-Eulerian model may also be required because at present only single mean bubble size (d_{32}) is permitted at a particular spatial position in the two-phase model. However, all these changes would make the model much less tractable to solution on a personal computer, and hence less practical as a design tool.

The model in this work may be employed with little changes to other gas-liquid flows, such as an airlift bioreactor, bubble column, bubbly flow in pipe and stirred tank bioreactor. At present, the model does not include any reaction or bioreaction process, but the model can be extended further to accommodate such a need e.g. by adding an oxygen sink term into the dissolved oxygen transport equation and by adding further transport equations for substrate concentration and cell mass. Since the population balance model and drag

model framework are already available in the current implementation, the model may also be modified with little effort to describe the solid-liquid or liquid-liquid flows encountered e.g. in crystallisation, agglomeration, precipitation, emulsions and any two-phase flow involving dynamics of a dispersed flow, such as oil-water dispersions in pipe among others. The only changes required are (i) in the kernels which are dependent on the process physics and (ii) the drag model. The drag model currently implemented in the model may be suitable for liquid-liquid dispersion without needing further modification, whereas the drag models for particles are already available as a default option in commercial CFD codes such as FLUENT.

Bibliography

Alcamo, R., Micale, G., Grisafi, F., Brucato, A. & Ciofalo, M. 2005, "Large-eddy simulation of turbulent flow in an unbaffled stirred tank driven by a Rushton turbine", *Chemical Engineering Science,* vol. 60, no. 8-9, pp. 2303-2316.

Alexiadis, A., Gardin, P. & Domgin, J.F. 2004, "Spot turbulence, breakup, and coalescence of bubbles released from a porous plug injector into a gas-stirred ladle", *Metallurgical and Materials Transactions B: Process Metallurgy and Materials Processing Science,* vol. 35, no. 5, pp. 949-956.

Alopaeus, V., Koskinen, J. & Keskinen, K.I. 1999, "Simulation of the population balances for liquid–liquid systems in a nonideal stirred tank. Part 1 Description and qualitative validation of the model", *Chemical Engineering Science,* vol. 54, no. 24, pp. 5887-5899.

Alopaeus, V., Laakkonen, M. & Aittamaa, J. 2006, "Numerical solution of moment-transformed population balance equation with fixed quadrature points", *Chemical Engineering Science,* vol. 61, no. 15, pp. 4919-4929.

Alopaeus, V., Laakkonen, M. & Aittamaa, J. 2007, "Solution of population balances with growth and nucleation by high order moment-conserving method of classes", *Chemical Engineering Science,* vol. 62, no. 8, pp. 2277-2289.

Alves, S.S., Maia, C.I. & Vasconcelos, J.M.T. 2002b, "Experimental and modelling study of gas dispersion in a double turbine stirred tank", *Chemical Engineering Science,* vol. 57, no. 3, pp. 487-496.

Alves, S.S., Maia, C.I. & Vasconcelos, J.M.T. 2004, "Gas-liquid mass transfer coefficient in stirred tanks interpreted through bubble contamination kinetics", *Chemical Engineering and Processing,* vol. 43, no. 7, pp. 823-830.

Anderson, T.B. & Jackson, R. 1967, "Fluid mechanical description of fluidized beds -- Equations of motion", *Industrial and Engineering Chemistry -- Fundamentals,* vol. 6, no. 4, pp. 527-539.

Andersson, R. & Andersson, B. 2006, "On the breakup of fluid particles in turbulent flows", *AICHE Journal,* vol. 52, no. 6, pp. 2020-2030.

Arjunwadkar, S.J., Sarvanan, K., Kulkarni, P.R. & Pandit, A.B. 1998, "Gas-liquid mass transfer in dual impeller bioreactor", *Biochemical Engineering Journal,* vol. 1, no. 2, pp. 99-106.

Armenante, P.M., Luo, C., Chou, C., Fort, I. & Medek, J. 1997, "Velocity profiles in a closed, unbaffled vessel: Comparison between experimental LDV data and numerical CFD predictions", *Chemical Engineering Science,* vol. 52, no. 20, pp. 3483-3492.

Ascher, U.M. & Petzold, L.R. 1998, "*Computer Methods for Ordinary Differential Equations and Differential Algebraic Equations*", 1st ed, Society for Industrial and Applied Mathematics Philadelphia, PA, USA.

Aubin, J., Fletcher, D.F. & Xuereb, C. 2004a, "Modeling turbulent flow in stirred tanks with CFD: the influence of the modeling approach, turbulence model

and numerical scheme", *Experimental Thermal and Fluid Science,* vol. 28, no. 5, pp. 431-445.

Aubin, J., Le Sauze, N., Bertrand, J., Fletcher, D.F. & Xuereb, C. 2004b, "PIV measurements of flow in an aerated tank stirred by a down- and an up-pumping axial flow impeller", *Experimental Thermal and Fluid Science,* vol. 28, no. 5, pp. 447-456.

Azbel D. & Athanasios, I.L. 1983, "A mechanism of liquid entrainment". In: N. Cheremisinoff, Editor, *Handbook of Fluids in Motion*, Ann Arbor Science Publishers, Ann Arbor, USA (1983), p. 473.

Bakker, A. 1992, "Hydrodynamics of Stirred Gas-Liquid Dispersions", *Ph.D. Thesis*, Delft University of Technology, Delft, The Netherlands.

Bakker, A., Haidari, A.H. & Oshinowo, L.M. 2001, "Realize greater benefits from CFD", *Chemical Engineering Progress,* vol. 97, no. 3, pp. 45-53.

Bakker, A. & Van den Akker, H. 1994a, "Computational model for the gas-liquid flow in stirred reactors", *Chemical Engineering Research & Design, Part A,* vol. 72, pp. 594-606.

Bakker, A., Smith, J.M. & Myers, K.J. 1994b, "How to disperse gases in liquids", *Chemical Engineering (New York),* vol. 101, no. 12, pp. 98.

Bakker, A. & Benz, G.T. 1996, "Mixing in Industrial Fermenters", 10th *International Biotechnology Symposium*, August 25-30, 1996, Sydney, Australia.

Bakker, A. & Oshinowo, L.M. 2004, "Modelling of turbulence in stirred vessels using large eddy simulation", *Chemical Engineering Research and Design,* vol. 82, no. 9, pp. 1169-1178.

Bandaiphet, C. & Prasertsan, P. 2006, "Effect of aeration and agitation rates and scale-up on oxygen transfer coefficient, kLa in exopolysaccharide production from Enterobacter cloacae WD7", *Carbohydrate Polymers,* vol. 66, no. 2, pp. 216-228.

Barigou, M. & Greaves, M. 1996, "Gas holdup and interfacial area distributions in a mechanically agitated gas-liquid contractor", *Chemical Engineering Research & Design,* vol. 74, pp. 397-405.

Barigou, M. & Greaves, M. 1992, "Bubble-size distributions in a mechanically agitated gas-liquid contactor", *Chemical Engineering Science,* vol. 47, no. 8, pp. 2009-2025.

Barigou, M. & Greaves, M. 1991, "Capillary suction probe for bubble size measurement", *Measurement Science & Technology,* vol. 2, no. 4, pp. 318-326.

Behzadi, A., Issa, R.I. & Rusche, H. 2004, "Modelling of dispersed bubble and droplet flow at high phase fractions", *Chemical Engineering Science,* vol. 59, no. 4, pp. 759-770.

Benz, G.T. 2003, "Optimize power consumption in aerobic fermenters", *Chemical Engineering Progress,* vol. 99, no. 5, pp. 32-35.

Birch, D. & Ahmed, N. 1996, "Gas sparging in vessels agitated by mixed flow impellers", *Powder Technology,* vol. 88, no. 1, pp. 33-38.

Boden, S., Bieberle, M. & Hampel, U. 2008, "Quantitative measurement of gas hold-up distribution in a stirred chemical reactor using X-ray cone-beam computed tomography", *Chemical Engineering Journal,* vol. 139, no. 2, pp. 351-362.

Bombac, A., Zun, I., Filipic, B. & Zumer, M. 1997, "Gas-filled cavity structures and local void fraction distribution in aerated stirred vessel", *AICHE Journal,* vol. 43, no. 11, pp. 2921-2931.

Bordel, S., Mato, R. & Villaverde, S. 2006, "Modeling of the evolution with length of bubble size distributions in bubble columns", *Chemical Engineering Science,* vol. 61, no. 11, pp. 3663-3673.

Bouaifi, M., Hebrard, G., Bastoul, D. & Roustan, M. 2001, "Comparative study of gas hold-up, bubble size, interfacial area and mass transfer coefficients in stirred gas-liquid reactors and bubble columns", *Chemical Engineering and Processing,* vol. 40, no. 2, pp. 97-111.

Brown, P.N., Byrne, G.D. & Hindmarsh, A.C. 1989, "VODE: A variable-coefficient ODE solver", *SIAM J. Sci. Comput.*, vol. 10, pp. 1038-1051.

Brucato, A., Grisafi, F. & Montante, G. 1998, "Particle drag coefficients in turbulent fluids", *Chemical Engineering Science,* vol. 53, no. 18, pp. 3295-3314.

Brucato, A., Ciofalo, M., Grisafi, F. & Micale, G. 1998, "Numerical prediction of flow fields in baffled stirred vessels: A comparison of alternative modelling approaches", *Chemical Engineering Science,* vol. 53, no. 21, pp. 3653-3684.

Bruijn, W., Van't Riet, K., Smith, J.M. 1974, "Power Consumption with Aerated Rushton Turbines", *Trans. Inst. Chem. Eng.*, **52**, pp. 88-104.

Bujalski, W., Nienow, A.W., Chatwin, S. & Cooke, M. 1987, "Dependency on scale of power numbers of Rushton disc turbines", *Chemical Engineering Science*, vol. 42, no. 2, pp. 317-326.

Bukur, D.B., Daly, J.G. & Patel, S.A. 1996, "Application of gamma-ray attenuation for measurement of gas holdups and flow regime transitions in bubble columns", *Industrial & Engineering Chemistry Research,* vol. 35, no. 1, pp. 70.

Bustard, M.T., Whiting, S. Cowan D.A. & Wright, P.C. 2002, "Biodegradation of high concentration isopropanol by a solvent-tolerant thermophile", *Bacillus pallidus*, *Extremophiles* vol. **6**, pp. 319–323.

Butcher, M. & Eagles, W. 2002, "Fluid mixing re-engineered", *Chemical Engineer,* , no. 733, pp. 28-29.

Calderbank, P.H. 1958, "Physical rate processes in industrial fermentation. Part I: the interfacial area in gas–liquid contacting with mechanical agitation", *Transactions of the Institute of Chemical Engineers,* vol. 36, pp. 443–463.

Carrica, P.M. & Clausse, A.A. 1993, "Mathematical description of the critical heat flux as nonlinear dynamic instability", In: Gouesbet, G., Berlemont, A. (Eds.), *Instabilities in Multiphase Flow.* Plenum Press, New York.

Chaouki, J., Larachi, F. & Dudukovic, M.P. 1997, "Noninvasive tomographic and velocimetric monitoring of multiphase flows", *Industrial & Engineering Chemistry Research,* vol. 36, no. 11, pp. 4476-4503.

Chaumat, H., Billet-Duquenne, A., Augier, F., Mathieu, C. & Delmas, H. 2005, "Application of the double optic probe technique to distorted tumbling bubbles in aqueous or organic liquid", *Chemical Engineering Science*, vol. 60, no. 22, pp. 6134-6145.

Chemineer, 2006, "Impellers", http://www.chemineer.com, Accessed 26 July 2006.

Chen, P., Sanyal, J. & Dudukovic, M.P. 2004, "CFD modeling of bubble columns flows: Implementation of population balance", *Chemical Engineering Science,* vol. 59, no. 22-23, pp. 5201-5207.

Chen, P., Sanyal, J. & Duduković, M.P. 2005, "Numerical simulation of bubble columns flows: effect of different breakup and coalescence closures", *Chemical Engineering Science,* vol. 60, no. 4, pp. 1085-1101.

Chesters, A.K. 1991, "Modelling of coalescence processes in fluid-liquid dispersions. A review of current understanding", *Chemical Engineering Research & Design,* vol. 69, no. 4, pp. 259-27.

Clift, R., Grace, J.R. and Weber, M.E., (1978), "*Bubbles, drops and particles*", Academic Press, New York.

Cooke, M. & Heggs, P.J. 2005, "Advantages of the hollow (concave) turbine for multi-phase agitation under intense operating conditions", *Chemical Engineering Science,* vol. 60, no. 20, pp. 5529-5543.

Costa, C.B.B., Maciel, M.R.W. & Filho, R.M. 2007, "Considerations on the crystallization modeling: Population balance solution", *Computers & Chemical Engineering,* vol. 31, no. 3, pp. 206-218.

Cui, Y.Q., van der Lans, R.G.J.M. & Luyben, K.C.A.M. 1996, "Local power uptake in gas-liquid systems with single and multiple rushton turbines", *Chemical Engineering Science,* vol. 51, no. 11, pp. 2631-2636.

Danckwerts, P.V. 1951, "Significance of Liquid-Film Coefficients in Gas Absorption", *Industrial & Engineering Chemistry,* vol. 43, no. 6, pp. 1460-1467.

Dantec Dynamics, 2006, "Product literature", www.dantecdynamics.com, Accessed on 26 July 2006.

Deen, N. G., (2001), "An Experimental and Computational Study of Fluid Dynamics in Gas-Liquid Chemical Reactors", *PhD Thesis*, Aalborg University Esbjerg, Denmark.

Deen, N.G. & Hjertager, B.H. 2002, "Particle image velocimetry measurements in an aerated stirred tank", *Chemical Engineering Communications,* vol. 189, no. 9, pp. 1208-1221.

Deen, N.G., Solberg, T. & Hjertager, B.H. 2002, "Flow generated by an aerated Rushton impeller: Two-phase PIV experiments and numerical simulations", *Canadian Journal of Chemical Engineering,* vol. 80, no. 4, pp. 638-652.

Degaleesan, S. 1997, "Fluid dynamic measurements and modeling of liquid mixing in bubble columns", *D.Sc. Thesis*, St. Louis, Missouri, USA: Washington University.

Devanathan, N. 1991, "Investigation of liquid hydrodynamics in bubble columns via computer automated radioactive particle tracking (CARPT)", *D.Sc. Thesis*, Washington University, St. Louis.

Fluent, (2005), Fluent 6.2 User Guide.

Fluent, (2006), Fluent 6.3 User Guide.

Delafosse, A., Line, A., Morchain, J. & Guiraud, P. 2008, "LES and URANS simulations of hydrodynamics in mixing tank: Comparison to PIV experiments", *Chemical Engineering Research and Design,* vol. 86, no. 12, pp. 1322-1330.

Derksen, J. 2001, "Assessment of large eddy simulations for agitated flows", *Chemical Engineering Research and Design,* vol. 79, no. 8, pp. 824-830.

Derksen, J.J., Doelman, M.S. & Van den Akker, H. 1999, "Three-dimensional LDA measurements in the impeller region of a turbulently stirred tank", *Experiments in Fluids,* vol. 27, no. 6, pp. 522-532.

Derksen, J. & Van den Akker, H. 1999, "Large eddy simulations on the flow driven by a Rushton turbine", *AICHE Journal,* vol. 45, no. 2, pp. 209-221.

Dhanasekharan, K.M., Sanyal, J., Jain, A. & Haidari, A. 2005, "A generalized approach to model oxygen transfer in bioreactors using population balances and computational fluid dynamics", *Chemical Engineering Science,* vol. 60, no. 1, pp. 213-218.

Diemer, R.B. & Ehrman, S.H. 2005, "Pipeline agglomerator design as a model test case", *Powder Technology,* vol. 156, no. 2-3, pp. 129-145.

Dorao, C.A. & Jakobsen, H.A. 2006, "The quadrature method of moments and its relationship with the method of weighted residuals", *Chemical Engineering Science,* vol. 61, no. 23, pp. 7795-7804.

Ducoste, J.J. & Clark, M.M. 1999, "Turbulence in flocculators: Comparison of measurements and CFD simulations", *AICHE Journal,* vol. 45, no. 2, pp. 432-436.

Escudie, R., Bouyer, D. & Line, A. 2004, "Characterization of Trailing Vortices Generated by a Rushton Turbine", *AICHE Journal,* vol. 50, no. 1, pp. 75-86.

Escudie, R. & Line, A. 2003, "Experimental analysis of hydrodynamics in a radially agitated tank", *AICHE Journal,* vol. 49, no. 3, pp. 585-603.

Fan, R., Marchisio, D.L. & Fox, R.O. 2004, "Application of the direct quadrature method of moments to polydisperse gas-solid fluidized beds", *Powder Technology,* vol. 139, no. 1, pp. 7-20.

Figueiredo, M.M.L. & Calderbank, P.H. 1979, "The scale-up of aerated mixing vessels for specified oxygen dissolution rates", *Chemical Engineering Science,* vol. 34, no. 11, pp. 1333-1338.

Flores, E.R., Perez, F. & de, I.T. 1997, "Scale-up of bacillus thuringiensis fermentation based on oxygen transfer", *Journal of Fermentation and Bioengineering,* vol. 83, no. 6, pp. 561-564.

Ford, J.J., Heindel, T.J., Jensen, T.C. & Drake, J.B. 2008, "X-ray computed tomography of a gas-sparged stirred-tank reactor", *Chemical Engineering Science,* vol. 63, no. 8, pp. 2075-2085.

Fuchs, N.A. & Sutugin, A.G. 1971, "High dispersed aerosols", In: G.M. Hidy and J.R. Brock, Editors, *Topics in Current Aerosol Research* **Vol. 2**, Pergamon Press, Oxford, p. 35.

Garcia-Cortes, D., Xuereb, C., Taillandier, P., Jauregui-Haza, U. & Bertrand, J. 2004, "Effect of dual impeller-sparger geometry on the hydrodynamics and mass transfer in stirred vessels", *Chemical Engineering and Technology,* vol. 27, no. 9, pp. 988-999.

Garcia-Ochoa, F., Gomez Castro, E. & Santos, V.E. 2000, "Oxygen transfer and uptake rates during xanthan gum production", *Enzyme and microbial technology,* vol. 27, no. 9, pp. 680-690.

Garcia-Ochoa, F. & Gomez, E. 2009, "Bioreactor scale-up and oxygen transfer rate in microbial processes: An overview", *Biotechnology Advances,* vol. 27, no. 2, pp. 153-176.

Gautschi, W. 1994, "Algorithm 726: ORTHPOL-A package of routines for generating orthogonal polynomials and gauss-type quadrature rules", *ACM Transactions on Mathematical Software,* vol. 20, no. 1, pp. 21-62.

Gelbard, F.M. & Seinfeld, J.H. 1978, "Coagulation and growth of a multicomponent aerosol", *Journal of Colloid and Interface Science,* vol. 63, no. 3, pp. 472-479.

Gelbard, F., Tambour, Y. & Seinfeld, J.H. 1980, "Sectional representations for simulating aerosol dynamics", *Journal of Colloid and Interface Science,* vol. 76, no. 2, pp. 541-556.

Gerstlauer, A., Motz, S., Mitrovic, A. & Gilles, E.-. 2002, "Development, analysis and validation of population models for continuous and batch crystallizers", *Chemical Engineering Science,* vol. 57, no. 20, pp. 4311-4327.

Gezork, K.M., Bujalski, W., Cooke, M. & Nienow, A.W. 2000, "The Transition from Homogeneous to Heterogeneous Flow in a Gassed, Stirred Vessel", *Chemical Engineering Research and Design,* vol. 78, no. 3, pp. 363-370.

Gillette, D.A. 1972, "A study of aging of lead aerosols—II: A numerical model simulating coagulation and sedimentation of a leaded aerosol in the presence of an unleaded background aerosol", *Atmospheric Environment (1967),* vol. 6, no. 7, pp. 451-462.

Gordon, R.G. 1968, "Error bounds in equilibrium statistical mechanics", *Journal of Mathematical Physics*, vol. **9**, pp. 655–663.

Greaves, M. & Barigou, M. 1988, "Estimation of gas hold-up and impeller power in a stirred vessel reactor", *Fluid Mixing III*Publ by European Federation of Chemical Engineering, Amarousion-Pefki, Greece, pp. 235.

Greaves, M. & Kobbacy, K.A.H. 1984, "Measurement of bubble size distribution in turbulent gas-liquid dispersions", *Chemical Engineering Research & Design,* vol. 62, no. 1, pp. 3-12.

Grenville, R.K. & Nienow, A.W. 2004, "Blending of miscible liquids". In: E.L. Paul, V. Atiemo-Obeng and S.M. Kresta, Editors, *The Handbook of Industrial Mixing*, Wiley, New York, USA (2004).

Guet, S., Luther, S. & Ooms, G. 2005, "Bubble shape and orientation determination with a four-point optical fibre probe", *Experimental Thermal and Fluid Science,* vol. 29, no. 7, pp. 803-812.

Hampel, U., Hristov, H.V., Bieberle, A. & Zippe, C. 2007, "Application of high-resolution gamma ray tomography to the measurement of gas hold-up distributions in a stirred chemical reactor", *Flow Measurement and Instrumentation,* vol. 18, no. 5-6, pp. 184-190.

Harris, C.K., Roekaerts, D., Rosendal, F.J.J., Buitendijk, F.G.J., Daskopoulos, P., Vreenegoor, A.J.N. & Wang, H. 1996, "Computational fluid dynamics for chemical reactor engineering", *Chemical Engineering Science,* vol. 51, no. 10, pp. 1569-1594.

Hartmann, H., Derksen, J.J., Montavon, C., Pearson, J., Hamill, I.S. & van den Akker, H.E.A. 2004, "Assessment of large eddy and RANS stirred tank simulations by means of LDA", *Chemical Engineering Science,* vol. 59, no. 12, pp. 2419-2432.

Hebrard, G., Destrac, P., Roustan, M., Huyard, A. & Audic, J.M. 2000, "Determination of the water quality correction factor α using a tracer gas method", *Water research,* vol. 34, no. 2, pp. 684-689.

Heindel, T.J., Gray, J.N. & Jensen, T.C. 2008, "An X-ray system for visualizing fluid flows", *Flow Measurement and Instrumentation,* vol. 19, no. 2, pp. 67-78.

Hewitt, C.J., Boon, L.A., McFarlane, C.M. & Nienow, A.W. 1998, "Use of flow cytometry to study the impact of fluid mechanical stress on Escherichia coli W3110 during continuous cultivation in an agitated bioreactor", *Biotechnology and bioengineering,* vol. 59, no. 5, pp. 612-620.

Higbie, R. 1935, "The rate of absorption of a pure gas into a still liquid during short periods of exposure", *Trans Am Inst Chem Eng*, vol. **31**, pp. 364–389

Hindmarsh, A.C. 1980, "LSODE and LSODI, two new initial value ordinary differential equation solvers", *ACM SIGNUM Newsletter,* vol. 15, pp. 10-11.

Holden, P.J., Wang, M., Mann, R., Dickin, F.J. & Edwards, R.B. 1999, "On Detecting Mixing Pathologies Inside a Stirred Vessel Using Electrical Resistance Tomography", *Chemical Engineering Research and Design,* vol. 77, no. 8, pp. 709-712.

Hounslow, M.J., Pearson, J.M.K. & Instone, T. 2001, "Tracer studies of high-shear granulation: II. Population balance modeling", *AICHE Journal,* vol. 47, no. 9, pp. 1984-1999.

Hulburt, H.M. & Katz, S. 1964, "Some problems in particle technology : A statistical mechanical formulation", *Chemical Engineering Science,* vol. 19, no. 8, pp. 555-574.

Hristov, H., Mann, R., Lossev, V., Vlaev, S.D. & Seichter, P. 2001, "A 3-D Analysis of Gas-Liquid Mixing, Mass Transfer and Bioreaction in a Stirred Bio-Reactor", *Food and Bioproducts Processing,* vol. 79, no. 4, pp. 232-241.

Hughmark, G.A. 1980, "Power requirements and interfacial area in gas-liquid turbine agitated systems", *Industrial & Engineering Chemistry, Process Design and Development,* vol. 19, no. 4, pp. 638-641.

Ishii, M. & Zuber, N. 1979, "Drag coefficient and relative velocity in bubbly, droplet or particulate flows", *AICHE Journal,* vol. 25, no. 5, pp. 843-855.

Islam, R.S., Tisi, D., Levy, M.S. & Lye, G.J. 2008, "Scale-up of Escherichia coli growth and recombinant protein expression conditions from microwell to laboratory and pilot scale based on matched k_La", *Biotechnology and bioengineering,* vol. 99, no. 5, pp. 1128-1139.

Jahoda, M., Mostek, M., Kukukova, A. & Machon, V. 2007, "CFD modelling of liquid homogenization in stirred tanks with one and two impellers using large eddy simulation", *Chemical Engineering Research and Design,* vol. 85, no. 5, pp. 616-625.

Jaworski, Z. & Zakrzewska, B. 2002, "Modelling of the turbulent wall jet generated by a pitched blade turbine impeller: The effect of turbulence model", *Chemical Engineering Research and Design,* vol. 80, no. 8, pp. 846-854.

Jaworski, Z. & Nienow, A.W. 2003, "CFD modelling of continuous precipitation of barium sulphate in a stirred tank", *Chemical Engineering Journal,* vol. 91, no. 2-3, pp. 167-174.

Jeong, J. & Hussain, F. 1995, "On the identification of a vortex", *Journal of Fluid Mechanics,* vol. 285, pp. 69-94.

Kalender, W.A. 2006, "X-ray computed tomography", *Physics in Medicine and Biology,* vol. 51, no. 13, pp. 29-43.

Kapic, A. & Heindel, T.J. 2006, "Correlating gas-liquid mass transfer in a stirred-tank reactor", *Chemical Engineering Research and Design,* vol. 84, no. 3, pp. 239-245.

Kawase, Y. & Moo-Young, M. 1988, "Volumetric mass transfer coefficients in aerated stirred tank reactors with Newtonian and non-Newtonian media", *Chemical Engineering Research & Design,* vol. 66, no. 3, pp. 284-288.

Kawase, Y. & Hashimoto, N. 1996, "Gas hold-up and oxygen transfer in three-phase external-loop airlift bioreactors: non-newtonian fermentation broths", *Journal of Chemical Technology and Biotechnology,* vol. 65, no. 4, pp. 325-334.

Kennard, E.H. 1938, "*Theory of gases*", Mc Graw-Hill, New York.

Kerdouss, F., Bannari, A. & Proulx, P. 2006, "CFD modeling of gas dispersion and bubble size in a double turbine stirred tank", *Chemical Engineering Science,* vol. 61, no. 10, pp. 3313-3322.

Kerdouss, F., Bannari, A., Proulx, P., Bannari, R., Skrga, M. & Labrecque, Y. 2008, "Two-phase mass transfer coefficient prediction in stirred vessel with

a CFD model", *Computers & Chemical Engineering,* vol. 32, no. 8, pp. 1943-1955.

Khan, F.R., Rielly, C.D. & Brown, D.A.R. 2006, "Angle-resolved stereo-PIV measurements close to a down-pumping pitched-blade turbine", *Chemical Engineering Science,* vol. 61, no. 9, pp. 2799-2806.

Khan, F.R., Rielly, C.D. & Hargrave, G.K. 2004, "A multi-block approach to obtain angle-resolved PIV measurements of the mean flow and turbulence fields in a stirred vessel", *Chemical Engineering and Technology,* vol. 27, no. 3, pp. 264-269.

Khopkar, A.R., Aubin, J., Xuereb, C., Le Sauze, N., Bertrand, J. & Ranade, V.V. 2003, "Gas-liquid flow generated by a pitched-blade turbine: Particle image velocimetry measurements and computational fluid dynamics simulations", *Industrial and Engineering Chemistry Research,* vol. 42, no. 21, pp. 5318-5332.

Khopkar, A., Aubin, J., Rubio-Atoche, C., Xuereb, C., Le Sauze, N., Bertrand, J., Ranade, V.V. 2004, "Flow generated by radial flow impellers: PIV measurements and CFD simulations", *Int. J. Chem. Reactor Eng.* **2**, A18.

Khopkar, A.R., Panaskar, S.S., Pandit, A.B. & Ranade, V.V. 2005a, "Characterization of gas-liquid flows in stirred vessels using pressure and torque fluctuations", *Industrial and Engineering Chemistry Research,* vol. 44, no. 9, pp. 3298-3311.

Khopkar, A.R., Rammohan, A.R., Ranade, V.V. & Dudukovic, M.P. 2005b, "Gas–liquid flow generated by a Rushton turbine in stirred vessel: CARPT/CT measurements and CFD simulations", *Chemical Engineering Science,* vol. 60, no. 8-9, pp. 2215-2229.

Khopkar, A.R. & Ranade, V.V. 2006, "CFD simulation of gas-liquid stirred vessel: VC, S33, and L33 flow regimes", *AICHE Journal,* vol. 52, no. 5, pp. 1654-1672.

Klopfenstein, R.W. 1971, "Numerical differentiation formulas for stiff systems of ordinary differential equations", vol. 32, no. 3, pp. 447-62.

Kolmogorov, A.N. 1941, "The local structure of turbulence in incompressible viscous fluid for very large Reynolds numbers", *Doklady Akademii Nauk SSSR*, vol. **30**, pp. 301–305.

Kovacs, T., Tragardh, C. & Fuchs, L. 2001, "Flow and turbulence in the discharge of radial pumping turbines: Influence of the Turbine type", *Chemical Engineering and Technology,* vol. 24, no. 10, pp. 1035-1044.

Kresta, S.M., Wood, P.E. 1993, "The flow field produced by a pitched blade turbine: Characterization of the turbulence and estimation of the dissipation rate", *Chemical Engineering Science*, vol. 48, no. 10, pp. 1761-1774.

Kuboi, R., Komasawa, I. & Otake, T. 1974, "Fluid and particle motion in turbulent dispersion--II: Influence of turbulence of liquid on the motion of suspended particles", *Chemical Engineering Science,* vol. 29, no. 3, pp. 651-657.

Kumaresan, T. & Joshi, J.B. 2006, "Effect of impeller design on the flow pattern and mixing in stirred tanks", *Chemical Engineering Journal,* vol. 115, no. 3, pp. 173-193.

Laakkonen, M., Honkanen, M., Saarenrinne, P. & Aittamaa, J. 2005a, "Local bubble size distributions, gas-liquid interfacial areas and gas holdups in a stirred vessel with particle image velocimetry", *Chemical Engineering Journal,* vol. 109, no. 1, pp. 37-47.

Laakkonen, M., Moilanen, P., Miettinen, T., Saari, K., Honkanen, M., Saarenrinne, P. & Aittamaa, J. 2005b, "Local bubble size distributions in agitated vessel comparison of three experimental techniques", *Chemical Engineering Research and Design,* vol. 83, no. 1, pp. 50-58.

Laakkonen, M., Moilanen, P. & Aittamaa, J. 2005c, "Local bubble size distributions in agitated vessels", *Chemical Engineering Journal,* vol. 106, no. 2, pp. 133-143.

Laakkonen, M., Moilanen, P., Alopaeus, V. & Aittamaa, J. 2006a, "Dynamic modeling of local reaction conditions in an agitated aerobic fermenter", *AICHE Journal,* vol. 52, no. 5, pp. 1673-1689.

Laakkonen, M., Alopaeus, V. & Aittamaa, J. 2006b, "Validation of bubble breakage, coalescence and mass transfer models for gas-liquid dispersion in agitated vessel", *Chemical Engineering Science,* vol. 61, no. 1, pp. 218-228

Laakkonen, M., Moilanen, P., Alopaeus, V. & Aittamaa, J. 2007a, "Modelling local bubble size distributions in agitated vessels", *Chemical Engineering Science,* vol. 62, no. 3, pp. 721-740.

Laakkonen, M., Moilanen, P., Alopaeus, V. & Aittamaa, J. 2007b, "Modelling local gas - Liquid mass transfer in agitated vessels", *Chemical Engineering Research and Design,* vol. 85, no. 5, pp. 665-675.

Lambin, P. & Gaspard, J.P. 1982, "Continued-fraction technique for tight-binding systems. A generalized-moments method", *Physical Review B*, vol. **26**, no. 8, pp. 4356–4368.

Lamont, J.C. & Scott, D.S. 1970, "Eddy cell model of mass transfer into the surface of a turbulent liquid", *AICHE Journal*, vol. 16, no. 4, pp. 513-519.

Lane, G.L., Schwarz, M.P. & Evans, G.M. 2005, "Numerical modelling of gas–liquid flow in stirred tanks", *Chemical Engineering Science,* vol. 60, no. 8-9, pp. 2203-2214.

Lane, G.L. 2005, "Computational modelling of gas-liquid flow in stirred tanks", *PhD Thesis,* The University of Newcastle, Australia.

Lane, G.L., Schwarz, M.P. & Evans, G.M. 2002, "Predicting gas-liquid flow in a mechanically stirred tank", *Applied Mathematical Modelling,* vol. 26, no. 2, pp. 223-235.

Launder, B.E. & Spalding, D.B. 1974, "Numerical computation of turbulent flows", *Computer Methods in Applied Mechanics and Engineering,* vol. 3, no. 2, pp. 269-289.

Lee, K.C. & Yianneskis, M. 1998, "Turbulence properties of the impeller stream of a Rushton turbine", *AICHE Journal,* vol. 44, no. 1, pp. 13-24.

Lee, K., Lee, J.H., Yang, D.R. & Mahoney, A.W. 2002, "Integrated run-to-run and on-line model-based control of particle size distribution for a semi-batch

precipitation reactor", *Computers & Chemical Engineering,* vol. 26, no. 7-8, pp. 1117-1131.

Lehr, F., Millies, M. & Mewes, D. 2002, "Bubble-size distributions and flow fields in bubble columns", *AICHE Journal,* vol. 48, no. 11, pp. 2426-2443.

Li, M., White, G., Wilkinson, D. & Roberts, K.J. 2005, "Scale up study of retreat curve impeller stirred tanks using LDA measurements and CFD simulation", *Chemical Engineering Journal,* vol. 108, no. 1-2, pp. 81-90.

Li, M., White, G., Wilkinson, D. & Roberts, K.J. 2004, "LDA measurements and CFD modeling of a stirred vessel with a retreat curve impeller", *Industrial and Engineering Chemistry Research,* vol. 43, no. 20, pp. 6534-6547.

Li, Z., Gao, Z., Smith, J.M. & Thorpe, R.B. 2007, "Large eddy simulation of flow fields in vessels stirred by dual rushton impeller agitators", *Journal of Chemical Engineering of Japan,* vol. 40, no. 8, pp. 684-691.

Lightnin, 2006, "Impellers", www.lightnin-mixers.com, Accessed 26 July 2006.

Lilly, D.K. 1966, "On the application of the eddy viscosity concept in the inertial subrange of turbulence", *NCAR Manuscript 123.*

Lilly, D.K. 1992, "Proposed modification of the Germano subgrid-scale closure method", *Physics of Fluids A (Fluid Dynamics),* vol. 4, no. 3, pp. 633.

Lindken, R. & Merzkirch, W. 2002, "A novel PIV technique for measurements in multiphase flows and its application to two-phase bubbly flows", *Experiments in Fluids,* vol. 33, no. 6, pp. 814-825.

Linek, V., Benes, P., Vacek, V. & Hovorka, F. 1982, "Analysis of differences in k_La values determined by steady-state and dynamic methods in stirred tanks", *Chemical Engineering Journal and the Biochemical Engineering Journal,* vol. 25, no. 1, pp. 77-88.

Lines, P.C. 2000, "Gas-liquid mass transfer using surface-aeration in stirred vessels, with dual impellers", *Chemical Engineering Research and Design,* vol. 78, no. 3, pp. 342-347.

Lu, W. & Chen, H. 1986, "Flooding and critical impeller speed for gas dispersion in aerated turbine-agitated vessels", *Chemical Engineering Journal and the Biochemical Engineering Journal,* vol. 33, no. 2, pp. 57-62.

Lu, W. & Ju, S. 1987, "Local gas holdup, mean liquid velocity and turbulence in an aerated stirred tank using hot-film anemometry", *Chemical Engineering Journal and the Biochemical Engineering Journal,* vol. 35, no. 1, pp. 9-17.

Lu, W. & Ju, S. 1989, "Cavity configuration, flooding and pumping capacity of disc-type turbines in aerated stirred tanks", *Chemical Engineering Science,* vol. 44, no. 2, pp. 333-342.

Lu, W. M., Hsu, R.C., Chien, W.C. & Lin L.C. 1993, "Measurement of local bubbles diameters and analysis of gas dispersion in an aerated vessel with disc-turbine impeller", *Journal of Chemical Engineering of Japan*, vol. **26**, pp. 551-557.

Lu, W., Wu, H., Chuang, N. & Lin, Y. 2000, "Effect of the blade size on the vortex structure and gas dispersion in gas-liquid stirred vessels with a single Rushton turbine impeller", *Proceedings of the National Science Council,*

Republic of China, Part A: Physical Science and Engineering, vol. 24, no. 3, pp. 166-175.

Lu, W.M. & Wu, H.Z. 2001, "Gas Dispersion Mechanism around the Rushton Turbine Impeller in a Mechanically Stirred Vessel", *Journal of Chemical Engineering of Japan*, vol. 34, pp. 662-670.

Luo, H., 1993, "Coalescence, breakup and liquid circulation in bubble column reactors", *D.Sc. Thesis*, Norwegian Institute of Technology.

Luo, H. & Svendsen, H.F. 1996, "Theoretical model for drop and bubble breakup in turbulent dispersions", *AICHE Journal,* vol. 42, no. 5, pp. 1225-1233.

Machon, V., Pacek, A.W. & Nienow, A.W. 1997, "Bubble sizes in electrolyte and alcohol solutions in a turbulent stirred vessel", *Chemical Engineering Research & Design,* vol. 75, pp. 339-348.

Marchal, P., David, R., Klein, J.P. & Villermaux, J. 1988, "Crystallization and precipitation engineering—I. An efficient method for solving population balance in crystallization with agglomeration", *Chemical Engineering Science,* vol. 43, no. 1, pp. 59-67.

Marchisio, D.L., Vigil, R.D. & Fox, R.O. 2003, "Quadrature method of moments for aggregation-breakage processes", *Journal of colloid and interface science,* vol. 258, no. 2, pp. 322-334.

Martínez-Bazán, C., Montañéz, J.L. & Lasheras, J.C. 1999, "On the breakup of an air bubble injected into a fully developed turbulent flow. Part 1. Breakup frequency", *Journal of Fluid Mechanics*, vol. **401**, pp. 157–182.

McGraw, R. 1997, "Description of aerosol dynamics by the quadrature method of moments", *Aerosol Science and Technology,* vol. 27, no. 2, pp. 255-265.

McGraw, R. & Wright, D.L. 2003, "Chemically resolved aerosol dynamics for internal mixtures by the quadrature method of moments", *Journal of Aerosol Science,* vol. 34, no. 2, pp. 189-209.

Melzak, Z.A. 1953, "The effects of coalescence in certain collision processes", *Q. J. Appl. Math.* Vol. 11, pp. 231.

Middleton J.C., Smith J.M. 2004, "Gas-liquid mixing in turbulent system", (Chapter 11 in *Handbook of industrial mixing, science and practice*, ed., Paul, E. L., Atiemo-Obeng, V. A., Kresta, S. M.), John Wiley & Sons, New Jersey, USA, pp. 585 – 638.

Miettinen, T., Laakkonen, M., Aittamaa, J. 2002, "The applicability of various flow visulization techniques for the characterization of gas-liquid flow in mixed tanks", AIChE 2002 annual meeting, Nov 3-11, *Industrial mixing and scale down*, Indianapolis, USA.

Min, J., Bao, Y., Chen, L., Gao, Z. & Smith, J.M. 2008, "Numerical simulation of gas dispersion in an aerated stirred reactor with multiple impellers", *Industrial and Engineering Chemistry Research,* vol. 47, no. 18, pp. 7112-7117.

Moilanen, P., Laakkonen, M. & Aittamaa, J. 2006, "Modeling aerated fermenters with computational fluid dynamics", *Industrial and Engineering Chemistry Research,* vol. 45, no. 25, pp. 8656-8663.

Moilanen, P., Laakkonen, M., Visuri, O. & Aittamaa, J. 2007, "Modeling local gas-liquid mass transfer in agitated viscous shear-thinning dispersions with CFD", *Industrial and Engineering Chemistry Research,* vol. 46, no. 22, pp. 7289-7299.

Moilanen, P., Laakkonen, M., Visuri, O., Alopaeus, V. & Aittamaa, J. 2008, "Modelling mass transfer in an aerated 0.2 m3 vessel agitated by Rushton, Phasejet and Combijet impellers", *Chemical Engineering Journal,* vol. 142, no. 1, pp. 95-108.

Montante, G., Paglianti, A. & Magelli, F. 2007, "Experimental Analysis and Computational Modelling of Gas–Liquid Stirred Vessels", *Chemical Engineering Research and Design,* vol. 85, no. 5, pp. 647-653.

Montante, G., Horn, D. & Paglianti, A. 2008, "Gas–liquid flow and bubble size distribution in stirred tanks", *Chemical Engineering Science,* vol. 63, no. 8, pp. 2107-2118.

Morud, K.E. & Hjertager, B.H. 1996, "LDA measurements and CFD modelling of gas-liquid flow in a stirred vessel", *Chemical Engineering Science,* vol. 51, no. 2, pp. 233-249.

Myers, K.J., Thomas, A.J., Barker, A. & Reeder, M.F. 1999, "Performance of a Gas Dispersion Impeller with Vertically Asymmetric Blades", *Chemical Engineering Research and Design,* vol. 77, no. 8, pp. 728-730.

Myers, K., Reeder, M., Bakker, A. & Rigden, M. 1996, "Agitating for success", *Chemical Engineer,* vol. 620, pp. 39-42.

Nere, N.K., Patwardhan, A.W. & Joshi, J.B. 2001, "Prediction of flow pattern in stirred tanks: New constitutive equation for eddy viscosity", *Industrial and Engineering Chemistry Research,* vol. 40, no. 7, pp. 1755-1772.

Nienow, A.W. 1996, "Gas-liquid mixing studies: A comparison of Rushton turbines with some modern impellers", *Chemical Engineering Research & Design,* vol. 74, pp. 417-423.

Nocentini, M., Magelli, F., Pasquali, G. & Fajner, D. 1988, "Fluid-dynamic study of a gas-liquid, non-standard vessel stirred by multiple impellers", *Chemical Engineering Journal and the Biochemical Engineering Journal,* vol. 37, no. 1, pp. 53-59.

Nouri, J.M. & Whitelaw, J.H. 1992, "Particle velocity characteristics of dilute to moderately dense suspension flows in stirred reactors", *International Journal of Multiphase Flow,* vol. 18, no. 1, pp. 21-33.

Ochieng, A., Onyango, M.S., Kumar, A., Kiriamiti, K. & Musonge, P. 2008, "Mixing in a tank stirred by a Rushton turbine at a low clearance", *Chemical Engineering and Processing: Process Intensification,* vol. 47, no. 5, pp. 842-851.

Oldshue, J.Y. 1966, "Fermentation mixing scale-up techniques", *Biotechnology Bioengineering*, vol. **VIII**, pp. 3–24.

Otomo, N., Bujalski, W., Nienow, A.W. & Takahashi, K. 2003, "Gassed power consumption and gas hold-up for a dual hollow blade impeller system in a stirred vessel", *Journal of Chemical Engineering of Japan,* vol. 36, no. 8, pp. 905-911.

Paglianti, A., Pintus, S. & Giona, M. 2000, "Time-series analysis approach for the identification of flooding/loading transition in gas-liquid stirred tank reactors", *Chemical Engineering Science,* vol. 55, no. 23, pp. 5793-5802.

Paglianti, A., Fujasova, M. & Montante, G. 2008, "A simple model for power consumption in gassed and boiling stirred vessels", *AICHE Journal,* vol. 54, no. 3, pp. 646-656.

Patwardhan, A.W. 2001, "Prediction of flow characteristics and energy balance for a variety of downflow impellers", *Industrial and Engineering Chemistry Research,* vol. 40, no. 17, pp. 3806-3816.

Patwardhan, A.W. & Joshi, J.B. 1999, "Relation between flow pattern and blending in stirred tanks", *Industrial and Engineering Chemistry Research,* vol. 38, no. 8, pp. 3131-3143.

Patwardhan, A.W., Joshi, J.B., Fotedar, S. & Mathew, T. 2005, "Optimization of gas–liquid reactor using computational fluid dynamics", *Chemical Engineering Science,* vol. 60, no. 11, pp. 3081-3089.

Petitti, M., Caramellino, M., Marchisio, D.L. & Vanni, M. 2007, "Two-scale simulation of mass transfer in an agitated gas-liquid tank", *ICMF 2007,* Leipzig, 9-13 July 2007.

Pinelli, D., Bakker, A., Myers, K.J., Reeder, M.F., Fasano, J. & Magelli, F. 2003, "Some features of a novel gas dispersion impeller in a dual-impeller configuration", *Chemical Engineering Research and Design,* vol. 81, no. 4, pp. 448-454.

Podila, K., Al Taweel, A.M., Koksal, M., Troshko, A. & Gupta, Y.P. 2007, "CFD simulation of gas-liquid contacting in tubular reactors", *Chemical Engineering Science,* vol. 62, no. 24, pp. 7151-7162.

Pohorecki, R., Moniuk, W., Bielski, P. & Sobieszuk, P. 2005, "Diameter of bubbles in bubble column reactors operating with organic liquids", *Chemical Engineering Research and Design,* vol. 83, no. 7, pp. 827-832.

Poncin, S., Nguyen, C., Midoux, N. & Breysse, J. 2002, "Hydrodynamics and volumetric gas-liquid mass transfer coefficient of a stirred vessel equipped with a gas-inducing impeller", *Chemical Engineering Science,* vol. 57, no. 16, pp. 3299-3306.

Press, W.H., Flannery, B.P., Teukolsky, S.A. & Vetterling, W.T. 1992, "*Numerical Recipes in C: The Art of Scientific Computing*" (2nd ed), Cambridge University Press (1992).

Prince, M.J. & Blanch, H.W. 1990, "Bubble coalescence and break-up in air-sparged bubble columns", *AICHE Journal,* vol. 36, no. 10, pp. 1485-1499.

Ranade, V.V. & Joshi, J.B. 1990, "Flow generated by a disc turbine. Part II. Mathematical modelling and comparison with experimental data", *Chemical Engineering Research & Design,* vol. 68, no. 1, pp. 34-50.

Ranade, V.V., Perrard, M., Xuereb, C., Le Sauze, N. & Bertrand, J. 2001, "Influence of gas flow rate on the structure of trailing vortices of a rushton turbine: PIV measurements and CFD simulations", *Chemical Engineering Research and Design,* vol. 79, no. 8, pp. 957-964.

Randolph, A. D. & Larson, M. A. 1971, "*Theory of particulate processes: Analysis and techniques of continuous crystallization*" New York, Academic Press.

Randolph, A.D. & Larson, M.A. 1988, "*Theory of Particulate Processes*" (second ed.), Academic Press, New York.

Reiher, T. 1978, "Statilitatsuntersuchungen bei ruckwartigen Dierentiationsformeln in Abhangigkeit von einem Parameter", Tech. Report #11, Sektion Mathematik, Humboldt-Universitat zu Berlin.

Revstedt, J., Fuchs, L. & Tragardh, C. 1998, "Large eddy simulations of the turbulent flow in a stirred reactor", *Chemical Engineering Science,* vol. 53, no. 24, pp. 4041-4053.

Rod, V. & Misek, T. 1982, "Stochastic modelling of dispersion formation in agitated liquid-liquid systems", *Transactions of the Institution of Chemical Engineers,* vol. 60, no. 1, pp. 48-53.

Rosner, D.E. & Pyykonen, J.J. 2002, "Bivariate moment simulation of coagulating and sintering nanoparticles in flames", *AICHE Journal,* vol. 48, no. 3, pp. 476-491.

Rotta, J.C. 1972, "*Turbulente Stromungen*", B .G. Teubner, Stuttgart.

Rutherford, K., Mahmoudi, S.M.S., Lee, K.C. & Yianneskis, M. 1996, "Influence of Rushton impeller blade and disk thickness on the mixing characteristics of stirred vessels", *Chemical Engineering Research & Design,* vol. 74, pp. 369-378.

Sardeing, R., Aubin, J., Poux, M. & Xuereb, C. 2004, "Gas–Liquid Mass Transfer: Influence of Sparger Location", *Chemical Engineering Research and Design,* vol. 82, no. 9, pp. 1161-1168.

Sbrizzai, F., Lavezzo, V., Verzicco, R., Campolo, M. & Soldati, A. 2006, "Direct numerical simulation of turbulent particle dispersion in an unbaffled stirred-tank reactor", *Chemical Engineering Science,* vol. 61, no. 9, pp. 2843-2851.

Scargiali, F., D'Orazio, A., Grisafi, F. & Brucato, A. 2007, "Modelling and Simulation of Gas–Liquid Hydrodynamics in Mechanically Stirred Tanks", *Chemical Engineering Research and Design,* vol. 85, no. 5, pp. 637-646.

Schwartzberg, H.G. & Treybal, R.E. 1968, "Fluid and particle motion in turbulent sirred tanks -- Particle motion", *Industrial and Engineering Chemistry -- Fundamentals,* vol. 7, no. 1, pp. 6-12.

Scott, W.T. 1968, "Analytic studies on cloud droplet coalescence", *J. Atmos. Sci.* vol. 25, pp. 54.

Schiller, L. & Naumann, L. 1935, "A drag coefficient correlation", *Z Ver Deutsch Ing*, vol. **77**, p. 318.

Schuetze J. & Hengstler, J. 2006, "Assessing aerated bioreactor performance using CFD", *Proceedings of the 12th European Conference on Mixing* Bologna, June 27–30, pp. 439–446.

Shampine, L.F. & Reichelt, M.W. 1997, "MATLAB ODE suite", *SIAM Journal on Scientific Computing,* vol. 18, no. 1, pp. 1-22.

Shih, T.-H., Liou, W.W., Shabbir, A., Yang, Z., Zhu, J. 1995, "A new k-ε eddy viscosity model for high Reynolds number turbulent flows", *Computers & Fluids*, vol. 24, no. 3, pp. 227-238.

Shimizu, K., Takada, S., Minekawa, K. & Kawase, Y. 2000, "Phenomenological model for bubble column reactors: prediction of gas hold-ups and volumetric mass transfer coefficients", *Chemical Engineering Journal,* vol. 78, no. 1, pp. 21-28.

Shukla, V.B., Parasu Veera, U., Kulkarni, P.R. & Pandit, A.B. 2001, "Scale-up of biotransformation process in stirred tank reactor using dual impeller bioreactor", *Biochemical Engineering Journal,* vol. 8, no. 1, pp. 19-29.

Smagorinsky, J. 1963, "General Circulation Experiments with the Primitive Equations. I. The Basic Experiment", *Month. Wea. Rev.*, vol. 91, pp. 99-164.

Smith, J.M. 2006, "Large Multiphase Reactors: Some Open Questions", *Chemical Engineering Research and Design,* vol. 84, no. 4, pp. 265-271.

Smith, J.M. & Gao, Z. 2001, "Power demand of gas dispersing impellers under high load conditions", *Chemical Engineering Research and Design,* vol. 79, no. 5, pp. 575-580.

Smith, J.M., Gao, Z. & Middleton, J.C. 2001, "The unsparged power demand of modern gas dispersing impeller in boiling liquids", *Chemical Engineering Journal,* vol. 84, no. 1, pp. 15-21.

Soderberg A. C. 1997, "Fermentation design", (Chapter 2 in *Fermentation and biochemical engineering handbook: principles, process design, and equipment*, ed. Vogel H. C. and Todaro C. L.) Noyes Publications, Westwood, N.J. pp. 67-120.

Spalart, P. R., Allmaras, S. R. 1992, "A One-Equation Turbulence Model for Aerodynamic Flows", *AIAA Paper* 92-0439.

Spalart P. R. 2001, "Young-Person's Guide to Detached-Eddy Simulation Grids", NASA/CR-2001-211032.

Spalart, P.R., Jou, W.-H., Strelets, M., Allmaras, S.R. 1997, "Comments on the Feasibility of LES for Wings, and on a Hybrid RANS/LES Approach", Advances in DNS/LES, 1st *AFOSR Int. Conference on DNS/LES*, 4–8 Aug. Greyden Press, Columbus, OH.

Squires, K.D., Forsythe, J.R. & Spalart, P.R. 2005, "Detached-eddy simulation of the separated flow over a rounded-corner square", *Journal of Fluids Engineering,* vol. 127, no. 5, pp. 959-966.

Stanbury, P. F. and Whitaker, A. 1984, "Principles of fermentation technology", Pergamon Press Ltd, Oxford.

Stenberg, O. & Andersson, B. 1988, "Gas-liquid mass transfer in agitated vessels - II. Modelling of gas-liquid mass transfer", *Chemical Engineering Science,* vol. 43, no. 3, pp. 725-730.

Stoots, C.M. & Calabrese, R.V. 1995, "Mean velocity field relative to a rushton turbine blade", *AICHE Journal,* vol. 41, no. 1, pp. 1-11.

Sudiyo, R. & Andersson, B. 2007, "Bubble trapping and coalescence at the baffles in stirred tank reactors", *AICHE Journal,* vol. 53, no. 9, pp. 2232-2239.

Sutugin, A.G. and Fuchs, N.A. 1970. Formation of condensation aerosols under rapidly changing environmental conditions. Theory and method of calculation, *Journal of Aerosol Science*, vol. **1**, pp. 287-293.

Sun, H., Mao, Z. & Yu, G. 2006, "Experimental and numerical study of gas hold-up in surface aerated stirred tanks", *Chemical Engineering Science,* vol. 61, no. 12, pp. 4098-4110.

Tatterson, G.B. 1994, "Scale-up and design of industrial mixing processes", MGraw-Hill Inc, New York.

Tolfo, F. 1977, "A simplified model of aerosol coagulation", *Journal of Aerosol Science,* vol. 8, no. 1, pp. 9-19.

Torré, J., Fletcher, D.F., Lasuye, T. & Xuereb, C. 2007, "Single and multiphase CFD approaches for modelling partially baffled stirred vessels: Comparison of experimental data with numerical predictions", *Chemical Engineering Science,* vol. 62, no. 22, pp. 6246-6262.

Tu, J., Yeoh, G.H. & Liu, C., 2008, "*Computational fluid dynamics: A practical approach*", Butterworth-Heinemann Elsevier, USA.

Tyagi, M., Roy, S., Harvey III, A.D. & Acharya, S. 2007, "Simulation of laminar and turbulent impeller stirred tanks using immersed boundary method and large eddy simulation technique in multi-block curvilinear geometries", *Chemical Engineering Science,* vol. 62, no. 5, pp. 1351-1363.

Van 't Riet, K. & Smith, J.M. 1975, "Trailing vortex system produced by Rushton turbine agitators", *Chemical Engineering Science,* vol. 30, no. 9, pp. 1093-1105.

Van't Riet, K. 1979, "Review of measuring methods and results in nonviscous gas-liquid mass transfer in stirred vessels", *Industrial & Engineering Chemistry, Process Design and Development,* vol. 18, no. 3, pp. 357-364.

Vasconcelos, J.M.T., Alves, S.S. & Barata, J.M. 1995, "Mixing in gas-liquid contactors agitated by multiple turbines", *Chemical Engineering Science,* vol. 50, no. 14, pp. 2343-2354.

Veera, U.P., Patwardhan, A.W. & Joshi, J.B. 2001, "Measurement of gas hold-up profiles in stirred tank reactors by gamma ray attenuation technique", *Chemical Engineering Research and Design,* vol. 79, no. 6, pp. 684-688.

Venneker, B.C.H., Derksen, J.J. & Van, d.A. 2002, "Population balance modeling of aerated stirred vessels based on CFD", *AICHE Journal,* vol. 48, no. 4, pp. 673-685.

Verzicco, R., Fatica, M., Iaccarino, G. & Orlandi, P. 2004, "Flow in an impeller-stirred tank using an immersed-boundary method", *AICHE Journal,* vol. 50, no. 6, pp. 1109-1118.

Vlaev, D., Mann, R., Lossev, V., Vlaev, S.D., Zahradnik, J. & Seichter, P. 2000, "Macro-Mixing and Streptomyces fradiae: Modelling Oxygen and Nutrient

Segregation in an Industrial Bioreactor", *Chemical Engineering Research and Design,* vol. 78, no. 3, pp. 354-362.

Vlaev, S.D., Staykov, P. & Popov, R. 2004, "Pressure distribution at impeller blades of some radial flow impellers in saccharose and xanthan gum solutions: A CFD visualization approach", *Food and Bioproducts Processing,* vol. 82, no. 1, pp. 13-20.

Vrábel, P., van der Lans, R.G.J.M., Luyben, K.C.A.M., Boon, L. & Nienow, A.W. 2000, "Mixing in large-scale vessels stirred with multiple radial or radial and axial up-pumping impellers: modelling and measurements", *Chemical Engineering Science,* vol. 55, no. 23, pp. 5881-5896.

Wang, M., Dorward, A., Vlaev, D. & Mann, R. 2000, "Measurements of gas-liquid mixing in a stirred vessel using electrical resistance tomography (ERT)", *Chemical Engineering Journal,* vol. 77, no. 1, pp. 93-98.

Wang, W., Mao, Z. & Yang, C. 2006, "Experimental and numerical investigation on gas holdup and flooding in an aerated stirred tank with Rushton impeller", *Industrial and Engineering Chemistry Research,* vol. 45, no. 3, pp. 1141-1151.

Warmoeskerken, M.M.C.G. & Smith, J.M. 1989, "Hollow blade agitator for dispersion and mass transfer", *Chemical Engineering Research & Design,* vol. 67, no. 2, pp. 193-198.

Warmoeskerken M.M.C.G. & Smith, J.M. 1982, "Description of the power curves of turbine stirred gas-liquid dispersions". In: *Proc. 4th European Conf. on Mixing*, Noordwijkerhout, The Netherlands, pp. 237–246.

Warmoeskerken, M.M.C.G. & Smith, J.M. 1985, "Flooding of disc turbines in gas-liquid dispersions: a new description of the phenomenon", *Chemical Engineering Science,* vol. 40, no. 11, pp. 2063-2071.

Wei, H., Zhou, W. & Garside, J. 2001, "Computational fluid dynamics modeling of the precipitation process in a semibatch crystallizer", *Industrial and Engineering Chemistry Research,* vol. 40, no. 23, pp. 5255-5261.

Wellek, R.M., Agrawal, A.K. & Skelland, A.H.P. 1966, "Shape of liquid drops moving in liquid media", *A.I.Ch.E.Journal,* vol. 12, no. 5, pp. 854-862.

Wilkinson, P.M. 1991, "Physical Aspects and Scale-up of High Pressure Bubble Columns", *D.Sc. Thesis*, University of Groningen, The Netherlands.

Wong, I., García, M.A., Rodríguez, I., Ramos, L.B. & Olivera, V. 2003, "Fermentation scale up for production of antigen K88 expressed in Escherichia coli", *Process Biochemistry,* vol. 38, no. 9, pp. 1295-1299.

Wong, I., Hernández, A., García, M.A., Segura, R. & Rodríguez, I. 2002, "Fermentation scale up for recombinant K99 antigen production cloned in Escherichia coli MC1061", *Process Biochemistry,* vol. 37, no. 11, pp. 1195-1199.

Woo, X.Y., Tan, R.B.H., Chow, P.S. & Braatz, R.D. 2006, "Simulation of Mixing Effects in Antisolvent Crystallization Using a Coupled CFD-PDF-PBE Approach", *Crystal Growth & Design,* vol. 6, no. 6, pp. 1291-1303.

Wright, D.L., McGraw, R. & Rosner, D.E. 2001, "Bivariate extension of the quadrature method of moments for modeling simultaneous coagulation and sintering of particle populations", *Journal of colloid and interface science,* vol. 236, no. 2, pp. 242-251.

Wu, H. & Patterson, G.K. 1989, "Laser-doppler measurements of turbulent-flow parameters in a stirred mixer", *Chemical Engineering Science,* vol. 44, no. 10, pp. 2207-2221.

Yakhot, V. & Orszag, S.A. 1986, "Renormalization group analysis of turbulence. I. Basic theory", *Journal of Scientific Computing,* vol. 1, no. 1, pp. 3-51.

Yapici, K., Karasozen, B., Schäfer, M. & Uludag, Y. 2008, "Numerical investigation of the effect of the Rushton type turbine design factors on agitated tank flow characteristics", *Chemical Engineering and Processing: Process Intensification,* vol. 47, no. 8, pp. 1340-1349.

Yeoh, G.H. & Tu, J.Y. 2005, "A unified model considering force balances for departing vapour bubbles and population balance in subcooled boiling flow", *Nuclear Engineering and Design,* vol. 235, no. 10-12, pp. 1251-1265.

Yeoh, S.L., Papadakis, G., Lee, K.C. & Yianneskis, M. 2004, "Large Eddy Simulation of turbulent flow in a Rushton impeller stirred reactor with sliding-deforming mesh methodology", *Chemical Engineering and Technology,* vol. 27, no. 3, pp. 257-263.

Yianneskis, M., Popiolek, Z. & Whitelaw, J.H. 1987, "Experimental study of the steady and unsteady flow characteristics of stirred reactors", *Journal of Fluid Mechanics,* vol. 175, pp. 537-555.

Yianneskis, M. & Whitelaw, J.H. 1993, "On the structure of the trailing vortices around Rushton turbine blades", *Chemical Engineering Research & Design,* vol. 71, pp. 543-550.

Yoon, H.S., Balachandar, S., Ha, M.Y. & Kar, K. 2003, "Large eddy simulation of flow in a stirred tank", *Journal of Fluids Engineering, Transactions of the ASME,* vol. 125, no. 3, pp. 486-499.

Zahradník, J., Mann, R., Fialová, M., Vlaev, D., Vlaev, S.D., Lossev, V. & Seichter, P. 2001, "A networks-of-zones analysis of mixing and mass transfer in three industrial bioreactors", *Chemical Engineering Science,* vol. 56, no. 2, pp. 485-492.

Zhang, Y., Yang, C. & Mao, Z. 2008, "Large Eddy simulation of the gas-liquid flow in a stirred tank", *AICHE Journal,* vol. 54, no. 8, pp. 1963-1974.

Zhou, G. & Kresta, S.M. 1996, "Distribution of energy between convective and turbulent flow for three frequently used impellers", *Chemical Engineering Research & Design,* vol. 74, pp. 379-389.

Zhu, Y., Bandopadhayay, P.C. & Wu, J. 2001, "Measurement of gas-liquid mass transfer in an agitated vessel-A comparison between different impellers", *Journal of Chemical Engineering of Japan,* vol. 34, no. 5, pp. 579-584.

Appendix

Derivation of analytical solution for power-law growth

PBE for growth only problem is given by:

$$\frac{\partial n}{\partial t}+\frac{\partial(Gn)}{\partial L}=0 \tag{A.1}$$

$$\frac{\partial n}{\partial t}+G\frac{\partial n}{\partial L}+n\frac{\partial G}{\partial L}=0 \tag{A.2}$$

The growth law is give by:

$$G=bL^{p} \tag{A.3}$$

After differentiation, the growth law:

$$\frac{dG}{dL}=bpL^{p-1} \tag{A.4}$$

Replacing equation A.4 into equation A.2:

$$\frac{\partial n}{\partial t}+G\frac{\partial n}{\partial L}=-nbpL^{p-1} \tag{A.5}$$

From method of characteristic, the characteristic line in which the PDE reduces to ODEs can be represented as follows:

$$n(L,t)=n(L(s),t(s)) \tag{A.6}$$

Applying the chain rule:

$$\frac{\partial n}{\partial s}=\frac{dL}{ds}\frac{\partial n}{\partial L}+\frac{dt}{ds}\frac{\partial n}{\partial L} \tag{A.7}$$

Comparing equation A.7 to A.5:

$$\begin{aligned}\frac{dt}{ds}&=1\\ \frac{dL}{ds}&=G\\ \frac{dn}{ds}&=-nbpL^{p-1}\end{aligned} \tag{A.8}$$

Since $t - t_0 = s - s_0$ assuming $t_0 = s_0 = 0$, thus $t = s$. The equations A.8 become:

$$\frac{dL}{dt}=bL^{p} \tag{A.9}$$

$$\frac{dn}{dt}=-nbpL^{p-1} \tag{A.10}$$

Integrating equation A.9 with respect to L and t:

$$\int_{L_0}^{L}\frac{dL}{L^p}=b\int_0^t dt$$

$$\left[\left(\frac{1}{1-p}\right)L^{1-p}\right]_{L_0}^{L}=bt \tag{A.11}$$

$$L=\left(L_0^{1-p}+(1-p)bt\right)^{\frac{1}{1-p}} \tag{A.12}$$

$$L_0=\left(L^{1-p}-(1-p)bt\right)^{\frac{1}{1-p}} \tag{A.13}$$

Integrating equation A.10:

$$\int_{n_0}^{n}\frac{dn}{n}=-bp\int_0^t L^{p-1}dt \tag{A.14}$$

$$\begin{aligned}\ln\frac{n}{n_0} &= -bp\int_0^t\frac{1}{L_0^{1-p}+(1-p)bt}dt\\ &=\left[-bp\frac{1}{(1-p)b}\ln\left(L_0^{1-p}+(1-p)bt\right)\right]_0^t\\ &=\frac{p}{p-1}\ln\left(\frac{L_0^{1-p}+(1-p)bt}{L_0^{1-p}}\right)\\ &=\ln\left(1+\frac{(1-p)bt}{L_0^{1-p}}\right)^{\frac{p}{p-1}}\end{aligned} \tag{A.15}$$

After rearranging:

$$n=n_0\left(1+\frac{(1-p)bt}{L_0^{1-p}}\right)^{\frac{p}{p-1}} \tag{A.16}$$

Replace L_0 with equation A.13:

$$
\begin{aligned}
n &= n_0(L_0)\left(1+\frac{(1-p)bt}{L^{1-p}-(1-p)bt}\right)^{\frac{p}{p-1}} \\
&= n_0(L_0)\left(\frac{L^{1-p}-(1-p)bt+(1-p)bt}{L^{1-p}-(1-p)bt}\right)^{\frac{p}{p-1}} \\
&= n_0(L_0)\left(\frac{L^{1-p}-(1-p)bt}{L^{1-p}}\right)^{\frac{p}{1-p}} \\
&= n_0(L_0)\left(1-\frac{(1-p)bt}{L^{1-p}}\right)^{\frac{p}{1-p}}
\end{aligned}
\qquad \text{(A.17)}
$$

The normal distribution is given by:

$$
\text{pdf} = \frac{1}{\sigma\sqrt{2\pi}}\exp\left(-\frac{(L-\bar{L})^2}{2\sigma^2}\right) \qquad \text{(A.18)}
$$

The final distribution at any time *t* is given by:

$$
n(L) = \frac{1}{\sigma\sqrt{2\pi}}\exp\left(-\frac{\left(\left(L^{1-p}+(1-p)bt\right)^{\frac{1}{1-p}}-\bar{L}\right)^2}{2\sigma^2}\right)\left(1-\frac{(1-p)bt}{L^{1-p}}\right)^{\frac{p}{1-p}} \qquad \text{(A.19)}
$$

Relevant Publications & Seminars/Conferences Presentation

Journals

1) J Gimbun, CD Rielly, ZK Nagy, Modelling of mass transfer in gas-liquid stirred tanks agitated by rushton turbine and CD-6 impeller: a scale-up study, *Chem Eng Res Des*, 87: 437-451.
2) J Gimbun, CD Rielly, ZK Nagy, Detached eddy simulation on turbulence flows in a stirred tank, *AIChEJ,* in preparation.
3) J Gimbun, ZK Nagy, CD Rielly, Simultaneous quadrature method of moments for the solution of population balance equations, using a differential algebraic equation framework, *Ind. Chem. Eng. Res.* submitted, Ref. no.: ie-2009-00548s.

Conferences

4) J. Gimbun, ZK Nagy, CD Rielly, CFD and PBM of gas-liquid stirred tanks, *ISMIP VI*, 16-21 Aug 2008, Niagara on the Lake, Canada.
5) J Gimbun, CD Rielly, ZK Nagy, Modelling of mass transfer in gas-liquid stirred tanks agitated by rushton turbine and CD-6 impeller, *European Conference on Mixing 13*, King College London, 11-13 April 2009.

Awards

6) Third prize winner at IChemE Fluid Mixing Processes Subject Group student competition 2009, King College, 7 January 2009.

Seminars

7) J. Gimbun, CD Rielly, ZK Nagy, Modelling of mass transfer in gas-liquid stirred tanks agitated by rushton turbine and cd-6 impeller: a scale-up study, IChemE FMPSG student competition 2009, King College, 7 January 2009.
8) J. Gimbun, ZK Nagy, CD Rielly, CFD and PBM of gas-liquid flow via QMOM, IChemE FMPSG student competition 2008, Loughborough University, 17 March 2008.
9) J. Gimbun, DES and RANS modelling of turbulence flows in a stirred tank, IChemE FMPSG student competition 2007, Birmingham University, 27 April 2007.
10) J. Gimbun, CFD and Population balance modelling of gas-liquid bioreactors, Pharmaceutical Crystallization Group Meeting, 27 June 2007
11) J. Gimbun, CFD of mixing tank, Pharmaceutical Crystallization Group Meeting, 30 May 2008
12) J. Gimbun, CFD and population balance modelling of gas-liquid flows, Chemical engineering research student seminar 2007, Loughborough University, 19 June 2007.